A NOVEL IN VIVO SYNCHROTRON RADIATION MICRO-CT IMAGING PLATFORM FOR THE DIRECT TRACKING OF REMODELING EVENTS IN CORTICAL BONE

A Thesis Submitted to the

College of Graduate and Postdoctoral Studies

In Partial Fulfillment of the Requirements

For the Degree of Doctor of Philosophy

In the Department of Anatomy, Physiology and Pharmacology

University of Saskatchewan

Saskatoon

By Kimberly Dawn Harrison

PERMISSION TO USE

In presenting this thesis/dissertation in partial fulfillment of the requirements for a Postgraduate degree from the University of Saskatchewan, I agree that the Libraries of this University may make it freely available for inspection. I further agree that permission for copying of this thesis/dissertation in any manner, in whole or in part, for scholarly purposes may be granted by the professor or professors who supervised my thesis/dissertation work or, in their absence, by the Head of the Department or the Dean of the College in which my thesis work was done. It is understood that any copying or publication or use of this thesis/dissertation or parts thereof for financial gain shall not be allowed without my written permission. It is also understood that due recognition shall be given to me and to the University of Saskatchewan in any scholarly use which may be made of any material in my thesis/dissertation.

Requests for permission to copy or to make other uses of materials in this thesis/dissertation in whole or part should be addressed to:

Head of the Department of Anatomy, Physiology and Pharmacology

Health Science Building

107 Wiggins Rd

University of Saskatchewan

Saskatoon, Saskatchewan S7N 5E5 Canada

OR

Dean

College of Graduate and Postdoctoral Studies

University of Saskatchewan

116 Thorvaldson Building, 110 Science Place

Saskatoon, Saskatchewan S7N 5C9 Canada

ABSTRACT

Throughout life, bone tissue continuously alters its microarchitecture in response to microdamage and other stimuli through remodeling. Specialized cellular groupings, Basic Multicellular Units (BMUs), conduct remodeling through 'coupling' bone resorption to formation. Osteoclasts within a BMU's cutting cone create a localized cylindrical space which osteoblasts concentrically refill, creating a secondary osteon (a.k.a. Haversian system). Continual production of secondary osteons by multitudes of BMUs creates a vast interconnected vascular network that permeates the cortex of bone, and therefore, BMUs are essential components in the overall maintenance of bone health. However, with increasing age or diseased states, such as osteoporosis (OP), remodeling can destabilize where resorbed bone is not entirely replaced (unbalanced) and/or where BMUs become 'uncoupled' preventing initiation of the bone formation following resorption. This increases porosity and thins cortices, leading to fragile, brittle bones much more susceptible to fracture. BMU behavior has never been replicated *in vitro* nor directly observed *in vivo*. The resorptive characteristics of BMUs, such as Longitudinal Erosion Rate (LER) – the rate of the advance of the cutting cone over time – are particularly poorly understood as our current understanding is inferred from indirect histological assessment of bone formation. Critically, BMUs have never been imaged in 4D (3D over time) due to limitations imposed by the radiation dose associated with conventional absorption-based imaging. This thesis explores in-line phase contrast synchrotron radiation micro-CT (SR micro-CT) as means of overcoming the limitations of conventional imaging. The goal was to develop a novel pre-clinical (animal) platform capable of directly tracking individual BMUs. The specific objectives of my thesis research were: 1) develop an *in vivo* imaging protocol to target individual BMU remodeling events within rabbit tibiae cortical bone to permit longitudinal imaging, using in-line phase contrast SR micro-CT; 2) Within rabbits, implement OP models of ovariectomy, glucocorticoids, a combination thereof and parathyroid hormone (PTH) to elevate cortical bone remodeling rates and, thus, the ability to observe BMU behavior on a large scale; and 3) directly measure BMU LER in 4D for the first time. A novel SR micro-CT protocol capable of detecting cortical porosity without any apparent radiation impacts was successfully developed on the BioMedical Imaging and Therapy Beamline of the Canadian Light Source. Compared to sham controls, elevated remodeling was found for all the OP models. PTH induced the highest rate of remodeling and it was selected as the model for direct assessment of LER.

Through a novel co-registration technique, where *in vivo* SR micro-CT and follow-up *ex vivo* micro-CT scans acquired two weeks later were combined, LER (23.79 μm/day) was directly assessed for the first time. This novel platform establishes a means of investigating BMU spatio-temporal behavior and thus has great potential to advance our understanding of the role of remodeling in bone aging, adaptation, and disease.

ACKNOWLEDGEMENTS

First and foremost, I give my sincerest gratitude to my advisor and mentor, Dr. David M. L. Cooper, for his unwavering guidance, encouragement, and overall support to succeed throughout my entire Ph.D. program. As a graduate student of Dr. Cooper's, the invaluable experiences, opportunities, and insight I have been afforded have undoubtedly enriched my attributes as not only an academic but also as an individual. Dr. Cooper is an exemplary example of what an academic advisor should strive to be, and I am truly fortunate to have gone through this academic journey under his guidance. Dave, you have brought me over to the 'light side' of imaging, and I am here to stay! I would also like to acknowledge the support of my committee members Dr. Dean Chapman, Dr. Julia Boughner, Dr. J. D. Johnston, and Dr. Brian Eames. I would like to thank Dr. Chapman as the synchrotron portion of my research would not have been possible without his insurmountable knowledge of all things physics and novel insight into the possibilities of synchrotron imaging. I could not have carried out the fatigue loading portion of my research without the gracious support of Dr. Johnston, and I would like to thank him for his generosity of time, resources, and expertise. Dr. Boughner and Dr. Eames, thank you for your continued enthusiasm and support through committee meetings, presentations, and editing feedback and for encouragement to approach my research from a different, even though foreign, new light at times. You have further broadened my horizons within the field of bone biology.

The undertaking of this research would not have been possible without the numerous groups and individuals that have so generously provided me with invaluable resources. Thank you, Dr. Arash Panahifar, Dr. Ning Zhu, Dr. Sergei Gasilov, and Dr. Adam Webb of the BioMedical Imaging and Therapy Beamline (BMIT), Canadian Light Source (CLS). I am genuinely thankful for the years of support over many beamtimes through set-up and testing protocols, troubleshooting issues, and modifying equipment to fulfill our imaging requirements. A special dedication goes out to Dr. George Belev, who made *in vivo* imaging at the CLS a reality and helped us achieve our first ever *in vivo* images. George, your knowledge, ingenuity, and dedication to BMIT and its users were commendable. I would like to express my gratitude to Dr. Melanie Gibbons, Dr. Kurtis Swekla, Michele Moroz, Laboratory Animal Services Unit (LASU) staff, and the University Animal Care Committee (UACC) staff. I am truly grateful for the invaluable resources for our research, as otherwise, it would not have come to fruition. Several individuals

have also provided access to equipment, and for that, I extend my appreciation to Dr. Ingrid Pickering and Dr. Natalia Dolgova for training and use of the confocal microscope, Dr. Aditya Manek and Karen Yuen for generously lending their expertise with optimizing the histology work, and Ted Toporowski and the Department of Physics and Engineering Physics machine shop for manufacturing our rabbit holder.

I owe much to my past and present lab mates for their constant source of wisdom, support, encouragement, but perhaps most importantly, the laughs and fun! Yasmin and Isaac, thank you for making me feel welcome in the Cooper lab and showing me the ropes when I first joined the lab. Janna, you are an inspiration for women in research, and I consider myself so fortunate to have had the opportunity to work with you. You made the all-night beamtimes that much more fun, and I always enjoyed our afternoon coffee runs! Arash, I always enjoyed undertaking research with you and admired your insightfulness (you also made all night beamtimes fun)! Finally, my more current lab mates, Gavin, Kush, Erika, and Beverly, thank you for always being there to bounce off ideas, the random afternoon office tangents, and the laughs; it truly did help keep me sane! Last but certainly not least, I would like to thank my co-author and friend, Beverly. You made research so efficient, effortless, and enjoyable, and for that, I cannot thank you enough. I very much enjoyed our office chats, late-night manuscript editing, and conference adventures (I am still not sure how we all survived that one)!

To my family, Mom, Dad, and Audra, your ongoing support, encouragement, and desire to see me succeed have not gone unnoticed, and words do not seem to suffice to convey my gratitude. Thank you for always supporting me and giving me advice when I needed it most. Mike, who knew it would have been this long of a road, but you have always supported me no matter what, and I could not have achieved my goals without you by my side. Your patience with the wild, crazy hours has been so appreciated, and this achievement is just as much yours as it is mine. Thank you for always understanding.

Finally, I would like to acknowledge institutions—the Canadian Institutes of Health Research, the University of Saskatchewan College of Medicine, Saskatchewan Innovative and Opportunity Scholarship, Arthur Smyth Scholarship—and individuals, Dr. Dave Cooper, that financially supported this thesis. Dave, thank you for your continual support and understanding throughout my program; I would not have finished otherwise.

DEDICATION

I dedicate this thesis to my family, for I would not be where I am today without your love and support.

TABLE OF CONTENTS

LIST OF TABLES

LIST OF FIGURES

LIST OF ABBREVIATIONS

°	Degrees
%	Percent
2D	Two-Dimensional
3D	Three-Dimensional
4D	Four-Dimensional
α	Alpha
ABL	Abaloparatide
Ac.f	Activation Frequency
a.Rm.Cr	Active Remodeling Center
$BaCL_2$	Barium Chloride
$BaSO_4$	Barium Sulfate
BFR	Bone Formation Rate
BMD	Bone Mineral Density
BMIT	BioMedical Imaging and Therapy Beamline
BMIT-BM	Bend Magnet
BMIT-ID	Insertion Device
BMU	Basic Multicellular Unit
BP	Bisphosphonate
BS	Bone Surface
BV/TV	Bone Volume fraction
Ca.Dm	Canal Diameter
Ct.Ar	Cortical Area
Ct.Po	Cortical Porosity
Ct.Th	Cortical Thickness
CCAC	Canadian Council on Animal Care
CLS	Canadian Light Source
CI	Confidence Interval

cm	Centimeter
CTAn	CTAnalyzer
CT	Computed Tomography
CTVol	CTVolume
Dkk1	Dickkopf-1
DIC	Differential Interference Contrast microscopy
dL.On	Double Labelled Osteon
dLS	Double labelled Bone Surface
Dmab	Denosumab
DXA	Dual-Energy X-ray Absorptiometry
Es.MS/BS	Endosteal Mineralizing Surface per Bone Surface
FDA	American Food and Drug Administration Agency
Fz	Frizzled
g	Gram
GC	Glucocorticoid *(referring to both the drug and within Chapter 3, the group of rabbits treated with glucocorticoids)*
GIO	Glucocorticoid-Induced Osteoporosis
Gy	Gray
HR-pQCT	High Resolution peripheral Quantitative Computed Tomography
HRT	Hormone Replacement Therapy
IGF	Insulin-like Growth Factor
I_{max}	Maximum second moment of area
I_{min}	Minimum second moment of area
Kg	Kilogram
kVp	Peak Kilovoltage
LER	Longitudinal Erosion Rate
LRP (5 or 6)	Wnt ligand
Ma.Ar	Marrow Area
MAR	Mineral Apposition Rate
micro-CT	Micro-Computed Tomography

ml	Milliliter
mg	Milligram
mm	Millimeter
ms	Millisecond
MS/BS	Mineralizing Surface per bone Surface
n	Sample size
Na_2SO_4	Sodium Sulfate
2NaCl	Sodium Chloride
ND	No Data
On.MAR	Osteonal Mineral Apposition Rate
OP	Osteoporosis
OPG	Osteoprotegerin
OVX	Ovariectomy *(referring to either the surgical procedure or the rabbit group subject to this procedure)*
OVX+GC	Ovariectomy & Glucocorticoid
PBS	Phosphate Buffered Saline
Ps.MS/BS	Periosteal Mineralizing Surface per Bone Surface
PHPT	Primary Hyperparathyroidism
PINP	Propeptide of type 1 procollagen
PMO	Postmenopausal Osteoporosis
PTH	Parathyroid Hormone *(referring to both the drug and within the rabbit group treated with parathyroid hormone)*
PTH1R	PTHrP type1 receptor
RANK	Receptor Activator of Nuclear factor Kappa-B
RANKL	Receptor Activator of Nuclear factor Kappa-β Ligand
ROI	Region of Interest
Rs.N	Resorption Cavity
Runx2	Runt-related transcription factor 2
σ_f	Osteon formation time
SD	Standard Deviation

SHAM	Sham control
sL.On	Single Labelled Osteon
sLS	Single Labelled Bone Surface
SOST	Sclerostin
SR	Synchrotron Radiation
Tb.N	Trabecular Number
Tb.Sp	Trabecular Spacing
Tb.Th	Trabecular Thickness
TGF- β	Transforming Growth Factor-β
TLD	Thermoluminescent dosimeter
Tt.Ar	Total Area
μA	Microampere
μg	Microgram
μm	Micron
VOI	Volume of Interest
vs	Versus
Wnt	Mammalian homologue of wingless-related integration site in drosophila
W.Th	Wall Thickness
Z_{pol}	Torsional section modulus

Chapter 1 Introduction

1.1 Preface

The aim of my doctoral thesis project was to use synchrotron imaging techniques to directly detect and follow over time (track) individual instances of localized tissue turnover (remodeling) in the compact cortical bone of animal models. Initially, these efforts focused on the rat. While great progress was made on the imaging front (as described in Chapter 2 and Appendix A), I was unable to experimentally replicate a widely reported model system (ulnar fatigue loading) that would enable investigation of the link between microdamage and bone turnover (Appendices B & C). This impasse led to a shift to rabbit models of osteoporosis which proved far more successful and enabled me to achieve my goal of directly tracking cortical bone remodeling for the first time.

1.11. Introduction

Worldwide, osteoporosis (OP) affects over 200 million people with annual fractures exceeding 8 million. In Canada, an estimated two million people suffer from OP, of which 1 in 3 women and 1 in 5 men will experience a fracture within their lifetime, with annual costs to the healthcare system most recently estimated at $4.6 billion (Tarride et al., 2012). Unfortunately, active bone degeneration can take place over a prolonged period without showing any symptoms, and thus, all too often, OP is recognized only after a fracture occurs, lending to its reputation as the 'silent disease' (Mafi Golchin et al., 2016) or ‘silent thief’ (2015). Fractures typically occur in load-bearing areas of the skeleton, such as the lumbar vertebrae, distal wrist, or proximal femur (Rochefort, 2014), and often lead to secondary health issues with ongoing pain, decreased mobility, and most drastically, mortality (Sözen et al., 2017). After one year, hip fractures alone correspond to a 15-20% increased mortality rate and a 2.5-fold increased risk for future fractures (Sözen et al., 2017, Kelly, 2014). Alarmingly, with increasingly aging populations, hip fractures are expected to increase by 240% for women and 310% for men by 2050 (IOP).

While its static, rigid exterior may seem otherwise, bone is an incredibly dynamic tissue that changes at the microscopic level via two distinct processes: 1) *modeling*, which manipulates external bone structure in relation to growth, and 2) *remodeling*, which internally renews mature bone (resorption spatially and temporally *coupled* to formation). Remodeling is carried out by

specialized cellular units, first described as Basic Metabolizing Units (Frost, 1964, Frost, 1966, Johnson, 1964) and later, more commonly referred to as Basic Multicellular Units (BMUs) (Frost, 1969). Under normal circumstances, the bone resorbed and replaced by a BMU is *balanced*, renewing the tissue and maintaining its overall mass/volume. In certain states such as aging or disease, an *unbalanced* state of remodeling (resorption exceeding formation) can result in the loss of bone mass and deterioration of the microarchitecture − cortical bone porosity is increased, and the cortices thinned, similar to thinned trabecular bone due to decreased thickness, number, and connectivity (Burr et al., 1997). The effects of this unbalanced state ultimately cause fragile, brittle bone that is highly susceptible to fracture – classically defined as the root cause of OP.

Most of what is known or theorized about remodeling is based on two-dimensional (2D) histomorphometry. However, this is a spatially and temporally confined view of BMUs as it can only provide a limited snapshot depicting their morphology and behavior. Theories about the mechanisms dictating remodeling have suggested BMUs can address microcrack-induced damaged regions of bone through targeted repair (Martin, 2002, Martin, 2007) and that different disruptions, beyond being unbalanced, (Andersen et al., 2013) can lead to OP. However, such theories have been difficult to test due to a lack of three-dimensional (3D) imaging techniques capable of rendering the small microarchitectural features of cortical bone at suitable radiation doses for *in vivo* imaging. Thus, we do not have a clear understanding of OP bone loss in its natural 3D context at the microscopic level at which it occurs. With advanced *in vivo* imaging techniques, the direct 3D and even four-dimensional (4D; 3D over time) investigation of the spatio-temporal behavior of BMUs within animal models is, as will be presented within this thesis, finally within reach.

1.12. Bone Anatomy

1.12.1. Microscopic Anatomy

Bones are highly dynamic and complex organs articulated in an organized fashion to form the skeleton, which provides support for the body, protects internal organs, encases red blood cell producing marrow, and stores reserve minerals, particularly calcium phosphate (Su et al., 2019). Fundamentally, bone is a composite material consisting of a mineral phase in which calcium phosphate and calcium hydroxide form crystals of hydroxyapatite that surround an organic phase

consisting mainly of Type I collagen fibers (Boskey, 2013), which make up to 90% of protein within bone (Currey, 2002). At the cellular level, bone is comprised of mesenchymal derived osteoblasts (and related cells of their lineage) and bone marrow hematopoietic progenitor derived osteoclasts (Bar-Shavit, 2007). Both of these cell types play essential roles in formation, growth, modeling, and remodeling driven by several signaling pathways (discussed further in Chapter 3). At their life cycle end, osteoblasts that do not go through apoptosis give rise to two other cell types. The first type is osteocytes−bone cells located within lacunae (i.e., bone cellular spaces) that connect via radiating canaliculi forming the lacuno-canalicular network that serves as a 'mechano-sensory network' among bone cells (Burger and Klein-Nulend, 1999). The second type is bone-lining cells – flat, quiescent osteoblasts (Currey, 2002) that cover all bone surfaces (i.e., the inner endosteum and outer periosteum). While the function of bone lining cells is not fully understood, they play an important role in regulating signaling pathways involved in bone resorption and formation (Florencio-Silva et al., 2015).

1.12.2. Gross Anatomy

At the gross level, the adult skeleton consists of two main types of tissue. The first is trabecular (cancellous, spongy) bone, which is composed of an intricate porous (40% – 95%) network of interconnected rod and plate-like structures known as trabeculae. The second is cortical (compact) bone, which is rigid, densely packed tissue that is much less porous (5% – 15%) (Morgan et al., 2018) (Figure 1.1). The theory that the overall shape and internal microarchitecture of bone is a product of its mechanical environment, specifically referring to the spatial arrangement of trabecular bone, is commonly referred to as Wolff's Law (1892). However, this law has been challenged as an over-simplification of the complex relationship between bone structure and function (Pearson and Lieberman, 2004). Defined at a basic level, the amount of bone, its location, spatial arrangement, and microarchitectural quality are all inherent to bone's ability to adapt and respond to the lifelong mechanical strains placed upon it. This is critical to bone's ability to maintain structural integrity and resist fracture – which occurs when loads exceed overall strength (Bouxsein and Seeman, 2009). Trabeculae located within irregular bones such as the vertebrae as well as within the epiphyses (ends) of long bones transmit mechanical forces from joint surfaces to the compact cortex of the diaphyses (shafts) of long bones, which mitigate bending and torsional loading (Cole and van der Meulen, 2011, Currey, 2012). This structure-function relationship is

achieved through *bone modeling* during development and growth and maintained via *bone remodeling* post maturity – concepts discussed in the following sections.

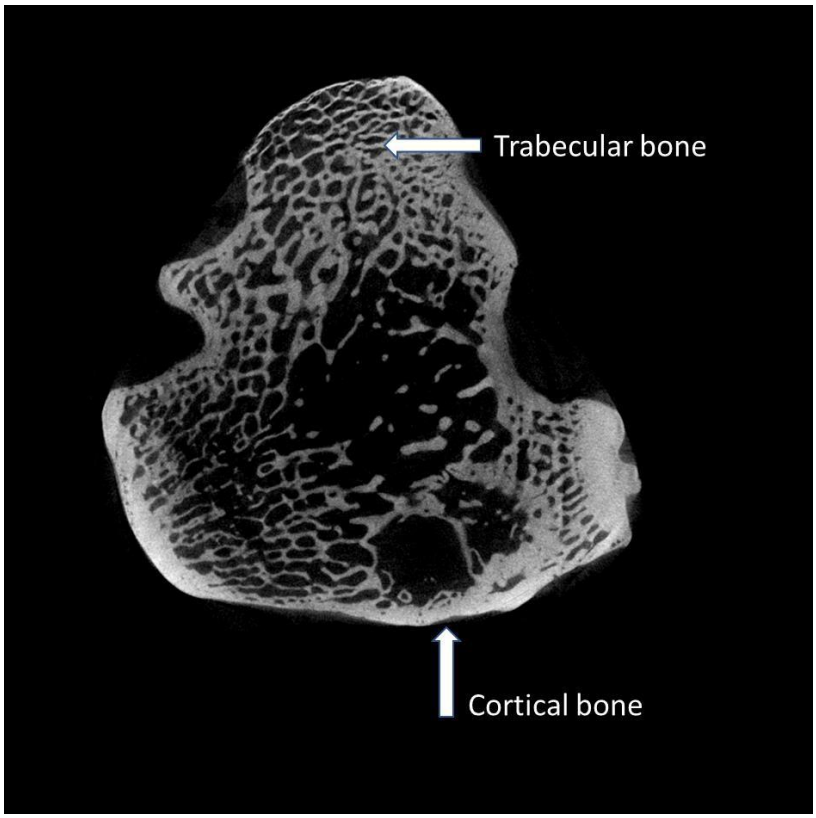

Figure 1.1. Microcomputed tomography slice of a rabbit tibial epiphysis (proximal). The cortical bone on the periosteal surface creates a dense, rigid wall containing the rod and plate-like trabecular bone and marrow cavity. This arrangement is typical in the epiphyses of the long bones of the skeleton.

1.13. Bone Development and Growth

During fetal development, migration of mesenchymal cells forms predetermined morphologies in regions of the skeleton where development will occur (Salhotra and Shah, 2020, Berendsen and Olsen, 2015). The flat bones including the cranial vault, mandible, maxilla, and clavicle, arise through intramembranous (direct osteoblast) ossification whereas the rest of the skeleton, including the long bones, form via endochondral (cartilaginous models preceding bone) ossification. Mesenchymal stem cells form mature skeletal tissues (i.e., bone and cartilage) via differentiation. The process of differentiation is based upon the activation of specific transcription factors such as Runt-related transcription factor 2 (RUNX2) and osterix (OSX). The expression of

these two genes activate differentiation of skeletal lineage cells into mature, bone forming osteoblasts (Salhotra and Shah, 2020).

The development and growth of long bones takes place over several stages of endochondral ossification. Mesenchymal cells start to congregate and differentiate into chondrocytes which form a cartilaginous model and surrounding perichondrium which defines the border of the developing bone (Berendsen and Olsen, 2015). This model serves as a blueprint for subsequent bone formation (Mauch and Schoenwolf, 2001). Within the center of the model, hypertrophic chondrocytes deposit collagen and fibronectin which alters the cartilaginous matrix and prompts calcification to occur (Breeland et al., 2021). Calcification however, prohibits the delivery of nutrients and thus starved chondrocytes undergo apoptosis, leaving behind voids which subsequently infill with blood vessels resulting in the formation of the marrow cavity (Breeland et al., 2021). This rich blood supply carrying osteogenic cells also promotes the perichondrium to transform into the periosteum (Setiawati and Rahardjo, 2018, Mauch and Schoenwolf, 2001) where osteoblasts deposit bone matrix, while osteoclasts simultaneously break down bone at the inner, endosteal surface lining the marrow cavity. As the perichondrium becomes vascularized, osteoblasts gather along the diaphyseal wall forming a bony collar in which bone is deposited forming the primary ossification center (Breeland et al., 2021). While chondrocytes within the primary ossification center signal for the surrounding cartilage to calcify, proliferating chondrocytes near the ends of the primary ossification center continue to deposit cartilage matrix towards the epiphyseal growth plates (Mauch and Schoenwolf, 2001) which causes the cartilage model to lengthen (Breeland et al., 2021). As the model grows in length, it also grows in width. Dictated by intramembranous bone formation, appositional growth, or widening of the diaphysis, is caused by osteoblast activity depositing tissue on the periosteum whereas osteoclasts remove tissue from the endosteum which maintains the overall shape of the cortices and the bone itself throughout growth (Shapiro, 2008).

After birth, secondary ossification centers develop within the epiphyses and cartilage only remains on the articular surfaces and epiphyseal growth plates. These growth plates separate the diaphysis from the epiphysis and lengthening of the bone continues throughout adolescence via chondrogenesis (i.e., chondrocyte proliferation, hypertrophy, and extracellular matrix secretion (Shim, 2015)) which drives the plates away from the diaphysis. Bone will continue to grow as

long as chondrocytes are being produced and it is this continuation throughout development and beyond that has been termed as ‘immature’ cartilage whereas cartilage that undergoes stages of change is considered ‘mature’ in nature (Gómez-Picos and Eames, 2015).

Replacement of cartilage with actual bone is the result of the invasion of the cartilaginous model by blood vessels as this causes hypertrophic chondrocytes to become apoptotic and osteoprogenitor cells differentiate into proliferating preosteoblasts (Moore et al., 2012). These preosteoblasts eventually transform into mature cuboidal osteoblasts, marked by the co-expression of bone matrix synthesizers alkaline phosphate and collagen type I, and the presence of matrix mineralization regulator proteins osteocalcin, osteopontin, and osteonectin (Florencio-Silva et al., 2015, Eriksen, 2010). In humans, this 'primary' bone, classified as either woven or lamellar, results in the overall growth of bone in both length and diameter until the end of the second decade of life, when longitudinal growth typically completes (Natalie and Martin, 2014).

In lamellar bone, highly organized parallel-fibers of collagen (Marotti, 1993) laid down in concentric layers of circumferential lamellae entrap blood vessels, forming primary osteons—fundamental structural units of bone that are associated with appositional growth (Matsuo et al., 2019). In woven bone, bone is rapidly laid down and formed during intramembranous ossification. Woven bone can also include primary osteons (Andronowski et al., 2017), but, unlike lamellar bone, it is composed of disorganized collagen bundles commonly found in flat bones such as those of the cranium, bone undergoing fracture repair (Gorski, 1998), and in trabecular and cortical bone undergoing rapid growth and turnover (Cooper et al., 2004). This overall process, whereby the gross morphology of bone (i.e., shape and size) is initially formed *in utero* and further altered during growth via bone resorption and formation (Frost, 1969), is known as bone *modeling*.

1.14. Post Development Maintenance: Bone Remodeling

In larger mammals including humans, once growth has ceased, primary bone will eventually be replaced by secondary bone through *remodeling* (Currey, 2012, Frost, 1969). Remodeling is both proactive and reactive; it is the mechanism by which mature bone adapts to environmental and mechanical stimuli to mitigate fracture risk and repair damage incurred in bone via cyclical loading (Burr, 2002). First described by Johnson (1964) and Frost (1969), remodeling involves BMUs creating “remodeling spaces” (Martin, 1994) in which the coordinated resorptive

and formative activities of both trabecular and cortical bone take place at the endosteal, periosteal, and intracortical surfaces. During remodeling, old or damaged bone is replaced with new, healthy tissue laid down in the form of osteoid, which eventually mineralizes into mature bone. However, the mechanism by which this occurs in trabecular versus cortical bone differs (Natalie and Martin, 2014).

On trabecular surfaces, BMUs resorb 'pits or cavities' which differentiating osteoblast precursors infill (Natalie and Martin, 2014) creating a trench-like 'hemi-osteon' (Parfitt, 1994). In cortical bone, localized resorption of a cylindrical space located at the BMU's osteoclastic cutting cone creates a tunnel or void within the matrix which is subsequently infilled around a central vascular canal, representing the osteoblastic closing cone (Frost, 1969) (Figure 1.2). The remodeling process results in the creation of secondary osteons (i.e., a central Haversian (vascular) canal surrounded by concentric bony lamellae) which are the fundamental structural units of cortical bone interconnected via transverse Volkmann's canals. This network facilitates transmission of the necessary neuro-vascular structures to support the surrounding cells and bone tissue.

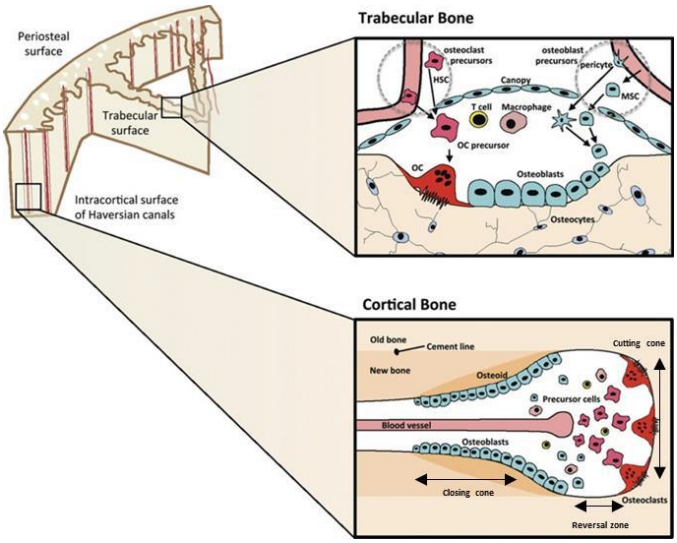

Figure 1.2. Illustration depicting Basic Multicellular Unit (BMU) remodeling within trabecular and cortical bone. In cortical bone, osteoclasts resorb bone at the BMU's cutting cone, creating a tunnel within the matrix infilled with osteoid by bone forming osteoblasts located within the closing cone, creating a secondary osteon or Haversian system. A reversal zone forms the border between the cutting and closing cone, and is the transitional zone between resorption and formation, respectively. This same process occurs within trabecular bone; however, osteoclasts resorb a pit or cavity-like depression on the bone surface, which produces a hemi-osteon. Modified from Sims and Martin (2014).

As first described by Frost (1969), remodeling occurs in a specific sequence beginning with *activation*, whereby osteoclast precursors are recruited and activated from circulation in response to targeted microdamage repair or nontargeted systemic hormonal fluctuations (Kenkre and Bassett, 2018). Next, *resorption* of a remodeling space is carried out by the osteoclasts, concluding with osteoblastic *formation* whereby the remodeling space is infilled via secretion of type 1 collagen-rich osteoid matrix (Kenkre and Bassett, 2018).

In certain states such as aging or disease, remodeling can become unbalanced. Overactive resorption and insufficient formation over collections of remodeling spaces causing increased porosity can occur in a couple distinct ways. Varied remodeling cycles can be: 1) coupled and unbalanced, where the remodeling space is only partially infilled due to failed bone formation, as is commonly associated with the onset of postmenopausal OP (PMO); or 2) uncoupled, in which an arrest within the reversal zone means formation never occurs and hence the remodeling space is entirely void of new bone tissue (Andersen et al., 2013)[1]. BMUs are also thought to actively target and steer towards areas of microdamage in the form of microcracks (Martin, 2002, Martin, 2007, Parfitt, 2002a, Burr, 2002). Therefore, extensive microdamage could create the potential for numerous BMUs targeting the same region of bone and possibly coalescing into singular, enlarged pores or clustered 'super-osteons' (Bell et al., 2001). Ultimately, compromised structure through increased porosity diminishes bone strength and ultimately leads to fragile, brittle bone much more susceptible to fracture (Rochefort, 2014)—the state classically observed in OP (discussed further in Chapter 3).

1.15. Basic Multicellular Unit Analysis — Limitations and Challenges

The mechanisms responsible for dysfunctional bone remodeling at the microscopic level, particularly for cortical bone, are not well known as this process has never been directly observed

[1] These various remodeling states approach cortical bone loss from the level of the individual BMU. However, it is of importance to note that within the literature, the term 'imbalanced' is at times interchangeably used with 'unbalanced' to refer to a more generalized, collective relationship between resorption and formation collectively. Consideration of BMU remodeling behavior through both *ex vivo* and *in vivo* analyses presented within this thesis is done so at the level of the BMU in line with those of ANDERSEN, T. L., ABDELGAWAD, M. E., KRISTENSEN, H. B., HAUGE, E. M., ROLIGHED, L., BOLLERSLEV, J., KJÆRSGAARD-ANDERSEN, P. & DELAISSE, J.-M. 2013. Understanding Coupling between Bone Resorption and Formation: Are Reversal Cells the Missing Link? *The American Journal of Pathology,* 183**,** 235-246.

in situ and *in vivo.* BMUs' resorptive behavior, such as its Longitudinal Erosion Rate (LER) – the amount of tissue traversed over time (Figure 1.4.) — remain poorly understood as BMUs have never been directly assessed and much of what we currently know regarding their behavior is indirectly inferred from histological assessments (see Chapter 5 for further discussion). Directly characterizing BMU cutting cone spatio-temporal behavior would be transformative for our current understanding of bone remodeling and create a powerful new platform for the study/refinement of OP and its treatments. Animal models provide an opportunity to investigate bone structural and functional alterations associated with OP (Castañeda et al., 2008) and preclinical testing of treatments, as per guidelines supplied by the American Food and Drug Administration Agency (Thompson et al., 1995). Furthermore, an *in vivo* animal model of OP would not only enable 4D longitudinal tracking of BMU-induced cortical porosity—the very pores of osteoporosis—but also the potential to experimentally manipulate their spatio-temporal characteristics such as size, LER, and targeted action through varying dose and administration regimens to ultimately achieve healthy, coupled and balanced remodeling that could reverse, or even prevent OP related bone loss.

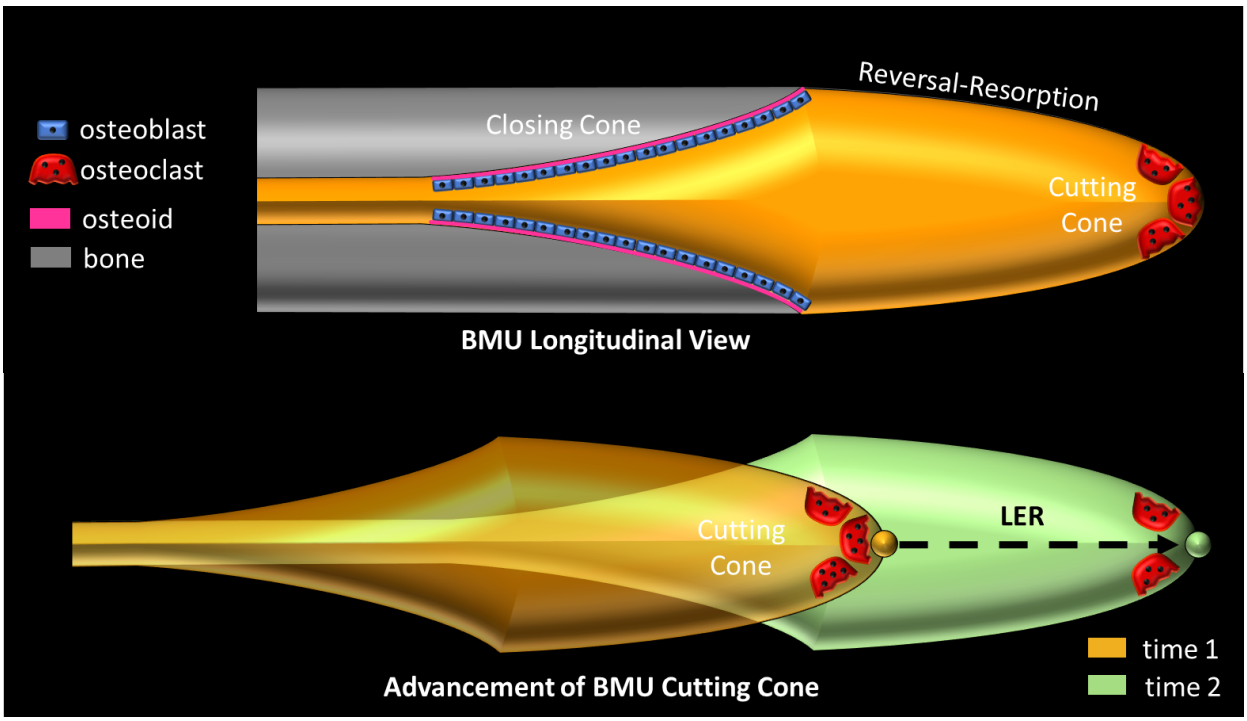

Figure 1.3. Schematic depicting a BMU in cortical bone at a single time point (top, time 1) and the advancement of the related porous resorption space over time (orange for time 2, green for time 2). LER is defined as the distance between time 1 (orange) and time 2 (green) divided by the time interval (μm/day).

Challenges associated with the direct, 3D and 4D study of cortical BMUs will be extensively discussed in Chapter 2. The critical issue is the relationship between imaging resolution and dose – as resolution increases, the radiation dose increases exponentially (Ford et al., 2003)—creating fundamental limits for *in vivo* imaging of live animals. Since its introduction by Feldkamp and colleagues (1989), micro-CT has been extensively implemented as a non-destructive, *ex vivo* 3D imaging technique to render both trabecular bone morphology and, increasingly, cortical porosity (Cooper et al., 2006, Cooper et al., 2003, Cooper et al., 2007, Britz et al., 2010, Basillais et al., 2007, Pazzaglia et al., 2010, Chen et al., 2010, Palacio-Mancheno et al., 2014, Bousson et al., 2004). However, such *ex vivo* systems require high resolutions to render the smaller pores of cortical bone and thus impart radiation doses not suitable for *in vivo* imaging (Pratt et al., 2015). To overcome this limitation, our research group has looked to monochromatic synchrotron radiation, which offers the opportunity to develop contrast through the refraction (phase contrast), as opposed to the conventional absorption of X-rays (Zhou and Brahme, 2008). Our efforts have focused on implementing in-line phase contrast synchrotron radiation micro-CT (SR micro-CT) for *in vivo* imaging of remodeling-related cortical porosity in animal models (Pratt et al., 2015).

Finding appropriate animal models for studying cortical bone remodeling and its role in OP presents an additional challenge. Standard small laboratory rodent (i.e., mouse and rat) models do not naturally remodel their cortical bone; therefore, cortical remodeling must be artificially induced, which has proven difficult (see Chapter 3 & Appendix B) and, even if successful may not model OP, *per se*. The rabbit model (detailed in Chapters 3 & 4), however, has been extensively used for OP bone research as rabbits naturally remodel their cortices similar to that observed in humans, with the caveat that rates tend to be low for *in vivo* analysis (Harrison et al., 2020). Remodeling rates in terms of activation frequency (i.e., number of new BMUs present in a unit of bone) (Frost, 1969), however, can be increased with OP models of elevated cortical bone remodeling via Ovariectomy (OVX), Glucocorticoid (GC), and a combination thereof (OVX+GC) (Castañeda et al., 2008) as well as via PTH, a known elevator of remodeling/porosity within the rabbit (Mashiba et al., 2001, Hirano et al., 2000). Thus, the potential exists to more accurately model human disease and simultaneously acquire large numbers of BMUs for *in vivo* analysis. These model systems are explored in Chapters 3 & 4 and subsequently implemented to track BMUs in 4D in Chapter 5.

1.2. Thesis Objectives

The overarching goal of this thesis was to develop a novel platform to investigate BMU behavior via the direct tracking of individual BMUs by testing three hypotheses:

1) In-line phase contrast SR micro-CT can safely image BMUs, *in vivo*, in the cortical bone of animal models.

2) Rabbit models of OP elevate BMU remodeling rate.

3) Combining SR micro-CT with rabbit models of OP would create a novel platform for the direct 4D measurement of BMU LER *in vivo*.

Testing these hypotheses required identifying BMU spatio-temporal behavior within a live animal's cortical bone over time. The specific objectives of my thesis research were:

1. Develop an *in vivo* imaging protocol to target individual BMU remodeling events within rabbit tibiae cortical bone to permit longitudinal imaging, using in-line phase contrast SR micro-CT.
2. Within rabbits, implement OP models of OVX, GC, OVX+GC, and PTH, to elevate cortical bone remodeling rates and, thus, the ability to observe BMU behavior on a large scale.
3. Directly measure BMU LER in 4D for the first time.

1.3. Organization of Thesis

This manuscript-style thesis is presented as a sequence of papers, each addressing one of my study objectives.

The present chapter, Chapter 1, introduces bone at the gross and microscopic levels and covers key concepts within bone biology pertinent to the thesis, particularly those focused on bone remodeling. This includes the organization of BMUs, their role within cortical bone remodeling, and, at a rudimentary level, the link to OP. Finally, the imaging modality and animal model pursued to achieve direct 4D tracking of BMUs are briefly introduced, as these topics are discussed in more detail in subsequent chapters.

Chapter 2 consists of the manuscript, “Modalities for the Visualization of Cortical Bone Remodeling: the Past, Present and Future”, published in the Journal Frontiers in Endocrinology

(Harrison and Cooper, 2015). My thesis research initially set out to track BMUs within rat cortical bone to test the hypothesis that remodeling targets microdamage in the form of microcracks. This paper served two primary purposes 1) review past, current, and future methodologies for imaging cortical bone remodeling in 3D and 2) present matched cortical bone scans in rats imaged *in vivo* using our in-line phase contrast SR micro-CT. The rat model was successfully employed to develop our *in vivo* imaging protocol (see also Appendix A); however, the implementation of a fatigue loading model to induce cortical bone remodeling (Appendices B & C) for tracking BMUs was not attainable. In light of this result, my thesis research shifted tactics to rabbit models of OP to reach my ultimate goal of tracking BMUs, *in vivo*.

Chapter 3 examines OP and mechanisms for inducing it experimentally in the rabbit (OVX, GC, OVX+GC and PTH) for elevating cortical bone remodeling. Remodeling and associated signaling pathways, along with their key regulators, are briefly described to enable the reader to appreciate how each model's cellular activity presents phenotypically, whether that be increased bone resorption, formation, or a combination thereof.

The concepts discussed in Chapters 2 and 3 are applied within Chapter 4's presentation of "Cortical Bone Porosity in Rabbit Models of Osteoporosis" published in the Journal of Bone and Mineral Research (Harrison et al., 2020). This manuscript, co-authored with Beverly Hiebert, a graduated Masters' student within our lab, describes the effects of OVX, GC, OVX+GC, and PTH on the remodeling of cortical bone within the rabbit. This initial *ex vivo* rabbit model study identified which OP model(s) were most successful at elevating remodeling and, thus, numbers of BMUs, for future *in vivo* studies (Chapter 5).

The third and final manuscript of the thesis presented in Chapter 5, "Direct Assessment of Cortical Bone Basic Multicellular Unit Longitudinal Erosion Rate: A 4D Based Synchrotron Approach," is under review (submitted Sept 28, 2021) with the Journal of Bone and Mineral Research and implemented the PTH rabbit model from Chapter 4 to achieve 4D tracking of BMUs, including direct measurement of LER, for the first time.

Chapter 6 concludes the thesis with a summary of the key findings and a discussion of future directions for how this novel rabbit model could be used for not only further investigation of BMU remodeling behavior associated with OP and its treatments, but also within other areas of bone biology such as the biomechanics.

Chapter 2 Modalities for Visualization of Cortical Bone Remodeling: the Past, Present and Future

This Chapter consists of the manuscript published in Frontiers in Endocrinology (Harrison and Cooper, 2015) and is open access under the **Creative Commons Attribution License (CC BY)**. *I was the lead author. This paper served as a review of imaging cortical bone remodeling in 3D and thus, sets the stage for the application of micro-CT imaging techniques, both ex vivo and in vivo, presented in this thesis. This manuscript has been reformattedfrom the original version for inclusion in this thesis.*

Kimberly D. Harrison[1], David M. L. Cooper[1*]

[1]University of Saskatchewan, Department of Anatomy & Cell Biology, SK, Canada

***Correspondence:**

Dr. David M. L. Cooper, University of Saskatchewan, Department of Anatomy & Cell Biology, 107 Wiggins Rd, Saskatoon, SK, S7N 5E5.

dml.cooper@usask.ca

2.1. Abstract

Bone's ability to respond to load-related phenomena and repair microdamage is achieved through the remodeling process which renews bone by activating groups of cells known as Basic Multicellular Units (BMUs). The products of BMUs, secondary osteons, have been extensively studied via classic two-dimensional (2D) techniques which have provided a wealth of information on how histomorphology relates to skeletal structure and function. Remodeling is critical in maintaining healthy bone tissue; however, in osteoporotic bone imbalanced[2] resorption results in increased bone fragility and fracture. With increasing life expectancy, such degenerative bone diseases are a growing concern. The three-dimensional (3D) morphology of BMUs and their correlation to function, however, are not well characterized and little is known about the specific mechanisms that initiate and regulate their activity within cortical bone. We believe a key limitation has been the lack of 3D information about BMU morphology and activity. Thus, this paper reviews methodologies for 3D investigation of cortical bone remodeling and, specifically, structures associated with BMU activity (resorption spaces) and the structures they create (secondary osteons), spanning from histology to modern *ex vivo* imaging modalities, culminating with the growing potential of *in vivo* imaging. This collection of papers[3] focuses on the theme of "putting the "*why"* back into bone archytecture". Remodeling is one of two mechanisms "*how*" bone structure is dynamically modified and thus an improved 3D understanding of this fundamental process is crucial to ultimately understanding the *"why"*.

[2] In line with the definitions used within this thesis, 'imbalanced' resorption is referring to 'coupled and unbalanced' bone remodeling. The dating of references within this Chapter reflected the timing of the publication and therefore, subsequent Chapters have supplemented the issue of 'uncoupling' more substantially.

[3] This paper was an invited Chapter for an edited volume within the journal of Frontiers of Endocrinology that focused on putting the "why" back into bone architecture.

2.2. Introduction

Bone tissue is three-dimensionally (3D) complex in structure and undergoes continual dynamic change. Despite its rigid structure, it is remarkable in its ability to adapt in response to mechanical stimuli associated with loading and to microdamage endured throughout life. Since Clopton Havers' (1691) description of 'Haversian' canals and iconic works describing microscopic bone structure/function relationships (Tomes and Morgan, 1853, Wolff, 1892), it has been well appreciated that bone renews itself via the turnover of tissue which we have come to know as 'remodeling' (Johnson, 1964). Remodeling is critical for maintaining healthy bone tissue; however, it can also lead to age-related bone loss through an imbalance between osteoclast (bone resorption) and osteoblast (bone formation) activity. A progressive deficit in bone formation leads to enlarged osteonal canals and thus increased cortical porosity (Rauch et al., 2007, Cooper et al., 2007, Rochefort, 2014). Ultimately this contributes to bone's fragility which is characteristic of osteoporosis (Rochefort, 2014, Torres-del-Pliego et al., 2013). Related fractures are significant events in the lives of those afflicted and are frequently associated with serious complications and even mortality. With increasing life expectancy, osteoporosis and other degenerative diseases of bone are a growing concern for health care systems worldwide (Borah et al., 2001). As such, study of the spatio-temporal regulation of remodeling is a topic of great significance within bone biology with the potential to impact many lives.

First described by Frost (1969), Basic Multicellular Units (BMUs) are the cellular groups responsible for carrying out the remodeling process. In cortical bone this is achieved through the localized resorption of a cylindrical space (osteoclastic "cutting cone") followed by concentric infilling of new tissue (osteoblastic "closing cone") (Figure 2.1). The resulting structure is referred to as a secondary osteon (synonymous with "*Haversian system"*). As BMUs organizationally lie between the level of the cell and that of the tissue, Frost referred to them as 'intermediary' (Frost, 1983). Despite decades of study, our understanding of the intermediary organization of bone remains rudimentary. BMUs are temporary collections of cells brought together to turnover a discrete packet of bone. Their course through bone tissue, their "behavior", is challenging to directly probe and thus much of our understanding has been inferred from osteon morphology. The orientations of secondary osteons appear to reflect principal stresses (Hert et al., 1994, Petrtyl et al., 1996, Basillais et al., 2007, Martin, 2007, Burr et al., 1985) and thus it has been hypothesized

that the progression of BMUs is influenced by mechanical stimuli. This is not surprising as the two-dimensional (2D) geometry of secondary osteons has been linked to the function of the bones in which they are found (Skedros et al., 2011, Skedros et al., 2003) and resultant mechanical strains (Judex et al., 1997). Additional examples include intra-element regional (i.e. anterior, posterior, lateral, medial) variation in osteon morphology (Martin et al., 1996, Skedros et al., 2009) and a relation between osteon size and weight observed in humans (Britz et al., 2009). To explain the link between mechanics and BMU orientation, computational (*in silico*) modeling has looked to stimuli such as localized strain (Smit and Burger (2000)) and strain-related fluid flow (Burger et al., 2003) around cutting cones. Such *in silico* models continue to become increasingly sophisticated, extending into the realm of simulation (van Oers et al., 2008). All models, however, have relied upon highly idealized BMU morphology and it is unclear how compatible their findings are with the more complex 3D morphologies which have been reported.

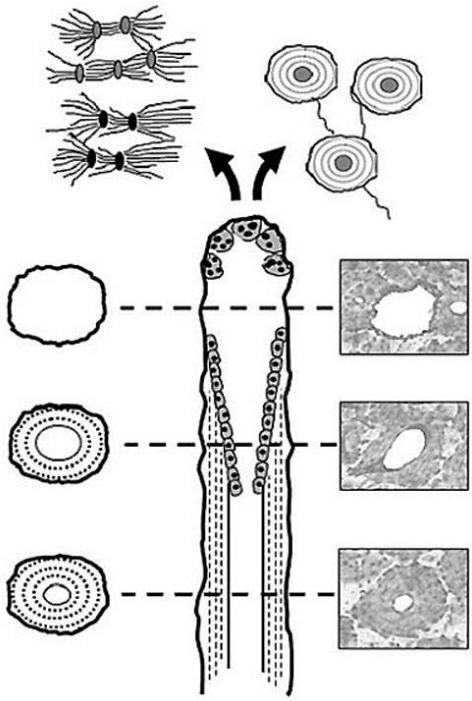

Figure 2.1. Illustration of a BMU showing the classic 'cutting' and 'closing' cone morphology. Osteoclasts located in the BMU's cutting cone are attracted to areas of damaged bone indicated by the microcrack (based on (Martin, 2002)) as well as change in the canalicular network (black lacunae indicative of osteocyte apoptosis) caused by mechanical stimuli such as cyclic loading (based on (Burger et al., 2003)).

Another hypothesis regarding BMU regulation holds that their activities are spatially 'targeted' (Parfitt, 2002b) to remove damage manifested as microcracks (Burr et al., 1985, Burr et al., 2002, Ehrlich and Lanyon, 2002, Ryser et al., 2009). While debate remains over the degree to which remodeling is targeted vs. untargeted (Martin, 2002), if targeting occurs, even for a portion of remodeling events, there must be mechanisms which actively steer BMUs towards damaged areas (Figure 2.1). This has been envisioned as attraction towards an "effective damage removal area" which provides the means by which the osteoclasts of a BMU are drawn towards microdamage (Martin, 2007). Although it has been demonstrated that remodeling-related resorption spaces are associated with microcracks (Bentolila et al., 1998), active steering has yet to be empirically demonstrated. It is possible BMUs are simply initiated in damaged areas. Further, other stimuli clearly play a role and thus a clear dichotomy between targeted vs. non-targeted views of BMU regulation is problematic and they need not necessarily be mutually exclusive (Parfitt, 2002b). The classical view of remodeling has always been envisioned as a multi-functional role – including mechanical and physiological functions (Martin, 2002) such as calcium homeostasis. Efforts to disentangle the multi-faceted regulation of remodeling would be greatly aided by more and better 3D data regarding BMUs and related structures.

In sum, the capacity to directly test hypotheses related to regulation of BMU activity and/or the validation of *in silico* models is limited by a general lack of 3D data. Indeed, the activity of BMUs has largely been inferred from the 2D observation of the secondary osteons they create. Our appreciation of the 3D structure of secondary osteons is, similarly, limited and those data which are available (discussed below) consistently hint at greater structural complexity than commonly appreciated. Improving our 3D understanding of cortical bone microarchitecturewould, thus, enhance our understanding of the remodeling process. As such, the objective of this paper is to provide an overview of methodologies for 3D investigation of cortical bone remodelingand, specifically, structures associated with BMU activity (resorption spaces) and the structures they create (secondary osteons). This review will survey a range of approaches spanning from histology to modern *ex vivo* imaging modalities, culminating with the growing potential of *in vivo*imaging. As such, it will span past, present and emerging approaches. This collection of papers focuses on the theme of "putting the "*why"* back into bone archytecture". Remodeling is one of two mechanisms "*how*" bone structure is dynamically modified and thus an improved 3D understanding of this fundamental process is crucial to ultimately understanding the *"why"*.

2.3. Past: Histological Approaches

Long before the advent of modern 3D imaging modalities (e.g., confocal microscopy, scanning electron microscopy and microcomputed tomography (micro-CT)), traditional light microscopy yielded a wealth of information about bone microarchitecture. Early applications of light microscopy revealed remodeling-related structures including resorption spaces, mature osteons and the canals within these osteons. The study of ground sections led to the first hypotheses pertaining to functional significance. Among the earliest of observations was a link between the extent of remodeling and age. Amprino and Bairati's (1936) study of compact bone from humans and animals was one of the first to show an association between age and osteon population density (i.e. the number of osteons/mm^2). Why this occurs, either through targeted replacement or through the accumulation of stochastic events remains a central debate in the field. It is not surprising then that much remains to be learned from histology and that histology, in various forms, remains a mainstay of bone biology to this day. There are, however, limitations to extrapolating 3D structure from sections – a leap which requires idealization and assumption (Parfitt et al., 1983). Indeed, histomorphology can vary significantly due to differences in sampling location. The formation of an osteon by a BMU is an excellent example. Remodeling can create a new osteon anywhere along a bone's diaphysis and the resorption space in which it forms can extend over several millimeters (Cooper et al., 2006). Stout and colleagues (1999) found that sectioning osteons at different points along their lengths could result in the erroneous classification of different morphological 'types'. They provided the example of a 'dumbbell-shaped' osteon being explained as the product of sectioning through a branching event. Beyond morphology of individual osteons, the rate of remodeling can vary within a bone. Skedros and colleagues (2003), for example, demonstrated that the number of osteons present in the calcanei of Rocky Mountain mule deer increased in a proximal to distal fashion. While larger fields of view (FOV) have become increasingly feasible through the use of tiling microscopes, FOV has been a significant limitation of microscopy. This is especially problematic for the measure of rate of remodeling – reflected by the measure 'activation frequency', which is defined as the number of new BMUs present in a particular unit of bone (Frost, 1969). Activation frequency can directly affect overall bone mass, because 'remodeling space' temporarily reduces overall bone mass until it is subsequently filled in (Martin, 1994). Thus, a high remodeling rate can, in part, account for low mass. Activation frequency can

be measured in either 2D sections (BMUs/mm^2/unit time) (Frost, 1969) or 3D volumes (BMUs/mm^3/unit time) based on the number of BMUs created per unit volume of cortex per unit time (Frost, 1964). The 3D extent of BMUs – their length or 'range' – is a very difficult parameter to assess from histology, even from longitudinal sections. This parameter has the potential to impact the regional assessment of activation frequency with longer resorption spaces having increased potential to be detected in section. Cooper and colleagues' (2006) micro-CT analysis of 99 BMUs in human bone provided a measure of range varying between ~0.8 mm – 5.4 mm and most likely longer as they were limited to a 7 mm FOV and some remodeling events extended beyond. Keeping in mind the significant impact of sample site selection, activation frequency measures based on how *many* BMU-related resorption spaces are visible in sections acquired only millimetres apart from one another could be very different. Another problem with typical activation frequency measures is that, in section it can be difficult to differentiate BMU-related resorption spaces from other structures such as Volkmann's canals (Martin, 1994). That being said, histology-based analytical techniques are still the gold standard for visualization of bone microstructure. Indeed, histology remains the primary means of investigating the relation between remodeling and microdamage. When identifying microdamage, in the form of microcracks, it is critical to ensure one is detecting *in vivo* damage and not artifacts of processing – particularly when utilizing grinding-based approaches as they can produce artifacts within bone that resemble cracks induced *in vivo* (Frost, 1960, Lee et al., 2003). Microcracks are generally observed in 2D sections (Presbitero et al., 2012, Thurner et al., 2006) and thus their overall morphology, and relation to remodeling events, can be difficult to ascertain. For example, comparison of microcrack morphological features, such as size and shape, viewed in 2D has been shown to exhibit differences, to the extent that individual cracks look like entirely distinct structures (Thurner et al., 2006, Larrue et al., 2011). This was seen to be the case in a study by Voide et al. (2009) which found certain microcracks appeared linear and confined in the cross-sectional plane, whereas viewed in the perpendicular plane, they appeared diffuse.

Serial sectioning can alleviate some of these issues associated with 2D histology. Multiple sections increase the amount of bone analyzed and provide direct insight into the 3D nature of microarchitecture. Cohen and Harris' (1958) analysis of serial decalcified sections from canine femora reported that osteons follow a spiral orientation around both the axis of the bone and axes of the osteons themselves. This seminal 3D study also reported that morphological characteristics

vary in their distribution and this variation is linked to the specific locations within the bone. They observed that osteon cross-sectional area increased as they coursed distally throughout the bone and were also greater in the endosteal as opposed to subperisosteal regions (Cohen and Harris, 1958), a finding suggestive of a mechanical influence on osteon morphology and thus BMU activity. Tappen's (1977) work with block section staining using silver nitrate revealed morphological characteristics of osteonal canals, lacunae, osteocytes and canaliculi. Tappen (1977) highlighted numerous features of osteons and the remodeling process which included: levels of stain uptake in bone can be used as an indicator of mineralization, BMU-related resorption spaces are continuous with canals, these spaces can tunnel in opposite directions from one another or in only one direction, and some unforeseen force(s) dictate osteon/resorption space diameter as evidenced by the areas of mineralized bone resorbed in active areas of remodeling.

Despite its advantages, serial sectioning is challenging and thus only a few significant attempts to investigate cortical bone microstructure by this approach have been published (Skedros et al., 2007, Cohen and Harris, 1958, Tappen, 1977, Stout et al., 1999). Notably, these few studies have not found consensus with respect to some general aspects of osteon morphology. For example, Stout and colleagues' (1999) digital analysis of Tappen's (1977) serial sections did not find evidence that osteons follow a spiral pattern around the axes of bone as suggested by Cohen and Harris (1958). Rather, they found a complex pattern of branching osteons. Indeed, all 3D studies have revealed greater structural complexity than is frequently appreciated in the literature. While the literature is dominated by the 'classical' BMU morphology presented in Figure 2.1., it should be noted that data indicating a complex diversity of remodeling-event types was reported in the mid 1960's by Johnson (1964). We would argue that a lack of practical and efficient 3D techniques has contributed to the corresponding lack of information regarding BMU and osteon morphology. Beyond the difficult and tedious nature of existing serial-sectioning approaches, no small measure of luck is required to target these techniques to study individual BMUs and/or their related structures. Methodological difficulties ultimately led to the exploration of imaging-based approaches to the study of bone remodeling.

2.4. Present: *ex vivo* Imaging

Since its introduction by Feldkamp and colleagues (1989), X-ray micro-Computed Tomography (micro-CT) has become the 'gold standard' for the non-destructive 3D analysis of

trabecular bone morphology. More recently this technology has increasingly been applied to cortical bone to analyze the porous network of canals in 3D (Cooper et al., 2006, Cooper et al., 2003, Cooper et al., 2007, Britz et al., 2010, Basillais et al., 2007, Pazzaglia et al., 2010, Chen et al., 2010, Palacio-Mancheno et al., 2014, Bousson et al., 2004). With respect to the study of remodeling, micro-CT represents an excellent approach for detection of BMU-related resorption spaces since their distinctive cutting cones generally stand out from the relatively smaller canals of completed osteons. Another key advantage of micro-CT is its ability to non-destructively survey a large volume of bone for active remodeling events. An excellent example of this is our group's recent use of a laboratory micro-CT system (SkyScan 1172, Bruker, Belgium) to locate and trace BMUs in complete diaphyses of *Ursus americanus* (black bear) metacarpals and metatarsals without the requirement of sectioning (Figure 2.2) (2014). In a more general sense, micro-CT can provide insight into remodeling through assessment of canal (and hence osteon) orientation (Britz et al., 2010) as well as the overall complexity of the canal network, which has been hypothesized to increase with cumulative remodeling activity (Cooper et al., 2006, Cooper et al., 2003). The potential exists to examine osteon 'steering' through assessment of localized canal orientation. Thus, the capabilities of micro-CT can alleviate or, at minimum, limit many issues associated with histological techniques for cortical bone: 1) interpolation of 3D structure from 2D sections is not needed as structures are observed directly and measured in 3D; 2) measures can be calculated in units of volume as opposed to area; 3) sample preparation is limited, eliminating structural alterations; 4) sample site location is less of an issue as visualization and analysis of larger volumes of interest – even of entire bones – becomes feasible. These advantages are just beginning to be brought to bear on the *ex vivo* study of cortical remodeling and micro-CT clearly has great potential to provide new insights through improved measures of morphology (including orientation, possible 'steering', and 3D range) and activation frequency.

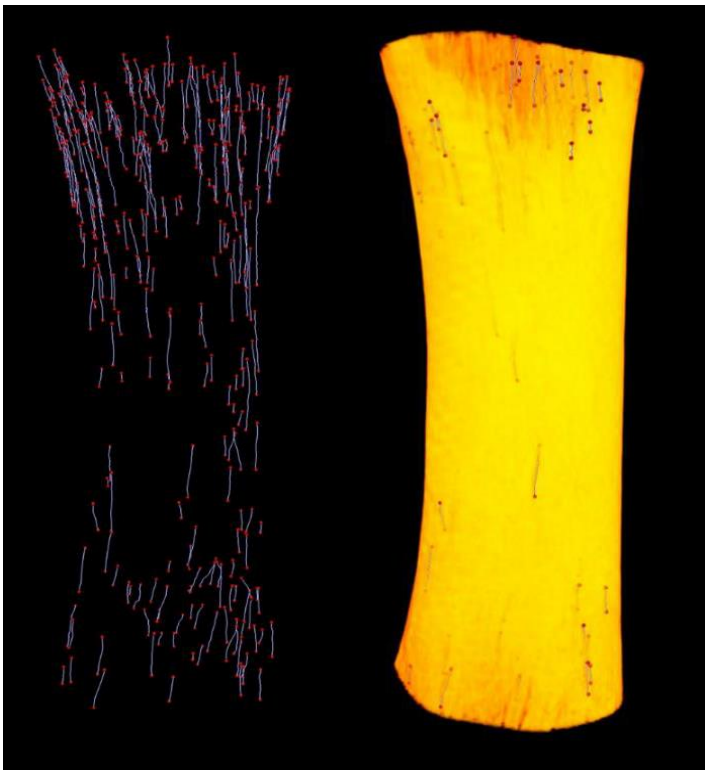

Figure 2.2. Left: Reconstructed micro-CT image of landmarked and skeletonized BMUs in a black bear metacarpal; Right: 3D render of bone diaphysis superimposed over BMUs. Diaphysis length = 31.84 mm.

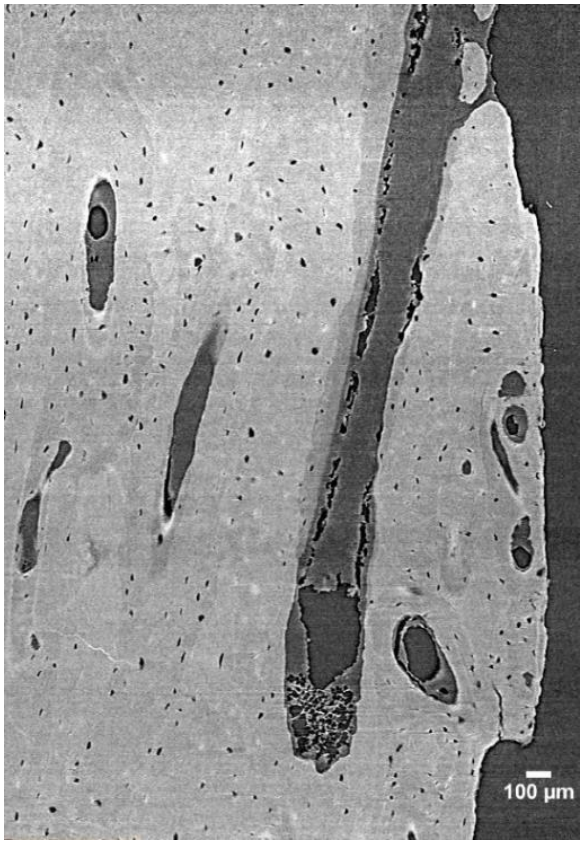

Figure 2.3. 3D reconstruction of a human femur section depicting BMUs and osteocyte lacunae acquired by SR micro-CT at a 1.47 µm resolution (Carter et al., 2013a). Image provided by Dr. Yasmin Carter.

Despite its many benefits micro-CT has several limitations. For cortical bone, the most notable is that while some delineation of osteon borders is possible from laboratory systems (Arhatari et al., 2011) this technology remains largely limited to detecting porosity at the vascular level and larger (e.g., osteonal canals and resorption spaces). Synchrotron radiation (SR) micro-CT, with its many advantages conveyed by greater X-ray flux, its monochromatic coherence and high brilliance as a result of a small source size, can be used to visualize smaller-scale structures including osteon borders (Dalstra et al., 2004, Cooper et al., 2011), different osteon morphologies (Cooper et al., 2011), osteocyte lacunae (Carter et al., 2013a, Langer et al., 2012, Schneider et al., 2007) (Figure 2.3) and even microcracks (Voide et al., 2009, Voide et al., 2011, Christen et al., 2012, Larrue et al., 2011).

A limitation shared by both micro-CT and SR micro-CT is that, in general terms, higher resolution comes at the cost of field of view. A further related limitation is that as resolution increases, so does the radiation dose. Improving resolution by a factor of 2 requires a dose increase by a factor of 16 to maintain image quality in micro-CT (Ford et al., 2003). This relation provides the practical limit on the resolution for *in vivo* X-ray based computed tomography. Thus, despite the fact that micro-CT imaging of trabecular bone microstructure in living animals is now commonplace (10-20 μm voxel size), its application to the internal microstructure of cortical bone is not. An exception to this is the increasing use of High Resolution peripheral Computed Tomography (HR-pQCT) to analyze cortical porosity in humans which will be discussed in the next section. The limited applications of micro-CT to the internal microstructure of cortical bone (e.g., osteonal canals) in animal models have all been *ex vivo* (Britz et al., 2012, Mader et al., 2013). Working *ex vivo*, it is even possible to image microcracks utilizing barium sulfate as a contrast agent (Turnbull et al., 2011, Leng et al., 2008, Landrigan et al., 2011). With the vascular porosity of cortical bone beyond the reach of conventional *in vivo* micro-CT, it goes without saying that the resolutions required for microcrack imaging are not compatible with live animal imaging. Voide and colleagues (2009) used SR micro-CT with a nominal resolution of 700 nm to visualize microcracks, *ex vivo*, in the femora of mice. Even if radiation dose were not an issue, holding a living animal still for sub-micron imaging would present a significant challenge in and of itself. Thus, while much can be learned about remodeling through *ex vivo* 3D imaging, *in vivo* detection and tracking of remodeling-related structures would represent a significant step forward with still

greater potential to improve our understanding of this process. As will be discussed, there are specific advantages of synchrotron-based imaging which have created the potential for *in vivo* imaging of cortical porosity – opportunities that are just beginning to be explored and thus lie on the future horizon.

2.5. Future: *in vivo* Imaging

A new generation of clinical research HR-pQCT scanners have given rise to a new opportunity for 3D, *in vivo*, characterization of human bone, both trabecular and cortical. With an isotropic voxel size of 82 µm, HR-pQCT has been at the forefront for micro-architectural analysis of the human appendicular skeleton (i.e. distal radius and tibia) (Burghardt et al., 2010, Macdonald et al., 2011) as it is particularly advantageous for measuring cortical porosity (Jorgenson et al., 2015). While HR-pQCT has been instrumental in studies concerned with osteoporosis induced change in microstructural cortical bone (Macdonald et al., 2011) its viability as a tool for targeting and tracking specific cortical structures, such as individual BMUs, is unclear due to resolution and other limitations associated with movement artifacts and the restriction to primary trabecular bone sites (i.e. wrists and ankles) (Engelke et al., 2013). When one considers that the size of a single HR-pQCT voxel is on the same scale as the average canal diameter within human cortical bone, ~120 µm for pooled sexes (Cooper et al., 2007), it becomes clear that this technology cannot resolve all osteonal canals. A recent study comparing HR-pQCT as a tool for measuring pore sizes against SR micro-CT showed that the accuracy of HR-pQCT was a factor of the size of the pores measured (Jorgenson et al., 2015)—current resolution limits its ability to recognize small pores, thus introducing partial volume effects into analyses (Engelke et al., 2013). That said, as BMU-related resorption spaces average 250 µm in diameter (e.g., the average diameter of an osteon in humans (Britz et al., 2009)), HR-pQCT may indeed hold the potential of tracking individual remodeling events in human cortical bone. Thus, while HR-pQCT represents a powerful new tool for the assessment of cortical porosity, it is limited to the largest of cortical pores located in the ultra-distal peripheral skeleton.

Human-based studies are clearly an important avenue for study, but more mechanistic studies will require controlled model systems. When considering animal models—particularly smaller animals—the punishing relation between resolution and radiation dose complicates *in vivo* imaging. The risks associated with high X-ray doses are not only harmful to a living subject in an

acute sense, they include the potential to alter bone structure, leading to osteopenia, growth arrest, fracture and malignancy (Pacheco and Stock, 2013) through altered osteoclast and osteoblast activity (Laperre et al., 2011). For example, at a voxel size 10.5 μm and a radiation dose of 845.9 mGy, longitudinal scans of the hind limb in mice acquired over a five-week period resulted in decreased bone volume and increased trabecular separation (Klinck et al., 2008). Even though SR micro-CT makes *in vivo* imaging of cortical porosity more plausible through higher resolution and shorter scan times, the limitations imposed by radiation dose are still a factor. As will be discussed, the monochromatic (single X-ray energy) capabilities of synchrotrons enable alternative methods of developing contrast beyond absorption. These so-called 'phase contrast' techniques are opening the door to new possibilities for *in vivo* imaging.

Several forms of phase contrast imaging, including in-line phase contrast, diffraction-enhanced imaging, and interferometer-based imaging, have been increasingly explored for their potential utilization in biomedical applications. An excellent overview of these methodologies is provided by Zhou and Brahme (2008). Unlike conventional radiography, where images are based on the differences in X-ray absorption related to an object's internal structure, phase contrast images contain information related to the refractive index of an object because the images produced are derived from the pattern of interference created from diffracted and undiffracted waves (Arfelli et al., 1998). Differences in refractive index of the sample's internal structure will refract or bend the X-ray wavefront as they pass through the target and these differences can be used to generate contrast (Zhou and Brahme, 2008). For in-line phase contrast imaging—the simplest of these techniques to implement—detection of changes in X-ray refractive indices within a sample can be optimized by altering the distance between the object and the detector (Zhou and Brahme, 2008, Pratt et al., 2015) **(**Figure 2.4**)**. Simple implementation and enhanced detection of internal features have made the fusion of SR computed tomography and phase contrast imaging particularly advantageous for visualization of microscopic bone structures such as osteocyte lacunae (Carter et al., 2014, Carter et al., 2013a, Carter et al., 2013b) and even nanoscopic structures such as the lacuno-canalicular network (Langer et al., 2012). Phase contrast is not dependent on X-ray attenuation and thus higher energies, where attenuation is lower, can be employed (Zhou and Brahme, 2008). This creates the possibility of higher resolution with equal or reduced dose compared with attenuation-based imaging.

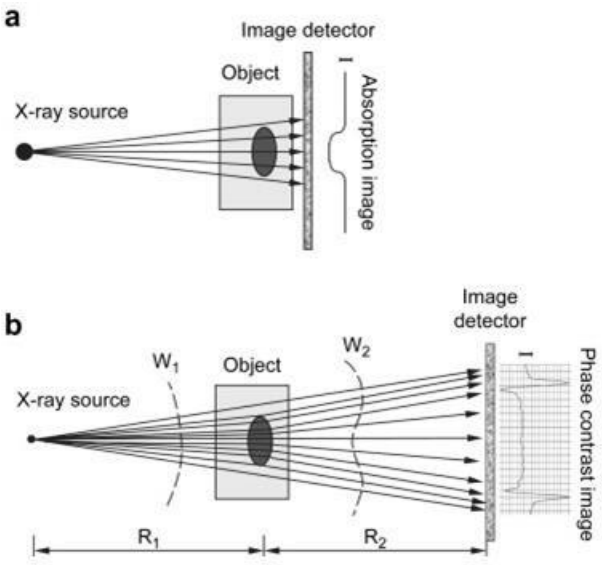

Figure 2.4. Part A: schematic of attenuation-based X-ray imaging where images are produced based on the degree of absorption relative to an object's internal structure. Part B: schematic of in-line phase-contrast imaging based on an object's refractive properties. As X-rays target an object at different angles, variations in the object's internal structure will refract the X-rays and cause a shift in the light wave as it propagates through and increasing the object-to-detector distance will produce a contrast image. (Zhou and Brahme, 2008). Reprint permission granted by the publisher.

Our group recently tested the feasibility of in-line phase contrast SR micro-CT for imaging the cortical porosity in the forelimb of rats with radiation doses comparable to those commonly employed *in vivo* for imaging trabecular microarchitecture (Pratt et al., 2015). Since its' first implementation (Kinney et al., 1995), numerous *in vivo* SR micro-CT protocols varying in both dose and image resolution have been utilized to visualize the microarchitecture of bone in small animal models (Bayat et al., 2005, Matsumoto et al., 2011, Pratt et al., 2015, Coan et al., 2010). Currently, there is no consensus for what is considered to be a safe dose for live animal *in vivo* imaging. Voxel sizes in the 10 µm – 15 µm range are typical for laboratory micro-CT with dose rates of 0.4 Gy, 0.338 Gy and 0.939 Gy, respectively (Waarsing et al., 2004, Campbell et al., 2011, Brouwers et al., 2007). However, at a voxel size of 11.7 µm, Matsumoto et al.'s (2011) *in vivo* scans of the knee joint in living mice involving 5 Gy showed no signs of radiation sickness. Based

upon this context, our goal was to create an *in vivo* imaging protocol involving a dose as close as possible to those used routinely in conventional micro-CT and no higher than 5 Gy.

In a proof-of-principle study, *ex vivo* data collected at the BioMedical Imaging and Therapy (BMIT) facility of the Canadian Light Source (CLS) synchrotron were compared against laboratory micro-CT protocols and their related doses. Studying rat forelimbs it was found that SR provided superior detection of cortical pores without a substantial increase in dose (11.8 µm voxels, 2.53 Gy) beyond that used in the laboratory systems (18 µm voxels, 1.2-1.5 Gy; 9 µm voxels, 11.7-18.2 Gy) (Pratt et al., 2015) (Figure 2.5). For in-line phase SR micro-CT, the optimal target-to-detector distance for our configuration was found to be 0.9 m. Subsequent to the *ex vivo* trials, the first *in vivo* trial was performed (Pratt et al., 2015) and the first longitudinal studies employing this protocol are under way – providing encouraging results with respect to tracking individual remodeling events (Figure 2.6).

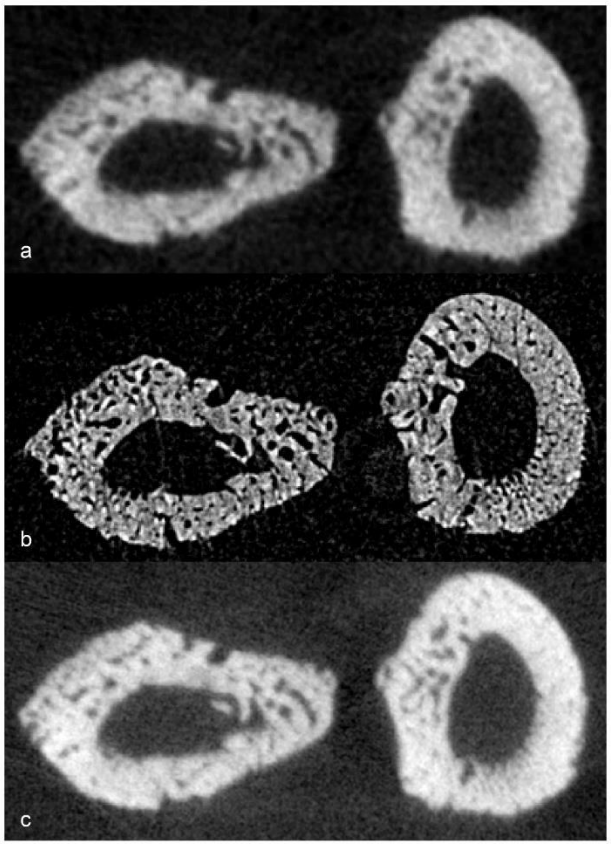

Figure 2.5. Reconstructed slices of rat forelimbs depicting visualization of cortical porositybased on the imaging system used: a) *in vivo* laboratory SkyScan 1176 micro-CT (18 μm, 1.2–1.5 Gy dose, b): *in vivo* synchrotron micro-CT slice measured using the C4742-56-12HR camera (11.8 μm, 2.53 Gy dose), c): *in vivo* laboratory SkyScan 1176 (9 μm, 11.7–18.2 Gy dose) (Pratt et al., 2015). Reprint permission granted by the publisher.

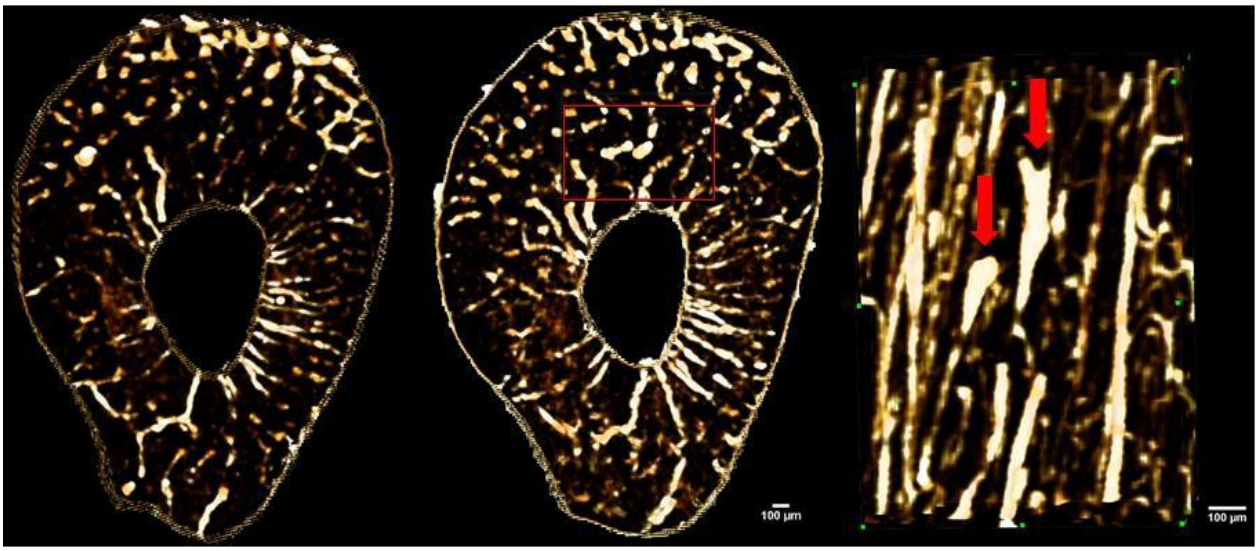

Figure 2.6. Images showing *in vivo* matched scans of a rat forelimb acquired with SR micro-CT (11.8 µm, 2.53 Gy). Scan B was carried out 2 weeks after scan A on the same rat's forelimb. Image C is an enlarged section of image B (red rectangle) displaying new remodeling events (red arrows).

SR micro-CT, taking advantage of in-line phase contrast, has brought about a new opportunity for *in vivo* imaging to directly test causative hypotheses relating to cortical bone remodeling; however, it too is not without its limitations. Access to synchrotrons is inherently limited due to the relative scarcity of such facilities and, in particular, those with biomedical-focused facilities capable of imaging live animals. Even with the high resolution afforded by SR micro-CT and the ability to minimize dose through use of in-line phase contrast imaging, some structures such as osteon borders and microcracks are not observable, *in vivo.* Indeed, such structures remain challenging to image *ex vivo*, requiring very high-resolution systems. Movement artifacts are problematic as the difficulty in holding the animal perfectly still increases along with resolution. The smallest of the standard animal models (e.g., mice and rats) have the further drawback of not exhibiting much, if any, natural cortical remodeling – although it can be induced by experimental means (e.g., fatigue loading in the rat (Bentolila et al., 1998)). Notably, this imaging approach has the potential to be extended to larger animal models including those such as the rabbit which exhibit remodeling under normal conditions. Larger cortical canals in such animals could also relax the resolution needs and, concomitantly, reduce radiation dose.

2.6. Conclusion

The remodeling process, carried out by the activity of BMUs, is of great interest to the bone biology community. This process represents the primary means of skeletal change after maturity and lies at the root of many chronic bone diseases, including osteoporosis. Visualization of cortical bone microarchitecture and, specifically, the remodeling process has progressed from 2D histological analysis through *ex vivo* 3D imaging and now to *in vivo* 3D analysis. This progression has paralleled but lagged behind visualization of trabecular bone microarchitecture due to the smaller scale of the target features and the need for high resolution which suffers the complication of increased radiation dose for X-ray based imaging. An important consideration is the caveat that while this progression involves a decreasing level of sample destruction/invasiveness, there is a trade off in terms of the structures one can visualize. The imaging approaches are best suited to detection of porosity. Thus, for some applications histology (serial or otherwise) remains the most powerful or possibly only approach available. That said, there is a great potential to combine the strengths of these approaches—fusing 2D and 3D imaging to maximize the information available. This will enable targeted histology—directed by imaging data. Looking to the near future we believe that this approach will see application in direct testing of hypotheses related to the regulation of BMU activity—including questions related to steering/orientation, the role of microcracks and the relation to other stimuli, including possibly cellular signals. Such data will, in turn, prove invaluable for validating *in silico* models—an area of increasing focus in bone biology. Ultimately, we believe the novel insights possible through 3D data will shed significant new light on the ‘how’ of bone aging, adaptation, and disease. Understanding the ‘how’ is critical to understand the “why”.

2.7. Epilogue (unpublished with original article)

Exploration of in-line phase contrast SR micro-CT as a dose-reducing, *in vivo* imaging technique to render the cortical porosity of rat ulnae (Pratt et al., 2015) (Chapter 2) served as the platform for testing an initial hypothesis of my thesis project: remodeling targets microdamage in the form of microcracks by tracking the progression of basic multicellular units (BMUs) within the cortical bone of rat ulnae. Remodeling occurs minimally, if at all, in rodent cortical bone and thus, must be induced. Fatigue loading has been reported to artificially induce intracortical remodeling in rats by applying axial compressive loads to the bone (Hsieh and Silva, 2002, Bentolila et al., 1998). The rat ulna is particularly well suited for fatigue loading. Axial compression induces bending along the natural medial-lateral curvature of the bone without introducing structural biases and maximum strain at the mid-diaphysis, which most likely represents the normal strain distribution exerted due to locomotion (Torrance et al., 1994). Utilizing our established in-line phase contrast SR micro-CT protocol (see Appendix A for further discussion), in vivo images of fatigue loaded rats showed some initial promising results (Chapter 2). I did not, however, consistently observe BMU-related resorption spaces via either laboratory micro-CT or ground section histology. After several modifications to the fatigue loading protocol that mimicked those reported (see Appendix B & C for further discussion), I could not replicate those results. Rather, SR micro-CT and micro-CT analysis of fatigue loaded ulnae in comparison to contralateral non-fatigued controls did not show a significant increase of BMUs. Shifting from a rat to a rabbit model of elevated remodeling to target and track BMUs *in vivo* was a necessary change of focus. Therefore, I set out to investigate whether **rabbit models of osteoporosis could elevate BMU remodeling, creating a novel platform for the direct 4D measurement of BMU LER *in vivo***.

2.8. Acknowledgements

The authors thank the organizers of this topic, Drs. Phil Salmon, Daniel Chappard and Andrew Pitsillides. The authors would also like to thank: the Canadian Light Source BMIT line staff, particularly Drs. George Belev, Ning Zhu and Adam Webb, Dr. Melanie van Der Loop and staff of the University of Saskatchewan's Laboratory Animal Services Unit and the support of Dr. Mike Doschak of the Pharmaceutical Orthopaedic Research Lab at the University of Alberta and the contributions of Dr. Dean Chapman, Dr. Yasmin Carter, Isaac Pratt, and Danielle Kabatoff. Finally, the authors thank Ms. Suyoko Tsukamoto for providing black bear bone samples (MB Conservation #WBO8992). Support for this research was provided by the Natural Sciences and Engineering Research Council (NSERC) of Canada via a Discovery Grant to DMLC (RGPIN-2014-05563) and the Canadian Foundation for Innovation and Canada Research Chairs program. KDH is supported by the University of Saskatchewan, College of Medicine, and is a CIHR-THRUST Fellow.

2.9. Conflicts and Interests

The authors declare that the research was conducted in the absence of any commercial or financial relationships that could be construed as a potential conflict of interest.

Chapter 3 Cellular Signaling Pathways of Rabbit Models of Osteoporosis

3.1. Clinical Definition of Osteoporosis

Osteoporosis is a skeletal disease that imposes deleterious effects on bone quantity (defined by bone mineral density (BMD) and geometry) and quality (microarchitectural structure and mineralization of bone that affects strength) (Compston, 2006), which increases an individual's risk for fracture(s) (NIH Consensus Development Panel on Osteoporosis Prevention and Therapy, 2001). Low bone quantity (BMD) measured through Dual-energy X-Ray absorptiometry (DXA) is a commonly accepted predictor for an individual's fracture risk (Khan et al., 2018). Clinically, an individual with a T-score 2.5 standard deviations (SD) below the mean BMD of a typical young adult would be considered osteoporotic based upon World Health Organization standards (Risk and Osteoporosis, 1994). Patients suffering from osteoporotic fracture have been shown to exhibit BMD in the osteopenic (i.e., low bone mass not considered osteoporotic; T-score of -1 to -2.5) range (Siris et al., 2004). Thus, OP is not merely a disease of low BMD but also one of poor microarchitectural quality.

Compromised bone quantity and quality associated with OP result from altered remodeling. Low bone quantity in the form of depleted bone mass also has a deleterious effect on bone quality through the deterioration of the microarchitecture, particularly for trabecular bone (Burr et al., 1997). The overall strength and integrity of cortical bone is related to its microarchitectural components, which includes porosity (Augat and Schorlemmer, 2006). At the heart of OP, continual deficit in bone formation, either through unbalanced or uncoupled BMUs, summed over multitude of BMUs can cause increased porosity and thinned cortices via coalescence of large porous spaces (Cooper et al., 2007) (Figure 3.1).

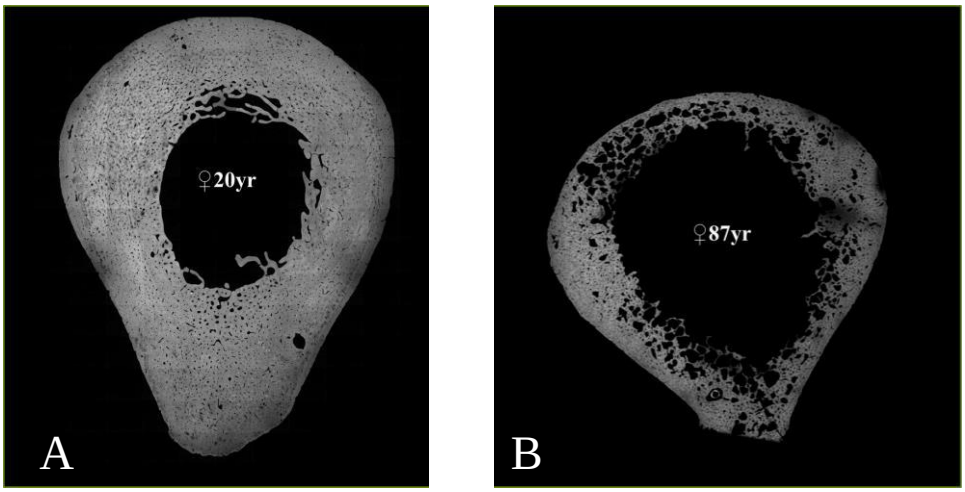

Figure 3.1. Microradiographs of human mid-femoral cross sections depicting normal (A) and aged (B) cortical bone. Age-related bone loss causes weak, fragile bone more susceptible to fracture through not only an increase in cortical porosity but also from endosteal thinning of the cortex, characteristics which can be observed in the 87-year-old female (B), compared to that of a young, healthy 20-year-old female (A). Microradiographs are courtesy of Dr. John Clement and David Thomas (Source: Melbourne Femur collection).

Osteoporosis is not strictly limited to the aged. Childhood/adolescent conditions that require use of corticosteroids (i.e., glucocorticoids (GCs)), diseases associated with malabsorption, or anorexia-associated hypogonadal states in young females, can reduce peak bone mass during growth. This reduction can cause OP or lead to its occurrence even without age-related accelerated bone loss (NIH Consensus Development Panel on Osteoporosis Prevention and Therapy, 2001). Indeed, depending on the underlying cause of the disease, OP can be classified as either primary or secondary. Primary OP is considered as either adult Type I (postmenopausal osteoporosis; PMO) – resulting from depleted estrogen levels at the onset of menopause and preferentially affecting trabecular bone, or Type II (age-related) OP – trabecular and cortical bone loss associated with advanced age in the elderly (Fan and Peh, 2016). In contrast, secondary OP is the result of some other condition, such as another disease like hyperparathyroidism (Rochefort, 2014), in which the parathyroid glands produce excessive amounts of PTH, or is caused by the treatment of an unrelated medical condition, such as GC therapy common to various autoimmune diseases.

There is no single causative factor attributed to the onset of OP (2015). Current treatment measures involve nonpharmacologic supplementation with calcium and vitamin D and lifestyle adjustments (Rebolledo et al., 2011). Pharmaceutical-based treatments are tailored towards reducing fracture risk by slowing bone loss (2015). Anti-resorptive drugs (i.e., bisphosphonates

(BPs)) that target overactive osteoclastic bone resorption or anabolic teriparatide (i.e., parathyroid (PTH) hormone) that promotes bone formation through increased osteoblast activity (Rebolledo et al., 2011) or a combination thereof are also commonly employed. While both groups of drugs have been shown to improve BMD and reduce fracture risk (Black and Rosen, 2016), they have side effects. Bisphosphonates are the most common treatment for OP, but they have been associated with infrequent mild hypocalcemia and muscle pain (Black and Rosen, 2016) and, more rarely, with atypical femoral diaphyseal fracture and osteonecrosis of the jaw (Khan et al., 2018). Due to its anabolic effects, intermittent PTH is an American Food and Drug Administration Agency (FDA) approved treatment for glucocorticoid-induced osteoporosis (GIO), the leading cause of secondary OP within humans (Weinstein, 2012). However, a net increase in bone effectsassociated with intermittent (i.e., once daily) PTH is constrained to 18 - 24 months of treatment due initial to pre-clinical studies observing significantly increased rates of osteosarcoma in rats treated long-term with high doses of PTH (Eastell et al., 2019), although only one instance has been known to occur in humans (Black and Rosen, 2016). Furthermore, when administered continuously, PTH produces a catabolic effect within bone which causes the very thing it is meantto treat, OP.

The diagnostic evasiveness and severe individual and economic burden attributed to OP highlights the need to prevent bone degeneration and implement efficient pharmacological treatments that prevent or slow down resorption and ensure adequate bone formation, especially within cortical bone as the significance of its microarchitectural deterioration in OP is increasingly recognized. The exact mechanisms responsible for this breakdown of remodeling remain unclear, however, tracking BMUs with suitable animal models can potentially shed light on the spatio-temporal regulation of remodeling (Cooper et al., 2016).

3.11. Animal Models of Osteoporosis – the Rat and Rabbit

When considering potential alternative paths forward for my research beyond the rat fatigue loading model, a literature review confirmed that a rat OP model would face similar limitations. The most common way to model PMO in animals is through ovariectomy (OVX) (Permuy et al., 2019) and the OVX rat model is commonly used in OP research because it exhibits trabecular bone loss (Turner et al., 2001, Yousefzadeh et al., 2020), mimicking the early effects of human PMO. As discussed further below, the onset of menopause first induces a period of elevated

resorption of trabecular bone followed by a secondary period where cortical bone loss (increased porosity and thinning) occur along with continued but slower trabecular loss (Yousefzadeh et al., 2020, Seeman and Delmas, 2006). It is with respect to cortical bone loss that the rat model is particularly lacking. Importantly, it has recently been argued that PMO associated cortical bone loss is as much if not more prevalent than trabecular loss due to the "feedback" nature of intracortical remodeling, where enlargement and coalescence of canals induce further remodeling of a continuously diminishing cortical matrix (Bjørnerem et al., 2018). The significance of this argument can be appreciated within the context that bone is 80% cortical (Bala et al., 2015, Zebaze et al., 2010) and that cortical bone sites account for 80% of nonvertebral fractures (Zebaze et al., 2010, Zebaze and Seeman, 2015). So although rats are a common animal model due to their affordability, availability, ease of handling and maintenance, and well-characterized trabecular bone loss in OVX, their lack of cortical remodeling (Turner et al., 2001) makes them a poor model to investigate OP related cortical porosity (Lelovas et al., 2008). This fact led to the recommendation by the FDA to include a non-rodent model (i.e., dog, pig, sheep, and nonhuman primate) that exhibits cortical remodeling (Thompson et al., 1995) in preclinical studies of OP.

While not directly listed within FDA guidelines, the rabbit has been investigated as a suitable animal model for OP (Castañeda et al., 2008, Castañeda et al., 2006, Baofeng et al., 2010, Permuy and López-Peña, 2019). Rabbits offer an alternative to the traditional OVX rat model as they are particularly well suited for studying cortical remodeling. This is due to several reasons: 1) they are the smallest, commonly employed laboratory animal model that naturally exhibits cortical remodeling similar to that of humans (Pazzaglia et al., 2007, Pazzaglia et al., 2009, Pazzaglia et al., 2010); 2) the remodeling period of rabbits is shorter than larger animal models, allowing earlier skeletal maturation (by 6–9 months) (Gilsanz et al., 1988) and more rapid response to increased remodeling via drug treatments; and, finally, 3) executing statistically robust *in vivo* studies with rabbits is more feasible, logistically and financially, than using larger animal models of OP (Cooper et al., 2016). It is for these reasons rabbits became the new focus for my thesis project.

3.2. Cellular Signaling Pathways of Bone

In this section two important orchestrators of bone cellular activity, the RANK/RANKL/OPG and Wnt signaling pathways (Kenkre and Bassett, 2018) are introduced.

The roles of these pathways in OP and, specifically, established rabbit models of OP (Castañeda et al., 2008), including primary ovariectomy (OVX), secondary glucocorticoids (GC), and a combination thereof (OVX+GC) are examined. Parathyroid hormone (PTH), a FDA approved treatment for secondary GIO in humans, and a known elevator of cortical remodeling within rabbits, is also addressed.

3.21. Osteoclast Differentiation: RANK/RANKL/OPG pathway

Characterization of bone remodeling, where bone resorption is coupled to formation, at the cellular level has become increasingly appreciated with continuing advancements in bone biology (Khosla, 2001), namely with the depiction of the RANK/RANKL/OPG pathway (Simonet et al., 1997) and its role within clinical metabolic diseases including OP (Hofbauer et al., 2004). This pathway consists of 1) RANK-Ligand (Receptor Activator of Nuclear factor Kappa-B Ligand - RANKL), a protein expressed by osteoblasts which plays a significant role in osteoclast formation, function, and survival through interaction with its receptor 2) RANK (Receptor Activator of Nuclear factor Kappa-B), located on both precursors and mature osteoclasts and lastly 3) Osteoprotegerin (OPG), a protein secreted by osteoblasts, which binds to RANKL and therefore inhibits its bone resorptive activities. The RANK/RANKL/OPG pathway and its role in driving osteoclast differentiation (Eriksen, 2010) led to the understanding that pre-osteoblastic/stromal cells dictate osteoclast development by expression of RANKL binding to its receptor, RANK, on osteoclast precursors (Khosla, 2001, Boyce and Xing, 2007, Tobeiha et al., 2020, Jones et al., 2002) which fuse to form mature, multinucleated osteoclasts which function to resorb bone (Figure 3.1). After resorption, osteoblasts drive bone formation through deposition of new, organic matrix and its subsequent mineralization. Within the BMU, this sequence of activation of osteoclastic bone resorption is followed by a reversal of osteoclast activity via apoptosis and, finally, a shift to osteoblastic bone formation, which permits coupled bone remodeling (Figure 1.2), and, therefore, the integrity of bone tissue (Khosla, 2001). In this sense, the binding of OPG to RANKL directly determines bone strength and integrity as the extent of OPG expression controls the amount of bone resorption that occurs (Boyce and Xing, 2008).

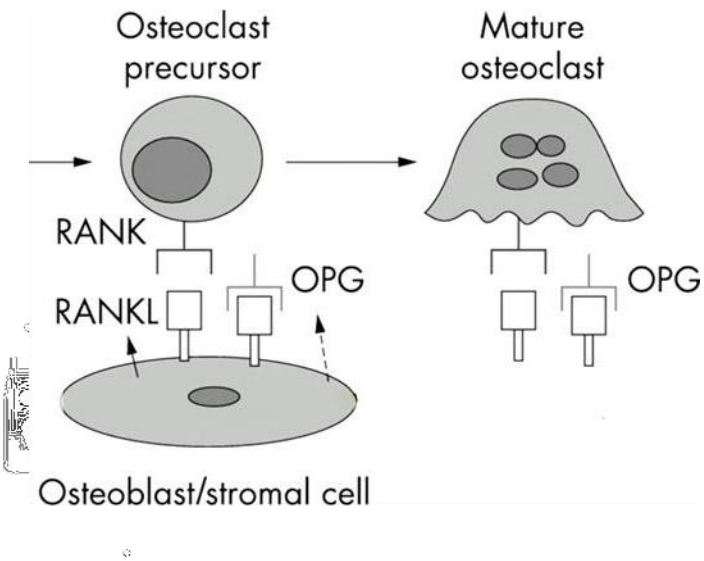

Figure 3.2. Illustration of the RANK/RANKL/OPG signaling pathway (modified from Jones et al. (2002)). The binding of RANKL to its receptor RANK on osteoclast precursors stimulates bone-resorbing activity in mature osteoclasts. Osteoblasts produce OPG, the decoy receptor for RANKL, and therefore, its expression inhibits osteoclastogenesis and osteoclast activation by binding to RANKL. Reuse in this thesis granted by the publisher (License # 5122680048352).

3.22. Osteoblast Differentiation: The Canonical Wnt signaling pathway

The canonical Wnt signaling pathway functions to promote osteogenesis through osteoblast differentiation (i.e., proliferation, survival, and functional lifespan). It is controlled by glycoproteins known as Wnt, which stimulate osteoblast precursor growth (Westendorf et al., 2004), among other biological functions such as ontogeny, morphogenesis, carcinogenesis, and maintenance of stem cells (Maeda et al., 2019). Wnt binds to its receptors Frizzled (Fz), and protein (LRP) 5 or 6 which in turn results in the accumulation of ß-catenin, which activates target gene transcription within the nucleus to promote osteoblast proliferation and differentiation (Kenkre and Bassett, 2018, Clevers and Nusse, 2012) (Figure 3.2), and is, therefore crucial for bone tissue formation (Eriksen, 2010). Canonical Wnt signaling also indirectly inhibits osteoclastogenesis through osteoblast-driven enhanced OPG expression (Matsuo et al., 2019).

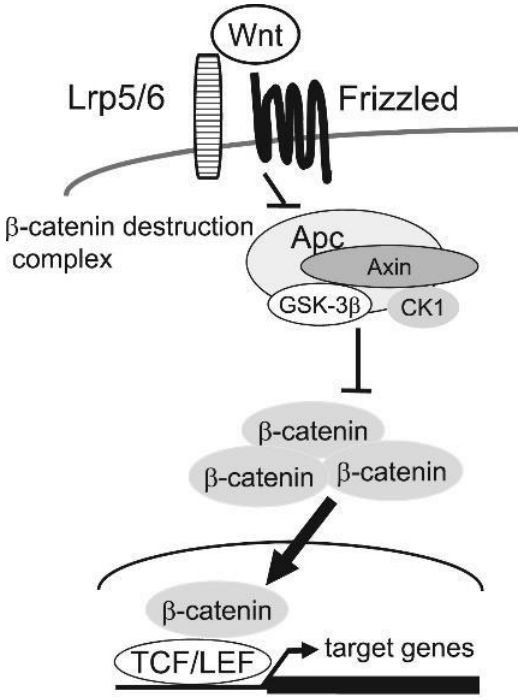

Figure 3.3. Illustration of the canonical Wnt pathway (modified from Matsuo et al. (2019)). Osteoblast proliferation and differentiation are based on the mechanism of ß-catenin, which is controlled by the Wnt ligands. Wnt ligands binding to their receptors frizzled, and LRP5/6 inhibits the destruction of ß-catenin and thus, promotes its accumulation into the cytoplasm. Accumulated ß-catenin translocates into the nucleus, which induces the expression of target genes involved in bone formation and OPG expression. Open access reuse provided by the publisher.

3.3. Models of Osteoporosis

3.31. Estrogen Deficiency and Osteoporosis: Cellular Mechanisms

The role of estrogen as a key hormonal regulator of bone metabolism (i.e., inhibiting bone resorption while regulating bone formation (Khosla et al., 2012)) was first recognized 70 years ago when Albright (1940) made the connection between menopause and bone loss. At the onset of menopause, estrogen levels rapidly decline (Eastell, 2005), which prompts a simultaneous increase in bone formation and bone resorption, albeit unbalanced as resorption outpaces formation (Eriksen, 2010, Jilka, 1998, Khosla et al., 2012), which is the primary mechanism behind age-related net bone loss. After menopause (12 consecutive months without a menstrual cycle), women can enter the life-long stage of PMO, with bone loss later in life characteristic of continual aging.

Postmenopausal osteoclastic resorption typically results in trabecular bone loss, whereas in advanced age, cortical bone loss due to decreased osteoblast activity is more commonly observed (Manolagas and Jilka, 1995).

Bone loss is a factor of the sex hormone estrogen, which plays a role in regulating osteoclastogenesis via the RANK/RANKL/OPG pathway. Decreased estrogen levels equate to decreased OPG and thus a decline in the associated inhibitory effect on the differentiation and activation of osteoclasts (Eastell, 2005, Khosla et al., 2012). Therefore, decreased OPG leads to expression of RANKL (Eriksen, 2010) and thus increased osteoclast-driven bone resorption. The importance of estrogen to bone health has been shown clinically; PMO women treated with estrogen exhibit increased BMD and hip fracture reduction by 33% (Cauley et al., 2003). At the level of the BMU, estrogen deficiency has also been associated with a temporary increase in bone formation, although concomitant bone resorption outpaces formation, which ultimately leads to a sustained decrease in bone mass (Khosla et al., 2012). Rodent studies have suggested a link between estrogen loss and bone marrow-associated osteoblast activity as a possible explanation for osteoblast progenitors' development (Manolagas and Jilka, 1995) hence, this initial period of increased formation. This uncoupled remodeling is the driving force behind osteoporotic bone loss, yet it is still not completely understood; however, cytokine IL-7—a promotor of osteoclastogenesis derived from bone marrow stromal cells and osteoblasts, has been shown to play a role in the uncoupling of bone formation from resorption (Weitzmann et al., 2002)[4]. Estrogen deficiency has been shown to elevate IL-7, thus limiting the necessary bone formation required to compensate for its osteoclastogenic derived bone resorptive actions (Weitzmann et al., 2002).

3.31.1 Estrogen effects within Bone

Overall, PMO bone loss is a combination of rapidly reduced trabecular bone from increased osteoclastic resorption and remodeling associated with menopause that can occur over five years (Parfitt et al., 1983) and ongoing cortical bone loss over time. Rodent studies have shown OVX

[4] Here, the term ‘uncoupling’ is being used by the authors to denote estrogen deficient driven increases in bone loss through outpaced bone resorption in comparison to bone formation, however this thesis would denote this as unbalanced remodeling in line with ANDERSEN, T. L., ABDELGAWAD, M. E., KRISTENSEN, H. B., HAUGE, E. M., ROLIGHED, L., BOLLERSLEV, J., KJÆRSGAARD-ANDERSEN, P. & DELAISSE, J.-M. 2013. Understanding Coupling between Bone Resorption and Formation: Are Reversal Cells the Missing Link? *The American Journal of Pathology,* 183**,** 235-246.classifications.

surgery results in overall trabecular bone loss through osteoclastic resorption (Dempster et al., 1995) leading to decreased BMD, trabecular thickness and number, and increased separation (Sharma et al., 2018). This pattern is like that of human PMO, decreased volumetric BMD from thinned trabeculae and disrupted microarchitecture (Riggs et al., 2004) leads to bone loss. That said, estrogen deficiency effects on cortical bone, particularly its porosity, cannot be overstated regarding bone's ability to resist bending to mitigate fracture risks (Perilli et al., 2015). In a study by Farr et al. (2013), PMO women receiving a placebo showed a 30% increase in cortical porosity within the distal radius compared to those receiving estrogen therapy. This destabilizing effect of estrogen-deficient increased porosity on cortical bone's structural integrity potentially has clinical relevance for reducing the risk of osteoporotic fracture (Farr et al., 2013).

Menopause also affects cortical bone, but this is more commonly observed with advancing age, accounting for much of age-related bone loss (Riggs et al., 2004). Porosity changes can occur through an increase in the number of pores, enlargement of pre-existing pores, or a combination thereof (Thomas et al., 2006). Studies of human OP have argued that age-related cortical bone loss due to increased porosity results from the remodeling of pre-existing canals and not increasing the number of pores (Andreasen et al., 2018, Perilli et al., 2015). An intriguing potential explanation for these enlarged canals is osteoclastic-driven osteocyte damage (Sharma et al., 2018). Human age-related bone loss has been associated with increased net resorption of the marrow cavity through increased endocortical bone resorption and decreased cortical bone BMD through increased cortical porosity (Riggs et al., 2004). This severe resorption of the cortical bone must eventually cause a breakdown of the lacunar-canalicular mechanosensory network (Riggs et al., 2004), causing a perpetuation of unregulated osteoclastic resorption. Thomas et al. (2006) noted that the mean pore area (accounting for 81% of porosity) increased towards the endosteum. Taken together, pores get larger as the endosteum is resorbed, and, in this sense, the enlarged, coalesced pores are indeed responsible for the degraded cortical bone morphology. However, one could argue the opposite in that due to the damaged osteocyte network, there is no "sensor" to turn off remodeling; therefore, increased porosity could be due to an increase in remodeling rate (activation frequency) or the number of new pores. Since these histological results are from a single snapshot in time, it is difficult to rule out the possibility that observing large numbers of pores due to increased remodeling that, by default, must coalesce within one another eventually, is not the cause of age-related cortical bone loss. Similar results have been observed in rodents, where OVX-

induced estrogen deficiency equated to increased cortical porosity and canal diameter due to enlargements of pre-existing canals, not increased remodeling rates (recalling that mice and rats do not remodel their cortex similar to humans) evidenced by the local matrix's altercations to the surface surrounding osteocytes (Sharma et al., 2018).

3.31.2. Estrogen effects within Rabbit Bone

OVX's efficacy as a stand-alone mechanism in the rabbit model has been questioned (see Chapter 4). Briefly, studies utilizing the OVX rabbit model to induce OP—verified through decreased BMD or deterioration of the trabecular microarchitecture via decreased trabecular thickness, trabecular number, and increased trabecular separation have provided conflicting results (Castañeda et al., 2008, Baofeng et al., 2010, Sevil and Kara, 2010, Jensen et al., 2014). Further, results specific to cortical bone are scarce (Chandler et al., 2019). When inducing OP within the bone of rabbits, it is typically recommended that OVX be implemented in conjunction with some other mechanism of increased remodeling, such as GC treatment which is a proven experimental OP rabbit model (Castañeda et al., 2006, Eberhardt et al., 2001, Castañeda et al., 2008, Liu et al., 2012, Grardel et al., 1994); however, this conflates primary and secondary OP within a single model system.

3.32. Glucocorticoids and Osteoporosis: Cellular Mechanisms

Glucocorticoids are part of the class of corticosteroid hormones that suppress inflammation and, thus, are commonly used to treat various clinical inflammatory, autoimmune, and allergy conditions (Guler-Yuksel et al., 2018). Unfortunately, extended use of GCs is commonly associated with bone loss, with 30% - 50% of patients suffering a fracture (Weinstein, 2012, Weinstein, 2011) only 3-6 months after commencement of treatment (Compston, 2018). An estimated 50% of long-term use patients develop OP (Carbonare et al., 2001), making GCs the leading cause of secondary OP, commonly referred to as GIO. In general, GCs can exert anabolic and catabolic effects on bone formation. Glucocorticoids promote osteoclast-mediated bone resorption through expression of RANKL and under expression of OPG (Kenkre and Bassett, 2018). Glucocorticoids also have been shown to reduce osteoclast precursors but extend the lifespan of osteoclasts, further promoting this resorptive effect. In a study by Jia et al. (2006), GCs

actions specific to osteoclasts were blocked in transgenic mice, yet GC dosing still reduced osteoclast precursor numbers in these mice, furthering supporting the argument that GCs act directly on osteoclasts to prolong their lifespan. In terms of bone formation, endogenous GC signaling has been shown to promote healthy bone metabolism (Sher et al., 2004) through differentiation of mesenchymal progenitor cells into osteoblasts (Seibel et al., 2013). However, in excess, GCs inhibit the Wnt pathway via overexpression of its inhibitors such as sclerostin (SOST) and dickkopf-related protein 1 (Dkk1) (Seibel et al., 2013), which results in decreased cell proliferation, differentiation, and apoptosis of both osteoblasts and osteoclasts (Weinstein et al., 1998, Weinstein, 2011, Weinstein, 2012) and thus, decreased bone formation.

Signaling of the Wnt pathway plays a significant role in GIO (Hayashi et al., 2009), and variations, in the form of over or under expression of its extracellular components, such as mutations of LRP5, have been shown to produce highly dense or significantly thinned bone tissue, respectively (Westendorf et al., 2004). Appreciation of these regulatory effects, in that osteocyte driven expression of Wnt inhibitors SOST and Dkk1 function to regulate the metabolic state of bone where decreased expression during remodeling promotes bone formation post resorption (Kenkre and Bassett, 2018), can help better understand pharmaceutical drugs that exhibit similar effects within bone. For example, overexpression of SOST, an antagonist molecule that binds to LRP5 co-receptors and thus inhibits Wnt signaling (Yavropoulou and Papapoulos, 2010), produced effects comparable to the decreased bone formation associated with extended treatment with GCs.

3.32.1. Glucocorticoid Effects within Bone

Glucocorticoid-induced bone loss is complex in that it occurs over two distinct phases (Weinstein, 2012) that are not yet fully understood. Failed bone formation rather than increased bone resorption is considered the primary mechanism of GC-mediated bone loss; however, a temporary but rapid increase of bone resorption is commonly observed at the onset of treatment. Within the first year, BMD is reduced by 6% – 12% (LoCascio et al., 1990) due to this rapid increase in resorption, which has been associated with high incidences of vertebral fractures among patients, particularly those on high dose GC regimens (Florez et al., 2020). Decreased bone formation mainly occurs through enhanced apoptosis of mature osteoblasts and osteocytes,delayed cell differentiation, and decreased bone-forming cells through insufficient cell replication,

which ultimately prevents the production of mature functioning osteoblasts (Canalis and Delany, 2002, Canalis, 2005). With continuous treatment, decreased osteoblastic bone formation accounts for the continual loss of BMD, however, at a more slow, steady pace (~ 3% annually) (LoCascio et al., 1990). The factors responsible for this shift are not well known, but decreased gonadotropin production, which results in increased bone resorption due to estrogen deficiency, has been suggested as a possibility (Canalis and Delany, 2002).

Beyond reduced bone quantity, GCs also adversely affect bone quality via osteocyte apoptosis; creating a proverbial 'perfect storm' – disruption of the osteocyte regulated lacunar-canalicular network inhibits detection of microdamage and subsequent remodeling repair, resulting in accumulation of deteriorated microarchitecture and increased fragility (Weinstein et al., 1998). This scenario has been shown in trabecular bone, in which GCs actively deteriorate the quality of the microarchitecture through decreased bone volume, wall thickness (i.e., trabecular packets representative of the end product of osteoblast activity in a remodeling site), and activation frequency (Weinstein et al., 1998, Carbonare et al., 2001). Interestingly, clinical trials have shown postmenopausal women undergoing GC therapy had higher fracture risk even with BMD's similar to non-users (Van Staa et al., 2003). Therefore, vertebral fractures positively associated with GC use are not solely explained by low BMD (Hayashi et al., 2009). This collective pattern of decreased bone quantity and quality has been suggested why GC users, especially those on high-dose regimens, experience the initial increase in bone resorption and fractures experienced at the onset of therapy.

3.32.2. Dosing Effects of Glucocorticoids

A commonly prescribed corticosteroid, prednisolone, has dosages typically defined as either: low (>7.5 mg/d), medium (7.5 mg – 30 mg/d), high (30 mg – 100 mg/d) or very high (>100 mg/d) (Gensler, 2013). The correlation between GC use and fracture risk is dose-dependent (Guler-Yuksel et al., 2018, Briot and Roux, 2015) with higher daily (as opposed to cumulative) (Van Staa et al., 2003) doses associated with increased fracture rates further exacerbated with longer duration (Seibel et al., 2013) and continuous use. Altogether, this has been shown to increase the relative risk of hip and vertebral fractures 7- and 14-fold, respectively (Steinbuch et al., 2004). A positive correlation was observed in a study that assessed the relationship between dose and duration of corticosteroid use with fracture risk; as prednisolone dose increased, so did the risk for both

vertebral and nonvertebral fractures (Van Staa et al., 2000). Recently, an extensive study investigating individuals receiving doses (low, moderate, or high) of either oral or peritoneal (injection) GCs for six months found that over a two-year follow-up period, compared to non-users, even low doses accounted for a significantly higher risk of vertebral fractures, and moderate and high doses significantly increased hip fracture risk in comparison to low-users (Koh et al., 2020), findings in agreement with a previous study that also found increased vertebral and hip fracture risks associated with GC dose (Van Staa et al., 2000). Interestingly, cessation of oral GC therapy has been shown to reduce fracture risk (Van Staa et al., 2000), indicating the effects of GCs are somewhat reversible, although never to baseline levels (Buehring et al., 2013).

3.32.3. Glucocorticoid Effects within Rabbit Bone

The rabbit is considered a suitable animal model for GIO research as GCs cause similar bone loss effects via decreased formation, as is observed clinically (Castañeda et al., 2008). GCs tend to cause a breakdown of rabbit trabecular microarchitecture through reductions in trabecular thickness, trabecular number, bone volume, and increased trabecular separation (Grardel et al., 1994, Baofeng et al., 2010, Liu et al., 2012, Chandler et al., 2019), with the caveat these studies carried out analyses on different regions of bone with varying dosing regimens. Cortical bone effects are much less known; however, elevated cortical porosity due to prolonged GC exposure has been recognized in human (Vedi et al., 2005) and sheep (Ding et al., 2012) studies. Recently, Chandler et al. (2019) indicated GCs combined with OVX elevated cortical porosity while decreasing the cortical area and cortical thickness in the femoral diaphysis of rabbits.

3.33. Parathyroid Hormone and Osteoporosis: Cellular Mechanisms

PTH, an 84-amino acid polypeptide, is produced by the parathyroid glands and regulates calcium and phosphate homeostasis through its direct action on bone and the kidneys (Osagie-Clouard et al., 2017) and indirect action on the gastrointestinal tract (via vitamin D) (Silva and Bilezikian, 2015) in both humans and animals. During states of dietary calcium deficiency (Huang et al., 2004), or hypocalcemia (Goltzman, 2018), where blood plasma calcium levels are low, endogenous PTH can promote calcium release through the resorption of bone's mineral hydroxyapatite (Lee and Partridge, 2009), tubular calcium reabsorption within the kidney, and

indirect calcium absorption through the gut to regain homeostatic levels of calcium (Silva and Bilezikian, 2015). In bone, when serum calcium levels are depleted, induced secretion of PTH causes catabolic increased resorption of bone tissue (Swarthout et al., 2002) through the indirect action of osteoblasts on osteoclasts, as osteoclasts do not express PTH receptors (Wein and Kronenberg, 2018). Via the RANK/RANKL/OPG pathway, the binding of PTH to its receptor, PTHrP type1 (PTH1R) located on the surface of osteoblasts (Goltzman, 2018) indirectly increases osteoclastic bone resorption. The binding of PTH to its receptor signals a phenotypic switch from osteoblast driven bone formation to osteoclastic driven bone resorption (Lee and Partridge, 2009, Dempster et al., 1993) which occurs due to PTH increasing the expression of RANKL and inhibiting OPG (Goltzman, 2018). Thus, the biphasic increased osteoblast activity and indirect osteoclastogenesis promote overall bone remodeling. This remodeling can lead to either a net increase in bone formation or resorption (Goltzman, 2018). Which outcome is dependent upon either a continuous or intermittent administration of PTH, which is further explored in following sections of this chapter. Overexpression of systemic PTH, however, can lead to severe side effects such as primary hyperparathyroidism. This condition leads to bone loss, the observation of which originally brought about the assumption that PTH is a catabolic hormone that primarily imparts negative consequences for skeletal tissues (Rubin and Bilezikian, 2003). However, the past 30 years of research have revealed PTH can also promote net bone formation through cellular manipulation of its anabolic properties via dosing regimens.

Since the revelation of its potential as a clinical treatment for OP (Reeve et al., 1980), PTH (1-84) and its active biological recombinant form, teriparatide (PTH 1-34), have been extensively reviewed as a mechanism for increasing bone mass and reducing fracture risk in both primary and secondary OP (Hodsman et al., 2005). Currently, PTH 1-34 is the only FDA approved clinical treatment for OP through stimulation of new bone formation (Wein and Kronenberg, 2018). From both human and animal studies, it has been recognized that the complexity of PTH is intrinsically linked to several factors such as its administration, dose, length of exposure, and timing of analysis which all play a pivotal role in its net effects.

3.33.1. Dosing of PTH – Intermittent versus Continuous Administration

Parathyroid hormone can be exogenously administered intermittently with once-daily subcutaneous injections or continuously through subcutaneous osmotic pumps, both of which

increase trabecular and cortical bone remodeling. However, rather than the method of drug delivery, the duration and periodicity of exposure ultimately dictate the net effect on bone mass (Silva and Bilezikian, 2015). The relationship between expression of PTH's anabolic versus catabolic phenotype within bone and its exogenous administration (Locklin et al., 2003) was first realized when rodents treated with an intermittent versus continuous administration showed distinct differences (Dobnig and Turner, 1997). Extended exposure through continuous administration of PTH has been shown to promote increased osteoclast activation and lifespan (Osagie-Clouard et al., 2017), thus increased bone resorption causes a net loss of bone mass, mimicking OP which is the very thing PTH is meant to treat. Even so, intermittent PTH use has been found to promote an overall net gain of bone via increased formation in humans (Hodsman et al., 1993) and rats (Dobnig and Turner, 1997, Hock and Gera, 1992).

While the link between PTH administration mode and its net effects is appreciated, the underlying mechanisms are not fully understood. What is known is that circulating PTH levels within the bloodstream undoubtedly play an essential role in bone metabolism. A study by Frolik et al. (2003), of PTH (1-34) dosed rats showed that a daily injection of 80 ug/kg administered in one dose or over six injections within one hour produced an anabolic increase in bone mass. The same study also showed that the same amount of PTH administered with six injections over a 6-hr period/day induced a catabolic decrease in bone mass. These results indicate circulating systemic PTH drops quickly after injection, but sustained levels due to prolonged exposure may overwhelm endogenous PTH, resulting in a catabolic response. Appreciation of the intermittent versus continuous administration effects of PTH at the cellular level and how this can trigger different genes to promote either bone resorption or formation (Locklin et al., 2003) warrants further review. In general, intermittent PTH has an anabolic effect, whereas continuous PTH dosing results in increased bone resorption. That said, intermittent PTH has been shown to increase cortical porosity in both human and animal studies (discussed below), and thus the mechanism in which PTH is administered (i.e., frequency and dosage) affects not only overall bone mass but the microarchitecture of bone, including cortical porosity (Takakura et al., 2017).

3.33.2. Intermittent PTH and its Anabolic Effect within Bone via Cellular Signaling

When administered intermittently, low doses of PTH activate binding to its receptor PTH1R to promote an anabolic effect of bone formation (Osagie-Clouard et al., 2017) via

increased number of osteoblasts, the proliferation of osteoblast precursors, reduced osteoblast apoptosis, and reactivated quiescent lining cells (Jilka, 2007). Intermittent PTH has been shown to promote bone formation via the upregulation of the runt-related transcription factor 2 (RUNX2) and insulin-like growth factors (IGF). RUNX2 and IGF dictate differentiation of stem cells along the osteoblastic lineage, maintain osteoblast maturity, and inhibit osteoblast apoptosis (Osagie-Clouard et al., 2017). Thus, upregulation of these factors through intermittent PTH supports the argument that differentiation rather than proliferation of osteoblasts is the main effect of PTH-mediated osteoblastogenesis (Silva and Bilezikian, 2015). Furthermore, lineage tracing studies using rodent models have also suggested that intermittent PTH may promote bone formation by delaying osteoblasts' differentiation into bone lining cells (Wein and Kronenberg, 2018).

The Wnt signaling pathway, crucial for bone formation through osteoblastogenesis, is also supported by intermittent PTH. By promoting the Wnt ligands LRP5 and LRP6, intermittent PTH promotes the accumulation of ß-catenin and hence, the transcription of Wnt-specific osteoblast differentiation genes and bone formation (Osagie-Clouardet al., 2017). Furthermore, intermittent PTH decreases SOST, an osteocyte-specific secretion which antagonizes the canonical Wnt pathway by binding to LRP5 and LRP6 and thus, reduces Wnt signaling resulting in reduced bone formation. Similar findings have been shown for Dkk1, a soluble inhibitor of Wnt/ ß-catenin which is expressed within the osteoblast lineage but acts similarly on LRP5/6 to inhibit Wnt signaling (Pinzone et al., 2009). Again, intermittent PTH has been shown to reduce Dkk1 which serves to promote the Wnt pathway and, therefore, increasing bone formation (Osagie-Clouard et al., 2017). The cellular mechanisms discussed here lend support to the conclusion that there is not one but rather several complex mechanisms driving intermittent PTH increases in bone formation and mass, something which is yet to be fully understood (Wein and Kronenberg, 2018). Beyond this, the length of treatment and timing of analysis also factor into how PTH interacts with bone.

3.33.3. The Anabolic Window of Intermittent PTH

During the early stage of PTH treatment, bone formation occurs on quiescent bone surfaces, a process referred to as the “bone modeling effect” (i.e., formation without prior resorption). In contrast, during later stages of treatment, bone formation decreases and shifts to increased remodeling-induced bone resorption, referred to as the “bone remodeling effect” (Silva and Bilezikian, 2015). This process has been described as the “anabolic window” of PTH—in

which bone formation is most prominent, supported by the early, rapid increase of bone formation markers such as alkaline phosphatase, osteocalcin, and amino-terminal pro-peptide of type 1 procollagen (PINP) (Ng et al., 2016) followed by increases in bone resorption markers thereafter (Bilezikian, 2008). This anabolic effect was noted in a ground-breaking study by Hodsman and Steer (1993), who found that tetracycline markers of bone formation given to osteoporotic women treated with PTH 1-34 for 28 days showed early increases in formation rate.

Evidence supporting PTH's stand-alone modeling effect has also been shown with rodent models. Rats dosed for 12 days with an intermittent PTH protocol exhibited increased bone mass even though bone resorption was chemically blocked (Hock et al., 1989), further supporting PTH's anabolic effect is not predicated upon prior bone resorption (Lotinun et al., 2002). This bone modeling effect has also been histologically characterized using osteon cement lines as markers. Lindsay et al. (2006) implemented a novel double set tetracycline labeling technique to analyze iliac biopsies of PMO women to interpret modeling versus remodeling through the observation of smooth or scalloped (indicating preceding resorption) cement lines, respectively. They showed that a one-month treatment with PTH 1-34 dramatically increased bone formation on cancellous and endocortical surfaces through an increased linear rate of matrix apposition and extension of the bone-forming surfaces, compared to controls who only depicted remodeling-based bone formation. Although accounting for only 30% of new bone formation, this study showed PTH could initiate bone modeling-based formation on previously quiescent surfaces that are entirely unrelated spatially or temporally to resorption, a type of response typically not seen in adult bone. However, limitations related to histological analysis of cement lines need to be considered as some of this "modeling" could be due to an increase in osteoblasts "spilling over" from a resorption cavity onto an adjacent site. Depending on the plane of section, this 'cell spillover' may misrepresent remodeling as modeling activity (Lindsay et al., 2006, Compston, 2006). Under no circumstances is treatment with PTH carried out beyond 24 months due to significantly increased rates of osteosarcoma in rats treated long-term with high doses of PTH (Eastell et al., 2019).

Moreover, due to PTH's anabolic window, its anabolic effects diminish throughout treatment (Eastell and Walsh, 2017), and BMD ceases to improve beyond this timeframe (Ng et al., 2016). Antiresorptive drugs are commonly prescribed after to maintain the anabolic gains of PTH (Eastell and Walsh, 2017) as rapid bone loss commonly occurs, but the reason as to why this occurs is not known.

3.33.4. Intermittent PTH effects on Trabecular Bone

Intermittent PTH has been shown to improve trabecular bone and its related microarchitecture in trabecular rich sites of the skeleton such as the iliac crest, lumbar spine, femoral neck, mandible, and proximal tibia. Specifically, increased BMD values have been histologically linked to improved trabecular bone microarchitecture via increased bone volume (Yamamoto et al., 2016, de Bakker et al., 2015, Uzawa et al., 1995, Sato et al., 2004, Jiang et al., 2003, Reeve et al., 1980, Jerome et al., 2001), trabecular number (Yamamoto et al., 2016, Hock and Gera, 1992, Dobnig and Turner, 1997, Sato et al., 2004, Hansen et al., 2013, Jerome et al., 2001), trabecular thickness (Mashiba et al., 2001, Hock and Gera, 1992, Uzawa et al., 1995, Jiang et al., 2003), and decreased trabecular separation (Yamamoto et al., 2016, Dobnig and Turner, 1997, Sato et al., 2004, Jerome et al., 2001). Intermittent PTH has also been shown to increase trabecular bone remodeling rate through increased activation frequency (Hodsman and Steer, 1993, Mashiba et al., 2001, Hodsman et al., 2000, Cosman et al., 2016, Boyce et al., 1996). One of the most extensive studies investigating PTH as a treatment for OP analyzed over 1600 PMO women treated with intermittent PTH 1-34 for 24 months (Neer et al., 2001). In comparison to controls, treatment with PTH increased total-body BMD (measured via DXA) and decreased the risk of vertebral fractures, suggesting PTH's positive effect on bone formation and thus, increased bone mass and strength in the predominately trabecular vertebrae. Trabecular microarchitecture contributes to bone's overall strength and stiffness; however, as noted by Neer et al. (2001), intermittent PTH also has positive effects on cortical bone microarchitecture. This is crucial for bone's ability to bear mechanical loads as cortical bone comprises most of the appendicular skeleton and is substantially impacted by age-related bone loss.

3.33.5. Intermittent PTH effects on Cortical Bone

The main effect of intermittent PTH on cortical bone is increased porosity, a characteristic

well established in nonhuman primates (Burr et al., 2001, Sato et al., 2004), rabbits (Burr et al., 2001, Hirano et al., 2000, Hirano et al., 1999, Sato et al., 2004, Jiang et al., 2003, Zebaze et al., 2017, Yamane et al., 2017) and human (Macdonald et al., 2011, Hansen et al., 2013, Jiang et al., 2003) studies through various imaging modalities (i.e., traditional dynamic histomorphometry, HR-pQCT, DXA, and *ex vivo* micro-CT). PTH elevates activation frequency (Mashiba et al., 2001, Hirano et al., 1999, Burr et al., 2001, Sato et al., 2004), osteonal mineral appositional rate (Burr et al., 2001, Cosman et al., 2016) and bone formation rate (Hirano et al., 1999, Burr et al., 2001, Sato et al., 2004), all of which directly influence increased bone formation. This porosity-based loss of cortical bone, however, contrasts with that of PTH mediated increased trabecular BMD, lending to "cortical steal" (Burr et al., 2001) and a general concern that fracture risk to the cortical appendicular skeleton comes at the cost of maintaining the trabecular axial regions (Burr et al., 2001, Rubin and Bilezikian, 2003). These potential region-specific microarchitectural differences brought about extensive review into the efficacy of PTH for treating OP in both trabecular and cortical bone. Interestingly, as noted previously, Neer et al. (2001) revealed the contrary; compared to control participants, women treated with PTH 1-34 over 19 months had a decrease in fracture risk of 65% in vertebral *and* 53% in nonvertebral regions.

While some cortical loss has been associated with specific sites such as the distal radius (Rubin and Bilezikian, 2003), the overall porosity-related cortical loss seems to be canceled out by concurrent bone surfaces apposition. Several clinical studies have revealed that despite this cortical porosity driven induced loss of cortical BMD (Ma et al., 2014, Macdonald et al., 2011, Winzenrieth et al., 2018), PTH also induces bone apposition at the periosteal and endosteal surfaces resulting in increased cortical thickness and cortical area (Ma et al., 2014, Hansen et al., 2013). Similar results have also been observed in animal studies. For example, treatment with intermittent PTH 1-34 caused increased porosity and new bone apposition on the periosteal and endosteal surfaces in rabbits (Hirano et al., 2000, Hirano et al., 1999) and on the endosteal surfaces of cynomolgus monkeys (Burr et al., 2001). From a biomechanical perspective, this may explain why PTH-induced cortical porosity does not seem to adversely alter bone's strength and its ability to resist fracture. Bone strength is related to its overall geometry, which is predicated upon the amount of bone present and how it is arranged spatially, in that bone diameter is proportional to the moment of inertia or the bending resistance (Burr et al., 2001). Model data from PTH-induced

changes to rabbit cortical bone have suggested most porosity localizes around or near the endocortical surface with simultaneous bone formation on the periosteal surface, resulting in an overall increase in the bending rigidity (Hirano et al., 2000). As noted by Burr et al. (2001), this endocortical distribution of porosity closest to the neutral axis would be less detrimental to the mechanical integrity of bone as opposed to bone loss localized to the periosteal surface. Interestingly, even in clinical settings where women treated with intermittent PTH 1-34 experienced a loss of trabecular bone reflected by decreased BMD and thinning of trabeculae (Macdonald et al., 2011), the simultaneously increased cortical porosity did not diminish bone strength even 18 months post-treatment (Hansen et al., 2013). Intermittent PTH has both formative characteristics throughout the trabecular-based axial and cortical-based appendicular regions of the skeleton. Apposition of bone surfaces coincides with the increased remodeling of bone surfaces and intracortically, resulting in a net positive balance of overall bone formation.

3.33.6. Continuous PTH and its Catabolic Effect within Bone via Cellular Signaling

Opposite to the effects observed with intermittent PTH, continuous administration produces high circulating PTH levels similar to primary hyperparathyroidism with similar bone loss effects (Silva et al., 2011). Osteoclastogenesis via increased osteoclast activity and lifespan leads to increased bone resorption (Osagie-Clouard et al., 2017), which is likely to be in large part due to the actions of PTH within the RANK/RANKL/OPG pathway. Continuous PTH increases RANKL and decreases OPG; promoting osteoclastogenesis and bone resorption (Osagie-Clouard et al., 2017), which has been supported from studies of people with hyperparathyroidism who exhibit increased serum RANKL and the RANKL/OPG ratio (Osagie-Clouard et al., 2017). Additionally, continuous PTH has been shown to degrade RUNX2 and hence its bone formative actions, further promoting bone resorptive activities (Osagie-Clouard et al., 2017).

3.33.7. Continuous PTH and its Effects on Trabecular and Cortical Bone

Through continuous administration, either via subcutaneous osmotic pumps in animal studies or a clinical setting with human patients exhibiting hyperparathyroidism, sustained exposure to PTH predominately favors its catabolic effect on bone. Several studies investigating cortical bone effects have shown that continuous administration of PTH causes increased endosteal

bone resorption exacerbated by increased cortical porosity (Zhou et al., 2001, Vu et al., 2013), decreased BMD (Silverberg et al., 1989, Vu et al., 2013), and thinner cortices (Parisien et al., 1990, Adami et al., 1998). Within trabecular bone, effects are more convoluted in that continuous PTH has been associated with the preservation and apposition of bone (Lotinun et al., 2004, Uzawa et al., 1995, Zhou et al., 2001, Dobnig and Turner, 1997, Parisien et al., 1990, Dempster et al., 1999) as well as bone loss (Hock and Gera, 1992, Vu et al., 2013, Adami et al., 1998). In a study by Uzawa et al. (1995), continuous infusion of PTH 1-34 for four weeks led to rats exhibiting hyperparathyroidism-like characteristics; trabecular bone volume and trabecular thickness were reduced with evidence of deterioration of the microarchitecture through tunnel-like resorption of deep-resorption pits, suggestive of enhanced resorption over formation. Trabecular tunneling has also been observed in dogs treated with PTH for five months (Boyce et al., 1996) and monkeys for 18 months (Jerome et al., 2001). Although these two studies used an intermittent course of PTH, the tunneling-induced reduction of trabecular bone observed could be a by-product of the long-term exposure of PTH reminiscent of a continuous administration (at least in duration). Initial anabolic thickening of trabeculae would inherently separate osteocytes from nutrient-rich bone surfaces, prompting their apoptosis and activation of resorption, in which trabeculae would become increasingly thinned (Brommage, 2020) to stabilize thickness, but at the expense of increased trabecular number (Jerome et al., 2001).

Inconsistencies associated with continuous PTH administration could also be methodologically based. In a review by Lotinun et al. (2002) in the bone biopsies of patients with hyperparathyroidism and rats treated with continuous PTH, bone formation was immeasurable for nearly half of the sample as double fluorochrome labels were indiscernible due to diffuse labeling; a common occurrence with rapid bone deposition and delayed mineralization. This effect of continuous PTH could lead to underestimating trabecular bone formation rates associated with continuous PTH (Lotinun et al., 2002).

3.33.8. PTH Effects on Rabbit Bone

Similar to PTH effects discussed in sections 3.33.1.– 3.33.5., studies have shown that overall, intermittent dosing of PTH 1-34 causes modeling-based bone formation in the skeletal tissues of New Zealand white rabbits noted by bone apposition on trabecular, endosteal, and

periosteal surfaces (Mashiba et al., 2001, Hirano et al., 2000, Hirano et al., 1999, Yamane et al., 2017, Zebaze et al., 2017, Vrahnas et al., 2018) even though cortical porosity is also increased. Effects associated with continuous administration of PTH within rabbit bone are vague. High phosphate diet-induced hyperparathyroidism studies that included serological measures of PTH along with histological examination of the parathyroid glands, kidney, and bones (Bai et al., 2012), or only the parathyroid glands and kidneys (Ma et al., 2010) indicated bone fibrosis, but did not directly access trabecular or cortical bone microarchitecture.

3.4. Conclusion

This chapter reviewed OP models (OVX, GC, and OVX+GC) and PTH as mechanisms to elevate remodeling within the cortical bone of rabbits. The cellular signaling pathways underpinning these models were explored regarding their effects on the microarchitecture of trabecular and cortical bone and overall remodeling (i.e., increased/decreased bone resorption or formation) for both human and rabbit bone (Table 3.1.)

		Trabecular Bone	Cortical Bone		Overall Remodeling Effect	
			Thickness	Porosity	Resorption	Formation
PMO	Human	↓	↓	↑	↑	
OVX	Rabbit	***	?	?	↑	
GC	Human	↓	↓	↑		↓
	Rabbit	↓	↓	↑		
PTH (Intermittent)	Human	↑	↑	↑		↑
	Rabbit	↑	↑	↑		
PTH (Continuous)	Human	↓	↓	↑	↑	
	Rabbit	?	?	?		

Legend on following page

Table 3.1. Overview of OP models effects on human and rabbit bone. Bone loss (red arrow) or gain (green arrow) indicative of reported OP model effects on a combination of individual bone parameters including trabecular bone volume fraction, number, and thickness and cortical bone porosity, thickness, and surface formation. The overall remodeling effect of each model (i.e., increased/decreased bone resorption or formation) is also displayed (black arrow). It is important to note OVX alone as an OP model in the rabbit has been meet with conflicting results and represented as such (***). Effects not known represented by a ?.

Conflicting results related to trabecular BMD and microarchitecture, combined with even less known cortical bone effects, have led to cautioning against OVX as a stand-alone mechanism to model PMO effects within rabbits; implementation in conjunction with some other mechanism of increased remodeling, such as GCs, is commonly recommended. Glucocorticoids have an inhibitory effect on bone formation and therefore increase cortical porosity through bone resorption and, in combination with OVX, induce elevated porosity while decreasing cortical thickness and area in rabbits. Lastly, while several factors such as mode of administration, dose and exposure, and timing of analysis play a role in its effect on bone, the catabolic effects of PTH (i.e., increased bone resorption), even when administered intermittently, makes it a suitable mechanism for elevating remodeling/cortical porosity in rabbits.

The application of these models served as the platform for our initial *ex vivo* micro-CT study that set out to ascertain the most efficient mechanism for elevating cortical porosity in the tibiae of New Zealand white rabbits (Chapter 4); setting the stage for future *in vivo* SR micro-CT imaging studies aimed at the direct 4D measurement of BMU LER *in vivo* (Chapter 5).

Chapter 4 Cortical Bone Porosity in Rabbit Models of Osteoporosis

This chapter consists of the manuscript published in the Journal of Bone and Mineral Research (Harrison et al., 2020) and is open access http://creativecommons.org/licenses/by-nc-nd/4.0/. *This manuscript is co-first-authored with Beverly Hiebert, a previous Masters' student within our lab. I was involved in overseeing all the animal trials described in this study, with Beverly primarily responsible for writing the PTH section and myselfwriting the OVX and GC sections. Presentation and discussion of the results and data have been written to adhere to the journal's publication guidelines, which discourages the dichotomous useof the p-value, but instead encourages more fluid, less strict interpretation of scientific data. This manuscript has been reformatted from the original version for inclusion in this thesis.*

Authors: Kim D. Harrison[1*], Beverly D. Hiebert[1*], Arash Panahifar[2,3], Janna M. Andronowski[4], Amir M. Ashique[5], Gavin King[1], Terra Arnason[6], Kurtis J. Swekla[7], Peter Pivonka[8], David M.L. Cooper[1]

* *co-lead authors*

1. Department of Anatomy, Physiology, and Pharmacology, College of Medicine, University of Saskatchewan, Saskatoon, Saskatchewan, Canada.
2. BioMedical Imaging and Therapy Beamline, Canadian Light Source, Saskatoon, Saskatchewan, Canada.
3. Department of Medical Imaging, College of Medicine, University of Saskatchewan, Saskatoon, Saskatchewan, Canada
4. Department of Biology, The University of Akron, Akron, Ohio, USA.
5. NGM Biopharmaceuticals, South San Francisco, CA, USA.
6. Department of Medicine, College of Medicine, University of Saskatchewan, Saskatoon, Saskatchewan, Canada.
7. Research Services and Ethics Office, Office of the Vice-President of Research, University of Saskatchewan, Saskatoon, Saskatchewan, Canada.
8. School of Mechanical, Medical, and Process Engineering, Queensland University of Technology, Brisbane. Australia.

- **Kim D. Harrison, MA.** Doctoral student.
- **Beverly D. Hiebert, B.Sc.** Master's student.
- **Arash Panahifar, PhD.**
- **Janna M. Andronowski, PhD.** Supported by the National Institute of Justice, Office of Justice Programs, U. S. Department of Justice.
- **Amir M. Ashique, PhD.**
- **Gavin King, B.Sc.** Master's student
- **Terra Arnason, M.D., PhD.** Department of Medicine and supported by the Canadian Institutes of Health Research.
- **Kurtis J. Swekla, BSc, DVM.**
- **Peter Pivonka, PhD.**
- **David M.L. Cooper, PhD.** Supported by the Canada Research Chairs program, Canadian Institutes of Health Research, Natural Engineering and Research Council of Canada and Social Sciences and Humanities Research Council of Canada.

Corresponding Author:

Dr. David M.L. Cooper

(306) 966-7895

dml.cooper@usask.ca

Disclosures: The authors declare no conflicts of interest.

4.1. Abstract

Cortical bone porosity is intimately linked with remodeling, is of growing clinical interest, and is increasingly accessible by imaging. Thus, the potential of animal models of osteoporosis (OP) to provide a platform for studying how porosity develops and responds to interventions is tremendous. To date, rabbit models of OP have largely focused on trabecular microarchitecture or bone density; some such as ovariectomy (OVX) have uncertain efficacy and cortical porosity has not been extensively reported. Our primary objective was to characterize tibial cortical porosity in rabbit-based models of OP including OVX, glucocorticoids (GC) and OVX+GC relative to controls (SHAM). We sought to: 1) test the hypothesis that intra-cortical remodeling is elevated in these models; 2) contrast cortical remodeling and porosity in these models with that induced by parathyroid hormone (1-34; PTH); and 3) contrast trabecular morphology in the proximal tibia across all groups. Evidence that an increase in cortical porosity occurred in all groups was observed, although this was the least robust for GC. Histomorphometric measures supported the hypothesis that remodeling rate was elevated in all groups and also revealed evidence of uncoupling of bone resorption and formation in the GC and OVX+GC groups. For trabecular bone, a pattern of loss was observed for OVX, GC, and OVX+GC groups, while the opposite was observed for PTH. Change in trabecular number best explained these patterns. Taken together, the findings indicated rabbit models provide a viable and varied platform for the study of OP and associated changes in cortical remodeling and porosity. Intriguingly, the evidence revealed differing effects on the cortical and trabecular envelopes for the PTH model.

4.2. Introduction

Globally, 200 million people live with osteoporosis (OP) (www.iofbonehealth.org) which places significant burdens on health care systems worldwide. Assessment of osteoporotic bone loss has classically focused on bone mass and density at common fracture sites such as the hip, wrist, and lumbar vertebrae; however, there is growing recognition of the role of microarchitecture in bone deterioration and fragility (2004). This trend has been driven by advances in imaging which have enabled assessment of microarchitecture – particularly for trabecular bone. More recently, imaging approaches to assess cortical bone microarchitecture (porosity) have emerged for both preclinical (animal model) and clinical assessment (Harrison and Cooper, 2015, Cooper et al., 2016), creating the potential to move beyond what has been termed a 'trabeculocentric' view of bone loss (Bala et al., 2015). Indeed, the majority of the appendicular skeleton is comprised of cortical bone which suffers from significant losses associated with age (Bala et al., 2015,McCalden et al., 1993, Cooper et al., 2007). Moreover, 80% of all fractures occur at sites of weakened, thinned cortical bone (Zebaze and Seeman, 2015, Poole et al., 2012). As recently reviewed, cortical bone porosity is associated with the mechanical strength of bone and is negatively related to material stiffness, toughness, and the capacity of bone to absorb impact (Cooper et al., 2016).

An increase in cortical porosity, at the scale of vascular pores (e.g., osteonal/Haversian canals and associated resorption spaces), is a physical manifestation of bone loss that arises as a result of an imbalance in cortical remodeling with bone resorption outweighing bone formation. Remodeling, in the strict sense that Frost defined, refers only to the creation of secondary tissue (turnover) in either cortical or trabecular bone. The cells responsible for an individual remodeling event are referred to as a Basic Multicellular Unit (BMU) (Frost, 1969). BMUs are activated on bone surfaces, leading to the replacement of cylindrical packets (secondary osteons) in the cortex and trench-like packets (hemi-osteons) in trabecular bone (Parfitt, 1994). Within cortical bone, BMUs are classically depicted as consisting of an osteoclastic cutting cone which creates a tunnel-like resorption space followed by an osteoblastic closing cone. A reversal zone separates them, but the two processes are spatially and temporally 'coupled' (Parfitt, 1982, Hattner et al., 1965) and continued resorption has been demonstrated in this "reversal-resorption" phase of the BMU (Lassen et al., 2017). Imbalance with resorption outweighing formation within individual

remodeling events is the underlying mechanism by which cortical porosity increases with age and/or disease. Increases in cortical porosity may be either a product of increased rate of remodeling, where formation lags behind resorption (Martin, 1991) also referred to as "transient remodeling spaces" (Heaney, 1994), or through "uncoupling" where there is an arrest during the reversal phase of the BMU (Andreasen et al., 2015, Hinge et al., 2015, Jensen et al., 2015). Strategies for the prevention and/or reversal of OP ultimately must seek to augment the balance between resorption and formation within individual BMUs and not simply the cessation of remodeling as reflected by the growing body of literature on the side-effects (e.g., osteonecrosis of the jaw, atypical fractures) of some anti-resorptive therapies for OP—mainly bisphosphonates, but also recently reported for Denosumab (Yoneda et al., 2016, Fung et al., 2016, Khan et al., 2016, Khow et al., 2017, Adler, 2016). High-resolution pre-clinical imaging of the resorptive phaseof individual BMUs holds great promise for novel spatial-temporal assessment of BMU regulation, both *ex vivo* (Cooper et al., 2006) and even *in vivo* (Harrison and Cooper, 2015, Pratt et al., 2015).

Given that cortical bone porosity is intimately linked with the remodeling process, is of clinical relevance, and presents an increasingly accessible target for imaging, there is a growing need for suitable animal models of OP to advance our understanding of how cortical porosity develops and how it is impacted by countermeasures. Inter-species variation in cortical microarchitecture can, however, limit the utility of common animal models. The cortical bone of larger vertebrates, including humans, tends to be dominated by secondary bone that is generated by remodeling while smaller species (mammals under 2 kg (Felder et al., 2017)), including mice and rats exhibit little, if any, cortical turnover and thus retain primary vascular canals throughout their lives (Sietsema, 1995, Turner, 2001, Jee and Yao, 2001, Pearce et al., 2007, Reinwald and Burr, 2008). Because of this, the American Food and Drug Administration (FDA) recommends the use of larger animals which remodel their cortices in addition to the common ovariectomy (OVX) rat model for OP studies (Thompson et al., 1995). Notably, larger species including rabbits, sheep, goats, dogs, and swine have all been employed in OP research (Reinwald and Burr, 2008, Sietsema, 1995, Turner, 2001, Pearce et al., 2007). Here we focus on the rabbit, the smallest commonly employed laboratory animal with well-defined spontaneous cortical remodeling similar to humans (Pazzaglia et al., 2007, Pazzaglia et al., 2009, Pazzaglia et al., 2010). Rabbits also have the advantage of a remodeling period that is shorter than larger animal models, a relatively rapid

skeletal maturation (by 6–9 months) (Gilsanz et al., 1988, Newman et al., 1995), and they are known to respond to Parathyroid Hormone (PTH) treatment with elevated remodeling and cortical porosity (Yamane et al., 2017, Hirano et al., 2000, Hirano et al., 1999, Zebaze et al., 2017). Taken together, these characteristics make the rabbit a promising platform for OP studies which is well suited for potential *in vivo* imaging (Voor et al., 2008) in future studies.

Animal models of OP generally focus on OVX to simulate post-menopausal decline in estrogen. In rabbits, however, the efficacy of this model is uncertain. OVX alone has been reported by several groups as ineffective at inducing OP in the rabbit (Castañeda et al., 2008, Liu et al., 2012, Baofeng et al., 2010), while others, conversely, have reported significant reductions in Bone Mineral Density (BMD) (Wanderman et al., 2018, Chen et al., 2015, Qi et al., 2012, Sevil and Kara, 2010). The efficacy of the rabbit OVX model for induction of cortical porosity, in particular, is uncertain as existing studies have primarily focused on trabecular bone. The administration of Glucocorticoids (GC) either alone or, more commonly, in combination with OVX (OVX+GC) is a proven approach for inducing trabecular (Grardel et al., 1994, Eberhardt et al., 2001, Castañeda et al., 2008, Castañeda et al., 2006, Liu et al., 2012, Wen et al., 2015, Baofeng et al., 2010) and cortical geometry/density changes (Liu et al., 2012, Castañeda et al., 2006) in the rabbit. That said, the impact of GC alone on cortical bone porosity in the rabbit has not yet been assessed and cortical porosity outcomes for OVX+GC have only recently been explored (Chandler et al., 2019). Rabbit OP models hold great potential as platforms for advancing our understanding of cortical remodeling and associated porosity; however, this potential can only be realized by filling these gaps in the literature.

Our primary objective was to characterize three-dimensional (3D) cortical bone porosity changes in rabbit models of OP (OVX, GC, and OVX+GC) at the distal tibia using *ex vivo* micro-computed tomography (micro-CT). Via correlative histomorphometry, we sought to test the hypothesis that cortical remodeling is elevated by these treatments relative to sham OVX controls (SHAM). Our secondary objective was to compare these changes with those caused by PTH, a known inducer of elevated intra-cortical remodeling and porosity in the rabbit. Finally, we sought to characterize 3D trabecular bone changes in the proximal tibia across these groups to enable assessment of changes in different bony compartments and to facilitate comparison with the more extensive literature pertaining to trabecular bone.

4.3. Materials and Methods

4.31. Animals

All animal work was approved by the University of Saskatchewan's University Animal Care Committee and adhered to the Canadian Council on Animal Care (CCAC) guidelines for humane animal use. Thirty-five skeletally mature, 6-month-old (3.7-3.9 kg), female New Zealand White rabbits were acquired from a commercial supplier, Charles River Laboratories (Quebec, Canada). Animals were housed individually in stainless steel rabbit racks in the University of Saskatchewan's Health Sciences Laboratory Animal Services Unit, a CCAC accredited facility. Room temperature and humidity were controlled by a computerized system and the light cycle was maintained at 12:12 (12 hours of dark and 12 hours of light). Standard rabbit chow (Hi-Pro Feeds, Trouw Nutrition Canada Inc., Sherwood Park, Alberta, Canada) and reverse osmosis water through an automated watering system were provided *ad libitum*. Animals were acclimatized for a minimum of 7 days before any experimental procedures commenced.

The rabbits were randomly divided into 5 groups of 7 animals each: SHAM, OVX, GC, OVX+GC, and PTH. The OVX and OVX+GC group underwent bilateral ovariectomy whereas the SHAM, GC, and PTH groups underwent bilateral sham OVX surgery. Fifty-six days (8 weeks) post OVX/SHAM surgery (pre-dosing period), the GC groups (GC and OVX+GC) received methylprednisolone sodium succinate (Pfizer, Kirkland, Canada) by daily subcutaneous injection of 1.5 mg/kg for 4 weeks, and the PTH group was dosed by daily subcutaneous injection for 4 weeks with human PTH (1-34) (Alfa Aesar, Ward Hill, MA, USA) at a concentration of 30 µg/kg (dosing period). The PTH dose used was intermediate to what has been used in recent studies analyzing the effects of PTH dosing regimens (10 µg/kg/day versus 40 µg/kg/day) on rabbit cortical bone (Yamane et al., 2017, Zebaze et al., 2017). The GC dose used was an intermediate-to-high dose (0.5 mg/kg/day versus 1.0 mg/kg/day versus 2.0 mg/kg/day) based on a previous study analyzing OVX and OVX+GC OP models in the rabbit (Castañeda et al., 2008). SHAM and OVX received daily subcutaneous injections of 1 ml saline for the corresponding 4-week dosing period. Dose initiation at 8 weeks post-surgery was selected based upon previous studies that found conflicting BMD results in relation to time (4, 6, or 8 weeks) post OVX (Castañeda et al., 2008,

Baofeng et al., 2010, Wen et al., 2015). Each animal was monitored daily at the time of injection, as well as weekly to assess weight. The bone labelling fluorochrome calcein (Sigma Aldrich, St. Louis, Missouri, USA) was administered by subcutaneous injection at a dose of 10 mg/kg on days 13 and 14 (label 1) and days 27 and 28 (label 2; end point) of the treatment period to facilitate dynamic histomorphometry. Animals were euthanized by intravenous injection of pentobarbital sodium (Euthanyl; Bimeda-MTC, Animal Health Inc, Cambridge, ON, Canada) at a dose of 0.4 ml/kg. Post-euthanasia, the right tibiae were removed and fixed in 10% formalin.

4.32. Micro-CT Analysis

The proximal epiphysis distal diaphysis (Figure 4.1 *A* & *C*) were imaged with a SkyScan 1172 desktop micro-CT scanner (Bruker, Konitch, Belgium) to assess cortical porosity and trabecular morphology, respectively. CTVolume (CTVol, version 2.3.2.0; Bruker) was used to generate 3D volumetric renderings of cortical porosity and trabecular bone morphology. For cortical porosity analysis, a volume of interest (VOI) along 1 cm of the diaphysis, beginning 3 cm proximal the distal end of the tibia, was scanned (Figure 4.1 *C*) at 75 kVp, 133 µA with 460 ms exposure, 0.2º rotation step, 4-frame averaging, and a 0.5 mm aluminum filter. Resolution dependency of micro-CT analysis has long been recognized for both trabecular bone morphology (Müller et al., 1996) and cortical bone porosity (Cooper et al., 2004). Here we chose a nominal resolution (voxel size) of 10 µm to specifically target cortical porosity on the scale of remodeling-related resorption spaces/osteons (~100 µm in rabbits (Jowsey, 1966)) with smaller spaces (including primary canals, mature secondary osteonal canals, osteocyte lacunae, and canaliculi) falling below the spatial resolution (Supplemental Figure 4.81). It should be noted that our resolution was higher (smaller voxel size) than that of micro-CT protocols previously applied to rabbit cortical bone (14 to 19 µm) (Baofeng et al., 2010, Yamane et al., 2017, Zebaze et al., 2017, Chandler et al., 2019). Important considerations for future study included that the 10 µm voxel size is similar in scale to that potentially available *in vivo* (Pratt et al., 2015, Harrison and Cooper, 2015) and the distal hind limb of the rabbit is well suited for live imaging with the animal in an upright position (Voor et al., 2008). We validated our 3D micro-CT outcomes through comparison with two-dimensional (2D) histological measures of osteon size, confirming correlation between the approaches and similar distributions of values from each (Supplemental Figure 4.82 and Supplemental Table 1). Finally, the distal tibia represents a region of elevated porosity relative to

the mid-diaphysis (Supplemental Figure 4.83) consistent with observations of elevated remodeling distally in lower limb elements (Lieberman et al., 2003).

For trabecular analysis, the proximal epiphysis of each tibia was scanned (Figure 4.1 *A*) at 75 kVp, 133 µA with 1080 ms exposure, 0.2° rotation step, 4-frame averaging, and a 0.5 mm aluminum filter at a voxel size of 13-µm. The trabecular envelope within the entire epiphysis proximal to the growth plate was segmented as the VOI (Figure 4.1 *A*). The epiphyseal subchondral trabecular bone was targeted for both consistency with the existing literature (Castañeda et al., 2008, Castañeda et al., 2006) and the fact that little trabecular bone was present in the metaphyses of the rabbits (Figure 4.1 *A*).

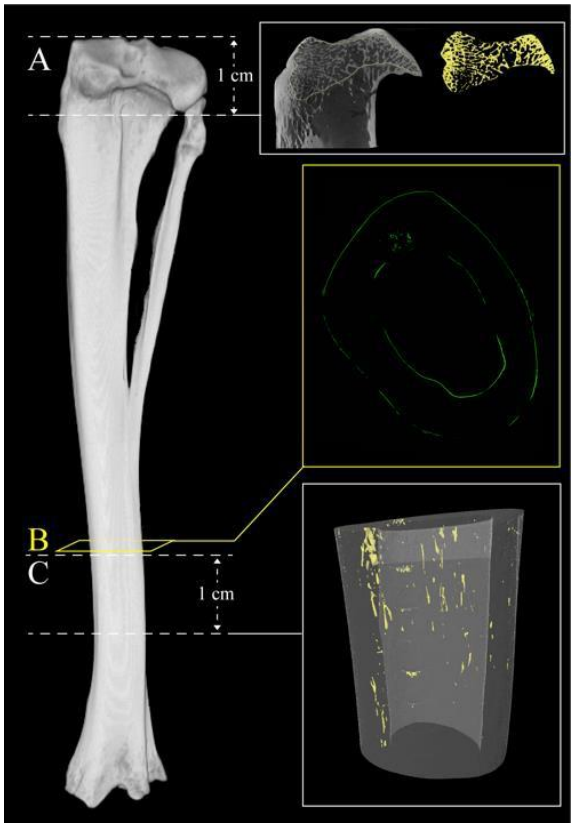

Figure 4.1. Micro-computed tomography (micro-CT) image of rabbit tibia depicting regions of analyses. (*A*) Location of trabecular bone micro-CT analysis. Scan field height is 1 cm. Reconstructed micro-CT image of proximal tibia scan and corresponding three-dimensional reconstructed image of isolated trabecular bone highlighted in yellow (right). (*B*) Location of histomorphometric analysis. Section is 300 µm thick. Fluorescent confocal microscopy image of transverse section of cortical bone (right). (*C*) Location of cortical bone micro-CT analysis. Scan field height is 1 cm. Three-dimensional reconstructed image of cortical bone with cortical porosity highlighted in yellow (right).

Micro-CT data were reconstructed using the NRecon software package (Bruker) and quantitative 3D analysis was conducted with CTAnalyser (CTAn; version 1.16.4.1; Bruker). To assess changes in cortical bone microarchitecture, cortical porosity (Ct.Po, %) and mean canal diameter (Ca.Dm, µm) were measured after application of a standardized global threshold.

Histograms representing the distribution of canal diameter sizes were produced to contrast patterns across the groups. For analysis of the trabecular VOIs, a standardized global threshold was again applied followed by 3D measurement of bone volume fraction (bone volume/tissue volume (BV/TV, %)), trabecular thickness (Tb.Th, mm), trabecular number (Tb.N, mm^{-1}), and trabecular separation (Tb.Sp, mm).

4.33. Dynamic Histomorphometry & Cortical Geometry

Confocal microscopy images were acquired from a cortical cross-section placed immediately proximal to the micro-CT VOI (Figure 4.1 *B*). The sections were cut using a low-speed sectioning saw with a diamond wafer blade and ground and polished to a thickness of 300 µm (Hennig et al., 2015). Mounted sections were subsequently imaged with a Leica (Leica Microsystems, Wetzlar, Germany) DMi8 confocal fluorescent microscope equipped with differential interference contrast microscopy (DIC) to capture fluorescent signals and cortical microstructure. 2D mosaics of the DIC and fluorescent images were produced and analyzed using basic ImageJ (https://imagej.nih.gov/ij/) functions (unless otherwise described).

Cross-sectional cortical geometry parameters, cortical area (Ct.Ar, mm^2), marrow area (Ma.Ar, mm^2), and total area (Tt.Ar, mm^2) were assessed and percent cortical and percent marrow area (%Ct.Ar, %Ma.Ar) were calculated relative to Tt.Ar. Cortical thickness (Ct.Th, µm) was measured using the BoneJ (Doube et al., 2010) plugin for ImageJ. To complement the cortical geometry measures, measures of resistance to bending (maximal and minimal second moments of area, I_{max}, I_{min}, mm^4) as well as torsion (torsional section modulus, Z_{pol}, mm^3) were acquired from the most proximal micro-CT cross-sectional image. These measures were performed on the micro-CT data as this modality enabled the impact of internal porosity/surface geometry to be better integrated into the measures.

To evaluate the extent of active mineralization on bone surfaces, single- and double-labeled bone surfaces (sLS, dLS, respectively), and total bone surface (BS) were measured on the endosteal (Es) and periosteal (Ps) surfaces. Mineralizing surface per bone surface (MS/BS) was calculated as (dLS+sLS/2)/BS on the endosteal (Es.MS/BS, %) and periosteal (Ps.MS/BS, %) surfaces.

Intracortical remodeling activity was then counted manually as single-labeled osteons (sL.On), double-labeled osteons (dL.On), and resorption cavities (Rs.N), defined as non-mineralizing pores characterized by eroded surfaces, no lamellar bone formation, and no calcein labelling. These parameters were normalized to Ct.Ar (sL.On/Ct.Ar, dL.On/Ct.Ar, and Rs.N/Ct.Ar, mm^{-2}) and used to calculate a ratio of labelled osteons versus resorption cavities ((sL.On+dL.On)/Rs.N). In cross-sections where Rs.N was zero, a denominator of 1 was used to maximize the inclusion of data. Activation frequency (Ac.f) was calculated as Ac.f = ((sL.On+dL.On)/Ct.Ar)/σ_f (#/mm^2/year), where σ_f, the osteon formation time, was calculated as W.Th/On.MAR (Frost, 1969). W.Th (μm) reflects osteon wall thickness, the distance between osteon canal and cement line. This was measured from 50 randomly selected osteons for each animal within each transverse section using transmitted light microscopy at ^{x}20 magnification. In sections with fewer than 50 osteons, all osteons present were measured. Osteonal mineral apposition rate (On.MAR, μm/d) was calculated as the inter-label distance, measured as the distance between two consecutive osteonal calcein labels, divided by the labeling period (14 days). On.MAR was measured in 20 randomly selected dL.On within each transverse section. In sections with fewer than 20 dL.On, all osteons present were measured. Ac.f was calculated from mean W.Th and On.MAR values for each animal and, therefore, only rabbits with On.MAR values were included in the mean calculation of Ac.f. Finally, to provide a measure of overall remodeling activity that did not rely upon normalization to σ_f, we calculated active remodeling centers (a.Rm.Cr, mm^{-2}) as the sum of resorption spaces and labelled osteons normalized to Ct.Ar: (sL.On+dL.On+Rs.N)/Ct.Ar.

4.34. Statistical Analysis

All statistical analyses were performed with SPSS version 26.0 (IBM, Armonk, NY, USA). The normality of all parameters was assessed by Shapiro-Wilk tests. Independent sample *t* tests were employed to evaluate animal weight percent change (testing difference from 0) across the entire experimental period (weeks 0 to 12) and also within the pre-dosing period (weeks 0 to 8) and the dosing period (weeks 8 to 12). When normally distributed for all groups, bone parameter data were assessed with one-way ANOVA ($\alpha = 0.05$) and, when significant, post-hoc Bonferroni tests were used to compare all groups versus SHAM. If non-normal distributions were detected for one or more groups, nonparametric Kruskal-Wallis H tests ($\alpha = 0.05$) with, when significant, post-

hoc pairwise comparisons versus SHAM using Dunn's procedure (Dunn, 1964) were carried out. To account for repeated pairwise post hoc tests, *p* value (mean difference, group/SHAM) or α (confidence interval (CI) of the mean/median differences versus SHAM) were adjusted using Bonferroni's method (Bonferroni, 1936). For most measures, the *p* value and CI were adjusted to account for the four pairwise comparisons versus SHAM resulting in *adjusted p* = *p* * 4 and %CI = 98.75% (1- α; where α = 0.05/4). For comparisons lacking the two GC-dosed groups, the two pairwise comparisons employed resulted in *adjusted p* = *p* * 2 and %CI = 97.5% (1- α; where α = 0.05/2). To calculate the CIs, additional independent *t* tests for the normal data and Hodges-Lehmann tests for the non-normal data were employed. Finally, fold changes relative to SHAM (group/SHAM) were calculated for all parameters.

4.4. Results

4.41. Animal Weight

Statistics for weight and % weight change are summarized in Table 4.1. and depicted in Figure 4.2. For the 8-week pre-dosing period, CI of the percent change in weight excluded zero for SHAM ($p = 0.008$), OVX ($p = 0.001$), and OVX+GC ($p = 0.049$), and was strongly offset from zero for PTH ($p = 0.053$) indicating weight gain in these groups. Conversely, the data for GC ($p = 0.894$) indicated no change in weight reflected by a CI evenly distributed about zero. CIs revealed that during the 4-week dosing period SHAM ($p < 0.001$) and OVX ($p = 0.006$) again gained weight while GC ($p = 0.008$), OVX+GC ($p = 0.011$), and PTH ($p = 0.012$) all lost weight. Considering the entire 12-week experimental period, SHAM ($p = 0.002$) and OVX ($p < 0.001$) exhibited overall weight gain, GC ($p = 0.037$) exhibited overall weight loss while OVX+GC ($p = 0.430$) and PTH ($p = 0.674$) exhibited no change with CIs well distributed about zero.

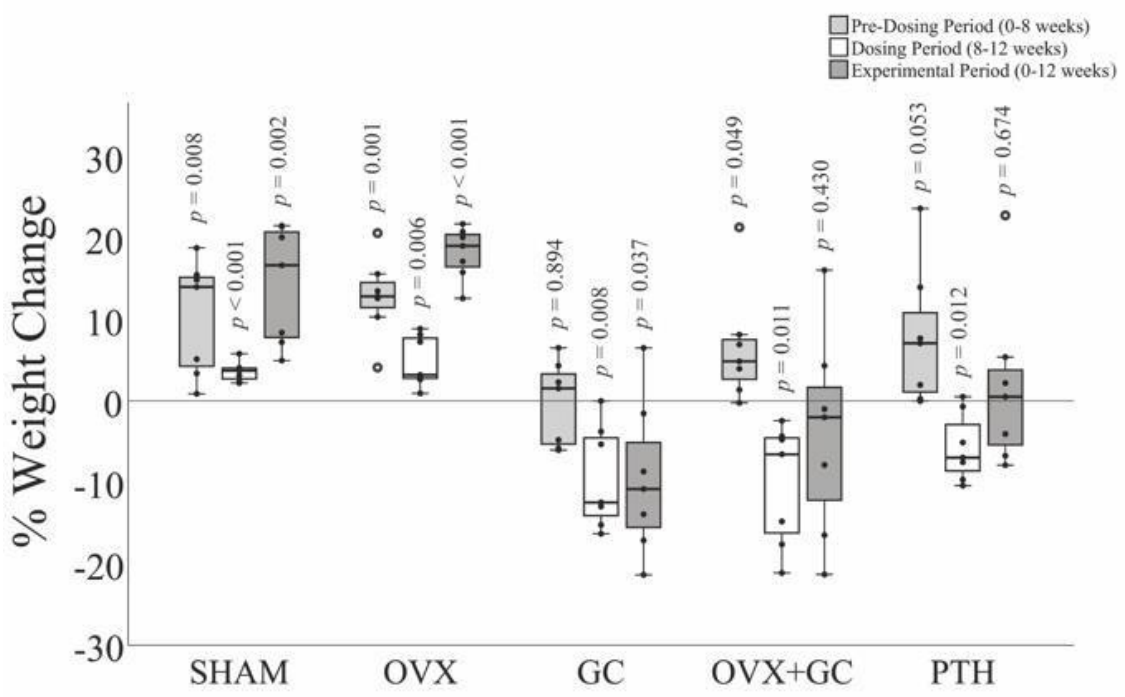

Figure 4.2. Analyses of mean changes in body weight in rabbit groups over experimental period (0 to 3 months). Data are presented by box plots with individual rabbits plotted as solid circles and outliers plotted as open circles. $n = 7$. Independent sample t tests ($\alpha = 0.05$) were employed for comparison to 0 with p values (unadjusted) shown in graph. SHAM = control; OVX = ovariectomy; GC = glucocorticoid; OVX+GC = ovariectomy and glucocorticoid; PTH = parathyroid hormone.

Table 4.1. Rabbit Weight Analyses

	SHAM			OVX			GC			OVX+GC			PTH		
Parameter	**Mean ± SD**	***vs.* 0** ***p***	**95% CI**	**Mean ± SD**	***vs.* 0** ***p***	**95% CI**	**Mean ± SD**	***vs.* 0** ***p***	**95% CI**	**Mean ± SD**	***vs.* 0** ***p***	**95% CI**	**Mean ± SD**	***vs.* 0** ***p***	**95% CI**
% Weight Change Pre-Dosing Period	10.37 ± 7.04	0.008	3.86, 16.87	12.80 ± 5.02	0.001	8.16, 17.45	-0.27 ± 5.19	0.894	-5.07, 4.53	6.63 ±7.11	0.049	0.05, 13.20	7.80 ± 8.58	0.053	-0.13, 15.74
% Weight Change Dosing Period	3.60 ± 1.23	<0.001	2.46, 4.74	4.86 ± 3.15	0.006	1.95, 7.77	-9.44 ± 6.33	0.008	-15.29, -3.58	-10.23 ± 7.45	0.011	-17.13, -3.34	-5.69 ± 4.22	0.012	-9.59, -1.78
% Weight Change Experimental Period	14.33 ± 7.24	0.002	7.64, 21.02	18.18 ± 3.21	<0.001	15.21, 21.15	-9.56 ± 9.49	0.037	-18.34, -0.78	-4.04 ± 12.62	0.430	-15.71, 7.64	1.75 ± 10.46	0.674	-7.92, 11.42

Values are reported as mean ± standard deviation. *N*=7. Independent sample *t* tests were employed. The reported *p* values are unadjusted. 95% confidence intervals (CI) of the mean are reported. SHAM = control. OVX = ovariectomy. GC = glucocorticoid. OVX+GC = ovariectomy & glucocorticoid. PTH = parathyroid hormone.

4.42. Cortical Porosity

Representative micro-CT 2D cross-sectional images and 3D renders of the VOIs are provided in Figure 4.3 *A*. Cortical pores appeared to be non-uniform and clustered within portions of the mid-cortex. Measurements of Ct.Po and Ca.Dm are summarized in Table 4.2. and Figure 4.3 *B,C*. CIs of the mean/median differences versus SHAM excluded zero for all groups with fold changes from SHAM ranging from 4.6 to 28.8, indicating increased porosity in all groups. Evidence supporting an increase in Ct.Po was the least robust for GC (*adj. p* = 0.256) which had the smallest fold increase (4.6) despite inclusion of a strongly positive outlier. For Ca.Dm, similar fold change increases from SHAM, ranging from 1.4 to 1.9, were observed in all groups and CIs excluding (OVX+GC, *adj. p* < 0.001; and PTH, *adj. p* = 0.049) or strongly offset (OVX, *adj. p* = 0.202; and GC, *adj. p* = 0.061) from zero were observed across all groups (Table 4.2.). The distributions of Ca.Dm values (Figure 4.3 *D*) reflected the relatively low proportion of large resorption-space sized pores in SHAM, although this group did exhibit a peak in distribution of values around the expected (100 µm) osteon/resorption space diameter for rabbits. A similar peak dominated the distributions for OVX and PTH. The two GC dosed groups (GC and OVX+GC) exhibited a different pattern with higher proportions of much larger pores.

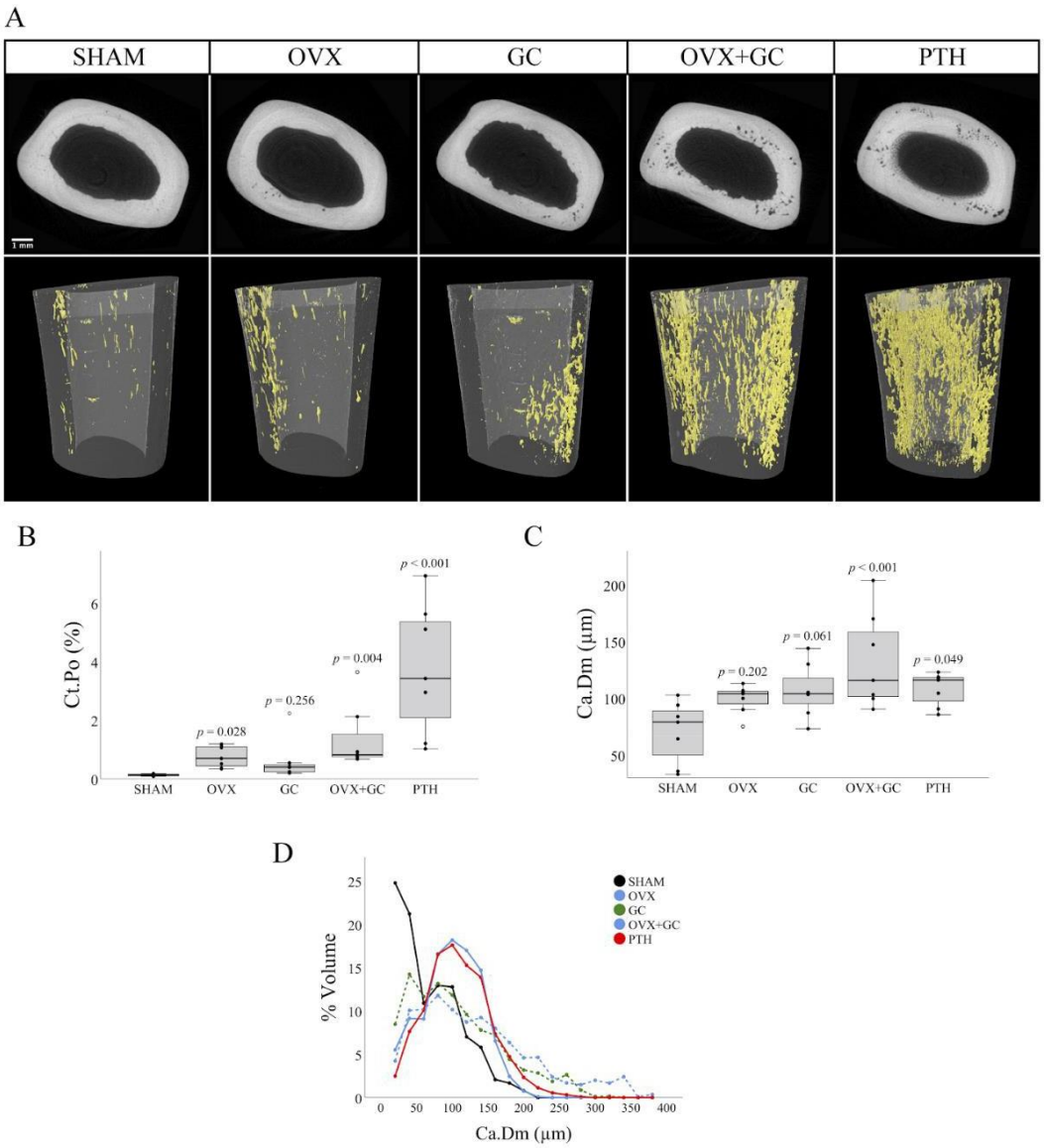

Figure 4.3. Micro-CT based analyses of cortical bone in rabbit tibiae. (*A*) Representative two-dimensional micro-CT cross sectional images of cortical bone in distal rabbit tibiae in various treatment groups with corresponding three-dimensional renders of volume of interest (*below*). Regions of cortical porosity at the level of vascular canals are highlighted in yellow. Scale bar = 1 mm. (*B*) Cortical porosity (Ct.Po) analysis in rabbit tibiae. Data are presented by boxplot with individual rabbits plotted as solid circles and outliers plotted as open circles. *n*=7. Kruskal-Wallis *H* test with post hoc Dunn's test was used to compare groups versus SHAM. Adjusted *p* values (Bonferroni method; *adj. p* = *p* * 4 for four-pairwise comparisons) are shown in graph. (*C*) Canal diameter (Ca.Dm) analysis in rabbit tibiae. Data are presented by boxplot with individual rabbits plotted as solid circles and outliers plotted as open circles. *n*=7. One-way ANOVA with post hoc Bonferroni test was used to compare groups versus SHAM. Adjusted *p* values (Bonferroni method; *adj. p* = *p* * 4 for four-pairwise comparisons) are shown in graph. (*D*) Histograms depicting distributions of canal diameters in rabbit tibiae for each group. SHAM = control. OVX = ovariectomy. GC= glucocorticoid. OVX+GC = ovariectomy & glucocorticoid. PTH = parathyroid hormone.

Table 4.2. Micro-CT Cortical Bone Parameters

		SHAM	OVX				GC				OVX+GC				PTH			
Parameter	**Overall Test *p***	**Mean ± SD (Median)**	**Mean ± SD (Median)**	***vs.* SHAM adj. *p***	**Mean/Median Difference (CI)**	**Fold Change**	**Mean ± SD (Median)**	***vs.* SHAM adj. *p***	**Mean/Median Difference (CI)**	**Fold Change**	**Mean ± SD (Median)**	***vs.* SHAM adj. *p***	**Mean/Median Difference (CI)**	**Fold Change**	**Mean ± SD (Median)**	***vs.* SHAM adj. *p***	**Mean/Median Difference (CI)**	**Fold Change**
Ct.Po (%)	<0.001	0.13 ± 0.04 (0.13)	0.75 ± 0.37 (0.69)	0.028	0.56 (0.20, 1.04)	5.8	0.60 ± 0.73 (0.39)	0.256	0.24 (0.06, 2.09)	4.6	1.38 ± 1.12 (0.82)	0.004	0.69 (0.57, 3.49)	10.6	3.75 ± 2.24 (3.42)	<0.001	3.29 (0.92, 6.78)	28.8
Ca.Dm (µm)	0.003	70.00 ± 27.40	99.00 ± 12.80	0.202	28.84 (–4.69, 62.37)	1.4	107.00 ± 24.10	0.061	36.41 (-4.09, 76.90)	1.5	133.00 ± 42.30	<0.001	62.59 (6.71, 118.47)	1.9	108.00 ± 14.80	0.049	37.68 (3.12, 72.23)	1.5

Values are reported as mean ± standard deviation. Median values are also reported for those parameters where at least one group was not normally distributed. n=7. One-way ANOVA with post-hoc Bonferroni tests were employed for normal data. Kruskal-Wallis H tests with post hoc Dunn's tests were employed for non-normal data. The p values were adjusted for multiple comparisons versus SHAM using Bonferroni method (*adj*. $p = p * 4$). Mean/median differences (Group - SHAM) and confidence intervals (CI) of the mean/median differences are reported from independent t tests for normal data and Hodges-Lehmann tests for non-normal data. CIs were adjusted for multiple comparisons versus SHAM = 98.75% (1- α ; where $\alpha = 0.05/4$). Fold changes are reported relative to SHAM (Group/SHAM). Ct.Po = cortical porosity; Ca.Dm = canal diameter; SHAM = control; OVX = ovariectomy; GC = glucocorticoid; OVX+GC = ovariectomy & glucocorticoid; PTH = parathyroid hormone.

4.43. Cortical Bone Geometry

Representative DIC images are provided in Figure 4.4. and all cross-sectional geometry measures are summarized in Figure 4.5. It was evident from these images, as well as the 2D histological and 3D micro-CT images (Figure 4.4 *G* and Figure 4.3 *A*, respectively), that net resorption occurred at the endosteal surfaces of the two GC-dosed groups (GC and OVX+GC) with large trench-like packets of bone being removed (Figure 4.4. *G*). Quantitatively (Table 4.3.), the geometric parameters exhibited individual variability reflected by many outliers but subtle overall fold changes relative to SHAM ranging from 0.8 to 1.2. CIs for GC excluded zero for Tt.Ar (*no post hoc*), Ct.Ar (*adj. p* = 0.004), Imin (*adj. p* = 0.029), Imax (*adj. p* = 0.068) and Zpol (*adj. p* = 0.013), all findings indicative of smaller, weaker bones in this group. This pattern was not observed in OVX+GC with the caveat that Ct.Ar (*adj. p* = 0.065) was reduced relative to SHAM with a CI excluding zero.

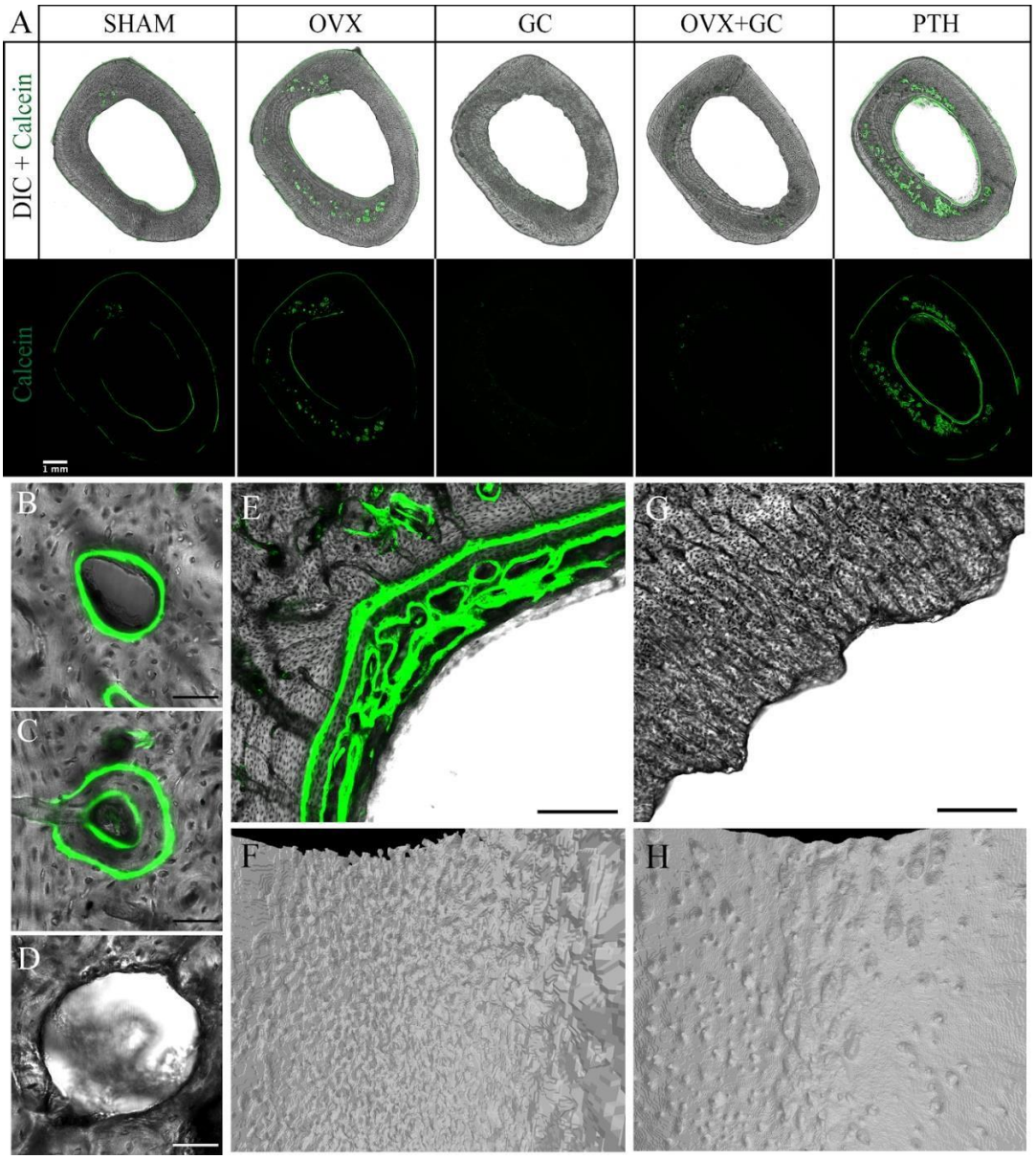

Figure 4.4. (*A*) Differential interference contrast (DIC) and fluorescent confocal microscopy images of transverse sections of rabbit tibiae in various treatment groups. Green fluorescent signal from calcein depicts areas of active bone formation. Absent signals from GC-treated rabbits are due to inhibition of osteoblastic-mediated bone formation by GC treatment. Scale bar = 1 mm. SHAM = control; OVX = ovariectomy; GC = glucocorticoid; OVX+GC = ovariectomy & glucocorticoid; PTH = parathyroid hormone. (*B-D*) Representative confocal microscopy images of (*B*) single-labeled osteon, (*C*) double-labeled osteon, and (*D*) resorption cavity. Scale bar = 50 μm. (*E*) Confocal microscopy image of PTH endosteal surface in transverse section. Note the trabecularized appearance of bone formed on the endosteal surface, a feature typical of woven bone. Scale bar = 150 μm. (*F*) Corresponding three-dimensional reconstructed micro-CT image of PTH endosteal surface. (*G*) Confocal microscopy image of GC endosteal surface in transverse section. Note scalloped appearance of endosteal bone. Scale bar = 150 μm. (*H*) Corresponding three-dimensional reconstructed micro-CT image of GC endosteal surface.

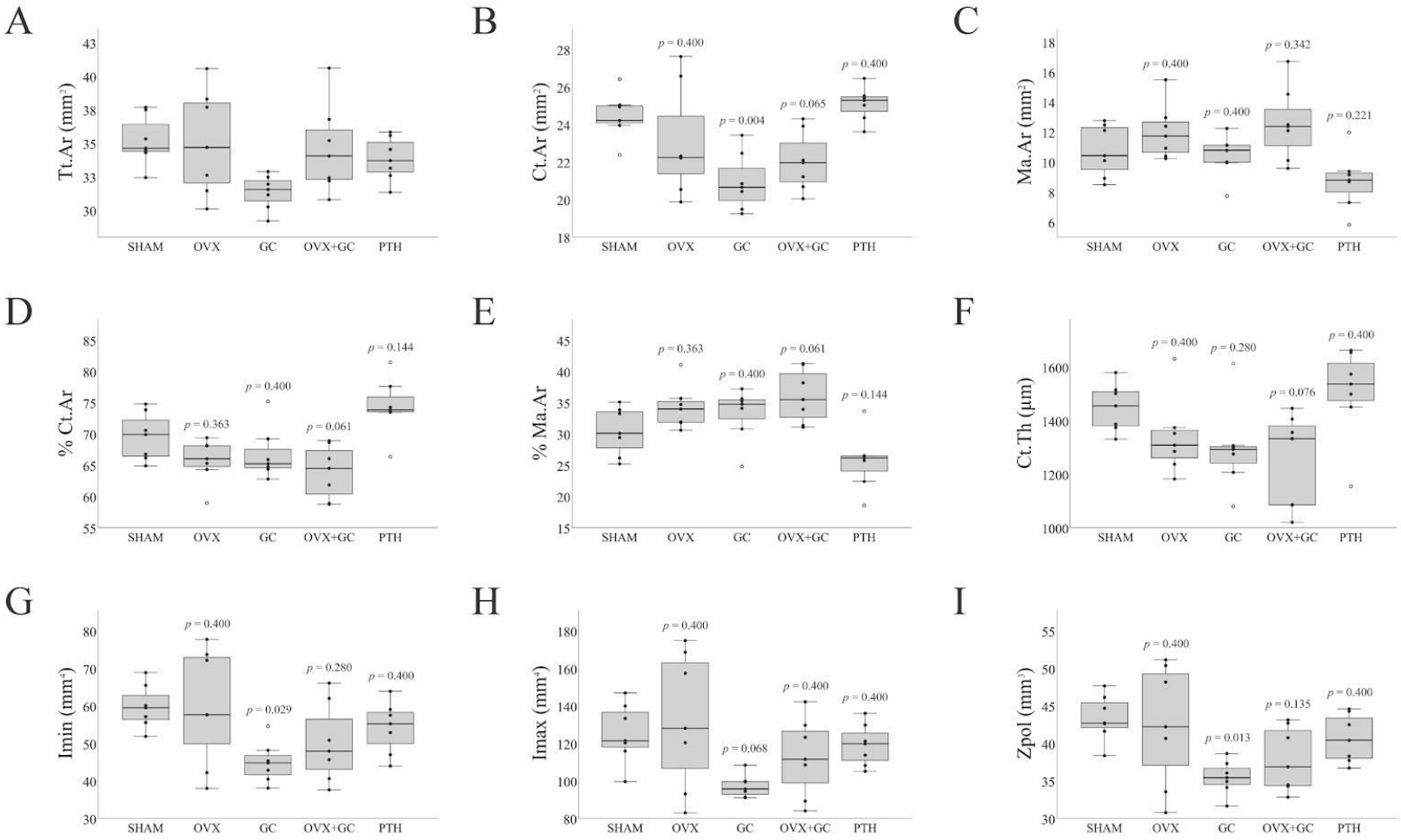

Figure 4.5. (*A-I*) Cortical bone geometry analyses in rabbit tibiae. Data are presented by boxplots with individual rabbits plotted as solid circles and outliers plotted as open circles. *n*=7. One-way ANOVA was employed and if $p < 0.05$, post hoc Bonferroni test was used to compare groups versus SHAM. Adjusted *p* values (Bonferroni method; *adj.* $p = p * 4$ for four-pairwise comparisons) are shown in graphs. Tt.Ar = total area; Ct.Ar = cortical area; Ma.Ar = marrow area; Ct.Th = cortical thickness; Imin = minimum second moment of area; Imax = maximum second moment of area; Zpol = torsional section modulus; SHAM = control; OVX = ovariectomy; GC = glucocorticoid; OVX+GC = ovariectomy & glucocorticoid; PTH = parathyroid hormone.

Table 4.3. Cortical Bone Geometry Parameters

		SHAM	OVX				GC				OVX+GC				PTH			
Parameter	**Overall Test *p***	**Mean ± SD**	**Mean ± SD**	***vs.* SHAM adj. *p***	**Mean Difference (CI)**	**Fold Change**	**Mean ± SD**	***vs.* SHAM adj. *p***	**Mean Difference (CI)**	**Fold Change**	**Mean ± SD**	***vs.* SHAM adj. *p***	**Mean Difference (CI)**	**Fold Change**	**Mean ± SD**	***vs.* SHAM adj. *p***	**Mean Difference (CI)**	**Fold Change**
Tt.Ar (mm^2)	0.059	35.20 ± 1.86	35.10 ± 3.91	-	-0.13 (-4.93, 4.67)	1.0	31.30 ± 1.28	-	-3.85 (-6.36, -1.34)	0.9	34.60 ± 3.33	-	-0.62 (-4.85, 3.62)	1.0	33.80 ± 1.62	-	-1.38 (-4.12, 1.36)	1.0
Ct.Ar (mm^2)	0.001	24.40 ± 1.23	23.10 ± 2.93	0.400	-1.40 (-4.92, 2.13)	0.9	20.90 ± 1.52	0.004	-3.52 (-5.69, -1.35)	0.9	22.00 ± 1.59	0.065	-2.42 (-4.65, -0.19)	0.9	25.10 ± 0.91	0.400	6.65 (-1.05, 2.34)	1.0
Ma.Ar (mm^2)	0.007	10.70 ± 1.72	12.00 ± 1.83	0.400	1.26 (-1.53, 4.05)	1.1	10.40 ± 1.42	0.400	-0.33 (-2.80, 2.14)	1.0	12.50 ± 2.46	0.342	1.80 (-1.53, 5.13)	1.2	8.72 ± 1.90	0.221	-2.02 (-4.87, 0.82)	0.8
% Ct.Ar (%)	<0.001	69.50 ± 3.83	65.70 ± 3.49	0.363	-3.82 (-9.57, 1.93)	0.9	66.80 ± 4.19	0.400	-2.78 (-9.08, 3.51)	1.0	63.90 ± 4.25	0.061	-5.63 (-11.97, 0.72)	0.9	74.40 ± 4.59	0.144	4.80 (-1.83, 11.42)	1.1
% Ma.Ar (%)	<0.001	30.40 ± 3.83	34.30 ± 3.49	0.363	3.82 (-1.93, 9.57)	1.1	33.20 ± 4.19	0.400	2.78 (-3.51, 9.08)	1.1	36.10 ± 4.25	0.061	5.63 (-0.72, 11.97)	1.2	25.60 ± 4.59	0.144	-4.80 (-11.42, 1.83)	0.8
Ct.Th (μm)	0.019	1448.63 ± 88.94	1338.49 ± 144.44	0.400	-110.14 (-298.27, 78.00)	0.9	1295.81 ± 161.98	0.280	-152.82 (-357.01, 51.38)	0.9	1247.01 ± 176.85	0.076	-201.61 (-421.16, 17.94)	0.9	1504.26 ± 172.80	0.400	55.63 (-159.61, 270.88)	1.0
I_{min} (mm^4)	0.030	59.79 ± 5.82	59.88 ± 15.62	0.400	0.09 (-18.40, 18.58)	1.0	44.92 ± 5.40	0.029	-14.88 (-23.69, -6.06)	0.8	50.10 ± 10.54	0.280	-9.69 (-23.05, 3.67)	0.8	54.22 ± 6.91	0.400	-5.57 (-15.60, 4.46)	0.9
I_{max} (mm^4)	0.039	125.35 ± 15.98	132.22 ± 36.29	0.400	6.87 (-37.12, 50.85)	1.1	97.16 ± 6.08	0.068	-28.19 (-47.15, -9.22)	0.8	112.65 ± 21.08	0.400	-12.70 (-42.04, 16.64)	0.9	119.14 ± 11.13	0.400	-6.21 (-27.81, 15.39)	1.0
Z_{pol} (mm^3)	0.019	43.40 ± 3.08	42.42 ± 8.07	0.400	-0.98 (-10.56, 8.59)	1.0	35.45 ± 2.26	0.013	-7.95 (-12.18, -3.71)	0.8	37.86 ± 4.29	0.135	-5.53 (-11.39, 0.32)	0.9	40.65 ± 3.20	0.400	-2.75 (-7.67, 2.17)	0.9

Values are reported as mean ± standard deviation. *n*=7, except for On.MAR and Ac.f measures for OVX (*n*=5) and SHAM (*n*=3). One-way ANOVA with post hoc Bonferroni tests were employed for normal data. The *p* values were adjusted for multiple comparisons versus SHAM using Bonferroni method (*adj. p = p* * 4). Mean differences (Group - SHAM) and confidence intervals (CI) of the mean differences are reported from independent *t* tests. CIs were adjusted for multiple comparisons versus SHAM = 98.75% (1- α ; where α = 0.05/4). Fold changes are reported relative to SHAM (Group/SHAM). Tt.Ar = total area; Ct.Ar = cortical area; Ma.Ar = marrow area; Ct.Th = cortical thickness; I_{min} = minimum second moment of area; I_{max} = maximum second moment of area; Z_{pol} = torsional section modulus; SHAM = control; OVX = ovariectomy; GC = glucocorticoid; OVX+GC = ovariectomy & glucocorticoid; PTH = parathyroid hormone.

4.44. Cortical Bone Histomorphometry

The calcein labels revealed active bone formation on the periosteal and endosteal surfaces as well as intracortical bone formation within actively forming osteons (Figures 4.4. and 4.6., Table 4.4.). Formation was most pronounced in the PTH group, particularly at the endosteal surface and intracortically (reflected qualitatively in many geometry parameters in Figure 4.5.). Conversely, the GC and OVX+GC groups exhibited reduced evidence of labeled bone formation on all surfaces (Figure 4.4. *A*). Because of the lack of formation, measures relying upon calcein labels were not assessable for GC and OVX+GC and were reported as no data (ND) in Table 4.4. Bone formation at both surfaces, Es.MS/BS and Ps.MS/BS, was increased in the PTH group (CIs excluding zero; *adj. p* < 0.001 and 0.040, respectively). Endosteal bone formation in PTH had a distinct pattern that included well-organized lamellar bone in places but also disorganized plates with a crude trabecular-like pattern reminiscent of woven bone in others (Figure 4.4. *E*,*F*). Ps.MS/BS was highly variable with large outliers detected for SHAM and OVX.

Evidence of elevated remodeling was most dramatically (8.4- to 26.3- fold increases) and consistently observed in PTH for sL.On/Ct.Ar (*adj. p* = 0.004), dL.On/Ct.Ar (*adj. p* = 0.008), Rs.N/Ct.Ar (*adj. p* < 0.001), a.Rm.Cr/Ct.Ar (*adj. p* < 0.001), and Ac.f (*adj. p* = 0.008) as reflected by CIs excluding zero. OVX exhibited a similar but less pronounced pattern (fold changes approximately half those of PTH) for these parameters with the caveat that the CI for Ac.f (*adj. p* = 0.203) included but was strongly offset from zero. For the glucocorticoid groups, Rs.N/Ct.Ar was elevated 10.1- and 17.5-fold for GC (*adj. p* = 0.064) and OVX+GC (*adj. p* < 0.001), respectively, with CIs excluding zero. The ratio of labeled osteons to resorption cavities (sL.On + dL.On)/Rs.N was 0.1- and 0.4-fold that of SHAM for OVX+GC (*adj. p* = 0.008) and GC (*adj. p* = 0.100), respectively, with the CI for the former excluding zero and the latter strongly offset from it.

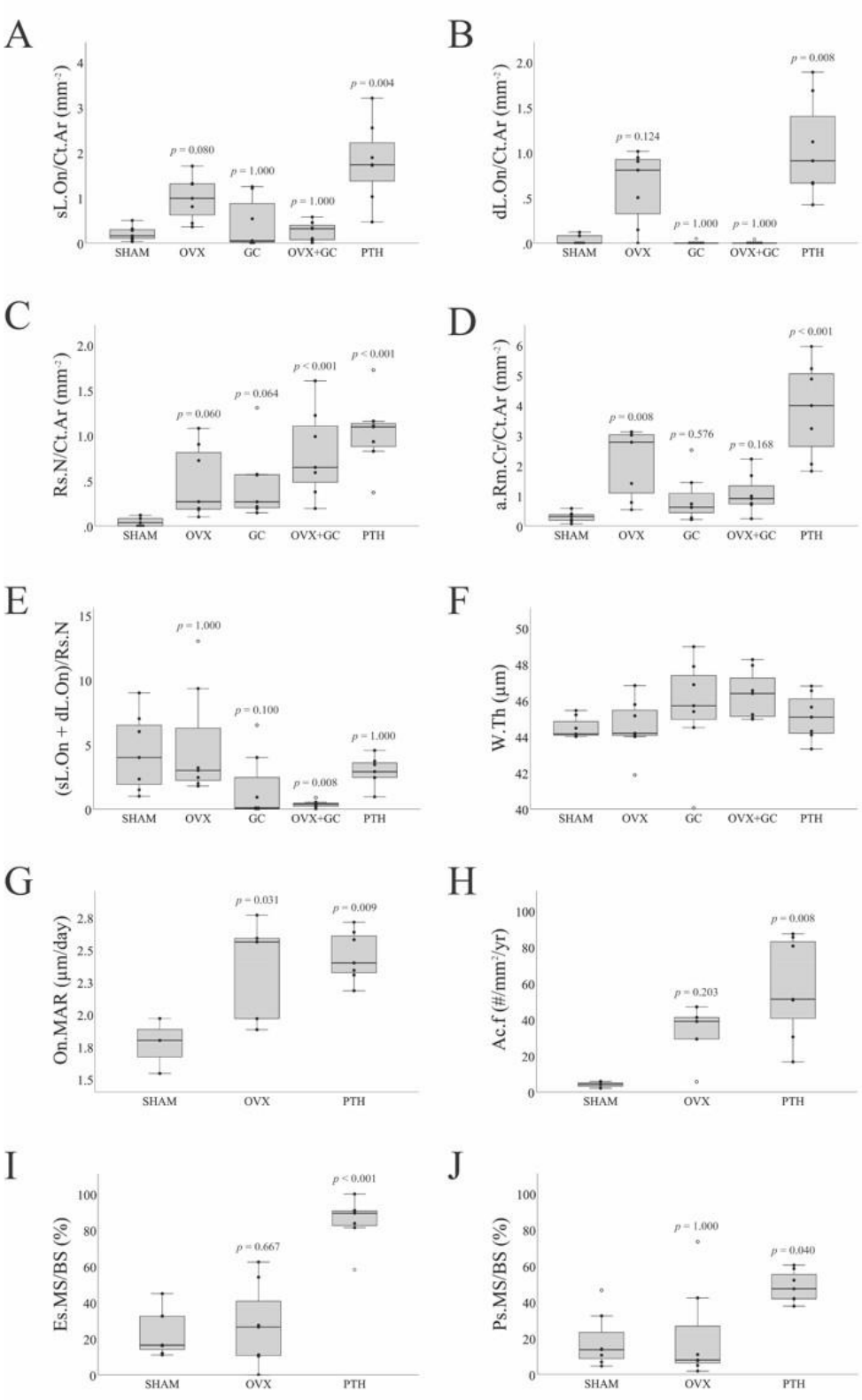

Legend on following page.

Figure 4.6. (*A-J)* Histomorphometric analyses of transverse cortical bone sections in rabbit tibiae. Data are presented by boxplots with individual rabbits plotted as solid circles and outliers plotted as open circles. *n*=7 except for On.MAR and Ac.f measures for OVX (*n*=5) and SHAM (*n*=3). For sL.On/Ct.Ar, dL.On/Ct.Ar, Rs.N/Ct.Ar, a.Rm.Cr/Ct.Ar, (sL.On + dL.On)/Rs.N, W.Th, and Es.MS/BS, Kruskal-Wallis *H* tests were employed and if $p < 0.05$, post hoc Dunn's test was used to compare groups versus SHAM. For On.MAR, Ac.f, and Ps.MS/BS, one-way ANOVA with post hoc Bonferroni tests were used to compare groups versus SHAM. Adjusted *p* values using Bonferroni method (*adj. p = p* * 4 for four-pairwise comparisons except for Es.MS/BS, Ps. MS/BS, On.MAR, and Ac.f where *adj. p = p* *2 to account for two-pairwise comparisons) are shown in graphs. sL.On = single-labeled osteon; dL.On = double labeled osteon; Rs.N = resorption cavity number; a.Rm.Cr = active remodeling centers; Ct.Ar = cortical area; W.Th = wall thickness; On.MAR = osteonal mineral apposition rate; Ac.f = activation frequency; Es = endosteal; Ps = periosteal; MS/BS = mineralizing surface per bone surface; SHAM = control; OVX = ovariectomy; GC = glucocorticoid; OVX+GC = ovariectomy & glucocorticoid; PTH = parathyroidhormone.

Table 4.4. Cortical Bone Histomorphometric Parameters

		SHAM	OVX				GC				OVX+GC				PTH			
Parameter	**Overall Test *p***	**Mean ± SD (Median)**	**Mean ± SD (Median)**	***vs.* SHAM adj. *p***	**Mean/Median Difference (CI)**	**Fold Change**	**Mean ± SD (Median)**	***vs.* SHAM adj. *p***	**Mean/Median Difference (CI)**	**Fold Change**	**Mean ± SD (Median)**	***vs.* SHAM adj. *p***	**Mean/Median Difference (CI)**	**Fold Change**	**Mean ± SD (Median)**	***vs.* SHAM adj. *p***	**Mean/Median Difference (CI)**	**Fold Change**
sL.On/Ct.Ar (mm^{-2})	0.001	0.21 ± 0.16 (0.16)	0.99 ± 0.49 (0.99)	0.080	0.80 (0.13, 1.42)	4.1	0.44 ± 0.57 (0.05)	1.000	-0.03 (-0.31, 1.12)	2.1	0.26 ± 0.22 (0.32)	1.000	0.02 (-0.28, 0.42)	1.2	1.80 ± 0.91 (1.73)	0.004	1.59 (0.34, 2.92)	8.4
dL.On/Ct.Ar (mm^{-2})	<0.001	0.04 ± 0.05 (0.00)	0.62 ± 0.41 (0.81)	0.124	0.78 (0.00, 0.95)	15.4	0.01 ± 0.02 (0.00)	1.000	0.00 (-0.08, 0.00)	0.2	0.01 ± 0.02 (0.00)	1.000	0.00 (-0.08, 0.00)	0.2	1.05 ± 0.55 (0.91)	0.008	0.91 (0.42, 1.81)	26.3
Rs.N/Ct.Ar (mm^{-2})	<0.001	0.05 ± 0.05 (0.04)	0.49 ± 0.40 (0.27)	0.060	0.23 (0.07, 1.00)	10.7	0.47 ± 0.41 (0.27)	0.064	0.23 (0.11, 1.22)	10.1	0.80 ± 0.50 (0.65)	<0.001	0.61 (0.19, 1.52)	17.5	1.03 ± 0.41 (1.10)	<0.001	1.01 (0.37, 1.64)	22.4
a.Rm.Cr/Ct.Ar (mm^{-2})	<0.001	0.30 ± 0.17 (0.31)	2.10 ± 1.15 (2.78)	0.008	2.43 (0.23, 2.92)	7.0	0.92 ± 0.81 (0.62)	0.576	0.38 (-0.13, 2.16)	3.1	1.07 ± 0.66 (0.91)	0.168	0.60 (0.04, 1.86)	3.6	3.87 ± 1.59 (4.00)	<0.001	3.68 (1.51, 5.60)	12.9
(sL.On + dL.On)/ Rs.N	0.003	4.40 ± 3.02 (4.00)	4.97 ± 4.39 (3.00)	1.000	0.33 (-5.80, 8.33)	1.1	1.66 ± 2.58 (0.09)	0.100	-2.33 (-7.00, 2.50)	0.4	0.37 ± 0.29 (0.37)	0.008	-3.63 (-8.62, -0.63)	0.1	2.93 ± 1.15 (2.90)	1.000	-1.38 (-6.05, 2.22)	0.7
W.Th (µm)	0.093	44.49 ± 0.59 (44.15)	44.56 ± 1.57 (44.19)	-	0.04 (-2.21, 2.36)	1.0	45.63 ± 2.89 (45.71)	-	1.42 (-4.04, 4.51)	1.0	46.34 ± 1.37 (46.39)	-	1.34 (-0.19, 3.94)	1.0	45.11 ± 1.29 (45.08)	1.000	0.43 (-1.15, 2.54)	1.0
On.MAR (µm/day)	0.013	1.77 ± 0.21	2.35 ± 0.40	0.031	0.58 (-0.18, 1.34)	1.3	ND	ND	ND	ND	ND	ND	ND	ND	2.45 ± 0.19	0.009	0.68 (0.30, 1.06)	1.4
Ac.f (#/mm^2/yr)	0.012	4.04 ± 1.89	32.43 ± 16.28	0.203	28.39 (-0.53, 57.31)	8.0	ND	ND	ND	ND	ND	ND	ND	ND	57. 54 ± 27.98	0.008	53.49 (7.45, 99.54)	14.2
Es.MS/BS (%)	<0.001	23.65 ± 13.01	27.39 ± 23.26	0.667	3.73 (-22.06, 29.52)	1.2	ND	ND	ND	ND	ND	ND	ND	ND	84.84 ± 13.17	<0.001	61.19 (43.27, 79.11)	3.6
Ps.MS/BS (%)	0.027	18.44 ± 15.34 (13.75)	21.34 ± 26.67 (7.98)	1.000	2.75 (-37.69, 27.40)	1.2	ND	ND	ND	ND	ND	ND	ND	ND	48.58 ± 8.77 (47.35)	0.040	33.14 (9.35, 47.51)	2.6

Values are reported as mean ± standard deviation. Median values are also reported for those parameters where at least one group was not normally distributed. n=7. One-way ANOVA with post hoc Bonferroni tests were employed for normal data. Kruskal-Wallis H tests with post hoc Dunn's tests were employed for non-normal data. The p values were adjusted for multiple comparisons versus SHAM using Bonferroni method ($adj.\ p = p * 4$). GC and OVX+GC were not analyzed for On.MAR, Ac.f, Es.MS/BS, and Ps.MS/BS due to a lack of detected labels and thus the p values were adjusted accordingly ($adj.\ p = p * 2$). Mean/median differences (Group - SHAM) and confidence intervals (CI) of the mean differences are reported from independent t tests for normal data and Hodges-Lehmann tests for non-normal data. CIs were adjusted for multiple comparisons: 98.75% for four-pair wise comparisons (1- α ; where α = 0.05/4) and 97.5% for two-pair wise comparisons (1- α ; where α = 0.05/2). Fold changes are reported relative to SHAM (Group/SHAM). sL.On = single-labeled osteon; dL.On = double-labeled osteon; Rs.N = resorption cavities; a.Rm.Cr = active remodeling centers; Ct.Ar = cortical area; W.Th = wall thickness; On.MAR = osteonal mineral apposition rate; Ac.f = activation frequency; Es= endosteal; Ps = periosteal; MS/BS = mineralizing surface per bone surface; SHAM = control; OVX = ovariectomy; GC = glucocorticoid; OVX+GC = ovariectomy & glucocorticoid; PTH = parathyroid hormone; ND = no data.

4.45. Trabecular Bone Micro-CT

Figure 4.7. *A* presents 3D renders of a portion of the VOI used for analysis of trabecular morphology. Overall, although fold changes (0.8 to 1.2) were more subtle than many of the cortical parameters, a pattern of loss was observed for OVX, GC, and OVX+GC groups, while the opposite was observed for PTH (Table 4.5. and Figure 4.7. *B*-*E*). A similar-sized reduction in BV/TV was observed in GC (*adj. p* = 0.024), OVX+GC (*adj. p* = 0.016) and OVX (*adj. p* = 0.448) with the CIs excluding (GC and OVX+GC) or strongly offset from zero (OVX). Conversely, PTH (*adj. p* = 0.880) exhibited the opposite pattern with the largest positive fold change (1.2) in BV/TV with a CI strongly offset from zero. Differences in Tb.N supported the overall patterns of change in BV/TV with CIs consistently excluding or being strongly offset from zero (*adj. p* < 0.05 for all groups). The outcomes for Tb.Sp and Tb.Th were less definitive exhibiting the lowest fold changes (0.9 to 1.2) and CIs clustered about zero with the caveat that Tb.Sp for GC (*adj. p* = 0.124) and OVX+GC (*adj. p* = 0.155) had CIs just including zero.

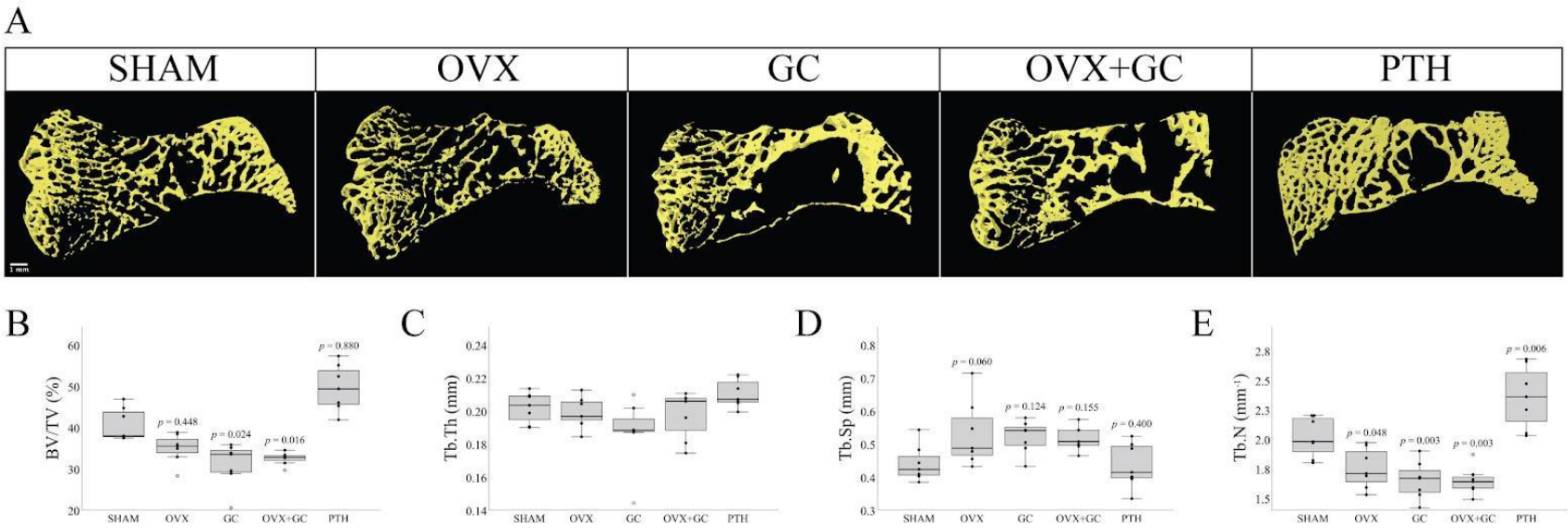

Figure 4.7. Micro-CT based analyses of trabecular bone in rabbit tibiae. (*A*) Three-dimensional reconstructed images of epiphyseal subchondral trabecular bone structure in rabbit tibiae of various treatment groups. Regions of trabecular bone are highlighted in yellow. Scale bar = 1 mm. (*B-E*) Three-dimensional trabecular bone analyses in rabbit tibiae. Data are presented by boxplots with individual rabbits plotted as solid circles and individual outliers plotted as open circles. *n*=7. For Tb.Th and BV/TV, One-way ANOVA was employed and if $p < 0.05$, post hoc Bonferroni test was used to compare groups versus SHAM. For Tb.Sp and Tb.N, Kruskal-Wallis *H* test with post hoc Dunn's test was used to compare groups versus SHAM. Adjusted *p* values (Bonferroni method; *adj.* $p = p * 4$ for four-pairwise comparisons) are shown in graphs. BV/TV = bone volume/tissue volume.; Tb.Th = trabecular thickness; Tb.N = trabecular number; Tb.Sp = trabecular separation; SHAM = control; OVX = ovariectomy; GC = glucocorticoid; OVX+GC = ovariectomy & glucocorticoid; PTH = parathyroid hormone.

Table 4.5. Micro-CT Trabecular Bone Parameters

		SHAM	OVX				GC				OVX+GC				PTH			
Parameter	**Overall Test *p***	**Mean ± SD (Median)**	**Mean ± SD (Median)**	***vs.* SHAM adj. *p***	**Mean/Median Difference (CI)**	**Fold Change**	**Mean ± SD (Median)**	***vs.* SHAM adj. *p***	**Mean/Median Difference (CI)**	**Fold Change**	**Mean ± SD (Median)**	***vs.* SHAM adj. *p***	**Mean/Median Difference (CI)**	**Fold Change**	**Mean ± SD (Median)**	***vs.* SHAM adj. *p***	**Mean/Median Difference (CI)**	**Fold Change**
BV/TV (%)	<0.001	40.73 ± 3.97 (37.93)	34.94 ± 3.57 (35.49)	0.448	-4.90 (-12.00, 0.87)	0.9	31.01 ± 5.33 (33.48)	0.024	-8.87 (-17.42, -2.33)	0.8	32.45 ± 1.54 (32.77)	0.016	-7.77 (-14.13, -4.10)	0.8	49.60 ± 5.62 (49.36)	0.880	8.28 (-0.84, 17.68)	1.2
Tb.Th (mm)	0.065	0.20 ± 0.01 (0.20)	0.20 ± 0.01 (0.20)	-	0.00 (-0.02, 0.01)	1.0	0.19 ± 0.02 (0.19)	-	-0.01 (-0.05, 0.01)	0.9	0.20 ± 0.02 (0.21)	-	0.00 (-0.03, 0.02)	1.0	0.21 ± 0.01 (0.21)	-	0.01 (-0.01, 0.02)	1.0
Tb.Sp (mm)	0.018	0.44 ± 0.06	0.53 ± 0.10	0.060	0.09 (-0.04, 0.22)	1.2	0.52 ± 0.05	0.124	0.08 (0.00, 0.16)	1.2	0.52 ± 0.04	0.155	0.08 (0.00, 0.15)	1.2	0.44 ± 0.07	0.400	-0.01 (-0.10, 0.09)	1.0
Tb.N (mm^{-1})	<0.001	2.02 ± 0.17	1.75 ± 0.17	0.048	-0.26 (-0.53, 0.00)	0.9	1.65 ± 0.16	0.003	-0.37 (-0.63, -0.11)	0.8	1.65 ± 0.12	0.003	-0.37 (-0.60, -0.14)	0.8	2.36 ± 0.27	0.006	0.34 (-0.01, 0.69)	1.2

Values are reported as mean ± standard deviation. Median values are also reported for those parameters where at least one group was not normally distributed. *n*=7. One-way ANOVA with post hoc Bonferroni tests were employed for normal data. Kruskal-Wallis tests with post hoc Dunn's tests were employed for non-normal data. The *p* values were adjusted for multiple comparisons versus SHAM using Bonferroni method (*adj. p* = *p* * 4). Mean/median differences (Group - SHAM) and confidence intervals (CI) of the mean/median differences are reported from independent *t* tests for normal data and Hodges-Lehmann tests for non-normal data. CIs were adjusted for multiple comparisons versus SHAM = 98.75% (1- α ; where α = 0.05/4). Fold changes are reported relative to SHAM (Group/SHAM). BV/TV = bone volume/tissue volume; Tb.Th = trabecular thickness; Tb.N = trabecular number; Tb.Sp = trabecular separation; SHAM = control; OVX = ovariectomy; GC = glucocorticoid; OVX+GC = ovariectomy & glucocorticoid; PTH = parathyroid hormone.

4.5. Discussion

In general, the animals tolerated the OVX/sham surgeries well and weight gain was observed in three of the groups during the pre-dosing period (SHAM, OVX, and OVX+GC) and suggested by offset CIs for the fourth (GC). Glucocorticoid dosing was not as well tolerated by the animals and weight loss was observed during the dosing period, an observation consistent withpast studies for GC (Grardel et al., 1994) and OVX+GC (Chandler et al., 2019). Three of the GC rabbits had a more extreme reaction to treatment exhibiting hair textural changes although it is unclear if this might have been linked to early (pre-dosing) lack of weight gain observed in this group. Notably, the 1.5 mg/kg/day dose we administered is moderate to high in the context of existing literature and 2 mg/kg/day has been reported as lethal (Castañeda et al., 2008). Further, administering lower doses (1 mg/kg/day) over longer lengths of time (6 weeks) had also resulted in the premature death of one animal (Chandler et al., 2019). As such, increasing GC dose or the length of dosing to possibly induce larger-scale differences in cortical bone parameters may not be feasible in terms of animal welfare. PTH dosing was well tolerated by the animals. Although they exhibited weight loss over the dosing period, it was less pronounced than that observed in the GC-dosed groups. Hirano and colleagues (1999) found a similar decrease in weight after dosing rabbits with 40 μg/kg/5 days a week of PTH for 20 weeks.

The characterization of cortical porosity in the OP models and PTH was our primary objective. Comparative data are limited as cortical porosity is only sparsely reported in the literature for rabbit OP models. In a recent report, Chandler and colleagues (2019) observed no difference in Ct.Po at the femoral mid-diaphysis between SHAM (0.50%) and OVX (0.43%) groups at 18 weeks post-surgery, whereas their OVX+GC group (dosed for 12 weeks commencing 6 weeks after OVX) had elevated Ct.Po (9.75%). It is unclear what underpins their lack of a difference for OVX compared with our study. It could relate to the different skeletal elements studied (femur versus tibia), relative location of the VOI (mid-shaft versus distal shaft), the larger (15 μm) voxel size used, and/or Chandler and colleagues (2019) longer duration post-surgery. Regarding the latter, their longer post-surgery phase for OVX, at 18 weeks versus our 12 weeks, may have enabled more time for cortical remodeling to reach steady state (see discussion of Ac.f below). PTH had the most pronounced difference in Ct.Po, a result consistent with recent reports.

Yamane and colleagues (2017) reported a Ct.Po of 3.62% in rabbit tibiae after treatment with 40 μg/kg/day of PTH for 4 weeks, assessed using micro-CT at a 19.1 μm voxel size, while Zebaze and colleagues (2017) reported a higher Ct.Po of 8.7% in rabbit femora using the same dosing regimen and imaging at 15 μm voxel size.

Across all our groups, qualitative inspection of the images suggested the cortical pores did not appear to be randomly distributed; rather, they were frequently clustered in the mid-cortex. The reason underpinning this is unclear, although it may be linked to developmental features and the localized age of the tissue. In rats, central bands or "islands" of calcified cartilage have been observed, indicating remnants of developmental tissues in the mid-cortex (Bach-Gansmo et al., 2013, Shipov et al., 2013). It is unclear if this was the case in our rabbits, although the central cortex had distinctly complex microarchitecture when compared with more organized lamellar bone, which was particularly evident at the periosteal surface. Mid-cortical porosity in PTH contrasts with observations by Zebaze and colleagues (2017) and Hirano and colleagues (Hirano et al., 2000) who reported increased porosity primarily adjacent to the marrow cavity in the proximal femur and tibial midshaft of rabbits, respectively. It is unclear if these endosteal pores reported by others may be related to the endosteal bone formation we observed.

Mean Ca.Dm values for SHAM where slightly lower (70 μm) than anticipated for remodeling-related resorption spaces in rabbits. This 3D micro-CT measure, however, includes all resolved pores ranging in size from the maximal diameter of cutting-cones, down through the contracting diameter of the closing cones and, ultimately, approaching the normal scale of mature quiescent canals. The latter were not resolved by our micro-CT protocol (Supplemental Figure 4.81). The distribution of Ca.Dm (Figure 4.3. D) for SHAM did reveal a peak in values at the expected 100 μm size for secondary osteons/resorption spaces in rabbits. The distributions of Ca.Dm were very similar for OVX and PTH, and their modal values (~100 μm) corresponded closely with the peak in SHAM. This suggests that the maximal diameters of the resorption spaces created in these groups are similar and of a scale consistent with past reports of normal secondary osteon size in rabbits. Conversely, the GC-dosed groups exhibited distributions skewed toward larger Ca.Dm, suggesting larger initial resorption spaces or the coalescence of spaces in the cortex. Two-dimensional data (Supplemental Figure 4.82) corroborate that pore sizes were increased in

the GC-dosed groups but also in PTH. Zebaze and colleagues (2017) have suggested PTH produces larger pores by enlarging existing canals, which then coalesce, evidenced by micro-CT analysis.

Our secondary objective was to test the hypothesis that elevations in cortical porosity are associated with increased remodeling rates in these rabbit OP models. Activation frequency represents the most direct measure of the rate of remodeling as it is a measure of the birth rate of new BMUs. That said, this measure presented several challenges for our study. First, both GC-dosed groups exhibited little sign of bone formation, rendering measures relying upon the labeled structures unassessable for these groups. This was consistent with the primary mechanism of GC-induced bone loss via osteoblast suppression (Canalis and Delany, 2002). The low numbers of double-labeled osteons in SHAM and OVX, including their absence in some animals, further complicated the assessment of Ac.f. which requires labeled osteons in its numerator and osteon formation time (σ_f = W.Th/On.MAR) in its denominator. This reduced the number of animals available for the comparisons of this parameter, diminishing statistical power and, thus, the generalizability of the results should be interpreted with caution. Finally, a key basis of this estimation of BMU birth rate is the assumption of a steady state where the same number of BMUs (generally quantified as labeled osteons) are being "born" and "dying". Given that we expected elevation in remodeling rate for the OP models and that it has been previously demonstrated for PTH, this assumption is dubious in our case. Further, equal birth and death rates for duration of the newly established σ_f is needed to reach a new steady state after experimental perturbation (Frost, 1969). Osteon formation time (σ_f) assessed in our study (based upon mean W.Th and On.MAR reported in Table 4.4.) was approximately 25, 19, and 18 days for SHAM, OVX, and PTH, respectively. There simply was not enough time in our 28-day dosing period, with calcein labels first administered at the midpoint, for a new steady state to have occurred for PTH and GC. Whether or not the OVX group had reached a new steady state is less clear, but it is more plausible since the first calcein label was administered 69 and 70 days after surgery. Despite these limitations, we have reported Ac.f here to facilitate comparison with existing studies (which may also not meet the underlying assumptions) and, in the case of OVX rabbits (8-fold increase relative to SHAM with the caveat that *adj. p* = 0.203), provide novel, albeit limited, data to the literature. Our Ac.f value for PTH was 14-fold higher than SHAM, a result that aligns well with a previous study of rabbits dosed with 40 μg/kg/day, 5 days per week for 20 weeks where Ac.f was reported

to increase 20-fold in tibiae (43.8) (Hirano et al., 1999). The higher Ac.f for PTH was associated with increased sL.On/Ct.Ar, dL.On/Ct.Ar, and Rs.N/Ct.Ar – findings again consistent with this previous PTH trial (Hirano et al., 1999). Ac.f was also reported in rabbits receiving a lower dose of PTH, 10 μg/kg/5 days per week, for 35 days. Due to this lower dose, Mashiba and colleagues (2001) reported only a 2-fold increase in Ac.f (29.3) in comparison to aged-matched controls. Although it has become standard to include only labeled osteons in Ac.f, Frost's early description indicated the numerator of Ac.f should be "the number of bone-forming or resorbing centers" (1969). Thus, to overcome some of the limitations of Ac.f, and provide a measure of overall remodeling rate/activity that included the GC-dosed groups, we calculated a measure of active remodeling centers, a.Rm.Cr/Ct.Ar, which was not normalized to any assumption about osteon formation time and included both labeled osteons and resorption spaces. By this measure, OVX and PTH were elevated related to SHAM 7- and 13-fold, respectively, and the approximately 3-fold increases for GC and OVX+GC support the conclusion of a difference in those groups as well. This observation for the glucocorticoid groups was corroborated by the large fold changes in Rs.N/Ct.Ar. OVX and PTH also exhibited elevated radial mineral apposition rates (On.MAR) within forming osteons, providing corroborating evidence of an increase in the formative activity of BMUs. Conversely, the ratio of labeled osteons to resorption cavities ((sL.On + dL.On)/Rs.N) was reduced for OVX+GC (0.1-fold) and GC (0.4-fold) indicating a lack of transition from bone resorption to formation (uncoupling ((Andreasen et al., 2015, Hinge et al., 2015, Jensen et al., 2015)) in the glucocorticoid groups. Taken together, the histomorphometric data supports the hypothesis that the rate of remodeling was elevated in all of these OP models.

Measures of cortical geometry and associated bone strength were relatively stable across groups which was not unexpected given the skeletal maturity of the animals and the short duration of the experiments. Distinct endosteal resorption was observed in the glucocorticoid groups whereby large packets of bone were being resorbed with no evidence of formation. Whether these spaces reflect uncoupled BMUs (Andreasen et al., 2015, Hinge et al., 2015, Jensen et al., 2015) or a negative (resorptive) modeling drift (Frost, 1969) is perhaps a semantic point. It did not appear that these resorptions represented trabecularization of the cortex created by coalescence of numerous individual BMUs. This pattern of endosteal bone loss did have sufficient time to produce definitive differences in cortical geometry compared with SHAM, although the results did reveal

smaller, weaker bones for GC. Notably, thinning of cortices through increased endocortical bone resorption has been reported in GC-treated rats (Turner et al., 1995). A previous report noted decreased cortical bone volume in GC-treated rabbits (Grardel et al., 1994). For OVX+GC, Liu et al. (2012) reported no significant changes in Ct.Th, whereas Chandler and colleagues (2019) found significantly lower Ct.Ar and Ct.Th.

Endosteal bone apposition induced by PTH administration has been well documented in animal (Mashiba et al., 2001, Hirano et al., 2000, Hirano et al., 1999, Yamane et al., 2017, Zebaze et al., 2017, Vrahnas et al., 2018) and human studies (Ma et al., 2014, Jiang et al., 2003) and it has been suggested that this bone formation may be compensating for the increase in intracortical porosity to limit negative biomechanical effects (Hirano et al., 1999, Burr et al., 2001). We observed extensive endosteal bone formation for PTH, which uniquely had a trabecular-like appearance in 2D and 3D (Figure 4.4. *E,F*). It has been suggested that this may be poorly developed woven bone (Yamane et al., 2017), a tissue type formed in states of high turnover/growth. Previous PTH rabbit studies have demonstrated small decreases in Ma.Ar (Hirano et al., 1999) and increases in Ct.Ar (Mashiba et al., 2001, Hirano et al., 1999, Hirano et al., 2000). Hirano and colleagues (Hirano et al., 1999) also found rabbits treated with PTH increased Tt.Ar, which was associated with periosteal bone formation, whereas several other large animal studies showed that the measure remained unchanged (Mashiba et al., 2001, Burr et al., 2001, Boyce et al., 1996). We observed increased bone formation at both the endosteal and periosteal surfaces for PTH, and although the changes to overall geometry were subtle (perhaps due to the short dosing period), themean values do support a pattern trending towards increased %Ct.Ar and Ct.Th along with decreased %Ma.Ar for PTH.

Our final objective was to contrast trabecular bone differences in the proximal tibia to facilitate contextual comparisons within the literature and compare effects across bone morphotypes. Previous reports are conflicted with respect to the effect of OVX on trabecular bone microarchitecture with one observing changes (Jensen et al., 2014) and two others reporting no change relative to sham-operated controls (Baofeng et al., 2010, Liu et al., 2012). For the former, BV/TV and Tb.N were reduced and Tb.Sp increased in OVX rabbits compared to controls (Jensen et al., 2014) at 27 weeks post OVX. Our OVX results are consistent with this single report of decreased BV/TV driven by loss of trabeculae (reduced Tb.N). GC has been reported to reduce

BV/TV (Baofeng et al., 2010) as well as reduce Tb.Th and Tb.N (Grardel et al., 1994), while OVX+GC rabbits have also been reported to have reduced Tb.N, Tb.Th, Tb.Sp and BV/TV (Baofeng et al., 2010, Liu et al., 2012, Wen et al., 2015). Again, our findings of reduced BV/TV driven by a decline in Tb.N for both glucocorticoid groups are consistent with these previous reports.

Trabecular bone formation induced by PTH administration has been extensively characterized in animal and human studies (Jerome et al., 2001, Jerome et al., 1999, Arita et al., 2004, Brouwers et al., 2009, Reeve et al., 1980, Graeff et al., 2007) although, increases in rabbit trabecular bone have been less consistent. In the lumbar vertebrae of rabbits, PTH at a dose of 10 μg/kg/day for 35 days increased BV/TV and Tb.Th; however, continuing PTH administration for an additional 35 days resulted in no differences in these parameters (Mashiba et al., 2001). Hirano and colleagues (Hirano et al., 1999) also reported no difference in trabecular parameters when rabbits were treated with 40 μg/kg/d for 20 weeks. We observed a pattern of increased BV/TV with associated higher Tb.N in PTH, which is consistent with the early effects reported for rabbit lumbar vertebrae.

This study has several limitations. First, while our group sizes (n = 7) match the scale used in previous characterizations of the rabbit for trabecular bone and cortical geometry/density (Castañeda et al., 2008, Castañeda et al., 2006, Liu et al., 2012, Wen et al., 2015), a great deal of variation was observed for many parameters, including outliers. Given there were no grounds to exclude them, all outliers were retained within our quantitative analyses. These factors ultimately limited our statistical power and certainly contributed to the uncertainty in a number of parameter changes despite considerable fold changes. Caution is thus warranted when determining significance of changes based upon p values alone, particularly where adjustments for multiple tests can make these comparisons occur on a very small scale. Consideration of CIs adds important contextual information, but it must also be recognized that CIs are directly related to α. The necessity of additional tests to calculate adjusted CI and discrepancies detected with the primary statistical tests further highlight the perils of relying strictly on p value for analysis and thus our discussion of results has avoided dichotomization based upon p value and embraced uncertainty. As already noted, sample size limitations were further exacerbated by the lack of labeling in the GC-dosed groups and the low numbers of double-labeled osteons in OVX and SHAM. Second,

for our micro-CT analysis, we employed an imaging resolution (10 μm voxels) that was effective at detecting porosity on the scale of remodeling-related resorption spaces; however, it was insufficient to detect all vascular-level cortical porosity in rabbit bone (Supplemental Figure 4.81). Further, although this approach was effective at detecting resorption spaces, it is not exclusive to them and larger canals that were not actively remodeling as well as some of the porosity associated with endosteal bone formation (particularly evident in the PTH group) contributed to the overall Ct.Po measure. Although the lack of bone formation observed within the GC-dosed groups is consistent with uncoupling within the BMU associated with GC treatment reported by Andreasen and colleagues (2015), the shift towards larger sizes suggests a further disruption of BMU regulation through either a coalescence of resorption spaces (initiation and/or steering) or an increase in the size of individual spaces. Third, turning to our histological measures, a limitation of our measure of Rs.N/Ct.Ar and hence also a.Rm.Cr/Ct.Ar, was the fact that not all large spaces observed in the histological images could be confirmed as actively resorbing at the end of the experiment. This was particularly the case for the OVX groups (OVX and OVX+GC) which had a longer timeframe during which remodeling could be initiated and potentially halted/uncoupled. That said, because of our inclusion of only those spaces with roughly eroded surfaces, no lamellar bone formation, and no calcein labeling, it is a fair assumption that these spaces overwhelmingly represented *recently* active events induced by OVX and/or subsequent dosing. A more refined delineation of pores (i.e., eroded, mixed eroded and formative, formative and quiescent pores) has recently been described (Andreasen et al., 2018) and presents a potential path forward for estimating the relative size/duration of the different phases of the BMU through their relative occurrences in 2D section. Such analysis paired with 3D morphological analysis of BMUs by micro-CT holds great potential for advancing our understanding of BMU spatio-temporal coordination. Expanding analysis beyond pores to the vasculature contained within them also holds great potential (Lafage-Proust et al., 2015) as factors like age and corticosteroids reduce bone perfusion while PTH has been shown to increase it (Prisby, 2019). Finally, a detailed analysis of the biomechanical impacts of increased porosity was beyond the scale of this study. Given the non-random distribution of cortical pores visually apparent across all the groups, a more detailed analysis of the interplay of mechanical axes and regional variation of bone microarchitecture across all envelopes (periosteal, intracortical, and endosteal) is certainly warranted. Any direct

mechanical testing would have to carefully consider the sampling site as this non-random distribution of porosity would certainly impact local bone material properties.

4.6. Conclusion

Our findings indicated that cortical porosity was elevated many fold for all treatments with the caveat that the data were the least robust for GC. Histomorphometric measures supported the hypothesis that remodeling rate was elevated in all groups. For trabecular bone, a pattern of loss was observed for OVX, GC, and OVX+GC groups, while the opposite was observed for PTH. The viability of the OVX model, in particular, adds new evidence to the conflicted literature. Overall, our results are encouraging for the further exploration of the role of cortical bone loss in OP using rabbits and highlight the need to consider both cortical and trabecular changes when looking at systemic bone loss. These rabbit models also have great potential to serve as a platform for more detailed analyses of BMU spatio-temporal coordination and the balance between bone resorption and formation within individual remodeling events, which cumulatively determine skeletal health. In this pursuit, *in vivo* imaging (Pratt et al., 2015, Harrison and Cooper, 2015) will certainly prove illuminating.

4.7. Acknowledgements

This research was funded by the Canadian Institutes of Health Research (Catalyst Grant FRN:151724 to DMLC, TA and AP), the Natural Sciences and Engineering Research Council (Discovery Grant RGPIN-2014-05563 to DMLC) of Canada as well as the Canada Research Chairs program (DMLC). The authors would like to acknowledge the help and support of the University of Saskatchewan Laboratory Animals Service Unit (LASU) which was critical to the success of this project. We would also like to acknowledge the assistance of Dr. Ingrid Pickering and her lab personnel for assistance with the confocal microscopy imaging. Finally, the authors dedicate this work in the memory of the late John G. Clement of the University of Melbourne whose encouragement and friendship over the last decade was instrumental in setting this program of research in motion.

Author's Roles: Study design: KH, BH, AP, JA, TA, PP, and DC. Study conduct: KH, BH, AP, AA, KS, and DC. Data collection: KH, BH, AP, AA, GK, KS, and DC. Data analysis: KH, BH, AA, GK, and DC. Data interpretation: KH, BH, GK, TA, PP, and DC. Drafting manuscript: KH, BH, and DC. Revising manuscript content: KH, BH, AP, JA, AA, GK, TA, KS, PP, and DC. Approving final version of manuscript: KH, BH, AP, JA, AA, GK, TA, KS, PP, and DC. DC takes responsibility for the integrity of the data analysis

4.8. Supplementary Material

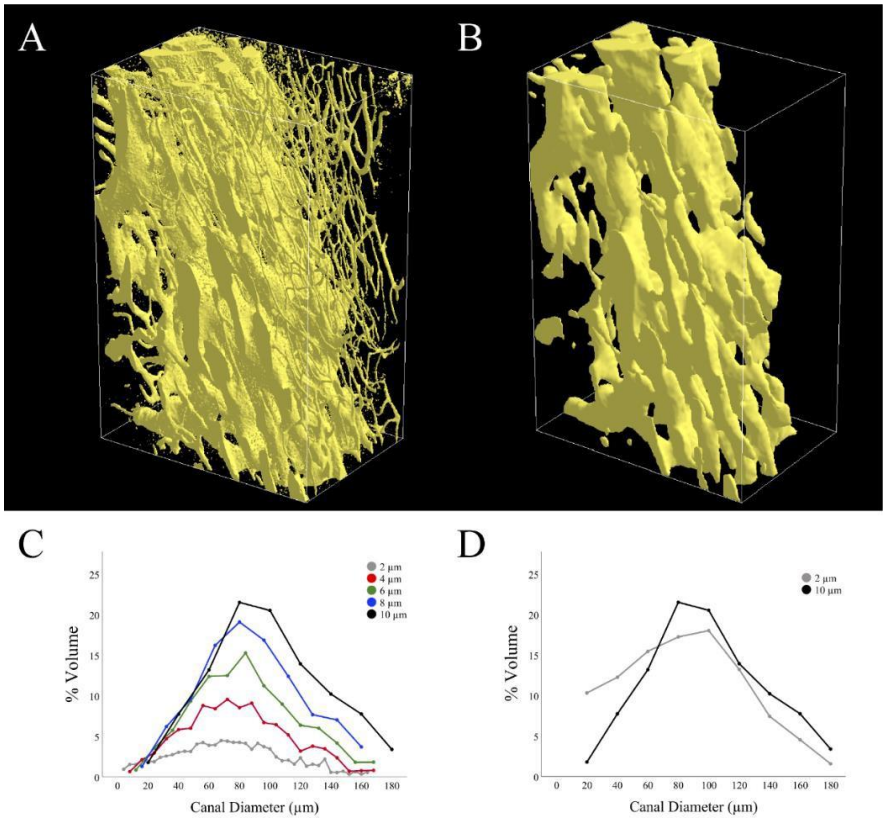

Figure 4.81. Micro-CT Ca.Dm Resolution Dependency. A block of distal tibial cortical bone (1.5 mm x 3.0 mm) from a PTH animal was imaged at 2, 4, 6, 8, and 10 μm voxel using the instrument and protocols described in the materials and methods. 3D renders of a matching volume of interest from the highest (2 μm; A) and lowest resolutions (10 μm; B) are depicted. The size of the bounding boxes around the render is approximately 950 x 1300 x 2250 μm. Below, % volume distributions of Ca.Dm (comparable to Figure 4.3 D) are plotted for all resolutions (C) and for just the highest and lowest resolutions with the former histogram data rescaled to match the latter (D). At 2 μm, there is intermittent detection of osteocyte lacunae as well as detection of quiescent primary and secondary canals whereas at 10 μm only the largest of pores, corresponding to active or recently active remodeling centers, were resolved. The pore size distributions quantitatively reflect what was visible in the 3D renders. As resolution was reduced, there was a loss of smaller pores and thus larger pores increasingly dominated the % volume distributions. Since the higher resolutions have smaller histogram bins (C) the contributions of each of these is relatively smaller, explaining the upward trend in percentages evident. When the histogram bin sizes were rescaled (C) it was clearly apparent that the higher resolution had a larger % contribution of smaller canals than the lower resolution scan. Notably, however, both distributions had a peak at the expected (~100 μm) size of normal rabbit secondary osteon diameter. Our analysis proceeded with the 10 μm voxel size as it afforded good characterization of remodeling-related pores, maximized field of view, minimized data size and, ultimately, exceeded resolutions previously employed to characterize cortical porosity in rabbit bone by micro-CT (see materials and methods).

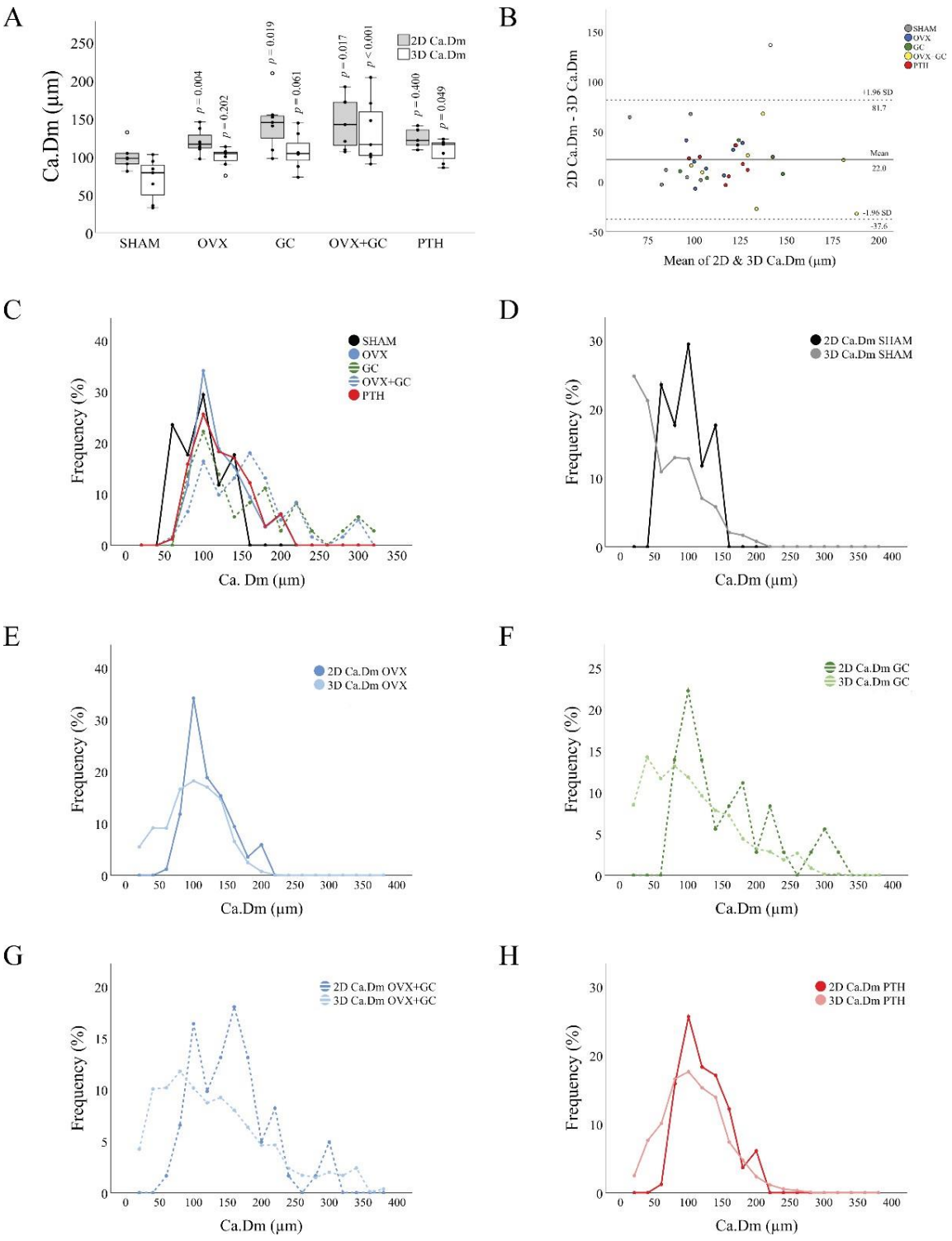

Legend on following page.

Figure 4.82. Validation of Micro-CT Assessment of Ca.Dm. To validate 3D micro-CT based measurements of Ca.Dm, the size (Feret's diameter) of up to 20 resorption cavities from each animal was assessed manually in 2D from the confocal DIC images using ImageJ. Matching the analysis presented in the manuscript, mean 2D Ca.Dm was assessed by ANOVA with post-hoc Bonferroni test to compare groups *vs.* SHAM (Supplementary Table 4.6). *P* values were adjusted to account for multiple comparisons using Bonferroni method (*adj. p* = *p* * 4) and the values reported in panel A reflect *adj. p*. Mean differences (Group - SHAM) and confidence intervals (CI) of the mean differences were calculated using independent *t* tests for normal data and CIs were adjusted for multiple comparisons versus SHAM = 98.75% (1- α ; where α = 0.05/4) (Supplementary Table 4.6). 2D Ca.Dm was elevated from SHAM 1.4 fold for GC (*adj. p* = 0.019) and OVX+GC (*adj. p* = 0.017) and 1.2 fold for PTH (*adj. p* = 0.400) and OVX (*adj. p* = 0.400), with CIs strongly offset from zero for all groups. This result was very similar to that of 3D Ca.Dm with CIs excluding (OVX+GC, *adj. p* < 0.001; and PTH, *adj. p* = 0.049) or strongly offset from zero (GC, *adj. p* = 0.061; and OVX, *adj. p* = 0.202) for all groups. A Bland-Altman plot (panel B) revealed an expected bias between the approaches with the 3D micro-CT measure generating lower values (mean of 22.0, one sample *t* test vs. 0, $p < 0.001$, 95% CI (11.40, 32.65)) due to the inclusion of canals ranging from the maximum diameter of cutting-cones down to the limits of the 10 µm nominal resolution (see Supplemental Figure 4.81.). While different, the two approaches produced moderately correlated results (r = 0.474, $p < 0.005$ overall; r = 0.668, $p < 0.001$ with the exclusion of the outlier evident in B; Pearson's, $p < 0.01$). Superimposed distributions of Ca.Dm from the experimental groups (C) were strikingly similar to the 3D equivalent shown in Figure 3 D. Superimposed distribution plots for the individual groups (panels D-H) clearly demonstrate the similarity of the two techniques with the 3D measure having a larger % volume contribution of smaller canal diameters. As noted for the 3D analysis in the manuscript, peaks at the expected size of 100 µm size of normal rabbit secondary osteons were observed in all groups except for those dosed with GC. These had distributions skewed towards larger canal diameters. Given the similarity between these approaches, despite fundamental differences in what they specifically measure, we have confidence in the validity of the 3D outcomes.

Table 4.6. Validation of Micro-CT Assessment of Ca.Dm

		SHAM	OVX				GC				OVX+GC				PTH			
Parameter	**Overall Test *p***	**Mean ± SD**	**Mean ± SD**	***vs.* SHAM adj. *p***	**Mean Difference (CI)**	**Fold Change**	**Mean ± SD**	***vs.* SHAM adj. *p***	**Mean Difference (CI)**	**Fold Change**	**Mean ± SD**	***vs.* SHAM adj. *p***	**Mean Difference (CI)**	**Fold Change**	**Mean ± SD**	***vs.* SHAM adj. *p***	**Mean Difference (CI)**	**Fold Change**
2D Ca.Dm (µm)	0.022	100.46 ± 17.31	119.61 ± 16.46	0.400	19.15 (-8.80, 47.11)	1.2	143.83 ± 36.25	0.019	43.37 (-5.06, 91.81)	1.4	144.52 ± 34.12	0.017	44.07 (-1.99, 90.12)	1.4	124.40 ± 4.64	0.400	23.95 (-0.56, 48.46)	1.2
3D Ca.Dm (µm)	0.003	70.00 ± 27.40	99.00 ± 12.80	0.202	28.84 (–4.69, 62.37)	1.4	107.00 ± 24.10	0.061	36.41 (-4.09, 76.90)	1.5	133.00 ± 42.30	<0.001	62.59 (6.71, 118.47)	1.9	108.00 ± 14.80	0.049	37.68 (3.12, 72.23)	1.5

Values are reported as mean ± standard deviation. *n*=7. One-way ANOVA with post hoc Bonferroni tests were employed for normal data. *P* values were adjusted (adj.) for multiple comparisons versus SHAM using Bonferroni method (*adj*. $p = p * 4$). Mean differences (Group - SHAM) and confidence intervals (CI) of the mean differences are reported from independent *t* tests for normal data. CIs were adjusted for multiple comparisons versus SHAM = 98.75% (1- α ; where $\alpha = 0.05/4$). Fold changes are reported relative to SHAM (Group/SHAM). Ca.Dm = canal diameter; SHAM = control; OVX = ovariectomy; GC = glucocorticoid; OVX+GC = ovariectomy & glucocorticoid; PTH = parathyroid hormone.

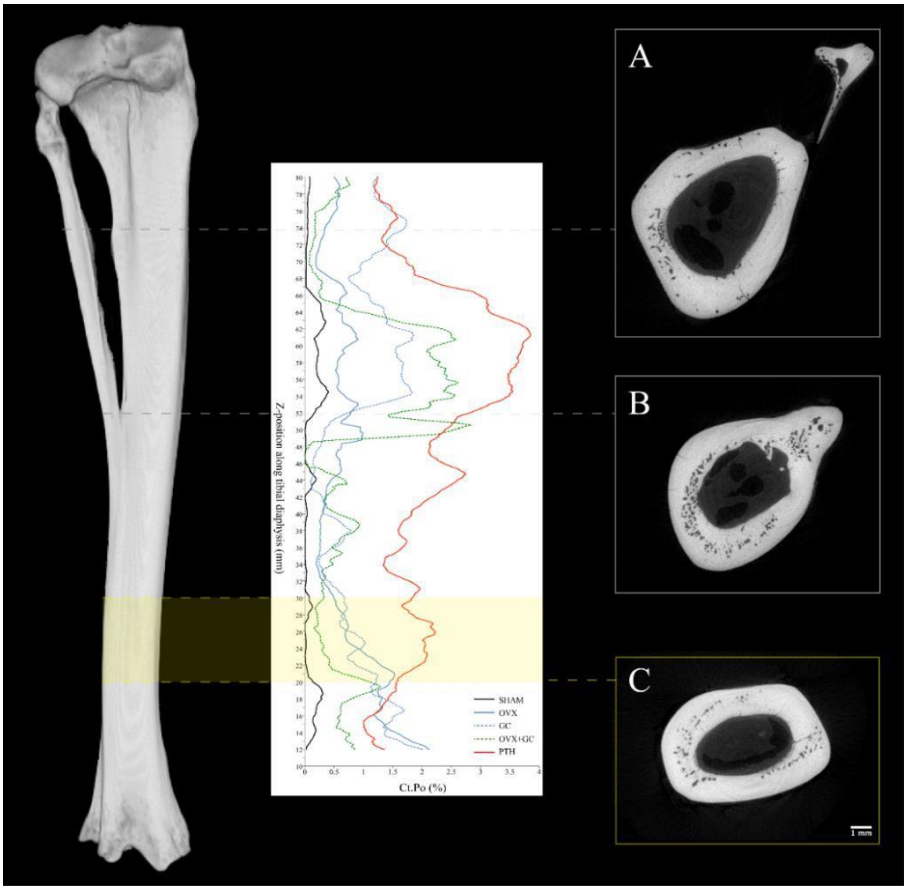

Figure 4.83. Variation in Cortical Porosity Within the Tibial Diaphysis. We explored variation in cortical porosity along the tibial diaphysis in order to select the optimal site for analysis, balancing the goals of suitability for future *in vivo* imaging and maximizing the detection of porosity/remodeling. Left tibiae (contra-lateral to those analyzed in the manuscript) from two animals from each of our experimental groups were imaged along their entire diaphyseal lengths using the 10 µm resolution and protocol previously described in the materials and methods. The tibiae had to be bisected in order to fit into the scanner. The presented results recombine the data with the caveat that some minimal data were lost at the location of the cut, which was placed just distal to the tibio-fibular junction. Mean percent cortical porosity (Ct.Po, %) for the two animals from each group was plotted relative to the position along the diaphysis starting at 1 cm from distal tibial plafond. A 200-slice (2 mm) rolling average was used to reduce noise and better facilitate comparisons across groups. Representative 2D cross-sectional images along the diaphysis are presented for context (*A*-*C*; scale bar = 1 mm). The pattern was similar across groups despite variation in the overall level of Ct.Po. Porosity was lowest in the mid-diaphysis and increased proximally and distally. At the point of the tibio-fibular junction Ct.Po increased markedly and continued to do so proximally before eventually declining towards the proximal epiphysis. Considering suitability for *in vivo* imaging, overall porosity level, and anatomical complexity (e.g., one *vs*. two bones), the distal tibia ultimately presented the best overall target for our analysis. The variation along and within the diaphyses was intriguing and warrants further analysis regarding the factors underpinning it (e.g., mechanical versus developmental).

Chapter 5 Direct Assessment of Cortical Bone Basic Multicellular Unit Longitudinal Erosion Rate: A 4D Synchrotron based Approach

This Chapter culminates the progression of 3D to 4D imaging of BMUs with the first in vivo analysis of BMU LER in the cortical bone of rabbits. This third and final manuscript is under review (submitted Sept 28, 2021) the Journal of Bone and Mineral Research for publication.

Authors

Kim D. Harrison[1], Erika Sales[1], Beverly D. Hiebert[1], Arash Panahifar[2,3], Ning Zhu[2], Terra Arnason[4], Kurtis J. Swekla[5], Peter Pivonka[6], L. Dean Chapman[1], David M.L. Cooper[1*]

Author Information

1. Department of Anatomy, Physiology, and Pharmacology, College of Medicine, University of Saskatchewan, Saskatoon, Saskatchewan, Canada.
2. BioMedical Imaging and Therapy Beamline, Canadian Light Source, Saskatoon, Saskatchewan, Canada.
3. Department of Medical Imaging, College of Medicine, University of Saskatchewan, Saskatoon, Saskatchewan, Canada.
4. Department of Medicine, College of Medicine, University of Saskatchewan, Saskatoon, Saskatchewan, Canada.
5. Animal Care and Research Support Office, Office of the Vice-President of Research, University of Saskatchewan, Saskatoon, Saskatchewan, Canada.
6. School of Mechanical, Medical, and Process Engineering, Queensland University of Technology, Brisbane. Australia.

* Corresponding author, David M. L. Cooper, PhD, Department of Anatomy, Physiology, and Pharmacology, College of Medicine, University of Saskatchewan, Saskatoon, Saskatchewan, Canada. E-mail: dml.cooper@usask.ca

5.1. Abstract

Cortical bone remodeling is driven by Basic Multicellular Units (BMUs) which couple resorption to formation. While fluorochrome labelling has facilitated study of BMU formative parameters since the 1960s, some resorptive parameters, including the Longitudinal Erosion Rate (LER), have remained beyond reach of direct measurement. Indeed, our only insights into this spatio-temporal parameter of BMU behavior come from classical studies which indirectly inferred LER. Here we demonstrate a 4D *in vivo* method to directly measure LER through in-line phase contrast synchrotron imaging. The tibiae of rabbits (n=15) dosed daily with parathyroid hormone were first imaged *in vivo* (synchrotron micro-CT) and then *ex vivo* 14 days later (conventional micro-CT). Mean LER assessed by landmarking the co-registered scans was 23.79 ± 1.83 µm/day. This novel approach holds great promise for the direct study of the spatio-temporal coordination of bone remodeling, its role in diseases such as osteoporosis, as well as related treatments.

5.2. Introduction

Bone is a highly dynamic tissue, continuously altering its microarchitectural properties in response to environmental and mechanical stressors (Burr, 2002). Through the process of remodeling, tissue turnover is carried out by specialized cellular groupings first described as Basic Metabolizing Units (Frost, 1964, Frost, 1966, Johnson, 1964) and later, more commonly referred to as Basic Multicellular Units (Frost, 1969) (Figure 5.1). In cortical bone, localized resorption by the BMU's osteoclastic cutting cone creates a cylindrical tunnel or remodeling space. In classical descriptions, this is followed by a quiescent or reversal zone where resorption has ceased, but formation has yet to start (Parfitt, 1983). Recent studies have revealed this region actually reflects a mixed reversal-resorption phase where osteoprogenitor expansion and osteoclastic radial resorption of the BMU co-occur until, it is postulated, a cellular density threshold of osteoprogenitor cells is reached and formation is initiated by osteoblasts (Delaisse et al., 2020). This final, formative phase of the BMU takes the form of a closing cone, filling the remodeling space with mineralizing osteoid around a contracting central vascular canal. The structuralproducts of remodeling in cortical bone, Haversian systems (synonymous with secondary osteons),permeate and vascularize the mineralized matrix; thus, BMUs are essential for the lifelong maintenance and optimization of bone material properties and microarchitecture.

Under normal conditions, the resorptive activities of the BMU are spatially and temporally ‘coupled’ to its formative activities, and the extent of each is balanced. Bone loss, such as that observed in osteoporosis (OP), occurs when remodeling becomes imbalanced (i.e., resorption outweighing formation) (Li and Wang, 2018, Kenkre and Bassett, 2018) or uncoupled (i.e., arrest within the reversal zone with no subsequent bone formation) (Andersen et al., 2013, Andreasen et al., 2015, Delaisse et al., 2020). In the cortex, net bone loss, summed across a multitude of individual BMUs, is manifested as increased cortical porosity and thinned cortices (Seeman and Delmas, 2006, Yousefzadeh et al., 2020), leading to fragile, brittle bones which are much more susceptible to fracture (Brommage and Ohlsson, 2018, Rochefort, 2014). Of particular concern is that increased porosity inherently creates a larger intracortical surface for further remodeling to occur upon (Bjørnerem et al., 2011). Worldwide hundreds of millions are afflicted with OP, and the costs reach into the billions (Rashki Kemmak and Rezapour, 2020); however, despite the daunting scale of these human and economic impacts, we know relatively little about the spatio-

temporal (3D over time, or 4D) regulation of BMU activity and this deficit is particularly acute for cortical bone. While OP research has traditionally focused on trabecular bone loss (mass and density), the cortex is increasingly understood to be a site of significant bone loss (Bala et al., 2015) and fracture (Bala et al., 2015).

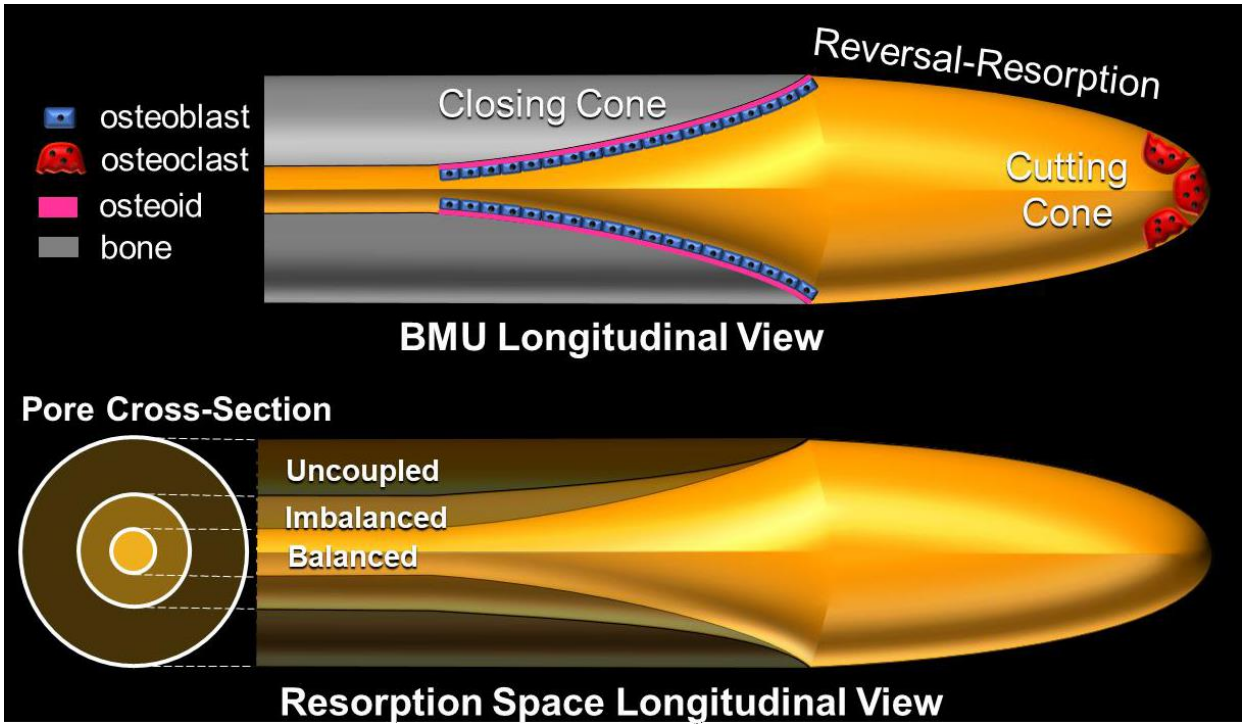

Figure 5.1. BMU morphology and remodeling states. Schematic view of the BMU in cortical bone (top) and its relation to porous structures (remodeling space and persisting vascular canal; orange) in the balanced, imbalanced, and uncoupled states (bottom).

The 4D behavior of BMUs has not been replicated *in vitro* and has never been directly observed *in vivo*. Consequently, what we currently know about coordination of cortical remodeling is derived from relatively few 3D serial/sequential sectioning studies of both trabecular and cortical bone (Cohen and Harris, 1958, Tappen, 1977, Robling and Stout, 1999, Stout et al., 1999, Andersen et al., 2013, Andersen et al., 2009, Andreasen et al., 2018, Andreasen et al., 2015, Lassen et al., 2017) which generate data that are inherently static in nature. Dynamic insight into BMU formative activities via fluorochrome (e.g., tetracycline) labeling was pioneered over 50 years ago by Frost, one of the most influential researchers to shape the field of skeletal biology (Turner et al., 2004). Over his illustrious career, Frost's contributions were unequivocal, and perhaps his most influential work was defining the BMU as a unified, regulatory intermediary unit (between the

level of cell and tissue) that dictates the coupling of bone resorption with formation. While the formative activities of the BMU could be tracked over time using Frost's innovative approach—including in 3D when combined with serial sectioning (Mohsin et al., 2002)—a similar assessment of the resorptive phase could not. A key example, and focus of the current study, is the Longitudinal Erosion Rate (LER)—the rate of advance of the BMU cutting cone over time. To date, LER has only ever been *inferred* in a few species (Figure 5.2), yielding measurements ranging from ~20-44 µm/day (Figure 5.2, Table 5.1).

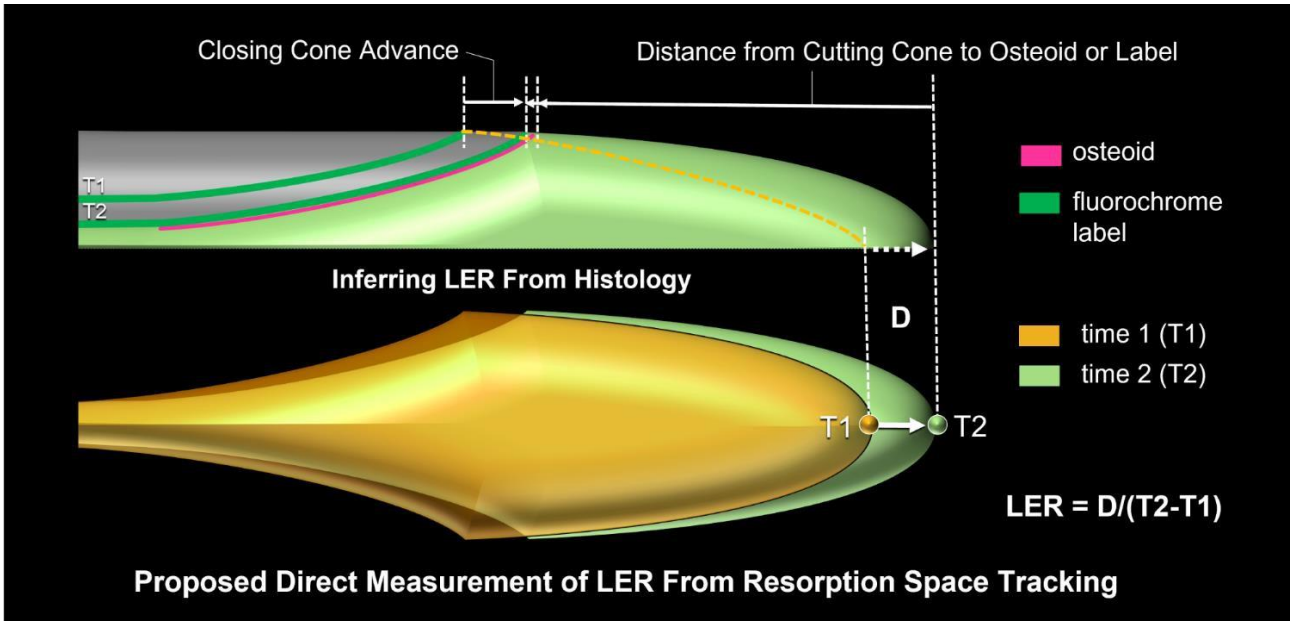

Figure 5.2. Assessment of BMU LER in cortical bone. Classical *indirect* method for inferring BMU LER from fluorochrome labeling of the closing cone (top) and the novel proposed *direct* method of measuring advancement of the cutting cone using *in-vivo* imaging and image registration (bottom).

Table 5.1. Summary of Classical Studies of LER

Publication	Species	Element	LER (μm/day)	Age	Sex	N
Jaworski & Lok, 1972	Dog	rib	39.2 ± 14	1 year	male	3
Jaworski et al., 1975	dog (*uremic*)	rib	27.97 ± 0.8	1 year	male	3
Jaworski et al., 1975	Dog	rib	43.61 ± 0.66	1 year	male	3
Takahashi et al., 1976	Dog	rib	40.8 ± 15.0	adult	male	5
Takahashi et al., 1976	Dog	humerus	34.9 ± 13.3	adult	male	5
Takahashi et al., 1976	Dog	radius	34.7 ± 13.5	adult	male	5
Takahashi et al., 1976	Dog	ulna	32.9 ± 11.7	adult	male	5
Takahashi et al., 1976	Dog	femur	39.2 ± 13.5	adult	male	5
Takahashi et al., 1976	Dog	tibia	37.0 ± 13.2	adult	male	5
Takahashi et al., 1976	Dog	fibula	42.6 ± 26.0	adult	male	5
Parfitt, A. M., 1983*	monkey	rib	36.7	N/A	N/A	N/A
Parfitt, A. M., 1983**	human	rib	27.0	N/A	N/A	N/A

** Unpublished data from Oliver and Crouch*

*** Human LER calculated based on the assumption that cortical remodeling between humans and monkeys is similar and thus, measures such as radial erosion rate are interchangeable between species (Parfitt, 1983).*

Jaworski and Lok (1972), for example, relied upon the assumption of a constant distance from the tip of the cutting cone back to fluorochrome labels or the osteoid seam for their LER measures, while Takahashi and Norimatsu (1976) inferred LER from the advance of the closing cone, assuming it was synchronized with the cutting cone advance. After decades, those pioneering studies remain our only assessments of LER, with the value of ~40 μm/day all but treated as a constant across skeletal elements, species, and disease states (Table 5.1). Indeed, many *in silico* studies use this value for analyzing different aspects of BMU behavior. For example, Buenzli et al. (2011) used LER of 40 μm/day to investigate the spatio-temporal distribution of osteoclastic and osteoblastic cell populations in the BMU at different maturation stages. They found that the precursor cells in the reversal zone play a crucial role in separating the cutting cone and closing cone. Furthermore, their model predicted that perturbing the biochemical environment in the BMU may lead to imbalanced remodeling which has been subsequently confirmed experimentally (see discussion above). A follow up study by Buenzli et al. (2012) looked at *in silico* modeling of

individual osteoclastic resorption events in cortical bone which shape the BMU cutting cone. For that study, the rate of blood vessel growth in the BMU, which produces osteoclastic precursor cells, was assumed 40 μm/day which led to a LER of similar magnitude. A study by Ryser et al. (2010) looked at removal of microcracks by BMUs and the potential of a single BMU to change its path in order to target microcracks/bone matrix damage. The latter work used a LER of 40 μm/day.

Treating LER as a constant is highly problematic as: 1. the original data from canines showed a great deal of variation undermining the very assumptions they were based upon(Jaworski and Lok, 1972, Takahashi and Norimatsu, 1976); 2. synchronicity of the phases of the BMU cannot be taken as a given—particularly in light of recent concepts focused on the role of uncoupling in bone loss; and 3. even the classical evidence suggested LER could vary in disease states such as uremia where it was depressed in afflicted vs. normal dogs (Jaworski et al., 1975). Moreover, the extremely limited data available for humans appears to suggest lower LER values relative to other species (*unpublished data*—(Parfitt, 1983)). Given all the problematic assumptionsin these classical studies and the enduring gaps in our knowledge, the larger significance of LER in BMU remodeling and consequently disease such as OP remains unclear. It remains an open question whether LER could play a role in BMU coupling. For example, is uncoupling associatedwith the faster advance of the closing cone resulting in a larger reversal-resorption zone and decreased time for the critical threshold of osteoprogenitors to be reached (Lassen et al., 2017, Delaisse et al., 2020)? Might the converse be true with a lower LER improving coupling and overall balance of BMU activity? Could modulation of LER present a new avenue for interventionsaimed at preventing or reversing bone loss? These questions have remained unanswered as we lacka direct means to assess LER *in vivo*.

Around the turn of the millennium, X-ray micro-computed tomography (micro-CT) underwent rapid development, seeing use first *ex vivo* and soon after *in vivo* for trabecular bone imaging and structural analysis. The latter has included longitudinally tracking changes at the level of individual trabeculae over time (David et al., 2003, Waarsing et al., 2004). While the translation of this technology to cortical bone porosity occurred relatively early (Cooper et al., 2003), the translation to *in vivo* cortical porosity imaging has been relatively rare (Altman et al., 2015, Li et al., 2015), being impeded by the need for higher resolution and, concomitantly, higher radiation

dose. Indeed, repetitive *in vivo* trabecular bone protocols with typical image resolutions of 9 - 18 µm (Bott et al., 2020, Longo et al., 2017, Willie et al., 2013) and radiation doses in the range of 0.5-1 Gy are known to cause adverse effects, such as reduced bone volume fraction in the tibiae of mice (Klinck et al., 2008, Laperre et al., 2011, Bott et al., 2020, Willie et al., 2013). *In vivo* synchrotron radiation (SR) scans of 13-week-old mice knees at a dose of 5 Gy have also reported adverse effects on trabecular bone (Matsumoto et al., 2011).

In X-ray tomography, resolution is inversely proportional to radiation dose, and the relationship is not linear—doubling resolution involves 16 times the dose if image quality is to be maintained (Ford et al., 2003), and multiple scans further exacerbate this over time (Oliviero et al., 2019). Thus, while micro-CT is certainly capable of resolving cortical bone porosity in pre-clinical animal models, including BMU-related remodeling spaces, *in vivo* tracking of these spaces has not been achieved. A potential solution to circumvent the punishing relationship between resolution and dose is through X-ray phase contrast SR micro-CT (Zhou and Brahme, 2008). In conventional X-ray imaging, the contrast mechanism is absorption of X-rays by tissue, which equates directly to dose. Exploiting the phase contrast created by the refraction and/or scattering of X-rays rather than absorption within a target creates the opportunity for improved contrast at equivalent or even potentially lower doses. This principle works particularly well for imaging cortical bone porosity with SR micro-CT, where there is a significant difference in the refractive indices between bone and the soft tissue within its pores (Pratt et al., 2015, Harrison et al., 2020).

Here our primary objective was to deploy this advanced imaging approach to directly track the LER of cortical BMUs *in vivo* for the first time. To achieve this, we developed a novel approach at the BioMedical Imaging and Therapy (BMIT) facility of the Canadian Light Source (CLS) synchrotron focused on the rabbit model—the smallest laboratory animal with cortical bone remodeling similar to humans (Pazzaglia et al., 2007, Pazzaglia et al., 2009, Pazzaglia et al., 2010, Harrison et al., 2020). Secondarily, we explored the potential impact of varied radiation dose (1, 2.5 and 5 Gy) on LER based upon the range of values reported in the literature.

5.3. Methods

5.31. Animals

Fifteen skeletally mature, 6-month-old (3.7-3.9 kg) female New Zealand White rabbits were acquired from Charles River Laboratories (Quebec, Canada). Animals were housed individually in stainless steel rabbit racks in the University of Saskatchewan's Health Sciences Laboratory Animal Services Unit, a Canadian Council on Animal Care (CCAC) accredited facility. A computerized system-controlled room temperature and humidity, and the light cycle was maintained at 12:12 (12 hours dark and 12 hours of light). Standard rabbit chow, alfalfa cubes, and reverse osmosis water via an automated watering system were provided *ad libitum*. Animals were acclimatized for a minimum of 7 days before any experimental procedures commenced. The University of Saskatchewan's Animal Care Committee approved all animal work and adhered to the CCAC guidelines for humane animal use.

5.32. PTH rabbit model of elevated remodeling

While rabbits do exhibit spontaneous cortical bone remodeling, the rate of remodeling or activation frequency (Ac.f—birth rate of new BMUs (#/mm^2/year)) is low; thus, we sought to increase the number of BMUs available for LER analysis through daily dosing with human parathyroid hormone (PTH) 1-34 (Alfa Aesar, Ward Hill, MA, USA), a known elevator of cortical remodeling/porosity within rabbits (Yamane et al., 2017, Hirano et al., 2000, Hirano et al., 1999, Zebaze et al., 2017, Harrison et al., 2020). The intermittent PTH rabbit model used in this study has been described previously (Harrison et al., 2020). Briefly, each rabbit received a daily dose (via subcutaneous injection) of human PTH (1-34) at a concentration of 30 µg/kg/day for 28 days. Animals were monitored daily at the time of injection, as well as weekly to assess weight. Weights were taken once before dosing commenced (week 0) and once weekly thereafter until the last weight (week 4). Imaging (see below) was performed *in vivo* on day 14. After the dosing period was complete (day 28), animals were euthanized by intravenous injection of pentobarbital sodium (Euthanyl; Bimeda-MTC, Animal Health Inc, Cambridge, ON, Canada) at a dose of 0.4 ml/kg. Post-euthanasia, the right and left tibiae were removed, dissected of soft tissue, and fixed in 10% formalin ahead of *ex vivo* laboratory micro-CT imaging.

5.33. *In vivo* SR micro-CT imaging protocol

All *in vivo* scans were acquired on the BMIT 05ID-2 beamline at the CLS synchrotron (Saskatoon, SK, Canada). Rabbits were anesthetized before imaging according to an established protocol using a trans-nasal delivery of a sedative and anesthetic cocktail (Dexmedetomidine (0.1 mg/kg), Midazolam (2.0 mg/kg), and Torbugesic (0.4 mg/kg)) and supported during imaging via inhaled isoflurane gas (Santangelo et al., 2016). During scanning, the rabbits were restrained in a custom holder adapted from a design by Voor and colleagues (2008). An indirect X-ray detector system comprised of a C11440-22CU Orca Flash 4.0 camera paired with an AA60 beam monitor (Hamamatsu, Japan) and LuAG:Ce 200 µm thick scintillator was used to achieve an effective pixel size of 13.05 µm at sample location. Source-to-sample distance was 58 m and sample-to-detector distance was 60 cm. The monochromatic X-ray beam, produced by a superconducting wiggler operated at 2.5 T, passed through a 3.3 mm of Al filter, and set at 37.5 keV energy. Potential radiation dose effects were assessed by dividing animals into 3 groups of 5: each imaged at approximately 1, 2.5, and 5 Gy. These doses were chosen based upon preliminary experiments with rats where we employed 2-3 Gy dose with no apparent short-term radiation-induced side effects and the dose of 5 Gy being previously reported in the literature for *in vivo* (trabecular) bone imaging at a synchrotron (Matsumoto et al., 2011). The higher doses of 2.5 and 5 Gy were achieved by collecting 1500 projections (as opposed to 1000 for the 1 Gy group) at a slower rotation speed over 180 degrees. Furthermore, if needed, dose rate was reduced by filtering beam with neutral density Lucite filters of various thicknesses. The dose rate was measured in air at the beam entrance into the experimental hutch in real time using a PinPoint ion chamber (model 31014, PTW, Germany). Then, dose rate at the animal location was calculated and experimentally confirmed, considering the environmental conditions, thickness of the animal leg holder (Lucite), attenuation in air, and the distance between the ion chamber and animal. Rotation speed required to achieve the desired incident surface dose was calculated factoring in the dose rate (Gy/s) at animal location and the number of projections. The estimated imaging doses were confirmed experimentally through Thermoluminescent dosimeter (TLD) chips (Mirion Technologies, Ontario, Canada). Each TLD chip was first secured onto the holder and subsequently placed at the mid-field of view (FOV) corresponding to the location of the *in vivo* scans. Fifteen chips (five/dose group) were imaged, *in vivo*, with the full *in vivo* protocol (including the initial vertical scout scan, described

below) and revealed an average radiation dose of 0.9, 2.4 and 5.4 Gy for the Low, Medium, and High groups, respectively.

The FOV was approximately 1 cm high and 2.6 cm wide, which readily encompassed the width of the distal tibia. A vertical scout scan (~ 8 cm) of the tibial diaphysis was taken before the rotational scan to locate the anatomical landmark, the plafond, from which the stage would be raised 2 cm to demark the start position of the *in vivo* scan. Vertical scout scans ensured consistent identification of the FOV of cortical bone within individual rabbits for subsequent *ex vivo* scans, but also among all the rabbits. The dose imparted during scout scans was included in final calculation of radiation dose. Post imaging, the rabbits were injected intramuscularly with the anesthetic reversal drugs Atipamezole (1 mg/kg) and Flumazenil (0.02 mg/kg) and monitored in a warmed recovery cage till fully recovered. For the two weeks post *in vivo* imaging, rabbits were monitored daily for indications of radiation sickness through visual inspection of both the imaging site (i.e., skin burns, hair loss) and overall health (i.e., loss of appetite, behavioral changes, grooming changes, defecation quality and consistency).

5.34. *Ex vivo* micro-CT imaging protocol

Post euthanasia, both the previously imaged right and contralateral control left tibiae from each rabbit were removed and dissected of soft tissue. To facilitate scan co-registration, the FOV of the right tibia scanned *in vivo* was identified on the same bone, *ex vivo*, with a single (2 cm) and double (3 cm) cut mark proximal to the plafond to denote the bottom and top of the FOV, respectively. *Ex vivo* scans were collected with a SkyScan 1172 desktop micro-CT scanner (Bruker, Belgium). The FOV between the cut marks was imaged at 74 kVp 133 µA with an exposure time of 460 ms, 0.2˚ rotation step, 4-frame averaging, Al 0.5 mm filter, and voxel size of 5 µm. The projectional data were reconstructed using the NRecon software package (Bruker, Belgium), and the data were subsequently binned (2 x 2) to 10 µm using the software package Tconvert (Bruker, Belgium) to reduce the size of the dataset and thereby facilitate scan co-registration in the imaging software package AMIRA (version 6.4 - https://www.thermofisher.com/amira-avizo).

5.35. Scan co-registration and LER measurement

Scan co-registration and BMU LER measurement were performed using AMIRA (version 2020.2). The *in vivo* SR micro-CT and *ex vivo* micro-CT scans of the right tibia for each rabbit were rendered in 3D (Figure 5.3 – left), and the BMU-related resorption spaces and vascular canals were segmented using a global threshold (Figure 5.3 – center). After segmentation, the 3D volume render of the *in vivo* SR micro-CT scan was manually aligned (translated and rotated) within the single and double-cut marks of the 3D volume rendering of the *ex vivo* micro-CT scan and further automatically co-registered via rigid and iso-scale transformation using the correlation metric implemented in AMIRA. The segmented porosity was then visually inspected to verify the fit of the co-registration between the two datasets. Surface renders of the cutting cones of an individual BMU were then manually landmarked (Figure 5.3 – right; a2), yielding 3D coordinates: X1, Y1, Z1 (*in vivo*) and X2, Y2, Z2 (*ex vivo*). LER (µm/day) was calculated as D/T2-T1, where D $=\sqrt{(X2-X1)^2+(Y2-Y1)^2+(Z2-Z1)^2}$ and denotes the distance of the cutting cones (in µm) and T2-T1 denotes the time between the two scans (i.e., 14 days) (Figure 5.3 – right; a2). In three of the 15 scan sets, regions of extensive PTH induced clustered porosity caused co-registration failure. A total 12 scan sets were successfully co-registered (n = 4/dose group) by the same operator and repeated five times in order to calculate intra-observer error. Five translation and rotation parameters were obtained, and for every scan pair, the difference between them was calculated, and the difference vector length was obtained separately. The average and standard deviation were calculated for the difference between repeats by the same operator. The transformation parameters from all registrations were analyzed by calculating the mean and SD of the translation distances (*X2-X1*, *Y2-Y1*, *Z2-Z1*) and the rotation angle between *in vivo* and *ex vivo* datasets. Reproducibility tests indicated a mean translation distance of 47 µm which suggests an error of ~3 µm/day over the 14-day period between scans. The mean rotation error of 1.7° can be attributed to initial manual adjustment of the two scan datasets before automated co-registration.

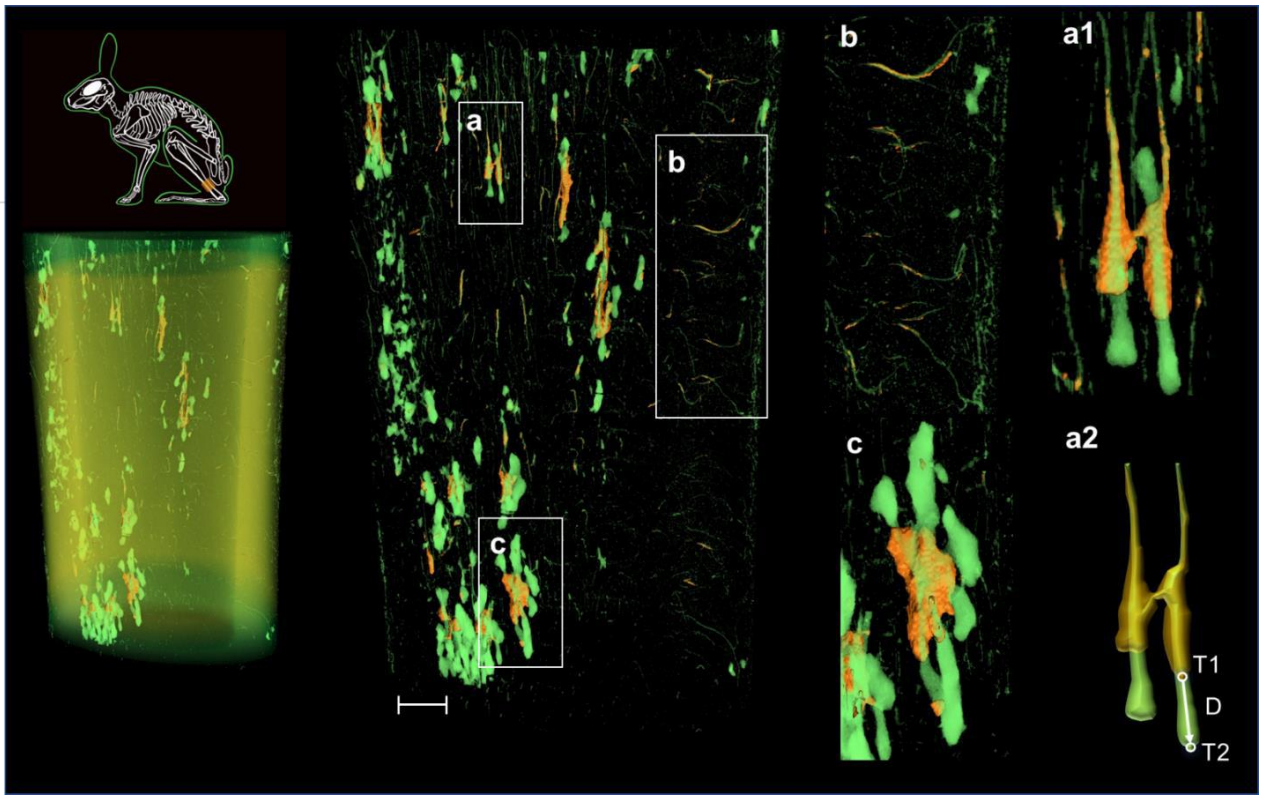

Figure 5.3. LER assessment based on SR micro-CT and Micro-CT co-registered scans. Top Left: Rabbit skeletal schematic displaying region of the distal tibia scanned (transparent, orange square). Bottom Left: The *in vivo* SR micro-CT scan (solid, orange render) at time 1 (T1, day 14) is co-registered within the *ex vivo* micro-CT scan (translucent, green render) from time 2 (T2, day 28). Centre: Cortical porosity rendered alone revealing (a) classically shaped BMU-related resorption spaces, (b) unchanged vascular canals, and (c) complex irregular BMU-related resorption spaces. Right: Zoomed in views (a1, b, c) from central panel and (a2) a schematic depiction of the direct method of LER assessment where LER = D/$_{T2-T1}$. Scale bar = 1 mm.

5.36. Cortical porosity and geometry measurement

Assessment of potential *in vivo* radiation-related impacts on cortical bone remodeling was performed on the corresponding 1 cm FOV region of the distal diaphysis in the imaging software package CTAnalyser (CTAn) (version 1.16.4.1; Bruker, Belgium). The FOV was binarized using a standard global threshold to measure 3D (cortical porosity (Ct.Po, %), canal diameter (Ca.Dm, µm,) and cortical thickness (Ct.Th, µm)) parameters. In correspondence with a previous study by our group (Harrison et al., 2020), a single, mid-point slice of the 1 cm region of bone was selected to analyze the 2D (total area (Tt.Ar, mm^2), cortical area (Ct.Ar, mm^2), and marrow area (Ma.Ar,

mm^2)) geometric parameters. This same process was also carried out on the left tibia of each rabbit to serve as an internal, non-irradiated contralateral control.

5.37. Statistical Analysis

Statistical analyses were performed with SPSS version 26.0 (IBM, New York). All measures were tested for normality by Shapiro-Wilk tests. One-way ANOVA ($\alpha = 0.05$), and when significant, post-hoc Bonferroni test between dose groups were used to assess LER for normally distributed data. Comparison of week 0 and week 4 weights were normally distributed and compared with paired t-test ($\alpha = 0.05$). Comparison of weight amongst the three dose groups over the PTH dosing period (4 weeks) was not normally distributed and thus assessed with the nonparametric Friedman test ($\alpha = 0.05$). Within animal comparisons of tibiae categorized by scan type (right *in vivo* SR micro-CT versus right *ex vivo* micro-CT and right *ex vivo* micro-CT versus control left *ex vivo* micro-CT) were carried out through repeated measures ANOVA ($\alpha = 0.05$). When significant, post-hoc Bonferroni tests between dose groups were used for normally distributed data. For parameters where at least one dose group was non-normal, the nonparametric Wilcoxon signed-rank test ($\alpha = 0.05$) manually categorized for each dose group, was used.

5.4. Results

5.41. Scans co-registration and LER assessment

Remodeling rates were successfully elevated. Intracortical porosity and endosteal formation were increased within the tibiae of the rabbits (Figure 5.3). Co-registration of the datasets in general revealed excellent matches between the scans (Figure 5.3), with close agreement between unchanged vascular canals and the paths of BMUs being trackable in many cases. The extent of remodeling varied with high complexity which complicated co-registration for many of the scan sets. LER was assessed for 186 BMUs from the 12 successfully co-registered tibia scan sets (4/group, ~ 12.4 BMUs/rabbit), and results are summarized in Table 5.2 and Figure 5.4. One rabbit from each dose group was excluded from the LER assessment due to co-registration errors. There were no differences in LER between any of the dose groups, and thus pooled LER was calculated to be 23.8 ± 1.83 μm/day.

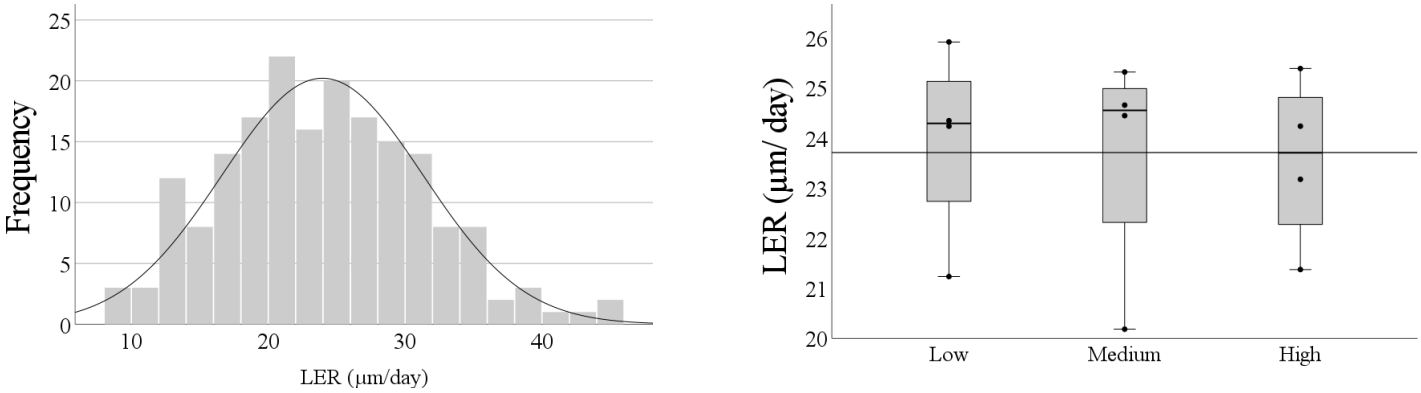

Figure 5.4. Direct assessment of BMU LER across dose groups. Individual LER measurements pooled across animals and groups (*n*=186) were normally distributed (left) and LER data by group (right) are presented by box plots with individual rabbits plotted as solid circles (*n* = 4/group). One-way ANOVA revealed no differences between radiation dose groups (α = 0.05).

Table 5.2. Direct calculation of BMU Longitudinal Erosion Rate for varied radiation dose (1, 2.5 and 5 Gy).

				Low Dose (1 Gy)	Medium Dose (2.5 Gy)	High Dose (5 Gy)
Parameter	**Overall Test *p***	**F value**	**df**	**Mean ± SD**	**Mean ± SD**	**Mean ± SD**
LER (µm/day)	0.961	0.040	2	23.93 ± 1.96	23.65 ± 2.34	23.54 ± 1.70

Assessment of BMU LER across dose groups (Low Dose, Medium Dose, and High Dose). *n* = 12. Pooled LER is reported as mean ± standard deviation. One-way ANOVA was employed. Significance level for the overall test was α = 0.05. F values and Degrees of Freedom (df) are reported.

5.42. Right Tibiae: *in vivo* versus *ex vivo* scans

Comparisons between the *in vivo* (day 14) and *ex vivo* (day 28) scans of the right tibiae reflected changes within the animals over time, as well as potential differences due to varied scan parameters (SR micro-CT versus micro-CT). Measurements of cortical porosity and geometry are summarized in Table 5.3 and Figure 5.5. Overall, variation between animals was considerable, as reflected by the numerous outliers in the boxplots (Figure 5.5). The only consistently significant difference observed across all dose groups was a decline in Ma.Ar at day 28, associated with increased Ct.Th in the Low (p = 0.043) and High (p = 0.043) dose groups. A trend towards

increased Ct.Po at day 28 was observed, but a significant difference was only observed for the High dose group ($p = 0.043$).

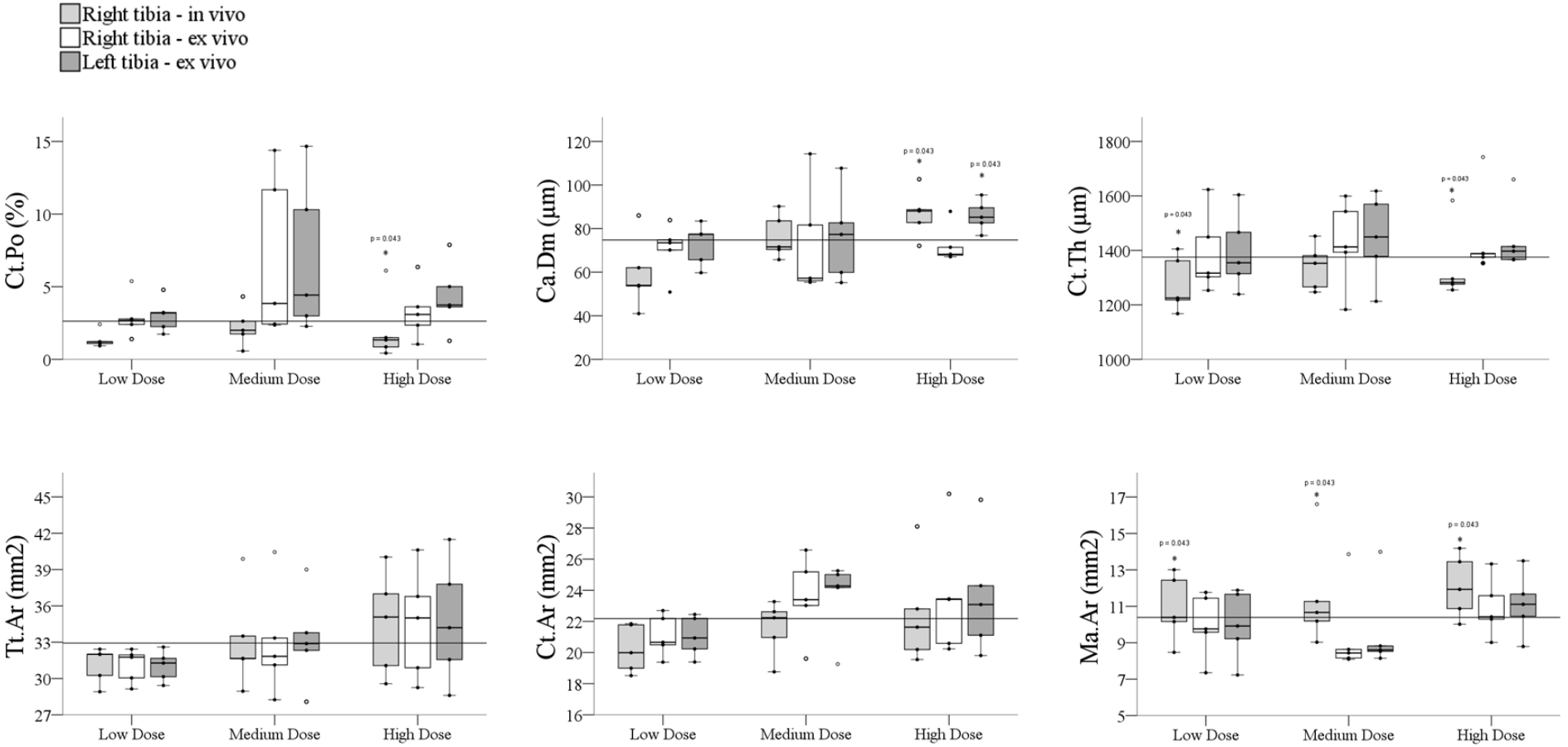

Figure 5.5. Comparison of parameters between the irradiated *in vivo* (SR micro-CT) and *ex vivo* (micro-CT) scans of the right tibiae and the irradiated (right micro-CT) and non-irradiated (left micro-CT) control tibiae. Data are presented by boxplots (light grey – R. *in vivo*, white – R. *ex vivo*, & dark grey – L. *ex vivo*) with individual rabbits plotted as solid circles and outliers plotted as open circles. $n = 5$. Repeated measures ANOVA with post-hoc Bonferroni tests were employed for normal data. Significance level for overall tests (normal data) and p values (non-normal) was $\alpha = 0.05$. Wilcoxon signed-rank test manually categorized by dose was employed for non-normal data. *Indicates $p < 0.05$ vs. irradiated (right) *ex vivo* micro-CT scan. 3D measures (top row): Ct.Po = cortical porosity; Ca.Dm = canal diameter; and Ct.Th = cortical thickness. 2D measures (bottom row) Tt.Ar = total area; Ct.Ar = cortical area; and Ma.Ar = marrow area.

Table 5.3. Right tibia micro-CT data: comparison of *in vivo* vs. *ex vivo* scans

				Right *in vivo* versus Right *ex vivo*											
				Low Dose				Medium Dose				High Dose			
Parameter	**Overall Test *p***	**F value**	**df**	***p***	**Z value**	**Mean ±SD (Median)**		***p***	**Z value**	**Mean ± SD (Median)**		***p***	**Z value**	**Mean ± SD (Median)**	
						R. *in vivo*	**R. *ex vivo***			**R. *in vivo***	**R. *ex vivo***			**R. *in vivo***	**R. *ex vivo***
Ct.Po (%)	**ND**	ND	ND	**0.080**	1.75	1.37 ± 0.71 (1.20)	2.93 ± 1.60 (2.68)	**0.080**	1.75	2.26 ± 0.71 (2.00)	6.94 ± 1.60 (3.85)	**0.043***	2.02	2.05 ± 0.71 (1.34)	3.29 ± 1.60 (3.09)
Ca.Dm (µm)	**ND**	ND	ND	**0.345**	-0.94	59.34 ± 16.71 (53.96)	70.65 ± 12.15 (73.52)	**0.500**	0.64	76.31 ± 25.62 (71.59)	72.94 ± 10.17 (57.23)	**0.043***	2.02	86.87 ± 11.07 (88.09)	72.49 ± 8.78 (68.21)
Ct.Th (µm)	**ND**	ND	ND	**0.043***	2.02	1257.70 ± 102.12 (1225.24)	1389.13 ± 149.67 (1316.81)	**0.138**	-1.48	1339.81 ± 84.51 (1352.83)	1426.34 ± 161.32 (1412.85)	**0.043***	2.02	1338.43 ± 137.72 (1282.33)	1449.65 ± 164.37 (1387.88)
Tt.Ar (mm^2)	**0.464**	0.57	1	**ND**	ND	31.12 ± 1.49	31.07 ± 1.40	**ND**	ND	33.13 ± 4.11	33.00 ± 4.56	**ND**	ND	34.55 ± 4.28	34.51 ± 4.57
Ct.Ar (mm^2)	**<0.001***	36.86	1	**0.807**	ND	20.23 ± 1.55	21.09 ± 1.34	**0.100**	ND	21.56 ± 1.78	23.56 ± 2.63	**0.533**	ND	22.46 ± 3.40	23.58 ± 4.00
Ma.Ar (mm^2)	**ND**	ND	ND	**0.043***	2.02	10.89 ± 1.84 (10.39)	9.98 ± 1.76 (9.76)	**0.043***	2.02	11.55 ± 2.94 (10.66)	9.44 ± 2.48 (8.44)	**0.043***	2.02	12.09 ± 1.73 (11.93)	10.93 ± 1.62 (10.42)

Bone parameters compared between the *in vivo* SR micro-CT (day 14) and *ex vivo* micro-CT (day 28) scan data for the irradiated (right) tibiae/dose group (n = 5). Values are reported as mean ± standard deviation. Median values are also reported for those parameters where at least one dose group was not normally distributed. Repeated measures ANOVA with post-hoc Bonferroni tests were employed for normal data. Wilcoxon signed-rank test manually categorized by dose were employed for non-normal data. Significance level for overall tests (normal data) and p values (non-normal data) was $\alpha = 0.05$. For nonparametric tests, no overall p test is reported (ND = no data) as pairwise comparisons were manually categorized by dose group. F values and Degrees of Freedom (df) are reported for repeated measures ANOVA whereas Z values are reported for Wilcoxon signed-rank tests. For ANOVA, post hoc tests are not reported for non-significant overall p values (ND = no data). For Wilcoxon signed-rank tests, no overall p test is reported (ND = no data) as pairwise comparisons were manually categorized by dose group. Ct.Po = cortical porosity, Ca.Dm = canal diameter, and Ct.Th = cortical thickness. 2D measures (bottom row) Tt.Ar = total area, Ct.Ar = cortical area, and Ma.Ar = marrow area.

5.43. Right versus Left Tibiae: *ex vivo* scans

Comparisons between the *ex vivo* scans reflected potential differences between the limbs of the same animals due to irradiation of the right versus non-irradiated contralateral control when scanned with identical protocols (micro-CT) at the same time (day 28) (Figure 5.6). Measurements of the 3D and 2D parameters are summarized in Table 5.4 and Figure 5.5. Again, a great deal of variation was observed, with many outliers apparent in the box plots (Figure 5.5) and few, if any, clear patterns emerged. The only difference observed was lower Ca.Dm (p = 0.043) in the irradiated limbs of the High dose group.

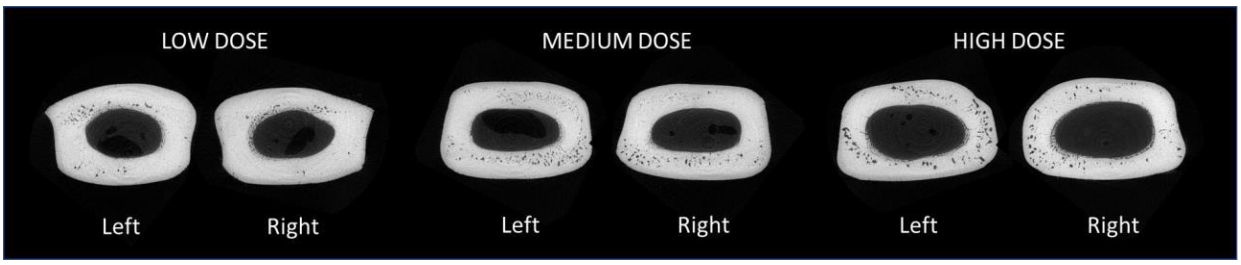

Figure 5.6. Comparison of *ex vivo* micro-CT scans. Two-dimensional micro-CT cross-sectional images of irradiated right and non-irradiated, contralateral control left tibiae at endpoint, representative of the cortical porosity observed among the rabbits imaged at the low (1 Gy), medium (2.5 Gy), and high (5 Gy) radiation dose.

Table 5.4. Right versus Left Tibiae: *ex vivo* scans

				Right *ex vivo* versus Left *ex vivo*											
				Low Dose				Medium Dose				High Dose			
Parameter	**Overall Test *p***	**F value**	**df**	***p***	**Z value**	**Mean ± SD (Median)**		***p***	**Z value**	**Mean ± SD (Median)**		***p***	**Z value**	**Mean ± SD (Median)**	
						R. *ex vivo*	**L. *ex vivo***			**R. *ex vivo***	**L. *ex vivo***			**R. *ex vivo***	**L. *ex vivo***
Ct.Po (%)	**0.212**	1.74	1	**ND**	ND	2.93 ± 1.48	3.04 ± 1.16	**ND**	ND	6.94 ± 5.67	6.93 ± 5.35	**ND**	ND	3.29 ± 1.97	4.30 ± 2.41
Ca.Dm (µm)	**ND**	ND	ND	**0.500**	0.67	70.65 ± 12.15 (73.52)	72.77 ± 9.71 (77.41)	**0.893**	0.14	72.94± 25.62 (57.23)	76.57 ± 20.87 (77.34)	**0.043***	2.02	72.49 ± 8.78 (68.21)	85.94 ± 7.04 (85.22)
Ct.Th (µm)	**ND**	ND	ND	**0.686**	0.41	1389.13 ± 149.67 (1316.81)	1395.87 ± 142.48 (1354.76)	**0.345**	0.94	1426.34 ± 161.32 (1412.85)	1445.71 ± 161.07 (1449.40)	**0.893**	-0.14	1449.65 ± 164.37 (1387.88)	1440.93 ± 124.53 (1397.19)
Tt.Ar (mm^2)	**0.592**	0.30	1	**ND**	ND	31.07 ± 1.40	31.03 ± 1.25	**ND**	ND	33.00 ± 4.57	33.22 ± 3.91	**ND**	ND	34.51 ± 4.57	34.73 ± 5.07
Ct.Ar (mm^2)	**ND**	ND	ND	**0.893**	0.14	21.09 ± 1.34 (20.66)	21.04 ± 1.29 (20.94)	**0.893**	0.14	23.56 ± 2.63 (23.40)	23.60 ± 2.47 (24.28)	**0.686**	0.41	23.58 ± 4.00 (23.42)	23.62 ± 3.87 (23.09)
Ma.Ar (mm^2)	**ND**	ND	ND	**0.893**	0.14	9.98 ± 1.76 (9.76)	9.98 ± 1.91 (9.92)	**0.225**	1.21	9.44 ± 2.48 (8.44)	9.62 ± 2.46 (8.61)	**0.893**	0.14	10.93 ± 1.62 (10.42)	11.10 ± 1.72 (11.11)

Bone parameters compared between the *ex vivo* micro-CT (day 28) scan data for the irradiated (right) and non-irradiated (left) control tibiae/dose group (n = 5). Values are reported as mean ± standard deviation. Median values are reported for those parameters where at least one dose group was not normally distributed. Repeated measures ANOVA with post-hoc Bonferroni tests were employed for normal data. Wilcoxon signed-rank test manually categorized by dose were employed for non-normal data. Significance level for overall tests (normal data) and p values (non-normal) was $\alpha = 0.05$. For nonparametric tests, no overall p test is reported (ND = no data) as pairwise comparisons were manually categorized by dose group. F values and Degrees of Freedom (df) are reported for repeated measures ANOVA whereas Z values are reported for Wilcoxon signed-rank tests. For ANOVA, post hoc tests are not reported for non-significant overall p values (ND = no data). For Wilcoxon signed-rank tests, no overall p test is reported (ND = no data) as pairwise comparisons were manually categorized by dose group. Ct.Po = cortical porosity, Ca.Dm = canal diameter, and Ct.Th = cortical thickness. 2D measures (bottom row) Tt.Ar = total area, Ct.Ar = cortical area, and Ma.Ar = marrow area.

5.44. Animal Weight

A two-tailed, paired t-test analysis of week 0 and week 4 revealed weight loss overall (p = 0.019), although a nonparametric Friedman test observed no difference in weight amongst the three dose groups (p = 0.270) at week 4.

5.5. Discussion

Our primary goal was to establish a novel method to directly measure BMU LER in 4D within the cortical bone of rabbits using phase contrast SR micro-CT. The successful 4D co-registration of the *in vivo* SR micro-CT and *ex vivo* micro-CT scans revealed BMUs advanced an average of 23.8 µm/day or 333 µm over the 14 days between the two scans. As discussed, comparative data are limited and consist of inferred values (Table 5.1), with previously reported mean LER of ~ 40 µm/day coming from two studies that histologically assessed 52 (Jaworski and Lok, 1972) and 58 (Takahashi and Norimatsu, 1976) BMU closing cones from three and five assumingly healthy, adult male dogs, respectively. Less cited are the results of 36.7 µm/day in monkeys (Parfitt, 1983) and 27.0 µm/day in humans (unpublished data—(Parfitt, 1983)). Albeit speculative, our smaller mean LER could be due to differences between species, the type of bone analyzed, age differences (Jaworski and Lok, 1972), or within-species microarchitectural cortical bone variation. Nevertheless, the proposed method here is the first approach for standardized tracking of BMUs in 4D in the same animal.

We also cannot rule out the potential impacts of supraphysiological PTH dosing in our rabbit model. Across the dose groups, mean Ct.Po from the right and left micro-CT scans ranged from 2.93% - 6.94%, which aligns with recent reports of varied Ct.Po among PTH-treated rabbits (Yamane et al., 2017, Zebaze et al., 2017, Harrison et al., 2020). Visually, micro-CT cross-sections revealed minor to moderate endosteal bone formation throughout majority of the three dose groups (Figure 5.6), with a few instances of extensive endosteal formation observed within rabbits from both the High (n = 1) and Medium (n = 2) dosed groups. This likely explained the higher, albeit nonsignificant, Ct.Po values (6.93% - right and 6.94% - left) observed within the Medium dose group in comparison to those of the Low (2.93% - right and 3.04% - left) and High (3.29% - right and 4.30% - left) dose groups. In rabbits, treatment with intermittent PTH has been associated with

increased endosteal bone formation (Yamane et al., 2017, Hirano et al., 2000, Hirano et al., 1999, Mashiba et al., 2001, Harrison et al., 2020) and appears to mimic the anabolic bone effects observed in human skeletons when PTH is administered therapeutically (Anastasilakis et al., 2020, Föger-Samwald et al., 2020, Cosman, 2020). We observed extensive endosteal bone formation in both the irradiated right and non-irradiated left control tibiae, indicating that inter-animal variation in response to PTH dosing—a finding consistent with our previous study (Harrison et al., 2020)—and not radiation exposure, is the root cause (Figure 5.7). The finding of proliferative endosteal bone is consistent with typical 'early-stage' PTH-mediated *bone modeling* behavior, referred to as the 'PTH anabolic window' (Silva and Bilezikian, 2015) in which bone formation is most prominent (Ng et al., 2016), followed by later stages of increased *bone remodeling* induced bone resorption (Silva and Bilezikian, 2015).

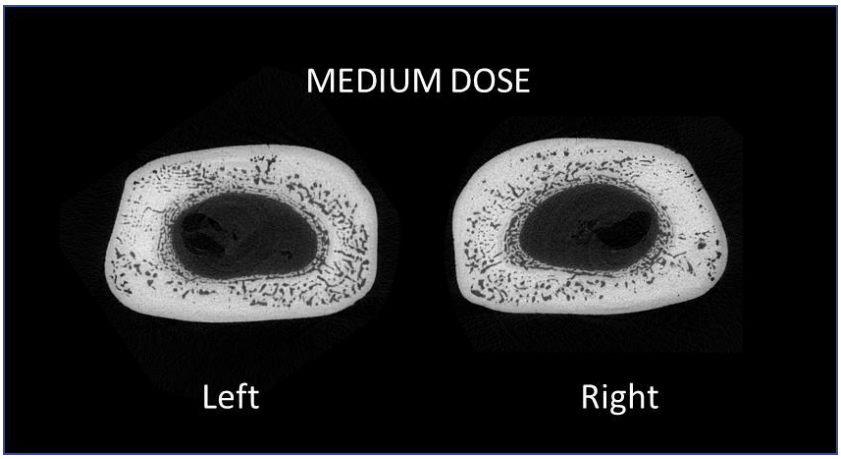

Figure 5.7. Extensive endosteal bone formation. Two-dimensional micro-CT cross-sectional image of a Medium (2.5 Gy) dosed rabbit displaying extensive cortical porosity and endosteal bone formation in both the irradiated right and nonirradiated control left tibiae indicative of PTH-induced formation.

The secondary objective of this study was to identify potential radiation dose impacts through the assessment of LER, cortical porosity parameters, and cross-sectional cortical geometric parameters across three radiation doses. Increased radiation dose equates to increased image quality (i.e., better signal-to-noise ratio) which we noted in our High dose group scans that overall had improved image quality. The Medium dose protocol provided sufficient image quality and co-registration capacity and thus serves as a suitable mid-point range that could also promote future applications for multiple *in vivo* scans or potentially extended periods between radiation

exposure and study endpoints. Firstly, LER did not differ across radiation dose groups. Secondly, the general lack of differences amongst the bone parameters between the irradiated right and non-irradiated left tibiae is suggestive that, overall, the parameters of the imaging protocol employed for this study did not have an overt effect on the cortical bone in these rabbits within the timescale of the study. This conclusion is further supported by the fact that weight loss, consistent with this model system (Harrison et al., 2020), did not differ by dose group and other indications of distress such as changes to behavior, appetite, and water intake were not observed in any group.

Radiation effects in bone tissue have been reported as both a factor of dose and time, with previous studies reporting variable responses in rabbit bones exposed to a single dose (therapeutic X-Ray) of 25, 50, and 100 Gy over a 4 – 52-week observation period (Takahashi et al., 1994). Exposure to a single radiation dose of 35 Gy has been shown to increase porosity and decrease cortical area in the femora of rats at 14- and 18-weeks post-dosing (Maeda et al., 1988). Similarly, suppressed bone formation (4 weeks) and increased porosity (12 weeks) have also been reported in rabbits after a single exposure to 50 Gy (Sugimoto et al., 1991). Interestingly, timed analysis of rabbit tibiae (7, 14, 21 days) post-exposure to a single dose of 30 Gy showed that the majority of impacted cortical parameters, including porosity, recovered to non-irradiated levels 14- and 21-days post-exposure, suggestive of a potential correlation between bone turnover recovery and time post-exposure (Borges and Rabelo, 2021). While the rabbits in our study had the added variable of PTH treatment, their cortices were subjected to non-therapeutic radiation doses and assessed after a shorter period (14 days) post *in vivo* imaging which may explain why we did not find significant radiation dose effects. Notably, in this study we only reported the incident dose, however, since the synchrotron beam used here was monoenergetic, the absorbed dose in the bone tissue here is less than the case of polychromatic X-ray beam from X-ray tube sources. Future studies where bone tissues analyzed from rabbits euthanized several weeks to months post *in vivo* SR micro-CT scanning would provide further support for the findings of this study since radiation damage has been observed in the cortical bone of animals subjected to radiation several weeks to months post-exposure (Takahashi et al., 1994, Maeda et al., 1988).

A limitation of our experimental protocol is the exclusion of a non-PTH control group. In a previous study, we found that PTH increased remodeling rate (activation frequency, Ac.f) 14.2-fold versus SHAM rabbits (Harrison et al., 2020); therefore, with our ~12 BMUs/rabbit, a matched

control group (n = 5) may only have provided an additional 2.2/rabbit or 11 BMUs in total for LER measurement. A low rate of baseline remodeling in normal rabbits was also confirmed in preliminary trials of our imaging protocol. As our objective here was to introduce a novel approach for measuring LER, and not to test a biological hypothesis, we chose to not include a control group due to concerns focused on the ethical use of animals and cost. Also, while the intended use of PTH to increase the number of active BMUs for LER measures was achieved, the efficiency at which this was done resulted in: 1) co-registration issues, with one rabbit per group excluded for analysis, and; 2) challenges locating classically shaped BMUs. Future application of the methodology could mitigate these limitations by potentially lowering the dose of PTH and/or increasing the size of FOV and thereby increasing the ability to locate suitable BMUs for analysis in both PTH-dosed and control animals.

A limitation of our imaging protocol was the use of different imaging platforms (SR micro-CT versus micro-CT) for the two scans of each animal; however, doing so meant that we did not require additional (inherently limited) synchrotron beamtime for the second scan. Although it would increase the complexity of the experiment, including acquiring and scheduling synchrotron access, multiple *in vivo* assessments could certainly be entertained for future studies. Such an approach would be particularly powerful for looking at dynamic modulation of individual BMU activity over time. Synchrotron imaging can also be limiting regarding the amount/type of skeletal element that can be imaged – methodologically, it is more feasible to image distal limbs at an effective dose compared to the vertebrae, for example. This is not dissimilar to human *in vivo* imaging platforms such as high-resolution peripheral quantitative computed tomography (HR-pQCT) restricted to the metaphyseal regions of the radius and tibia (Mikolajewicz et al., 2020).

Finally, using a rabbit model for investigating cortical remodeling-related spatio-temporal behavior also exhibited high levels of variation, particularly for Ct.Po. Such variation was manifested as outliers within the data; however, a comparison of the 3D parameters in which the outliers were removed did not alter the results (*data not shown*) and therefore all data were retained for analysis, especially considering our small sample sizes. Despite these limitations, when compared to small laboratory rodent models (e.g., mice and rats), which do not naturally exhibit cortical bone remodeling (Lelovas et al., 2008), the rabbit does display cortical remodeling similar

to that observed in human bone remodeling (Pazzaglia et al., 2007, Pazzaglia et al., 2009, Pazzaglia et al., 2010) and thus offers an excellent option for the study of cortical remodeling *in vivo*.

Data obtained from the direct, 4D measurement of LER could provide the ability to assess the morphology or shape of the BMU to investigate characteristics such as the closing cone or the scale of the reversal-resorption zone (Delaisse et al., 2020, Andreasen et al., 2015) which could have significant clinical relevance in humans. Osteoporosis treatments typically involve antiresorptive (inhibiting bone resorption activity, e.g., bisphosphonates (Russell et al., 2008)) or anabolic (stimulating bone formation, e.g., PTH (Ng et al., 2016)) therapies. That said, rare, but substantial adverse side effects such as osteonecrosis of the jaw (Migliorati et al., 2006) or atypical femoral fracture (Gedmintas et al., 2013) have been associated with anti-resorptive therapies. In contrast, complicated drug delivery schedules associated with PTH (i.e., intermittent versus continuous administration), can result in undesirable catabolic instead of expected anabolic effects. The methodology presented here provides a novel platform to better investigate BMU spatio-temporal modulation by OP drugs directly in a preclinical model for the first time. Thus, a unique opportunity exists to potentially reduce unwanted side effects via more gauged dosing regimens. If BMUs can be reduced in size, slowed in their progression, spatially constrained to avoid coalescence into larger pores, and closely coupled with balanced resorption and formation, bone strength can be more safely preserved or even increased – reducing the overall burden of OP. There is also potential application to investigating hypotheses regarding BMU spatio-temporal behavior in general. For example, BMUs are thought to actively target and steer remodeling towards areas of microdamage in the form of microcracks (Martin, 2002, Martin, 2007, Parfitt, 2002b, Burr, 2002) and/or other mechanical stimuli such as strain (Smit and Burger, 2000, van Oers et al., 2008), strain loading-induced fluid flow (Smit et al., 2002, Burger et al., 2003, Estermann and Scheiner, 2018) and loading-induced hydrostatic pressure (Scheiner et al., 2016). The approach demonstrated here thus holds great potential to also test these hypothesized relations for the first time empirically.

This study represents the first direct assessment of LER in 4D. We found LER values in rabbits to be lower than those previously reported (and often cited) for dogs, but not inconsistent with limited inferred data for humans. Further, our results indicated that the imaging protocol employed did not have an overt impact on the cortical bone parameters of rabbits during the study

timeframe. The method developed within this study serves as a novel platform to further advance our fundamental understanding of BMU spatio-temporal regulation and its role in bone aging, adaptation, and disease.

5.6. Acknowledgments

Part or all the research described in this paper was performed at the Canadian Light Source, a national research facility of the University of Saskatchewan, which is supported by the Canada Foundation for Innovation (CFI), the Natural Sciences and Engineering Research Council (NSERC), the National Research Council (NRC), the Canadian Institutes of Health Research (CIHR), the Government of Saskatchewan, and the University of Saskatchewan. This specific research was primarily supported by a CIHR Catalyst Grant (FRN: 151724). We also acknowledge Dr. George Belev's significant contributions towards the implementation of the *in vivo* imaging portion of this research as well as Gavin King for his assistance with production of images for the manuscript. Finally, the authors acknowledge the support of the University of Saskatchewan Laboratory Animals Service Unit (LASU) which was essential for the success of this research.

5.7. Authors' Contributions

KDH: Conceptualization; data curation; formal analysis; investigation; methodology; visualization; writing-original draft; writing-review and editing. **ES:** Formal analysis, methodology; visualization; writing-original draft, writing-review and editing. **BDH:** Data curation; methodology; writing-review and editing. **AP:** Conceptualization; funding acquisition; data curation; investigation; methodology; visualization; writing-original draft; writing-review and editing. **NZ:** Data curation; writing review and editing. **TA:** Conceptualization; funding acquisition; methodology; writing-review and editing. **KS:** Data curation; investigation; methodology; writing-review and editing. **PP:** Conceptualization; funding acquisition; methodology; writing-original draft; writing-review and editing. **DC**: Conceptualization; methodology; writing-review and editing. **DMLC:** Conceptualization; data curation; formal

analysis; funding acquisition; investigation; methodology; project administration; supervision; writing-original draft; writing-review and editing.

Ethics Declaration

The authors have no conflict of interest to declare.

Chapter 6 Thesis Summary and Conclusions

6.1. Thesis Overview

Remodeling is fundamental for maintaining bone tissue throughout life. In aged or diseased bone, remodeling within the BMU can become unbalanced (i.e., excessive resorption) or uncoupled (i.e., failure of bone formation), which can lead to increased cortical porosity and thinned cortices classically associated with osteoporosis (OP). BMU spatio-temporal behavior lies at the heart of OP; however, remodeling has never been directly observed *in vivo* within its natural, three-dimensional (3D) context. This has been primarily due to imaging constraints—high resolution capable of rendering the small scale of BMU-related resorption spaces has required prohibitively high radiation dose. Secondarily, research in this area has been impeded by the focus on rodent models which exhibit little, if any, cortical remodeling. Finally, while histomorphometry utilizing fluorochrome labelling has provided a wealth of insights into remodeling, it is incapable of providing direct dynamic evidence regarding the resorptive phase of the BMU. This thesis set out to overcome these limitations, aiming to develop a novel platform to enable direct tracking of BMU behavior, *in vivo*, within cortical bone through the combined use of an animal model and 4D imaging. I hypothesized that: 1) In-line phase contrast SR micro-CT can safely image BMUs, *in vivo*, in the cortical bone of animal models; 2) rabbit models of OP elevate BMU remodeling; and 3) combining SR micro-CT with rabbit models of OP would create a novel platform for the direct 4D measurement of BMU LER *in vivo*.

Chapter 2 presented the first manuscript of this thesis, "Modalities for the Visualization of Cortical Bone Remodeling: the Past, Present and Future" (Harrison and Cooper, 2015). This paper reviewed past, current, and future methodologies for imaging cortical bone remodeling in 2D and 3D. I initially set out to test the hypothesis that remodeling targets microdamage in the form of microcracks by tracking BMUs within the cortical bone of rat ulnae, and therefore, this manuscript also presented the first example of matched cortical bone scans in rats via *in vivo* imaging using in-line phase contrast SR micro-CT (see also Appendix A). However, as was discussed in Appendices B & C, inducing remodeling within rat cortical bone through a fatigue loading model was not successful and, ultimately, I needed an alternative model system. That said, imaging of

the rat model resulted in the development of a successful *in vivo* imaging protocol, which was further refined to reduce initial scan times of 38 minutes down to < 1 minute. This set the stage for tracking BMU remodeling events within the cortical bone of rabbits.

Chapter 3 explored the cellular underpinnings of OP models (i.e., OVX, GC, OVX+GC) and PTH, used to elevate cortical bone remodeling rates in rabbits which were then experimentally explored in Chapter 4 which presented the second manuscript of this thesis, "Cortical Bone Porosity in Rabbit Models of Osteoporosis" (Harrison et al., 2020). Evidence of elevated cortical remodeling/porosity was observed in all the OP models and, most extensively, within the PTH treated rabbits. An intriguing, but unexpected result was the evidence of increased cortical porosity within the OVX group, as OVX as a stand-alone treatment has been considered insufficient as an OP model in the rabbit.

Finally, Chapter 5 presented the third and final manuscript (*under review*; submitted to JBMR, Sept. 28, 2021), "Direct Assessment of Cortical Bone Basic Multicellular Unit Longitudinal Erosion Rate: A 4D Synchrotron based Approach". This study represented a "putting together of the pieces." Using the highly effective rabbit PTH model from Chapter 4 combined with our in-line phase contrast SR micro-CT imaging protocol from Chapter 2. This study represented the first time BMU LER was directly assessed in 4D within the cortical bone of a live animal. BMU LER of 23.79 μm/day was not found to differ among the different radiation dose groups (1, 2.5, and 5 Gy).

6.2. Limitations

The proof of principle study presented in Chapter 5 represented the attainment of my initial goal of directly tracking remodeling. That said, the need to elevate remodeling rate to create a viable model, whether it be fatigue loading in the rat or OP models in the rabbit, including PTH dosing, means that the remodeling induced is not spontaneous nor is it necessarily normal. However, with the demonstrated feasibility of the platform, we are exploring further studies to better understand how these model systems impact LER and other characteristics such as BMU morphology. For example, subsequent *in vivo* studies have already been extended to investigating the effects of OVX and GCs (study in progress) and PTH withdrawal effects (see next section).

The *in vivo* protocol for tracking BMUs is also limited by the small (particularly vertical) field of view of a single scan. To overcome this, in subsequent trials we have altered our *in vivo* imaging protocol to include two adjacent fields of view. This doubles the volume of bone that can studied and thereby increases the number of BMUs imaged. The goal is to increase the feasibility of studying BMU dynamics in experimental groups with lower rates of remodeling, including control animals. BMIT is also pursuing further technological and methodological advancements which hold the potential to improve imaging further. Through optimization of beam monitor lenses, the potential exists to improve the efficiency of detection and thereby either improve image quality or future reduce radiation dose. Combined with an expanded beam – an initiative being pursued by Chapman and colleagues (Martinson et al., 2014, Martinson et al., 2015)—larger fields of view could be captured in a single scan. Alternatively, spiral scanning currently being explored at BMIT may offer another avenue for greater vertical fields of view that can be rapidly acquired. Finally, through further reduction of radiation dose, more complex experimental designs with multiple *in vivo* scans may help yield more detailed 4D data.

6.3. Future Directions

The evolution of this thesis project has culminated in the potential to investigate BMUs and remodeling at exploratory levels not previously possible. A peripheral but relevant underlying theme brought forth in this research is that bone remodeling and OP-related treatments are dynamically intertwined and heavily predicated upon several factors, including drug types (anabolic versus antiresorptive), drug combinations, the timing of drug deliveries, and dosing. A substantiative advantage afforded by this novel platform is that we can dose rabbits for a few short weeks and observe treatment effects within individual BMUs instead of dosing animals for several months and examining overall changes in bone microstructure.

In consideration with the current landscape of OP treatments, a unique path forward would be to employ this 4D platform to further explore the direct impacts of clinical-based pharmaceutical treatments on remodeling such as PTH and bisphosphonates. Current FDA approved treatments for OP fall under two main approaches: 1) antiresorptive agents that target osteoclast function and osteoclastogenesis via bisphosphonates (BPs) (e.g., alendronate,

ibandronate, risedronate, and zoledronic acid), and denosumab (Dmab), and 2) anabolic agents which stimulate bone formation through osteoblast differentiation, function, and survival via parathyroid hormone (PTH 1-34; teriparatide), abaloparatide (ABL), and romosozumab (ROMO) (Cosman et al., 2014, Anastasilakis et al., 2020). Within our group, Masters student Erika Sales has further investigated whether PTH-mediated increased remodeling rate is also extended to BMU LER via manipulated dosing regimens (i.e., PTH and PTH Withdrawal (PTHW)) and hypothesized that LER would be higher during active dosing (abstract presented at the American Society for Bone and Mineral Research (ASBMR) 2021 meeting). Contrary to our hypothesis, results from this study have shown that the median LER was lower in the PTH group (33.4 μm/day) versus the PTHW group (39.5 μm/day; p= 0.026). This is quite an intriguing finding. It suggests that the effects of PTH on bone formation and resorption within the BMU are not uniform, but rather coupling is enhanced through an increase in bone formation with a simultaneous slowing of resorption and, thus, even though activation frequency is increased, PTH still has an overall anabolic effect.

Via a New Frontiers in Research Fund, our lab will also explore OP treatment impacts on bone remodeling through the direct, 4D observation of the impact of the bisphosphonate alendronate and PTH at varying doses in the OVX rabbit model. Combination therapies of PTH with bisphosphonates have been clinically shown to impede the formative actions of PTH (Wein and Kronenberg, 2018); thus, we hypothesized that alendronate would slow and/or stop active BMUs and inhibit activation of new BMUs, whereas PTH would slow LER and enhance formation within BMU closing cones. The multifaceted characteristics of OP therapies allude to a concept that purposefully timed augmentation, rather than elimination of remodeling, presents a better strategy to target, treat and potentially even prevent OP-induced bone loss.

In a review by Anastasilakis et al. (2020), a trial of treatment-naïve postmenopausal women showed that combination therapies of PTH with Dmab increased BMD across several sites, including the lumbar spine, femoral neck, total hip, and radius in comparison to either agent administered alone after 12 (Tsai et al., 2013) or 24 (Leder et al., 2014) months of treatment. However, these studies only measure BMD, which cannot probe the proximate effects on BMUs and lack follow-up analyses that reveal how long positive effects on BMD remain after cessation of treatment. For example, would a follow-up study compare BMD rates six months or one-year

post-treatment show differences amongst postmenopausal women who received various PTH combination therapies compared to stand-alone PTH? What implications could this have for clinical treatment protocols? Could this negate the need for antiresorptive agents post PTH? Previous research has suggested that effectiveness of combined PTH and Dmab treatment, due to Dmab inhibiting PTH-mediated resorption, is more effective than PTH and bisphosphonate combination therapy (Tsai et al., 2013). In this sense, certain antiresorptive drugs seem to support the natural progression of PTH's anabolic window, where initial bone formation gives way to eventual bone resorption. If this is true, perhaps augmenting either the timing of administration and/or dose of these drugs could extend this window and increase current maximum drugschedules beyond the recommended two-year period for PTH and/or eliminate the need of subsequent antiresorptive drugs.

Such experimental questions could be addressed with our PTH rabbit model – the impacts on BMU behavior can be directly investigated and conclusions can be drawn more quickly as opposed to those obtained from more general morphological measures taken over multitudes of BMUs at study end-points. Alterations to drug schedules and their associated effects could also be extended to the other models of OP tested within this thesis. Recalling the *ex vivo* study of models of OP in the rabbit presented in Chapter 4, OVX did elevate cortical porosity. This was unexpected as stand-alone OVX is not typically recommended for investigating OP within the rabbit, and therefore, data on its effect duration is not well known. Utilizing a rabbit OVX model, an *ex vivo* micro-CT study that 'time-out' the duration of elevated porosity relative to time post-OVX surgery could serve as a baseline for OVX effects within rabbit bone. This could further serve as a model permitting the direct 4D assessment of remodeling behavior associated with age-related OP bone loss and associated clinical treatments.

Upon cessation of treatment with both PTH and Dmab, bone loss can occur rapidly, and antiresorptive treatments, typically BPs, are recommended to maintain BMD. That said, residual effects from BP treatment have been shown to last for several years beyond their discontinuation (Anastasilakis et al., 2020). Such factors have led to further drug administration studies investigating the effects of different combinations and drug regimens. Anastasilakis et al. (2020) provide an extensive overview of current clinical approaches for OP treatment. Sequential (i.e., transitioning from an anabolic to antiresorptive) and combination (i.e., simultaneous dosing of an

anabolic and antiresorptive) are most commonly prescribed to treat OP. However, less common approaches can include the sequential administration of distinct antiresorptive agents or repetitive therapies of individual anabolics. Overall, initial treatment with an anabolic such as PTH followed by an antiresorptive agent seems to be most effective for maintaining gained BMD. On the other hand, in patients with severe OP, combination therapy (i.e., PTH and Dmab or PTH and zoledronate) has displayed both long-term and shorter-term advantages over PTH therapy alone. Despite these results, combination treatment is not commonly approved due to associated drug costs and a lack of data showing a definitive improved capacity for limiting fractures over stand-alone PTH therapy, as these effects have not been established in either ABL or ROMO with PTH. Our novel BMU tracking platform would be advantageous for exploring the efficacy of pharmacotherapy and treatment duration, a factor that has not been established beyond current clinical applications for any OP-related pharmaceutical (Anastasilakis et al., 2020).

Finally, another possibility arising from this thesis is the investigation of OP-related remodeling behavior within males. Most FDA-approved therapies are based on postmenopausal women's studies (Cosman et al., 2014). A lack of male OP focused research has resulted in issues with male OP being commonly under-represented and under-treated (Rinonapoli et al., 2021) yet with increasing age, OP fracture risk in men can increase by 13 to 25% (Adler, 2018). Implementing our GC rabbit OP model in male rabbits, for example, would be an intriguing future avenue of research to add 4D data about male OP-related remodeling and address an area of research currently lacking within the literature.

Initially, this thesis sought to investigate the theory that BMUs are spatially ‘targeted’ (Parfitt, 2002b) to remove damage manifested as microcracks (Burr et al., 1985, Burr et al., 2002, Ehrlich and Lanyon, 2002, Ryser et al., 2009) through a fatigue loading model of induced cortical bone remodeling in rat ulnae. While this was not successful in the rat model, testing of this theory could be revisited in the rabbit as ulnar stress fractures caused by axial fatigue loading have been shown to induce an intracortical repair response in proximity to the microdamage (Buettmann and Silva, 2016). Images acquired *in vivo* before loading and *ex vivo* after an adaptation period would directly track pre-existing BMUs. Therefore, any change in their behavior in response to the mechanical stimuli could be rendered in 3D and further quantified through histomorphometric analysis of fluorochrome labeled microcracks in the proximity of BMUs.

The impacts of mechanical unloading on BMU behavior could also be explored. Disuse osteoporosis associated with events such as spinal injury-induced bed rest or weightless environments (i.e., spaceflight) (Bikle et al., 2003) is typically due to increased resorption from unbalanced remodeling (Wojda et al., 2013). Thus, BMU activity in response to reduced mechanical loading could be studied by imaging PTH-treated rabbits *in vivo* before implementing a single limb immobilization by casting or neurogenic paralysis (Meakin et al., 2014) for an adaptation period before *ex vivo* analysis. A subsidiary study to further build on this could involve subsequent 'repair' of unloaded bone through pharmaceutical treatment with sequential or combination therapies to provide a window into the pharmaceutical reversal of bone loss. Finally, targeted remodeling could also be investigated via defects that introduce injury to the bone. A cortical bone defect could be introduced into a PTH rabbit's tibia through an osteotomy using a surgical drill or surgical implant and then carry out multiple *in vivo* scans during the healing process. This procedure would directly test BMU steering theories through the hypothesis that BMUs would re-direct their trajectory within the bone and actively steer towards the injury site and systematically decrease with continuous healing.

In conclusion, this thesis successfully: 1) developed an imaging protocol that permitted the direct assessment of individual BMUs within animal models; 2) established several rabbit-based models of elevated remodeling to permit investigation of BMU spatio-temporal behavior on a large scale, and 3) directly measured BMU LER in 4D for the first time. This novel, 4D platform for investigating BMU behavior, *in vivo*, at a level not previously feasible, will be transformative in our understanding of bone microstructural dynamics. Such advances promise to improve current and future clinical-based treatments for degenerative bone diseases such as OP and beyond.

Appendix A Development of the *in vivo* imaging micro-CT protocol

A.1. *In Vivo* Imaging - Summary of Protocol Development

Overall, the following have been addressed in pursuit of developing a working *in vivo* imaging protocol:

1) **Scan protocol**—continuous scan instead of a step and shoot. This drastically reduced scan times from approximately **38 min to 14 min** which was beneficial for two reasons: 1) the animals were under anaesthesia for a shorter period and 2) more animals could be scanned in an 8-hour beam time shift. From anaesthetization to post-scan recovery, each rat took approximately 45 min.
2) **Limb holder—**after trial and error, the three-point contact holder designed by Dr. Ning Zhu proved successful in eliminating movement in the forelimb of rats during scans (Figure A.2.).
3) **Matched scans—**our protocol that visually matched scout images of the growth plate and incorporated the average limb growth in a two-week period was shown to be successful at targeting the same area within the bone. In one rat, we were also able to identify new remodeling events in a matched scan, indicating this protocol could serve to identify and target BMUs.
4) **Field of View—**testing the BMIT-ID line and ORCA Flash camera has resulted in a significantly larger FOV ~ 8.9 mm compared to the previously obtained 1.0 - 1.5 mm FOV on the BMIT-BM line using the C4742-56-12HR fiber optic window x-ray camera (Figure A.5.).
5) **Scan times—**the shift to the BMIT-ID line drastically reduced scan times from **14 min to roughly 30 seconds** which was beneficial for two reasons: 1) the animals were under anaesthesia for a shorter period and 2) more animals could be scanned in an 8-hour beam time shift. Of importance, daily monitoring for all animals (rats and rabbits) imaged to date have not shown any obvious signs of radiation sickness or signs of hair loss or skin burns in the area directly imaged.
6) **Rabbit imaging and holder redesign—**redesign of the rabbit holder was carried out to mitigate breathing issues during imaging (Figure A.6.). The new holder was better for the animals (respiration rates were consistently much more stable), and the time required to sedate, image, and recover a rabbit was significantly reduced from upwards of 2.5 hours to as little as 35 minutes. Since the implementation of this redesign, several *in vivo* rabbit studies have been successfully carried out.

A.2. *In vivo* imaging of cortical bone within rat ulnae

A Hamamatsu C4742-56-12HR fiber optic window x-ray camera on the BMIT-BM beamline at 37 keV and a 10 μm pixel size was used to image peripheral forelimbs (ulnae being the primary targets) of live rats kept under isoflurane gas anesthetic. Exposure times gave mean photon counts of around 2000-3000 per image. Varied dose was a consequence of varied projection numbers with 0.36 or 0.5-degree rotational step giving 500, or 750 projections over 180 degrees. This resulted in doses of approximately 2 Gy, and 3 Gy, respectively. The stage distance from the detector was set at 0.9 m. The stage/holder design only exposed the limb imaged to the beam and kept the animal under anesthetic during the scan. Each animal was exposed alongside a Lithium Fluoride dosimeter chip to measure the scattered dose to the body, and a Keythley ion chamber was used to measure the dose to the forelimb in real time. Animal vitals (i.e., temperature, heart rate, breathing rate, and SpO2) were recorded every 5 minutes during anaesthetisation and throughout scanning. Post-scanning, animals were provided saline fluids subcutaneously and monitored. Uponfull recovery from anaesthesia, they were returned to their respective cage.

A.21. *In vivo* imaging Results - Rat Model

A.21.1. Nov/Dec 2013 - First longitudinal imaging

Imaging Results: Most canals within the cortical bone were observable at both radiation doses (2 and 3 Gy). Notably, larger canals with morphologies resembling those of the classic 'cutting cone' associated with BMUs were also apparent (Figure A.1). Scan times averaged: **35 min** (6 controls), **34 min** (6 rats dosed at 3 Gy) and **38 min** (6 rats dosed at 2 Gy).

Radiation Dose Results: Daily monitoring of each rat for indicators of radiation sickness (i.e., skin burns, hair loss, behavioral changes, dietary changes, grooming changes) did not show obvious signs that radiation damage had occurred for either dose. Interestingly, there was no evidence of radiation damage in the forelimb area directly imaged on any of the 12 experimental rats.

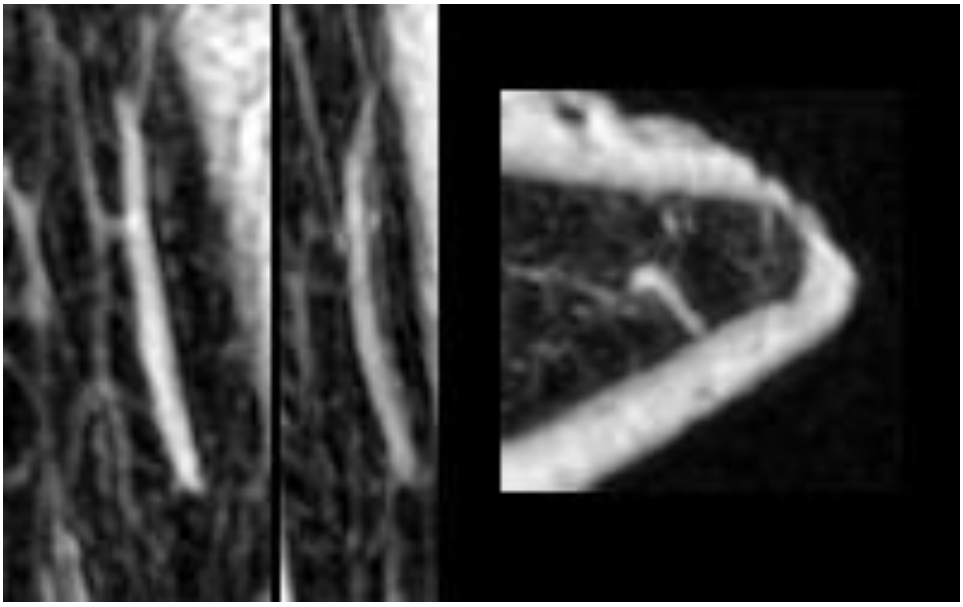

Figure A.1. Standard deviation projections of the same BMU from an individual rat showing the 'cutting cone' (12μm, 3 Gy).

A.21.2. May 2014 - Reduced scan times

This round of beam time was plagued with several issues. Scanning initiated with the control animals using the protocol derived in Dec 2013 however, we experienced hardware/software issues. The computer used during the Dec 2013 run malfunctioned, so BMIT's beamline scientist, Dr. George Belev, configured the imaging program for our protocol onto a 32-bit Vista system. Unfortunately, we eventually realized a 64-bit windows 7 system was required to run the scanning protocol properly. During the control scans, it was noted that the software for the detector was not calibrating radiation dose properly; changes in exposure time were not subsequently changing camera capture times, and therefore, we had no control over the dose to maintain an overall 2 or 3 Gy maximum. This resulted in the testing of a new, continuous scan protocol that automatically calculated the dose according to the following parameters: the desired dose entered (2 Gy or 3 Gy), calibration dose (0.0045), ring current during calibration, micro-step of the stage (20), # of projections, time (int. time = 015, Max time = 3000 ms) and the detector and camera (C4742-56-12 HR (Hamamatsu), C4742-95-12 HR), respectively. This brought scan times down to approximately **14 min**. Besides issues with the scanning protocol, we noticed frequent

movement occurrences within the scans, which resulted in a complete reconfiguration of the limb holder apparatus.

A.21.3. June 2014 - Limb holder modification

Like May, June's beam time was also problematic. While we had the new (faster) scanning protocol in place, the other issue that still needed to be addressed was frequent movement during scans. Using the College of Medicine's 3D printer, I enlisted the help of Dr. Ken Gagnon to design a more rigid forelimb holder that could be incorporated into our existing stage. Unfortunately, the process in which the printer sequentially lays down material creates an internal 'honeycomb' pattern which resulted in a significant amount of phase artifacts within scans. Thus, while this design limited movement artifacts, it introduced phase artifacts and, therefore, we needed to construct a different holder.

A.21.4. Nov/Dec 2014 - Matching scan regions over consecutive scans

This beam time was focused on addressing our scan movement issue and fine-tuning our ability to target the same region of bone to match consecutive scans for each rat. Dr. Ning Zhu designed a three-point contact holder system that would safely immobilize the limb at all three main joints (shoulder, elbow, and wrist) during scanning (Figure A.2). This new design also minimized 'slumping' throughout a scan as the arm was held in a plane level to the chest wall. Before imaging live animals, we ran scans on excised limbs to test the holder and the area desired for imaging. To consistently target the same area of the limb between successive *in vivo* scans, the growth plate would be placed at the top of the FOV, and then the stage would be dropped by 5 mm to place the beam within cortical bone, at which point we would take a scout image. That scout image would be used for the second *in vivo* scan to ensure the top of the FOV was placed in the same area. This system proved to be successful as reconstruction immediately following scan completion did not show movement artifacts and we were able to target the same area of bone on each animal (Figures A.3 & A.4). To match the scan area for each rat, we would compare the scout images of the growth place taken in November. After matching the scout images, the stage would be dropped 6.4 mm down from the growth plate to account for the growth of the limb in the two-

week timeframe between scans. The ulnae of male Sprague-Dawley rats at eight weeks of age grow approximately 1.4 mm in two weeks, so 5 mm + 1.4 mm = 6.4 mm. All scans were successful.

Figure A.2. Three-point contact holder**.** Photograph showing the three-point contact holder system to limit movement in the limb during scans. The top plate and clear plastic tubing were adjustable for each rat.

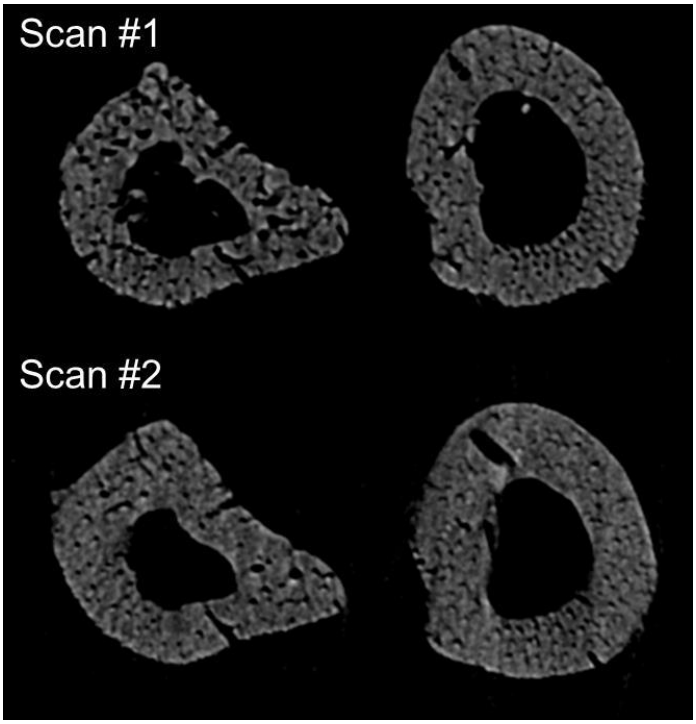

Figure A.3. Images showing matched scans of an individual rat demonstrating the same area on an individual rat can be targeted longitudinally. Scan #2 was taken two weeks after Scan # 1.

A.21.5. Dec 2015 – Integration of a new detector into the imaging protocol

The purpose of this beam time was to test BMIT's new ORCA Flash camera therefore, no live animal imaging occurred. Compared to the C4742-56-12HR fiber optic window x-ray camera used previously, the ORCA Flash camera has a much faster read-out rate, yielding better image quality at the same dose rate. Test scans on excised rat limbs confirmed this, and it was decided future live animal imaging would use the ORCA Flash camera.

A.3. *In vivo* imaging – BMIT-ID line – reduced scan times and increased FOV

Up to this point, we carried out all live animal studies on BMIT's bend magnet line and successfully have imaged the cortical vasculature of rat forelimbs bones at both a 2 and 3 Gy radiation dose without any signs of radiation sickness. These scans took approximately **13 to 14 minutes** to complete. The BMIT-BM line had a maximum beam height of 7 mm at a 23 m source-to-sample distance. However, we found that at 37 keV, there was only about 1.0 - 1.5 mm of optimal beam height. BMIT's new ORCA-FLASH camera and the ID lines much higher energy range (20-100 keV) compared to the BM-line (15-40 keV) revealed a 7.4 mm FOV was achievable while maintaining dose and resolution (Figure A.5). In live animal scans, we achieved an 8.9 mm FOV at both a 2 and 3 Gy dose with a slight loss in resolution – 11.8 µm down to 12.8 µm. That said, the drastically reduced scans times of **20 seconds** outweighed the slight loss in resolution. Overall, imaging on the ID line was a better approach for live animal imaging: 1) it promoted the welfare of the animals as they were under anesthesia for much shorter lengths of time, 2) the FOV was significantly increased and therefore imaging larger areas of the forelimb bones would significantly increase our ability to track the progression of BMUs throughout the bone and 3) significantly more animals could be imaged in a shift due to the drastic increase in scan times.

Figure A.4. Image showing FOV differences between BMIT's bend magnet (right; FOV = 1.01 mm) and insertion device (left; FOV = 8.9 mm) lines. The yellow color is used to infill the main marrow cavity and porosity for visualization purposes.

A.31.1. May 2016 – First imaging of fatigued loaded rat ulnae

During this beam time, I imaged the first fatigue loaded forelimbs, *in vivo*, on the BMIT-ID line using the ORCA-Flash camera. Most of the scans were a success, except for two from the first imaging session that showed some minor movement. Due to the ID line's higher flux and energy, we achieved a FOV of 8.9 mm, a significant increase from the bend magnet line's 1.0 – 1.5 mm FOV **(**Figure A.4). This should have made tracking individual BMU's much more efficient and FOV placement between successive scans less critical. The average scan time also significantly decreased—**30 seconds** compared to the 10 -14 minutes on the bend magnet. On average, an animal could be anesthetized, imaged, and recovered in roughly 30 minutes, thus with this protocol, a large sample size of animals was feasible for future purposes. Finally,

reconstruction of scans showed some evidence of resorption spaces; however, further analysis (described in July 2016) showed this was not to the extent we expected. A TLD chip was scanned after every three animals scanned for dosage verification.

A.31.2. July 2016 – Confirmation attempts of fatigue loading through post-mortem, *ex vivo* scans

Based on the recommendations received from my July 7th, 2016, annual committee meeting, I imaged, *ex vivo*, the fatigued and contralateral ulna for each of the rats that were fatigue loaded and imaged, *in vivo* (May 2016). The purpose of this was to confirm that the fatigue loading protocol was successful compared to non-fatigued contralateral control left forelimb. Comparison of these two datasets indicated that while there was some evidence of remodeling in the fatigued limbs, it was not to the extent that was anticipated – increased remodeling activity in the fatigued limb compared to the contralateral control limb was not consistently observed. This finding meant further fatigue loading protocol testing was required, which altered beamtime schedules discussed in the following sections.

A.31.3. Nov-Dec 2016 – Imaging of barium sulfate stained microcracks

Originally, this beam time was intended to: 1) scan fatigued forelimbs of rats, *in vivo*, using the same protocols established in May 2016, and 2) test barium sulfate ($BaSO_4$) as a label for a contrast-enhanced high-resolution SR-micro-CT protocol to visualize microcracks**.** However, it was decided further *in vivo* imaging of animals at the CLS before the fatigue loading protocol was verified was not a proficient use of either beamtime or research animals. Thus, fatigued animals were not imaged at the CLS for these allotted shifts. Further testing of the fatigue loading protocol had been carried out, and additional beamtime had been requested.

A.31.4. March - May 2018 – End of rat fatigue loading analyses

Originally, this beam time was to be used to: 1) scan forelimbs of rats, *in vivo*, fatigued to 30% displacement with the new fatigue loading protocol refined in Aug 2018 and 2) test a modified barium sulfate ($BaSO_4$) protocol based on discussion with the original author, as a label for a contrast enhanced high-resolution SR-micro-CT protocol to visualize microcracks**.** However,

further inconclusive results meant it was decided that further *in vivo* imaging of animals at the CLS before the fatigue loading protocol was verified was not a proficient use of either beamtime or research animals. Thus, fatigued animals were not imaged at the CLS for these allotted shifts and no further proposals for *in vivo* imaging will be submitted till the issue with the fatigue loading can be sorted out.

A.32. *In vivo* Imaging Results – Rabbit Model

A.32.1. May 2016 – First *in vivo* imaging using New Zealand white rabbits

First *in vivo* scans on rabbits on the BMIT-ID line. Challenging beamtime, issues with rabbit holder design, animal respiration during imaging (one rabbit died) and personnel leaving mid-way through the project.

A.32.2. July 2016 – Testing of rabbit imaging protocol

In vivo imaging of three rabbits treated with GC was done. Rabbits were successfully imaged; however, a re-design of the rabbit holder was needed as respiration issues were still occurring.

A.32.3. June 2018 – Imaging of PTH treated rabbits and testing of redesigned rabbit holder

Fifteen rabbits treated with PTH were imaged *in vivo* on the BMIT-ID line. With the assistance of Dr. Ning Zhu of BMIT and the Department of Physics machine shop, I redesigned the rabbit holder (Figure A.5.) and trialed it for the first time, which proved to be quite successful. The new holder was better for the animals (respiration rates were consistently much more stable), and it reduced the amount of time required to sedate, image, and recover a rabbit, from upwards of 2.5 hours to as little as 35 minutes.

A.32.4. Sept 2019 – Imaging of OVX and GC treated rabbits

Twenty rabbits divided into four groups of five animals each: SHAM, OVX, GC, and OVX+GC were successfully imaged *in vivo* on the BMIT-ID line. Repeated use of the redesigned rabbit holder (A.5.) has continued to prove beneficial.

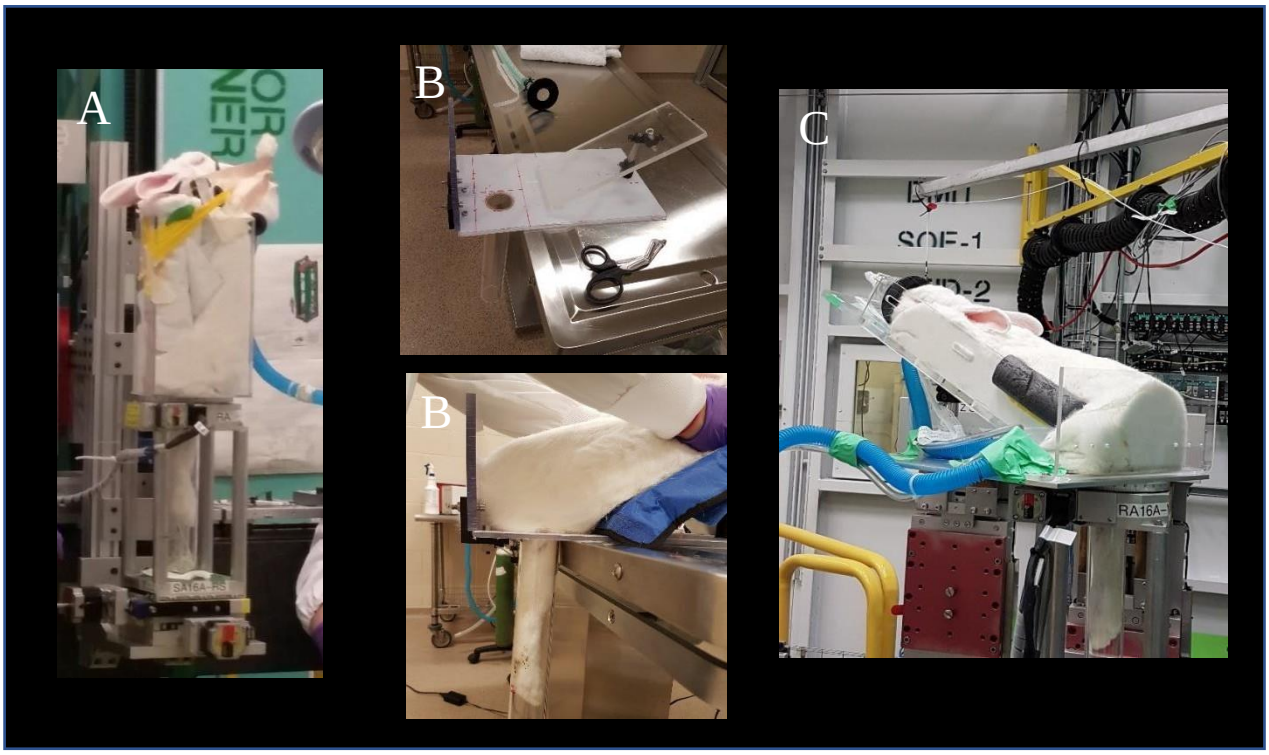

Figure A.5. Progression of rabbit holder used for *in vivo* imaging. The original holder (A), based on (Voor et al., 2008), placed the body of the rabbit in a vertical position with caused respiratory-related (i.e., shallow breaths and/or cessation of breathing) issues. The holder was redesigned (B-top) to position the rabbit's torso at more of a natural angle which minimized 'slumping' of the internal anatomy and thus, promoting a consistent, open airway under anesthesia while restraining the right, hindlimb distally for *in vivo* imaging (B-bottom). Testing of the holder (C) proved to be quite successful and since its implementation, subsequent *in vivo* rabbit experiments carried out on the BMIT-ID line (C) have proceeded without incidence of breathing issue or loss of animal life.

Appendix B Induction of cortical bone remodeling in the rat ulna through fatigue loading

B.1. Background

Remodeling occurs minimally, if at all, in the cortical bone of rats and therefore must be artificially induced. A method reported in the literature to do is fatigue loading of the ulna. In a study by Hsieh and Silva (2002) resorption space and osteoclast density was shown to significantly increase after fatigue loading and the presence of osteoblasts situated adjacent to osteoclasts in numerous resorption spaces was indicative of the formation of BMUs. Bentolila et al. (1998) showed that fatigue loading of rat ulnae positively correlated with the presence of intracortical remodeling, whereas no remodeling occurred in control bones. Rat ulnae are optimal for fatigue loading for two main reasons: 1) they can be loaded in their natural medial-lateral curvature using axial compression to induce bending of the bone, without introducing structural biases, and; 2) the natural curvature of the bone induces maximum strain located at the mid-diaphysis likely reflecting the natural strain distribution exerted as a result of natural locomotion (Torrance et al., 1994). Based on the reported success of this model, I selected fatigue loading as the means to induce bone remodeling in the cortical bone of rats' ulnae in order to study the relation between BMU initiation and steering in relation to microdamage. Specifications for this fatigue loading system required a means to: 1) hold and load bones in their correct anatomical orientation; 2) compress bone at predetermined forces and cycles for specific periods; 3) provide constant feedback regarding the time, force, number of cycles and bone displacement and perhaps most importantly; 4) a mechanism to cease the application of load if the specimen reaches a predetermined decline in stiffness to avoid fracture.

B.2. Fatigue loading design and testing

The most common way to induce loading in a rat's ulna is to use a constant-load, cam-driven device that applies an axial compressive load to the bone. In collaboration with Dr. J. D. Johnston and graduate students Dustin Eichhorn, Matt McDonald, and Kadin Majcher of the University of Saskatchewan's Department of Mechanical Engineering, we designed a non-invasive mechanical loading system that applied axially directed compressive loads to bone, both *in vivo* and *ex vivo* based on systems used previously (Torrance et al., 1994, Bentolila et al., 1998). The limb holder was designed to fit the flexed carpus and ulna with adequate depth and width to avoid using padding in the cups. This was based on email correspondence with Dr. Mitch Schaffler (City College of New York), who indicated padding induces friction between the skin and cups, causing significant tissue abrasions. Padding in the cups would also interfere with the force (N) directly applied to the bone. To create a 'best fit,' a fully intact rat forelimb was impressed in modeling putty at both the flexed carpus and elbow to serve as a template for the manufacture of the cups. Specific parts (i.e., limb holder and support plate for the animal) were manufactured by the University of Saskatchewan's Physics Department machine shop.

B.21. Fatigue loading protocol overview

All initial testing of fatigue loading occurred *ex vivo* – both on excised limbs and intact rat carcasses. Axial compressive loads were applied to the ulnae via the MTS Bionix 858 materials test machine with an MTS 250 N load cell (Figure B.1). During loading, the rat was placed on a platform that positions the forelimb vertically within the materials test machine to secure it at both the flexed carpus and elbow within the custom cups previously described (Figure B.1.). To induce remodeling within the rats' ulnae, the *in vivo* fatigue loading procedure was based on previously reported protocols (Bentolila et al., 1998, Torrance et al., 1994, Hsieh and Silva, 2002, Hsieh and Turner, 2001, Macione et al., 2011) and our *ex vivo* protocol verification tests.

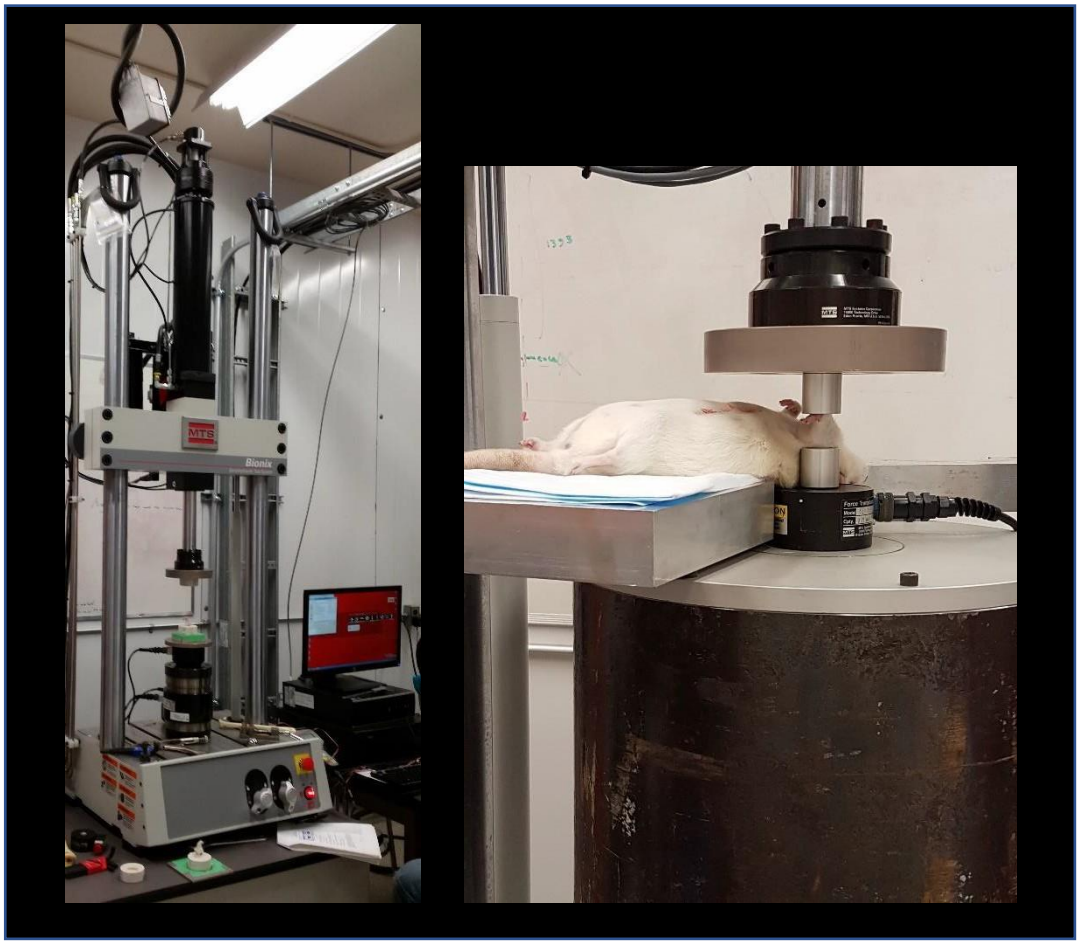

Figure B.1. Setting up of the MTS Bionix 858 materials test machine. *Ex vivo* testing of the fatigue loading protocol and the custom design of the custom cups securing the flexed carpus and elbow. Initial tests were performed on excised (left) and intact (right) forelimbs of rat cadavers before ensuing any fatigue loading on live animals.

B.22. *Ex vivo* tests

For this study, a 30% maximum decrease in ulnar whole bone stiffness was selected as a pre-failure stopping point which results in damage of the bone matrix but not fracture (Verborgt et al., 2000, Schaffler et al., 1989, Schaffler et al., 1990, Burr et al., 1997, Bentolila et al., 1998). A pre-failure stopping point >30% has been used previously to induce significant microdamage and thus ensure a response within bone, however the risk of fracture significantly increases (Hsiehand Silva, 2002). A literature review has shown that a force of 20 N (3500-4500 microstrain) elicits a response within bone (Bentolila et al., 1998, Torrance et al., 1994) in the form of intracortical resorption. The relationship between strain and loading cycles also needs to be taken into consideration. Carter et al. (1981) noted that bone could fracture at a relatively low number of

cycles (1000 – 100,000) when the strain is significant (5000 – 10,000 microstrain). Torrance et al. (1994) showed that loads of 17 N delivered at 10 and 20 Hz over 1200 or 12,000 cycles produced the same responses within bone, but when a 20 N load delivered at the same frequency and number of cycles was tested, a significant response within the bone was noted. Thus, we tested a 20 N at a low number of cycles and speed; 1000 and 1 & 2 Hz, respectively on excised Sprague-Dawley rat forelimbs that were secured in PPMA cups for placement within the materials test machine as the customized cups were not available at that time. There are several benefits from both an animal welfare and logistics standpoint for implementing a high strain at a low frequency over a small number of cycles: 1) the potential of causing soft tissue damage and bone fracture was reduced while still administering sufficient strain to the bone to induce a remodeling response, 2) the length of time the animal was under anaesthesia was reduced and 3) a short protocol means that numerous animals could be fatigued in one day. The materials test machine which supplies the load was controlled by a custom software program. A RAMP function instructed the actuator to apply an initial 10 N to the ulna, then cycle on a sine wave between 20 N and no load for the prescribed number of cycles. Testing showed that at a 20 N, 2 Hz, 1000 cycle, loading took a total of 10 minutes, whereas the same protocol ran at 1 Hz took 16 minutes. The limb fatigued at 2 Hz fractured. The fracture could have been due to the angle the limb was fixed at in the PPMA cup, however because the rate of loading does not seem to be as significant of a factor in inducing a remodeling response, it was decided the slower 1 Hz rate was better suited for the wellbeing of the rat and was used for all subsequent loading. A coding error in the software program was noted as data from the tests did not record and this was subsequently fixed. The *ex vivo* tests provided a means to test both the materials test machine as well as the software program to identify any potential problems that needed to be addressed before introducing live animals. The results were subsequently used for the two phases of live animal fatigue loading: 1) protocol verification and 2) *in vivo* fatigue loading for synchrotron imaging.

B.23. Protocol verification

This portion of the experiment tested both the fatigue loading protocol and timeframe at which BMU remodeling appears through intracortical resorption, reported to occur 10 days post loading (Bentolila et al., 1998). Six Sprague-Dawley rats' (aged 8 weeks) right limbs were fatigue loaded and divided into two euthanasia time points to ensure the presence of BMUs for subsequent

imaging at the CLS. I euthanized 3 rats, 5 days' post loading and then another 3 rats, 10 days' post loading. Both the control and fatigued forelimb from each animal was dissected and imaged in the desktop Micro CT. Scans were reconstructed using NRecon and rendered in AMIRA to qualitatively verify the presence or absence of BMU resorption spaces. The control limbs showed no overt signs of BMU activity. Forelimbs from the 10-day group showed slightly more of response within the bone (i.e., porosity which potentially resembled BMUs) compared to the 5-day group. It was decided that the optimal timeframe between fatigue loading and the first *in vivo* imaging session for imaging BMUs in live animals at the CLS.

B.24. First fatigue loading test

The results from both the *ex vivo* and protocol verification pilot data were used to carry out optimal fatigue loading and synchrotron imaging protocols and schedules. Twelve Sprague-Dawley rats' (aged 8 weeks) right limbs were fatigue loaded using a 20 N, 1,000 cycle, 1 Hz protocol. The left limbs served as contralateral controls. Throughout loading, animals were kept under isoflurane gas anesthesia and vital signs were recorded in five-minute intervals using a rectal probe thermometer and a pulse oximeter. Post loading, animals were supported with fluids administered subcutaneously at a dose of 10 ml/kg/hr. In the event an animal sustained a fracture during loading, the materials test machine would stop, and the animal would be immediately euthanized by overdose of isoflurane gas (although fortunately, this never occurred). Control of the MTS Bionix 858 materials test machine and software was carried out by engineering graduate students Dustin Eichhorn and Matt McDonald. Post loading, animals were monitored for signs of pain or distress in the form of limping, favoring, or gnawing/chewing of the fatigued limb. Each animal's limb was inspected at both the carpus and elbow after loading for signs of tissue damage, to which none were noted. During recovery from anaesthesia, the animals quickly regained use of the fatigued limb within ~20 minutes, indicating no severe impediment to the bone or tissues had occurred. Thus, all 12 animals were loaded with no incident of fracture.

B.24.1. *In vivo* imaging of fatigued animals - Results

To identify if the fatigue loading protocol was inducing BMU remodeling within the cortical bone of the rats' ulnae, *in vivo* and *ex vivo* scans collected on the BMIT-ID line were

compared. This resulted in three scan sets per animal, one *in vivo* fatigued ulna scan (May 2016) and an *ex vivo* scan for both the fatigued and contralateral control limb (July 2016). An assessment of the 3D renders using AMIRA indicated relatively little evidence of remodeling in the fatigued limbs, – increased remodeling activity in the fatigued limb compared to the contralateral control limb was not consistently observed (Figure B.2.).

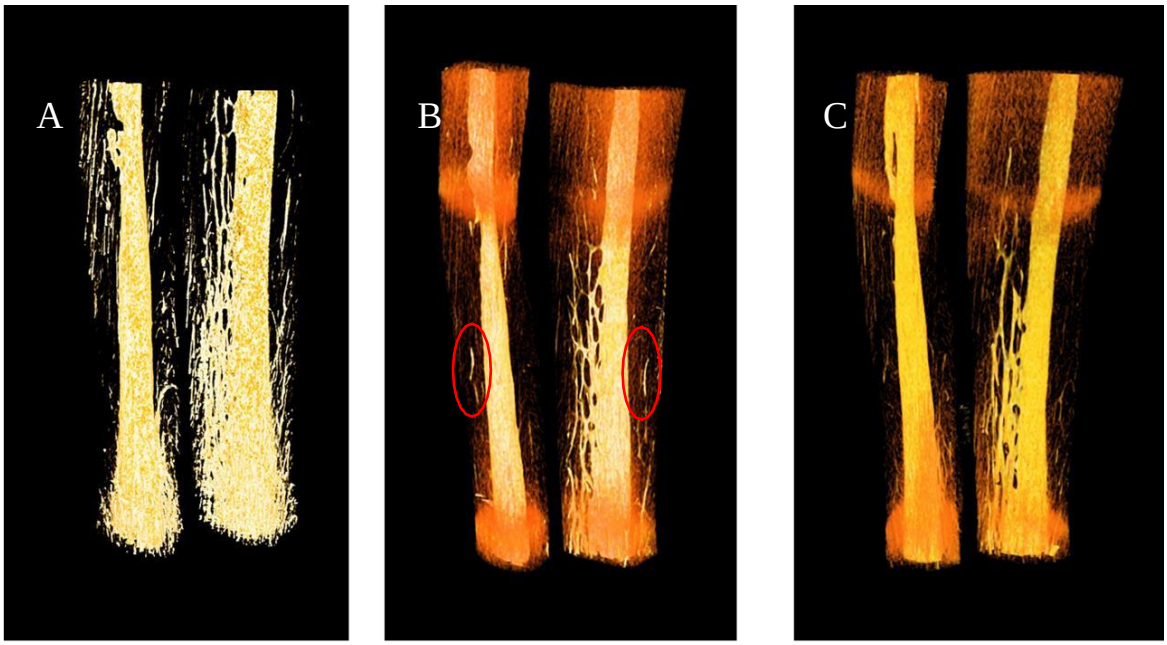

Figure B.2. Images of fatigue loaded forelimbs. Comparison of fatigue loaded (right - A & B) and contralateral control (left - C) indicated potential evidence, however slight, of induced BMU remodeling (red circles).

B.3. Fatigue loading – Protocol refinement

The protocol used to fatigue the first group of rats, *in vivo* was carried out on right limbs using a 20 N, 1,000 cycle, 1 Hz protocol. The left limbs were used as contralateral controls. This protocol was chosen initially as a literature review implied that force (N) outweighed the rate (Hz) or number of cycles for inducing fatigue. A low cycle protocol would be optimal for several reasons, including larger sample sizes and diminished anesthesia times. However, the biggest benefit would be logistic. Animals were not permitted to remain in the Engineering lab overnight and thus must be transported daily in correspondence with the LASU lab technicians work schedule – animals can be dropped off earliest 8 am and picked up latest 3:30 pm. Incorporating time required for machine set-up, anaesthesia and recovery times, a long cycle protocol would mean substantially fewer animals could be fatigued per day which would limit the sample number overall. Also, animals first *in vivo* scan occurs 10 days' post loading, thus fatiguing over several consecutive days is not feasible for beamtime scheduling – the beam cannot be scheduled several days in a row and then again two weeks later. As discussed previously, the fatigue loading protocol tested in May 2016 was to be implemented for subsequent *in vivo* imaging of additional fatigued animals on the BMIT-ID in Nov/Dec 2016. However, based on the inconclusive results, it was decided the fatigue loading protocol required adjustment and further verification.

B.31. Fatigue loading protocol modification – *Ex vivo* tests

Before fatiguing any further live animals, carcasses of Sprague-Dawley rats of appropriate size and weight were selected for testing protocol modifications. To induce a marked BMU remodeling response, we mimicked the protocol of Bentolila et al. (1998), who successfully induced remodeling in the ulnae of Sprague-Dawley rats via a 20 N load administered over 4 Hz at 8853 ± 4201 cycles. This protocol cycled at a significantly faster rate, so to begin with, we fatigued three limbs at 20 N for 200 cycles @ 4 Hz to identify if that speed would result in bone fracture(s). Two out of the three limbs did fracture, but this was determined to be a calibration issue, not the cycle rate. To further verify this, we tested a 20 N, 1000 cycle @ 4 Hz protocol to which the limb did not incur any fractures. Next, we tested the mean (20 N @ 4 Hz, 8853 cycles) and max (20 N @ 4 Hz, 13, 054 cycles) rates Bentolila et al. (1998) required to reach a 30% decrease in ulnae whole bone stiffness. The limbs for both cycles performed well, no fractures

were incurred, but some external tissue damage was noted. Compared to the original fatigue time of 16 minutes, the mean and max protocols took 36 minutes and 50 minutes to complete, respectively. To identify if this new fatigue loading protocol would induce sufficient microdamage to elicit a remodeling response in live animals, the ulnae were dissected out of the forelimbs, cleaned, and stained using basic fuchsin to identify the presence of microcracks. Herman et al. (2010) hypothesized that bone resorption is dependent upon the type of microdamage present 1) diffuse damage consistent of clusters of microcracks too small (less than 1-2 μm in length) to distinguish from one another and 2) linear damage consistent of cracks measuring 10 -100+ μm in length. Their findings indicated that 14 days' post loading, intracortical resorption was only observed in the ulnae of rats that also exhibited linear microcracks. Therefore, if microcracks were observed in the ulnae that we fatigued *ex vivo*, this would be indicative that a BMU remodeling response would also have been observed had these limbs been fatigued in live animals. The mid-diaphysis was removed and stained using a graduated protocol that requires the bone to be immersed in 1% basic fuchsin mixed in a series of 80%, 90% and 100% ETOH under vacuum (Burr and Hooser, 1995). Due to equipment malfunction, sections had to be hand ground which was difficult due to the very small size of the ulnae (~2.5 mm in diameter) thus polishing out all surface scratches from thin sectioning was not achieved however there was evidence of microcracks stained with basic fuchsin present in one of the bones fatigued using the 20 N, 13, 054 cycle @ 4 Hz. The results from the fatigue protocol modifications tests and the subsequent histological analysis was used to submit an ethics amendment to run the fatigue loading modification in live rats.

B.32. Fatigue loading protocol modification – Testing *in vivo*

Six rats were acquired for testing the fatigue loading protocol modification *in vivo*. The right ulnae of three animals were fatigued under the mean (8853) cycle and two under the max (13,054) cycle protocols. Left limbs served as contralateral controls. One rat served as a control and did not undergo anaesthesia or fatigue loading. During fatiguing, no fractures occurred, and all animals ambulated on all four paws roughly 50 min after being taken off isoflurane gas. The tissues that contacted the cups during fatigue exhibited minimal damage. Post fatigue, animals were monitored daily for signs of distress or discomfort both overall and in the fatigued limb, to which none were observed. Ten days' post loading, all six rats were euthanized and the right and

left forelimbs for each animal were immediately removed and preserved in 10% neutral buffered formalin for further analysis. To further verify these results, the fatigued and contralateral control ulnae were stained with barium sulfate ($BaSO_4$) (Turnbull et al., 2011) and imaged on the BMIT-ID line. The mechanism of $BaSO_4$ staining is that it precipitates into any voids present within a tissue and 'highlights' microdamage such as microcracks (see Appendix C for further discussion). Thus, the much higher resolution capabilities of the BMIT-ID line would enable us to target above the k-edge of barium and illuminate any microcracks and resorption spaces present within these ulnae which would be a positive indication that the new protocol induces enough fatigue to induce a remodeling response within the bone.

Post euthanasia, the ulnae from both the fatigued and contralateral control limb were removed and imaged *ex vivo* in the desktop 1172 micro-CT and subsequently stained with $BaSO_4$ and imaged, *ex vivo* on the BMIT-ID line to identify the presence of microcracks. Full diaphysis scans for each limb were acquired via the 'oversize' scan setting in the 1172 SkyScan Micro-CT (Bruker, Belgium) with the following settings: 20 µm, 60 keV, 0.5 step, 3 frame ave, 120 ms exp with an Al filter. Microdamage is reported to concentrate in the mid-diaphyseal, medial region of the bone that undergoes compression during loading (Herman et al., 2010, Seref-Ferlengez et al., 2014, Muir et al., 2007, Tami et al., 2003) thus, a higher resolution (10 µm, 60 keV, 0.5 step, 3 frame ave, exposure 160 mm/s) scan was also carried out at the mid-diaphysis portion of the bone. Regions of woven bone at the periosteal surface in the more distal region of the ulna was noted in a few of the bones so 10 µm distal scans were also taken. Initially, this protocol looked promising, as analysis of both the mid-diaphysis and distal 10 µm scans showed the two rats fatigued for 13,054 (high) cycles displayed potential bone remodeling and evidence of a reaction to the loading on the periosteal surface through new bone formation in the right fatigued ulna compared against the contralateral left ulna (Figure B.3). In comparison, only one of the three rats fatigued for 8,853 (mean) cycles showed a marked difference in remodeling and periosteal bone reaction (Figure B.3). However, upon further analysis from the high-resolution SRµCT scans, classic BMU resorption spaces were not extensively observed. Bewilderingly, the micro-CT scans of the one control animal showed what seemed to be remodeling activity in both the right and left ulnae even though this animal was not fatigued nor received any different treatment in comparison to the experimental rats. Secondly, while microcracks were observed in the fatigued ulnae, non-fatigued

contralateral limbs from two rats also exhibited microcracks and even more surprisingly, microcracks in the control rat were also apparent.

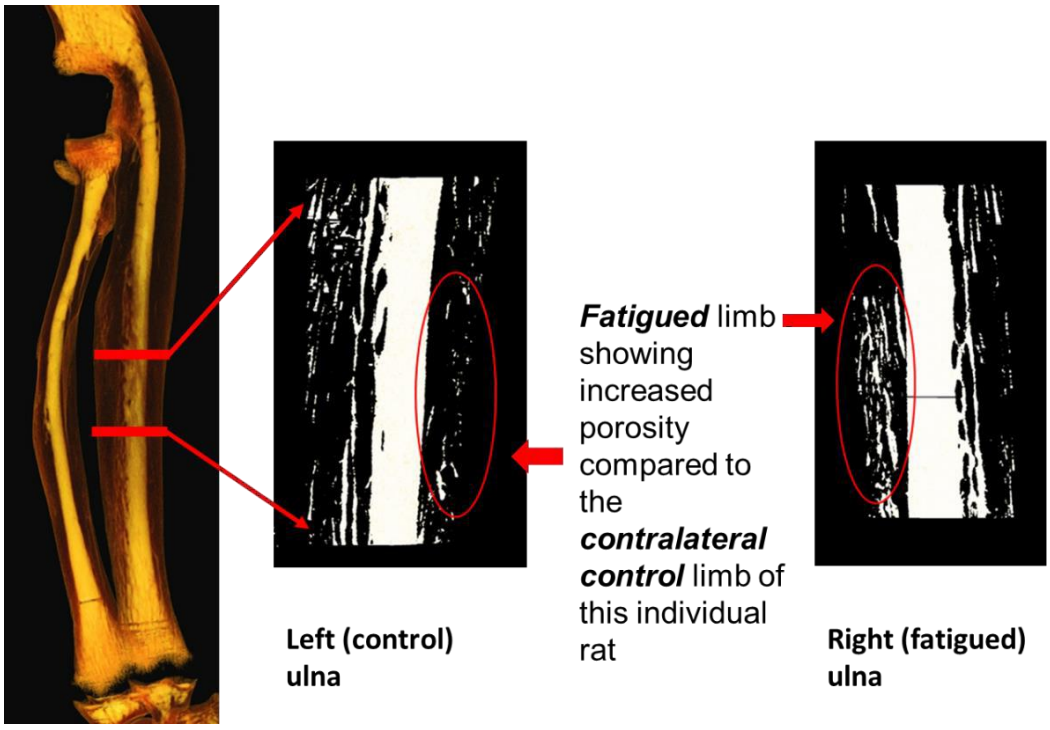

Figure B.3. Modified fatigue loading protocol tested *ex vivo*. Desktop micro-CT analysis indicated some evidence of increased porosity at both the minimum (20 N @ 4 Hz, 8853 cycles – image above) and max (20 N @ 4 Hz, 13, 054 cycles – image below) protocols required to induce BMU remodeling previously reported by (Bentolila et al., 1998).

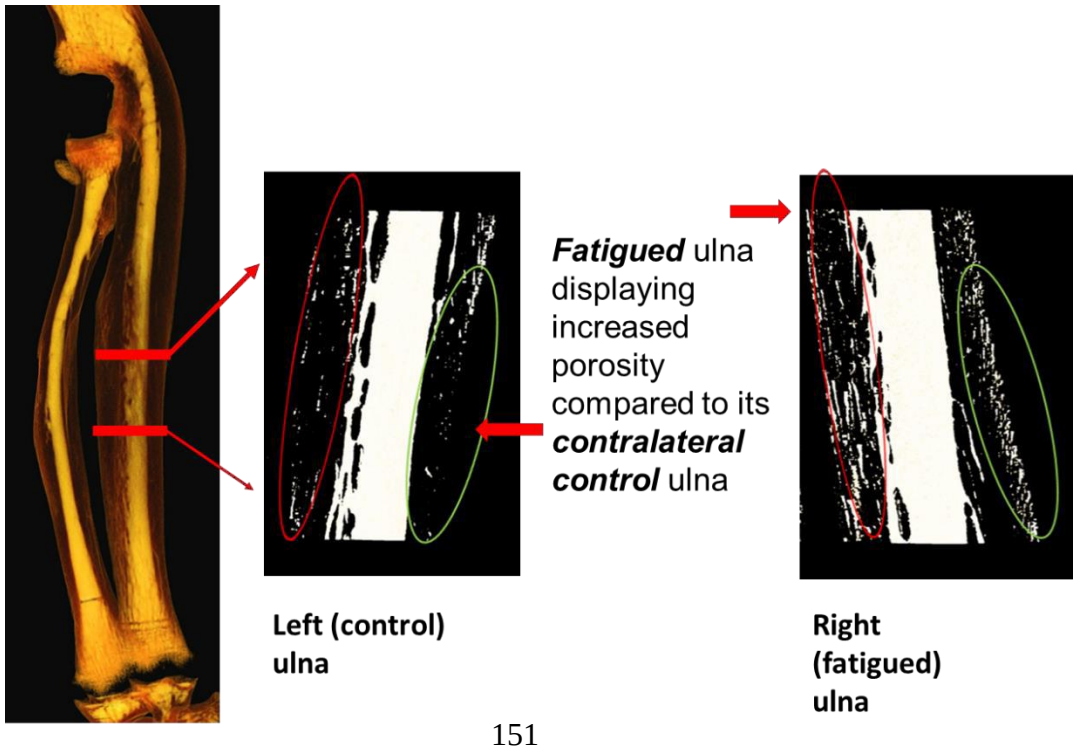

B.33. Fatigue loading protocol modification – 30% ulnar stiffness displacement

Based on discussions with Dr. Johnston, it was determined the MTS Bionix 858 materials test machine could be programmed to fatigue each animal's forelimb until 30% displacement in ulnar stiffness was achieved, as opposed to a pre-determined number of cycles. After the forelimb has been placed into the contact cups, the actuator arm compresses the forelimb to apply the appropriate force and cyclically loads the forelimb for 500 cycles to displace skin and soft tissue. Upon completion of 500 cycles, the actuator arm returns to the starting position which gave the measure L0: maximum displacement value at 20 N which was subsequently used to calculate, K1: initial stiffness measure at 500 cycles. Measure K2 is 70% of measure K1 (aka 30% loss) and this value was then used to calculate value Dx which indicated to the program that 30% displacement of ulnar stiffness had been reached (Force (F)/K2 = -20 N/K2). With the assistance of engineering graduate student, Kadin Majcher, we tested this protocol on the right forelimb of 8 rats, *in vivo*, in Aug-Sept 2017. Euthanasia was carried out 14 (n=4) or 20 (n=4) days post loading. Frost (1983) described the remodeling cycle takes approximately 12 weeks to complete—activation requires 3 – 5 days, resorption commences in 22 days and the remainder of time is allotted for bone formation. A review of the literature indicates resorption spaces appear within 10 – 14 days' post loading (Kennedy et al., 2012) with peak intracortical resorption occurring in some cases 12 days (Hsieh and Silva, 2002) and 14 days (Seref-Ferlengez et al., 2014, Muir et al., 2007) post fatigue loading in the ulnae of rats. Thus, this euthanasia schedule should prove successful for observing BMUs induced by the loading protocol. Again, post euthanasia, the fatigued and contralateral control limb were stained with $BaSO_4$ and imaged on the BMIT-ID line to identify if both BMUs and microcracks were present. Unfortunately, due to numerous technical issues, only two ulnae were successfully imaged and therefore, subsequent micro-CT scans were carried out on the desktop micro-CT. Qualitative analysis of the reconstructed data from these scans was again underwhelming, very few BMUs were observed (Figure B.4). This finding was puzzling as I measured the total length of both the fatigued and non-fatigued contralateral control ulna for each rat and all, but one, showed a difference in length between the two ulnae ranging from 0.24 mm – 0.82 mm so clearly, the fatigue loading did impact the displacement of the bone.

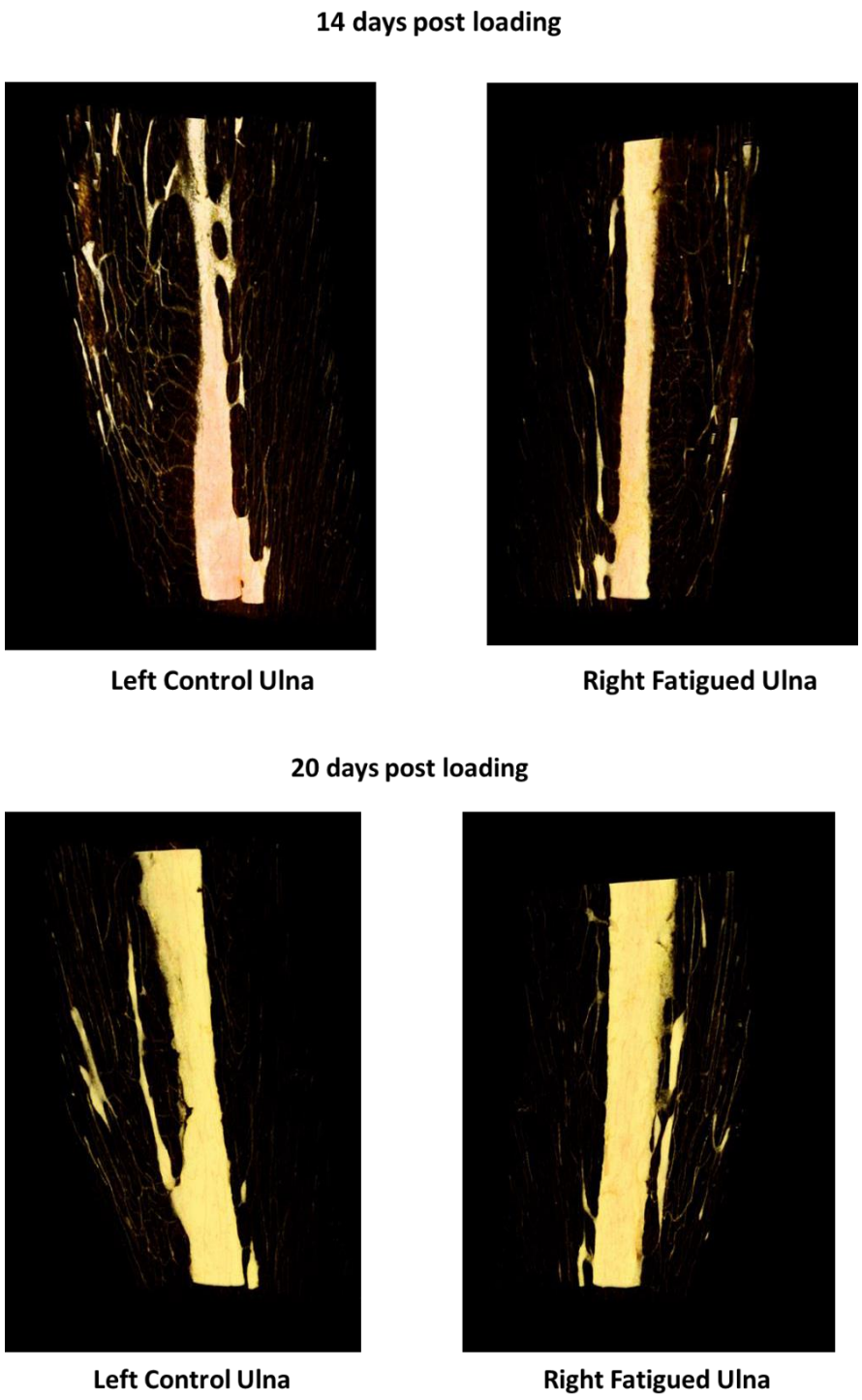

Figure B.4. 30% ulnar stiffness displacement fatigue loading protocol. Comparison of right (fatigued) and left (control) ulnae within individual rats fatigued to the previously reported 30% ulnar stiffness displacement did not induce extensive BMU remodeling in 14 (top)- or 20 (bottom)-days post loading.

C.1. Conclusions – Rat fatigue loading model

For reasons unknown, replicating this published model for inducing BMU remodeling within the ulnae of rats was challenging. As has been described, numerous modifications to the fatigue loading protocol were carried out, yet I was not able to extensively induce BMU remodeling within the cortical bone of rat ulnae. A final modification to the pre-load cycle that displaces skin and soft tissues has been tested. However due to the numerous issues associated with this model, no further loading in live rats was pursued. The decision was made especially because of the success that we have had with the rabbit osteoporosis models that served as the animal model for the remainder of my thesis research.

Appendix C Barium sulfate ($BaSO_4$) Stain

Due to the destructive and tedious nature of traditional histology, non-destructive techniques such as contrast-enhanced micro-CT are becoming increasingly popular for detecting microdamage in both trabecular and cortical bone (Wang et al., 2007, Leng et al., 2008, Landrigan et al., 2011, Turnbull et al., 2011) and their accuracy has been strongly correlated to that of basic fuchsin histology (Landrigan et al., 2011). Microcracks are typically too small to detect with conventional micro-CT however, introducing a contrast agent that has a higher x-ray attenuation than that of bone (e.g., barium) makes it possible to delineate and thus detect such damage. In particular, $BaSO_4$ has been shown to successfully highlight areas of microdamage in human cortical (Landrigan et al., 2011) and bovine bone (Lee et al., 2003, Wang et al., 2007) due to the precipitation reaction of the staining mechanism where $BaCL_2\,(aq) + Na_2SO_4\,(aq) \rightarrow BaSO_4\,(s) + 2NaCl\,(aq)$ causing barium and sulfate ions to concentrate into void spaces within the tissue such as microcracks, vasculature and areas of damage (Leng et al., 2008). Even with the addition of a contrast agent, it should be noted that while indeed areas of microdamage are detectable in the form of areas of bright voxels situated along propagating cracks (Leng et al., 2008), conventional micro-CT is still resolution limited for delineating the 3D structure of the microcracks similar as to what is seen using histology. However, groups at both the European Synchrotron (ESRF) and Swiss Light Source (SLS) have shown that microcracks in human trabecular and cortical bone can be detected using SR micro-CT (Larrue et al., 2011, Haupert et al., 2014, Thurner et al., 2006) with image settings comparable to what can be achieved on the ID line at BMIT. The addition of the $BaSO_4$ contrast agent (which was not used for the ESRF or Swiss Light Source studies) will help overcome challenges with achieving sufficient resolution.

C1. $BaSO_4$ protocol

The $BaSO_4$ protocol used here is based on (Turnbull et al., 2011). Each ulna was placed within a falcon tube and submerged in a solution of $BaCl_2$ which was created by mixing 50 ml of $BaCl_2 \cdot 2H_2O$ with 50 ml acetone and 50 ml phosphate buffered saline. Samples were placed under vacuum for 72 hours. To promote perfusion while simultaneously minimizing evaporation of the solution, falcon tubes were loosely caped with a small puncture inthe caps. After 72 hours, the

bones were rinsed with DI water and placed in a solution of 50ml Na_2SO_4 mixed with 50 ml acetone and 50 ml phosphate buffered saline for an additional 72 hours under vacuum. After 72 hours, bones were rinsed with DI water and rea ready for imaging.

References

2004. WHO scientific group on the assessment of osteoporosis at primary health care level. *WHO Scientific Group on the Assessment of Osteoporosis at the Primary Health Care Level.* Brussels, Belgium: WHO Press.

2015. *Osteoporosis Canada* [Online]. Available: www.osteoporosis.ca.

ADAMI, S., BRAGA, V., SQUARANTI, R., ROSSINI, M., GATTI, D. & ZAMBERLAN, N. 1998. Bone measurements in asymptomatic primary hyperparathyroidism. *Bone,* 22**,** 565-70.

ADLER, R. A. 2016. Bisphosphonates and atypical femoral fractures. *Curr Opin Endocrinol Diabetes Obes,* 23**,** 430-434.

ADLER, R. A. 2018. Update on osteoporosis in men. *Best Practice & Research Clinical Endocrinology & Metabolism,* 32**,** 759-772.

ALBRIGHT, F. 1940. Postmenopausal osteoporosis. *Trans. A. Amer. Phys.,* 55**,** 298-305.

ALTMAN, A. R., TSENG, W.-J., DE BAKKER, C. M. J., CHANDRA, A., LAN, S., HUH, B. K., LUO, S., LEONARD, M. B., QIN, L. & LIU, X. S. 2015. Quantification of skeletal growth, modeling, and remodeling by in vivo micro computed tomography. *Bone,* 81**,** 370-379.

AMPRINO, R. & BAIRATI, A. 1936. Processi di ricostruzione e di riassorbimento nella sostanza compatta delle ossa dell'uomo. *Zeitschrift für Zellforschung und Mikroskopische Anatomie,* 24**,** 439-511.

ANASTASILAKIS, A. D., POLYZOS, S. A., YAVROPOULOU, M. P. & MAKRAS, P. 2020. Combination and sequential treatment in women with postmenopausal osteoporosis. *Expert Opinion on Pharmacotherapy,* 21**,** 477-490.

ANDERSEN, T. L., ABDELGAWAD, M. E., KRISTENSEN, H. B., HAUGE, E. M., ROLIGHED, L., BOLLERSLEV, J., KJÆRSGAARD-ANDERSEN, P. & DELAISSE, J.-M. 2013. Understanding Coupling between Bone Resorption and Formation: Are Reversal Cells the Missing Link? *The American Journal of Pathology,* 183**,** 235-246.

ANDERSEN, T. L., SONDERGAARD, T. E., SKORZYNSKA, K. E., DAGNAES-HANSEN, F., PLESNER, T. L., HAUGE, E. M., PLESNER, T. & DELAISSE, J.-M. 2009. A Physical Mechanism for Coupling Bone Resorption and Formation in Adult Human Bone. *The American Journal of Pathology,* 174**,** 239-247.

ANDREASEN, C. M., DELAISSE, J.-M., VAN DER EERDEN, B. C. J., VAN LEEUWEN, J. P. T. M., DING, M. & ANDERSEN, T. L. 2018. Understanding age-induced cortical porosity in women: Is a negative BMU balance in quiescent osteons a major contributor? *Bone,* 117**,** 70-82.

ANDREASEN, C. M., DING, M., OVERGAARD, S., BOLLEN, P. & ANDERSEN, T. L. 2015. A reversal phase arrest uncoupling the bone formation and resorption contributes to the bone loss in glucocorticoid treated ovariectomised aged sheep. *Bone,* 75**,** 32-9.

ANDRONOWSKI, J. M., PRATT, I. V. & COOPER, D. M. L. 2017. Occurrence of osteon banding in adult human cortical bone. *American Journal of Physical Anthropology,* 164**,** 635-642.

ARFELLI, F., ASSANTE, M., BONVICINI, V., BRAVIN, A., CANTATORE, G., CASTELLI, E., PALMA, L. D., MICHIEL, M. D., LONGO, R., OLIVO, A., PANI, S., PONTONI, D., POROPAT, P., PREST, M., RASHEVSKY, A., TROMBA, G., VACCHI, A.,

VALLAZZA, E. & ZANCONATI, F. 1998. Low-dose phase contrast x-ray medical imaging. *Physics in Medicine and Biology,* 43**,** 2845.
ARHATARI, B. D., COOPER, D. M., THOMAS, C. D., CLEMENT, J. G. & PEELE, A. G. 2011. Imaging the 3D structure of secondary osteons in human cortical bone using phase-retrieval tomography. *Phys Med Biol,* 56**,** 5265-74.
ARITA, S., IKEDA, S., SAKAI, A., OKIMOTO, N., AKAHOSHI, S., NAGASHIMA, M., NISHIDA, A., ITO, M. & NAKAMURA, T. 2004. Human parathyroid hormone (1-34) increases mass and structure of the cortical shell, with resultant increase in lumbar bone strength, in ovariectomized rats. *J Bone Miner Metab,* 22**,** 530-40.
AUGAT, P. & SCHORLEMMER, S. 2006. The role of cortical bone and its microstructure in bone strength. *Age Ageing,* 35 Suppl 2**,** ii27-ii31.
BACH-GANSMO, F. L., IRVINE, S. C., BRÜEL, A., THOMSEN, J. S. & BIRKEDAL, H. 2013. Calcified cartilage islands in rat cortical bone. *Calcif Tissue Int,* 92**,** 330-8.
BAI, R. J., CHENG, X. G., YAN, D., QIAN, Z. H., LI, X. M., QU, H. & TIAN, W. 2012. Rabbit model of primary hyperparathyroidism induced by high-phosphate diet. *Domest Anim Endocrinol,* 42**,** 20-30.
BALA, Y., ZEBAZE, R. & SEEMAN, E. 2015. Role of cortical bone in bone fragility. *Curr Opin Rheumatol,* 27**,** 406-13.
BAOFENG, L., ZHI, Y., BEI, C., GUOLIN, M., QINGSHUI, Y. & JIAN, L. 2010. Characterization of a rabbit osteoporosis model induced by ovariectomy and glucocorticoid. *Acta Orthopaedica,* 81**,** 396-401.
BAR-SHAVIT, Z. 2007. The osteoclast: a multinucleated, hematopoietic-origin, bone-resorbing osteoimmune cell. *J Cell Biochem,* 102**,** 1130-9.
BASILLAIS, A., BENSAMOUN, S., CHAPPARD, C., BRUNET-IMBAULT, B., LEMINEUR, G., ILHARREBORDE, B., HO BA THO, M.-C. & BENHAMOU, C.-L. 2007. Three-dimensional characterization of cortical bone microstructure by microcomputed tomography: validation with ultrasonic and microscopic measurements. *Journal of Orthopaedic Science,* 12**,** 141-148.
BAYAT, S., APOSTOL, L., BOLLER, E., BROCHARD, T. & PEYRIN, F. 2005. In vivo imaging of bone micro-architecture in mice with 3D synchrotron radiation micro-tomography. *Nuclear Instruments and Methods in Physics Research Section A: Accelerators, Spectrometers, Detectors and Associated Equipment,* 548**,** 247-252.
BELL, K. L., LOVERIDGE, N., REEVE, J., THOMAS, C. D. L., FEIK, S. A. & CLEMENT, J. G. 2001. Super-osteons (remodeling clusters) in the cortex of the femoral shaft: Influence of age and gender. *The Anatomical Record,* 264**,** 378-386.
BENTOLILA, V., BOYCE, T. M., FYHRIE, D. P., DRUMB, R., SKERRY, T. M. & SCHAFFLER, M. B. 1998. Intracortical remodeling in adult rat long bones after fatigue loading. *Bone,* 23**,** 275-81.
BERENDSEN, A. D. & OLSEN, B. R. 2015. Bone development. *Bone,* 80**,** 14-18.
BIKLE, D. D., SAKATA, T. & HALLORAN, B. P. 2003. The impact of skeletal unloading on bone formation. *Gravit Space Biol Bull,* 16**,** 45-54.
BILEZIKIAN, J. P. 2008. Combination anabolic and antiresorptive therapy for osteoporosis: Opening the anabolic window. *Current Osteoporosis Reports,* 6**,** 24-30.
BJØRNEREM, Å., GHASEM-ZADEH, A., BUI, M., WANG, X., RANTZAU, C., NGUYEN, T. V., HOPPER, J. L., ZEBAZE, R. & SEEMAN, E. 2011. Remodeling markers are

associated with larger intracortical surface area but smaller trabecular surface area: A twin study. *Bone,* 49**,** 1125-1130.
BJØRNEREM, Å., WANG, X., BUI, M., GHASEM-ZADEH, A., HOPPER, J. L., ZEBAZE, R. & SEEMAN, E. 2018. Menopause-Related Appendicular Bone Loss is Mainly Cortical and Results in Increased Cortical Porosity. *Journal of Bone and Mineral Research,* 33**,** 598-605.
BLACK, D. M. & ROSEN, C. J. 2016. Postmenopausal Osteoporosis. *New England Journal of Medicine,* 374**,** 254-262.
BONFERRONI, C. E. 1936. Teoria statistica delle classi e calcolo delle probabilità. *Pubblicazioni del R Istituto Superiore di Scienze Economiche e Commerciali di Firenze.*
BORAH, B., GROSS, G. J., DUFRESNE, T. E., SMITH, T. S., COCKMAN, M. D., CHMIELEWSKI, P. A., LUNDY, M. W., HARTKE, J. R. & SOD, E. W. 2001. Three-dimensional microimaging (MRmicroI and microCT), finite element modeling, and rapid prototyping provide unique insights into bone architecture in osteoporosis. *Anat Rec,* 265**,** 101-10.
BORGES, J. S. & RABELO, G. D. 2021. Cortical Bone Modifications after Radiotherapy: Cortex Porosity and Osteonal Changes Evaluated Over Time. 32**,** 9-15.
BOSKEY, A. L. 2013. Bone composition: relationship to bone fragility and antiosteoporotic drug effects. *BoneKEy reports,* 2**,** 447-447.
BOTT, K. N., YUMOL, J. L., PETERS, S. J. & WARD, W. E. 2020. Sex-specific responses in trabecular and cortical microstructure of tibia due to repeated irradiation from micro-computed tomography in adult CD-1 mice. *Bone Rep,* 12**,** 100232.
BOUSSON, V., PEYRIN, F., BERGOT, C., HAUSARD, M., SAUTET, A. & LAREDO, J.-D. 2004. Cortical Bone in the Human Femoral Neck: Three-Dimensional Appearance and Porosity Using Synchrotron Radiation. *Journal of Bone and Mineral Research,* 19**,** 794-801.
BOUXSEIN, M. L. & SEEMAN, E. 2009. Quantifying the material and structural determinants of bone strength. *Best Pract Res Clin Rheumatol,* 23**,** 741-53.
BOYCE, B. F. & XING, L. 2007. The RANKL/RANK/OPG pathway. *Current Osteoporosis Reports,* 5**,** 98-104.
BOYCE, B. F. & XING, L. 2008. Functions of RANKL/RANK/OPG in bone modeling and remodeling. *Archives of biochemistry and biophysics,* 473**,** 139-146.
BOYCE, R. W., PADDOCK, C. L., FRANKS, A. F., JANKOWSKY, M. L. & ERIKSEN, E. F. 1996. Effects of intermittent hPTH(1–34) alone and in combination with 1,25(OH)2d3 or risedronate on endosteal bone remodeling in canine cancellous and cortical bone. *Journal of Bone and Mineral Research,* 11**,** 600-613.
BREELAND, G., SINKLER, M. A. & MENEZES, R. G. 2021. Embryology, Bone Ossification. *StatPearls.* Treasure Island (FL): StatPearls Publishing

BRIOT, K. & ROUX, C. 2015. Glucocorticoid-induced osteoporosis. *RMD open,* 1**,** e000014-e000014.
BRITZ, H. M., CARTER, Y., JOKIHAARA, J., LEPPÄNEN, O. V., JÄRVINEN, T. L. N., BELEV, G. & COOPER, D. M. L. 2012. Prolonged unloading in growing rats reduces cortical osteocyte lacunar density and volume in the distal tibia. *Bone,* 51**,** 913-919.

BRITZ, H. M., JOKIHAARA, J., LEPPANEN, O. V., JARVINEN, T. & COOPER, D. M. 2010. 3D visualization and quantification of rat cortical bone porosity using a desktop micro-CT system: a case study in the tibia. *J Microsc,* 240**,** 32-7.

BRITZ, H. M., THOMAS, C. D., CLEMENT, J. G. & COOPER, D. M. 2009. The relation of femoral osteon geometry to age, sex, height and weight. *Bone,* 45**,** 77-83.

BROMMAGE, R. 2020. New Targets and Emergent Therapies for Osteoporosis. *Handb Exp Pharmacol,* 262**,** 451-473.

BROMMAGE, R. & OHLSSON, C. 2018. Translational studies provide insights for the etiology and treatment of cortical bone osteoporosis. *Best Practice & Research Clinical Endocrinology & Metabolism,* 32**,** 329-340.

BROUWERS, J. E., LAMBERS, F. M., VAN RIETBERGEN, B., ITO, K. & HUISKES, R. 2009. Comparison of bone loss induced by ovariectomy and neurectomy in rats analyzed by in vivo micro-CT. *J Orthop Res,* 27**,** 1521-7.

BROUWERS, J. E. M., VAN RIETBERGEN, B. & HUISKES, R. 2007. No effects of in vivo micro-CT radiation on structural parameters and bone marrow cells in proximal tibia of wistar rats detected after eight weekly scans. *Journal of Orthopaedic Research,* 25**,** 1325-1332.

BUEHRING, B., VISWANATHAN, R., BINKLEY, N. & BUSSE, W. 2013. Glucocorticoid-induced osteoporosis: an update on effects and management. *J Allergy Clin Immunol,* 132**,** 1019-30.

BUENZLI, P. R., JEON, J., PIVONKA, P., SMITH, D. W. & CUMMINGS, P. T. 2012. Investigation of bone resorption within a cortical basic multicellular unit using a lattice-based computational model. *Bone,* 50**,** 378-89.

BUENZLI, P. R., PIVONKA, P. & SMITH, D. W. 2011. Spatio-temporal structure of cell distribution in cortical bone multicellular units: a mathematical model. *Bone,* 48**,** 918-26.

BUETTMANN, E. G. & SILVA, M. J. 2016. Development of an in vivo bone fatigue damage model using axial compression of the rabbit forelimb. *Journal of biomechanics,* 49**,** 3564-3569.

BURGER, E. H. & KLEIN-NULEND, J. 1999. Mechanotransduction in bone--role of the lacuno-canalicular network. *Faseb j,* 13 Suppl**,** S101-12.

BURGER, E. H., KLEIN-NULEND, J. & SMIT, T. H. 2003. Strain-derived canalicular fluid flow regulates osteoclast activity in a remodelling osteon—a proposal. *Journal of Biomechanics,* 36**,** 1453-1459.

BURGHARDT, A. J., BUIE, H. R., LAIB, A., MAJUMDAR, S. & BOYD, S. K. 2010. Reproducibility of direct quantitative measures of cortical bone microarchitecture of the distal radius and tibia by HR-pQCT. *Bone,* 47**,** 519-528.

BURR, D. B. 2002. Targeted and nontargeted remodeling. *Bone,* 30**,** 2-4.

BURR, D. B., FORWOOD, M. R., FYHRIE, D. P., MARTIN, R. B., SCHAFFLER, M. B. & TURNER, C. H. 1997. Bone Microdamage and Skeletal Fragility in Osteoporotic and Stress Fractures. *Journal of Bone and Mineral Research,* 12**,** 6-15.

BURR, D. B., HIRANO, T., TURNER, C. H., HOTCHKISS, C., BROMMAGE, R. & HOCK, J. M. 2001. Intermittently Administered Human Parathyroid Hormone(1–34) Treatment Increases Intracortical Bone Turnover and Porosity Without Reducing Bone Strength in the Humerus of Ovariectomized Cynomolgus Monkeys. *Journal of Bone and Mineral Research,* 16**,** 157-165.

BURR, D. B. & HOOSER, M. 1995. Alterations to the en bloc basic fuchsin staining protocol for the demonstration of microdamage produced in vivo. *Bone,* 17**,** 431-3.
BURR, D. B., MARTIN, R. B., SCHAFFLER, M. B. & RADIN, E. L. 1985. Bone remodeling in response to in vivo fatigue microdamage. *J Biomech,* 18**,** 189-200.
BURR, D. B., ROBLING, A. G. & TURNER, C. H. 2002. Effects of biomechanical stress on bones in animals. *Bone,* 30**,** 781-6.
CAMPBELL, G., OMINSKY, M. & BOYD, S. 2011. Bone quality is partially recovered after the discontinuation of RANKL administration in rats by increased bone mass on existing trabeculae: an in vivo micro-CT study. *Osteoporosis International,* 22**,** 931-942.
CANALIS, E. 2005. Mechanisms of glucocorticoid action in bone. *Current Osteoporosis Reports,* 3**,** 98-102.
CANALIS, E. & DELANY, A. M. 2002. Mechanisms of glucocorticoid action in bone. *Ann N Y Acad Sci,* 966**,** 73-81.
CARBONARE, L. D., ARLOT, M. E., CHAVASSIEUX, P. M., ROUX, J. P., PORTERO, N. R. & MEUNIER, P. J. 2001. Comparison of Trabecular Bone Microarchitecture and Remodeling in Glucocorticoid-Induced and Postmenopausal Osteoporosis. *Journal of Bone and Mineral Research,* 16**,** 97-103.
CARTER, D. R., CALER, W. E., SPENGLER, D. M. & FRANKEL, V. H. 1981. Fatigue behavior of adult cortical bone: the influence of mean strain and strain range. *Acta Orthop Scand,* 52**,** 481-90.
CARTER, Y., SUCHORAB, J. L., THOMAS, C. D. L., CLEMENT, J. G. & COOPER, D. M. L. 2014. Normal variation in cortical osteocyte lacunar parameters in healthy young males. *Journal of Anatomy,* 225**,** 328-336.
CARTER, Y., THOMAS, C. D., CLEMENT, J. G., PEELE, A. G., HANNAH, K. & COOPER, D. M. 2013a. Variation in osteocyte lacunar morphology and density in the human femur--a synchrotron radiation micro-CT study. *Bone,* 52**,** 126-32.
CARTER, Y., THOMAS, C. D. L., CLEMENT, J. G. & COOPER, D. M. L. 2013b. Femoral osteocyte lacunar density, volume and morphology in women across the lifespan. *Journal of Structural Biology,* 183**,** 519-526.
CASTAÑEDA, S., CALVO, E., LARGO, R., GONZALEZ-GONZALEZ, R., DE LA PIEDRA, C., DIAZ-CURIEL, M. & HERRERO-BEAUMONT, G. 2008. Characterization of a new experimental model of osteoporosis in rabbits. *J Bone Miner Metab,* 26**,** 53-9.
CASTAÑEDA, S., LARGO, R., CALVO, E., RODRÍGUEZ-SALVANÉS, F., MARCOS, M. E., DÍAZ-CURIEL, M. & HERRERO-BEAUMONT, G. 2006. Bone mineral measurements of subchondral and trabecular bone in healthy and osteoporotic rabbits. *Skeletal Radiol,* 35**,** 34-41.
CAULEY, J. A., ROBBINS, J., CHEN, Z., CUMMINGS, S. R., JACKSON, R. D., LACROIX, A. Z., LEBOFF, M., LEWIS, C. E., MCGOWAN, J., NEUNER, J., PETTINGER, M., STEFANICK, M. L., WACTAWSKI-WENDE, J. & WATTS, N. B. 2003. Effects of estrogen plus progestin on risk of fracture and bone mineral density: the Women's Health Initiative randomized trial. *Jama,* 290**,** 1729-38.
CHANDLER, H., BROOKS, D. J., HATTERSLEY, G., BOUXSEIN, M. L. & LANSKE, B. 2019. Abaloparatide increases bone mineral density and bone strength in ovariectomized rabbits with glucocorticoid-induced osteopenia. *Osteoporosis International,* 30**,** 1607-1616.

CHEN, H., ZHOU, X., SHOUMURA, S., EMURA, S. & BUNAI, Y. 2010. Age- and gender-dependent changes in three-dimensional microstructure of cortical and trabecular bone at the human femoral neck. *Osteoporos Int,* 21**,** 627-36.

CHEN, X., GIAMBINI, H., BEN-ABRAHAM, E., AN, K. N., NASSR, A. & ZHAO, C. 2015. Effect of Bone Mineral Density on Rotator Cuff Tear: An Osteoporotic Rabbit Model. *PLoS One,* 10**,** e0139384.

CHRISTEN, D., LEVCHUK, A., SCHORI, S., SCHNEIDER, P., BOYD, S. K. & MÜLLER, R. 2012. Deformable image registration and 3D strain mapping for the quantitative assessment of cortical bone microdamage. *Journal of the Mechanical Behavior of Biomedical Materials,* 8**,** 184-193.

CLEVERS, H. & NUSSE, R. 2012. Wnt/β-Catenin Signaling and Disease. *Cell,* 149**,** 1192-1205.

COAN, P., WAGNER, A., BRAVIN, A., DIEMOZ, P. C., KEYRILÄINEN, J. & MOLLENHAUER, J. 2010. In vivo x-ray phase contrast analyzer-based imaging for longitudinal osteoarthritis studies in guinea pigs. *Physics in Medicine and Biology,* 55**,** 7649.

COHEN, J. & HARRIS, W. H. 1958. The Three-Dimensional Anatomy of Haversian Systems. *The Journal of Bone & Joint Surgery,* 40**,** 419-434.

COLE, J. & VAN DER MEULEN, M. H. 2011. Whole Bone Mechanics and Bone Quality. *Clinical Orthopaedics and Related Research®,* 469**,** 2139-2149.

COMPSTON, J. 2006. Bone quality: what is it and how is it measured? *Arq Bras Endocrinol Metabol,* 50**,** 579-85.

COMPSTON, J. 2018. Glucocorticoid-induced osteoporosis: an update. *Endocrine,* 61**,** 7-16.

COOPER, D. M., ERICKSON, B., PEELE, A. G., HANNAH, K., THOMAS, C. D. & CLEMENT, J. G. 2011. Visualization of 3D osteon morphology by synchrotron radiation micro-CT. *J Anat,* 219**,** 481-9.

COOPER, D. M., KAWALILAK, C. E., HARRISON, K., JOHNSTON, B. D. & JOHNSTON, J. D. 2016. Cortical Bone Porosity: What Is It, Why Is It Important, and How Can We Detect It? *Curr Osteoporos Rep,* 14**,** 187-98.

COOPER, D. M., THOMAS, C. D., CLEMENT, J. G. & HALLGRIMSSON, B. 2006. Three-dimensional microcomputed tomography imaging of basic multicellular unit-related resorption spaces in human cortical bone. *Anat Rec A Discov Mol Cell Evol Biol,* 288**,** 806-16.

COOPER, D. M., TURINSKY, A. L., SENSEN, C. W. & HALLGRIMSSON, B. 2003. Quantitative 3D analysis of the canal network in cortical bone by micro-computed tomography. *Anat Rec B New Anat,* 274**,** 169-79.

COOPER, D. M. L., MATYAS, J. R., KATZENBERG, M. A. & HALLGRIMSSON, B. 2004. Comparison of Microcomputed Tomographic and Microradiographic Measurements of Cortical Bone Porosity. *Calcified Tissue International,* 74**,** 437-447.

COOPER, D. M. L., THOMAS, C. D. L., CLEMENT, J. G., TURINSKY, A. L., SENSEN, C. W. & HALLGRÍMSSON, B. 2007. Age-dependent change in the 3D structure of cortical porosity at the human femoral midshaft. *Bone,* 40**,** 957-965.

COSMAN, F. 2020. ANABOLIC THERAPY AND OPTIMAL TREATMENT SEQUENCES FOR PATIENTS WITH OSTEOPOROSIS AT HIGH RISK FOR FRACTURE. *Endocr Pract*.

COSMAN, F., DE BEUR, S. J., LEBOFF, M. S., LEWIECKI, E. M., TANNER, B., RANDALL, S. & LINDSAY, R. 2014. Clinician's Guide to Prevention and Treatment of Osteoporosis. *Osteoporos Int,* 25**,** 2359-81.

COSMAN, F., DEMPSTER, D. W., NIEVES, J. W., ZHOU, H., ZION, M., ROIMISHER, C., HOULE, Y., LINDSAY, R. & BOSTROM, M. 2016. Effect of Teriparatide on Bone Formation in the Human Femoral Neck. *J Clin Endocrinol Metab,* 101**,** 1498-505.

CURREY, J. D. 2002. *Bones : structure and mechanics,* Princeton, N.J., Princeton, N.J. : Princeton University Press.

CURREY, J. D. 2012. The structure and mechanics of bone. *Journal of Materials Science,* 47**,** 41-54.

DALSTRA, M., KARAJ, E., BECKMANN, F., ANDERSEN, T. & CATTANEO, P. M. Osteonal mineralization patterns in cortical bone studied by synchrotron-radiation-based computed microtomography and scanning acoustic microscopy. 2004. 143-151.

DAVID, V., LAROCHE, N., BOUDIGNON, B., LAFAGE-PROUST, M.-H., ALEXANDRE, C., RUEGSEGGER, P. & VICO, L. 2003. Noninvasive In Vivo Monitoring of Bone Architecture Alterations in Hindlimb-Unloaded Female Rats Using Novel Three-Dimensional Microcomputed Tomography. *Journal of Bone and Mineral Research,* 18**,** 1622-1631.

DE BAKKER, C. M., ALTMAN, A. R., TSENG, W. J., TRIBBLE, M. B., LI, C., CHANDRA, A., QIN, L. & LIU, X. S. 2015. μCT-based, in vivo dynamic bone histomorphometry allows 3D evaluation of the early responses of bone resorption and formation to PTH and alendronate combination therapy. *Bone,* 73**,** 198-207.

DELAISSE, J. M., ANDERSEN, T. L., KRISTENSEN, H. B., JENSEN, P. R., ANDREASEN, C. M. & SØE, K. 2020. Re-thinking the bone remodeling cycle mechanism and the origin of bone loss. *Bone,* 141**,** 115628.

DEMPSTER, D. W., BIRCHMAN, R., XU, R., LINDSAY, R. & SHEN, V. 1995. Temporal changes in cancellous bone structure of rats immediately after ovariectomy. *Bone,* 16**,** 157-61.

DEMPSTER, D. W., COSMAN, F., PARISIEN, M., SHEN, V. & LINDSAY, R. 1993. Anabolic Actions of Parathyroid Hormone on Bone*. *Endocrine Reviews,* 14**,** 690-709.

DEMPSTER, D. W., PARISIEN, M., SILVERBERG, S. J., LIANG, X. G., SCHNITZER, M., SHEN, V., SHANE, E., KIMMEL, D. B., RECKER, R., LINDSAY, R. & BILEZIKIAN, J. P. 1999. On the mechanism of cancellous bone preservation in postmenopausal women with mild primary hyperparathyroidism. *J Clin Endocrinol Metab,* 84**,** 1562-6.

DING, M., DANIELSEN, C. C. & OVERGAARD, S. 2012. The effects of glucocorticoid on microarchitecture, collagen, mineral and mechanical properties of sheep femur cortical bone. *Journal of Tissue Engineering and Regenerative Medicine,* 6**,** 443-450.

DOBNIG, H. & TURNER, R. T. 1997. The effects of programmed administration of human parathyroid hormone fragment (1-34) on bone histomorphometry and serum chemistry in rats. *Endocrinology,* 138**,** 4607-12.

DOUBE, M., KLOSOWSKI, M. M., ARGANDA-CARRERAS, I., CORDELIERES, F. P., DOUGHERTY, R. P., JACKSON, J. S., SCHMID, B., HUTCHINSON, J. R. & SHEFELBINE, S. J. 2010. BoneJ: Free and extensible bone image analysis in ImageJ. *Bone,* 47**,** 1076-9.

DUNN, O. 1964. Multiple Comparisons Using Rank Sums. *Technometrics,* 6**,** 241-252.

EASTELL, R. 2005. Role of oestrogen in the regulation of bone turnover at the menarche. *Journal of Endocrinology,* 185**,** 223.

EASTELL, R., ROSEN, C. J., BLACK, D. M., CHEUNG, A. M., MURAD, M. H. & SHOBACK, D. 2019. Pharmacological Management of Osteoporosis in Postmenopausal Women: An Endocrine Society* Clinical Practice Guideline. *The Journal of Clinical Endocrinology & Metabolism,* 104**,** 1595-1622.

EASTELL, R. & WALSH, J. S. 2017. Anabolic treatment for osteoporosis: teriparatide. *Clin Cases Miner Bone Metab,* 14**,** 173-178.

EBERHARDT, A. W., YEAGER-JONES, A. & BLAIR, H. C. 2001. Regional trabecular bone matrix degeneration and osteocyte death in femora of glucocorticoid- treated rabbits. *Endocrinology,* 142**,** 1333-40.

EHRLICH, P. J. & LANYON, L. E. 2002. Mechanical strain and bone cell function: a review. *Osteoporosis International: A Journal Established As Result Of Cooperation Between The European Foundation For Osteoporosis And The National Osteoporosis Foundation Of The USA,* 13**,** 688-700.

ENGELKE, K., LIBANATI, C., FUERST, T., ZYSSET, P. & GENANT, H. K. 2013. Advanced CT based In Vivo Methods for the Assessment of Bone Density, Structure, and Strength. *Current Osteoporosis Reports,* 11**,** 246-255.

ERIKSEN, E. F. 2010. Cellular mechanisms of bone remodeling. *Reviews in Endocrine and Metabolic Disorders,* 11**,** 219-227.

ESTERMANN, S.-J. & SCHEINER, S. 2018. Multiscale modeling provides differentiated insights to fluid flow-driven stimulation of bone cellular activities. *Frontiers in Physics,* 6**,** 76.

FAN, Y. L. & PEH, W. C. 2016. Radiology of Osteoporosis: Old and New Findings. *Semin Musculoskelet Radiol,* 20**,** 235-245.

FARR, J. N., KHOSLA, S., MIYABARA, Y., MILLER, V. M. & KEARNS, A. E. 2013. Effects of estrogen with micronized progesterone on cortical and trabecular bone mass and microstructure in recently postmenopausal women. *J Clin Endocrinol Metab,* 98**,** E249-57.

FELDER, A. A., PHILLIPS, C., CORNISH, H., COOKE, M., HUTCHINSON, J. R. & DOUBE, M. 2017. Secondary osteons scale allometrically in mammalian humerus and femur. *R Soc Open Sci,* 4**,** 170431.

FELDKAMP, L. A., GOLDSTEIN, S. A., PARFITT, M. A., JESION, G. & KLEEREKOPER, M. 1989. The direct examination of three-dimensional bone architecture in vitro by computed tomography. *Journal of Bone and Mineral Research,* 4**,** 3-11.

FLORENCIO-SILVA, R., SASSO, G. R. D. S., SASSO-CERRI, E., SIMOES, M. J. & CERRI, P. S. 2015. Biology of bone tissue: structure, function, and factors that influence bone cells. *BioMed Research International*.

FLOREZ, H., HERNÁNDEZ-RODRÍGUEZ, J., CARRASCO, J. L., PRIETO-GONZÁLEZ, S., MUXI, A., FILELLA, X., RUIZ-GASPÀ, S., GÓMEZ-PUERTA, J. A., CID, M., ESPINOSA, G., MONEGAL, A., GUAÑABENS, N. & PERIS, P. 2020. Vertebral fracture risk in glucocorticoid-induced osteoporosis: the role of hypogonadism and corticosteroid boluses. *RMD Open,* 6**,** e001355.

FÖGER-SAMWALD, U., DOVJAK, P., AZIZI-SEMRAD, U., KERSCHAN-SCHINDL, K. & PIETSCHMANN, P. 2020. Osteoporosis: Pathophysiology and therapeutic options. *Excli j,* 19**,** 1017-1037.

FORD, N. L., THORNTON, M. M. & HOLDSWORTH, D. W. 2003. Fundamental image quality limits for microcomputed tomography in small animals. *Medical Physics,* 30**,** 2869-2877.
FROLIK, C. A., BLACK, E. C., CAIN, R. L., SATTERWHITE, J. H., BROWN-AUGSBURGER, P. L., SATO, M. & HOCK, J. M. 2003. Anabolic and catabolic bone effects of human parathyroid hormone (1-34) are predicted by duration of hormone exposure. *Bone,* 33**,** 372-379.
FROST, H. 1960. Presence of microscopic cracks in vivo in bone. *Henry Ford Hosp Med Bull,* 8**,** 35.
FROST, H. The bone dynamics in osteoporosis and osteomalacia. 1966.
FROST, H. M. 1964. Bone remodeling dynamics. By H. M. Frost, M.D. Springfield, Illinois, Charles C Thomas Company, 1963. 175 pp., 184 references, 12 appendices, 40 figures. $8.50. *Arthritis & Rheumatism,* 7**,** 545-545.
FROST, H. M. 1969. Tetracycline-based histological analysis of bone remodeling. *Calcif Tissue Res,* 3**,** 211-37.
FROST, H. M. 1983. The skeletal intermediary organization. *Metab Bone Dis Relat Res,* 4**,** 281-90.
FUNG, P., BEDOGNI, G., BEDOGNI, A., PETRIE, A., PORTER, S., CAMPISI, G., BAGAN, J., FUSCO, V., SAIA, G., ACHAM, S., MUSTO, P., PETRUCCI, M. T., DIZ, P., COLELLA, G., MIGNOGNA, M. D., PENTENERO, M., ARDUINO, P., LODI, G., MAIORANA, C., MANFREDI, M., HALLBERG, P., WADELIUS, M., TAKAOKA, K., LEUNG, Y. Y., BONACINA, R., SCHIODT, M., LAKATOS, P., TAYLOR, T., RIU, G., FAVINI, G., ROGERS, S. N., PIRMOHAMED, M., NICOLETTI, P. & FEDELE, S. 2016. Time to onset of bisphosphonate-related osteonecrosis of the jaws: a multicentre retrospective cohort study. *Oral Dis*.
GEDMINTAS, L., SOLOMON, D. H. & KIM, S. C. 2013. Bisphosphonates and risk of subtrochanteric, femoral shaft, and atypical femur fracture: a systematic review and meta-analysis. *J Bone Miner Res,* 28**,** 1729-37.
GENSLER, L. S. 2013. Glucocorticoids: complications to anticipate and prevent. *The Neurohospitalist,* 3**,** 92-97.
GILSANZ, V., ROE, T. F., GIBBENS, D. T., SCHULZ, E. E., CARLSON, M. E., GONZALEZ, O. & BOECHAT, M. I. 1988. Effect of sex steroids on peak bone density of growing rabbits. *Am J Physiol,* 255**,** E416-21.
GOLTZMAN, D. 2018. Physiology of Parathyroid Hormone. *Endocrinology and Metabolism Clinics of North America,* 47**,** 743-758.
GÓMEZ-PICOS, P. & EAMES, B. F. 2015. On the evolutionary relationship between chondrocytes and osteoblasts. *Frontiers in genetics,* 6**,** 297-297.
GORSKI, J. P. 1998. Is all bone the same? Distinctive distributions and properties of non-collagenous matrix proteins in lamellar vs. woven bone imply the existence of different underlying osteogenic mechanisms. *Crit Rev Oral Biol Med,* 9**,** 201-23.
GRAEFF, C., TIMM, W., NICKELSEN, T. N., FARRERONS, J., MARÍN, F., BARKER, C. & GLÜER, C. C. 2007. Monitoring teriparatide-associated changes in vertebral microstructure by high-resolution CT in vivo: results from the EUROFORS study. *J Bone Miner Res,* 22**,** 1426-33.
GRARDEL, B., SUTTER, B., FLAUTRE, B., VIGUIER, E., LAVASTE, F. & HARDOUIN, P. 1994. Effects of glucocorticoids on skeletal growth in rabbits evaluated by dual-photon

absorptiometry, microscopic connectivity and vertebral compressive strength. *Osteoporos Int,* 4**,** 204-10.
GULER-YUKSEL, M., HOES, J. N., BULTINK, I. E. M. & LEMS, W. F. 2018. Glucocorticoids, Inflammation and Bone. *Calcif Tissue Int.*
HANSEN, S., HAUGE, E. M., BECK JENSEN, J. E. & BRIXEN, K. 2013. Differing effects of PTH 1-34, PTH 1-84, and zoledronic acid on bone microarchitecture and estimated strength in postmenopausal women with osteoporosis: an 18-month open-labeled observational study using HR-pQCT. *J Bone Miner Res,* 28**,** 736-45.
HARRISON, K., TSUKAMOTO, S. & COOPER, D. M. L. 2014. Abstracts - AAPA Presentations. *American Journal of Physical Anthropology,* 153**,** 64-283.
HARRISON, K. D. & COOPER, D. M. 2015. Modalities for Visualization of Cortical Bone Remodeling: The Past, Present, and Future. *Front Endocrinol (Lausanne),* 6**,** 122.
HARRISON, K. D., HIEBERT, B. D., PANAHIFAR, A., ANDRONOWSKI, J. M., ASHIQUE, A. M., KING, G. A., ARNASON, T., SWEKLA, K. J., PIVONKA, P. & COOPER, D. M. 2020. Cortical Bone Porosity in Rabbit Models of Osteoporosis. *Journal of Bone and Mineral Research,* 35**,** 2211-2228.
HATTNER, R., EPKER, B. N. & FROST, H. M. 1965. Suggested sequential mode of control of changes in cell behavior in adult bone remodeling. *Nature,* 206**,** 489-490.
HAUPERT, S., GUERARD, S., PEYRIN, F., MITTON, D. & LAUGIER, P. 2014. Non destructive characterization of cortical bone micro-damage by nonlinear resonant ultrasound spectroscopy. *PLoS One,* 9**,** e83599.
HAVERS, C. 1691. *Osteologia nova, or, some new observations of the bones and the parts belonging to them, with the manner of their accretion, and nutrition, communicated to the Royal Society in several discourses,* Ann Arbor: University Microfilms International.
HAYASHI, K., YAMAMOTO, M., MURAKAWA, Y., YAMAUCHI, M., KAJI, H., YAMAGUCHI, T. & SUGIMOTO, T. 2009. Bone fragility in male glucocorticoid-induced osteoporosis is not defined by bone mineral density. *Osteoporos Int,* 20**,** 1889-94.
HEANEY, R. P. 1994. The bone-remodeling transient: implications for the interpretation of clinical studies of bone mass change. *J Bone Miner Res,* 9**,** 1515-23.
HENNIG, C., THOMAS, C. D. L., CLEMENT, J. G. & COOPER, D. M. L. 2015. Does 3D orientation account for variation in osteon morphology assessed by 2D histology? *Journal of Anatomy,* 227**,** 497-505.
HERMAN, B. C., CARDOSO, L., MAJESKA, R. J., JEPSEN, K. J. & SCHAFFLER, M. B. 2010. Activation of bone remodeling after fatigue: Differential response to linear microcracks and diffuse damage. *Bone,* 47**,** 766-772.
HERT, J., FIALA, P. & PETRTYL, M. 1994. Osteon orientation of the diaphysis of the long bones in man. *Bone,* 15**,** 269-77.
HINGE, M., DELAISSE, J. M., PLESNER, T., CLASEN-LINDE, E., SALOMO, M. & ANDERSEN, T. L. 2015. High-dose therapy improves the bone remodelling compartment canopy coverage and bone formation in multiple myeloma. *Br J Haematol,* 171**,** 355-65.
HIRANO, T., BURR, D. B., CAIN, R. L. & HOCK, J. M. 2000. Changes in geometry and cortical porosity in adult, ovary-intact rabbits after 5 months treatment with LY333334 (hPTH 1-34). *Calcif Tissue Int,* 66**,** 456-60.

HIRANO, T., BURR, D. B., TURNER, C. H., SATO, M., CAIN, R. L. & HOCK, J. M. 1999. Anabolic effects of human biosynthetic parathyroid hormone fragment (1-34), LY333334, on remodeling and mechanical properties of cortical bone in rabbits. *J Bone Miner Res,* 14**,** 536-45.

HOCK, J. M. & GERA, I. 1992. Effects of continuous and intermittent administration and inhibition of resorption on the anabolic response of bone to parathyroid hormone. *Journal of Bone and Mineral Research,* 7**,** 65-72.

HOCK, J. M., HUMMERT, J. R., BOYCE, R., FONSECA, J. & RAISZ, L. G. 1989. Resorption is not essential for the stimulation of bone growth by hPTH-(1-34) in rats in vivo. *Journal of Bone and Mineral Research,* 4**,** 449-458.

HODSMAN, A. B., BAUER, D. C., DEMPSTER, D. W., DIAN, L., HANLEY, D. A., HARRIS, S. T., KENDLER, D. L., MCCLUNG, M. R., MILLER, P. D., OLSZYNSKI, W. P., ORWOLL, E. & YUEN, C. K. 2005. Parathyroid hormone and teriparatide for the treatment of osteoporosis: a review of the evidence and suggested guidelines for its use. *Endocr Rev,* 26**,** 688-703.

HODSMAN, A. B., FRAHER, L. J., OSTBYE, T., ADACHI, J. D. & STEER, B. M. 1993. An evaluation of several biochemical markers for bone formation and resorption in a protocol utilizing cyclical parathyroid hormone and calcitonin therapy for osteoporosis. *J Clin Invest,* 91**,** 1138-48.

HODSMAN, A. B., KISIEL, M., ADACHI, J. D., FRAHER, L. J. & WATSON, P. H. 2000. Histomorphometric evidence for increased bone turnover without change in cortical thickness or porosity after 2 years of cyclical hPTH(1-34) therapy in women with severe osteoporosis. *Bone,* 27**,** 311-8.

HODSMAN, A. B. & STEER, B. M. 1993. Early histomorphometric changes in response to parathyroid hormone therapy in osteoporosis: Evidence for de novo bone formation on quiescent cancellous surfaces. *Bone,* 14**,** 523-527.

HOFBAUER, L. C., KÜHNE, C. A. & VIERECK, V. 2004. The OPG/RANKL/RANK system in metabolic bone diseases. *J Musculoskelet Neuronal Interact,* 4**,** 268-75.

HSIEH, Y. F. & SILVA, M. J. 2002. In vivo fatigue loading of the rat ulna induces both bone formation and resorption and leads to time-related changes in bone mechanical properties and density. *J Orthop Res,* 20**,** 764-71.

HUANG, J. C., SAKATA, T., PFLEGER, L. L., BENCSIK, M., HALLORAN, B. P., BIKLE, D. D. & NISSENSON, R. A. 2004. PTH Differentially Regulates Expression of RANKL and OPG. *Journal of Bone and Mineral Research,* 19**,** 235-244.

IOP. *International Osteoporosis Foundation* [Online]. https://www.iofbonehealth.org.

JAWORSKI, Z. F. & LOK, E. 1972. The rate of osteoclastic bone erosion in Haversian remodeling sites of adult dog's rib. *Calcified Tissue Research,* 10**,** 103-112.

JAWORSKI, Z. F., LOK, E. & WELLINGTON, J. L. 1975. Impaired osteoclastic function and linear bone erosion rate in secondary hyperparathyroidism associated with chronic renal failure. *Clin Orthop Relat Res***,** 298-310.

JEE, W. S. & YAO, W. 2001. Overview: animal models of osteopenia and osteoporosis. *J Musculoskelet Neuronal Interact,* 1**,** 193-207.

JENSEN, P. R., ANDERSEN, T. L., HAUGE, E. M., BOLLERSLEV, J. & DELAISSÉ, J. M. 2015. A joined role of canopy and reversal cells in bone remodeling--lessons from glucocorticoid-induced osteoporosis. *Bone,* 73**,** 16-23.

JENSEN, P. R., ANDERSEN, T. L., PENNYPACKER, B. L., DUONG, L. T. & DELAISSÉ, J.-M. 2014. The Bone Resorption Inhibitors Odanacatib and Alendronate Affect Post-Osteoclastic Events Differently in Ovariectomized Rabbits. *Calcified Tissue International,* 94**,** 212-222.

JEROME, C. P., BURR, D. B., VAN BIBBER, T., HOCK, J. M. & BROMMAGE, R. 2001. Treatment with human parathyroid hormone (1-34) for 18 months increases cancellous bone volume and improves trabecular architecture in ovariectomized cynomolgus monkeys (Macaca fascicularis). *Bone,* 28**,** 150-9.

JEROME, C. P., JOHNSON, C. S., VAFAI, H. T., KAPLAN, K. C., BAILEY, J., CAPWELL, B., FRASER, F., HANSEN, L., RAMSAY, H., SHADOAN, M., LEES, C. J., THOMSEN, J. S. & MOSEKILDE, L. 1999. Effect of treatment for 6 months with human parathyroid hormone (1-34) peptide in ovariectomized cynomolgus monkeys (Macaca fascicularis). *Bone,* 25**,** 301-9.

JIA, D., O'BRIEN, C. A., STEWART, S. A., MANOLAGAS, S. C. & WEINSTEIN, R. S. 2006. Glucocorticoids Act Directly on Osteoclasts to Increase Their Life Span and Reduce Bone Density. *Endocrinology,* 147**,** 5592-5599.

JIANG, Y., ZHAO, J. J., MITLAK, B. H., WANG, O., GENANT, H. K. & ERIKSEN, E. F. 2003. Recombinant human parathyroid hormone (1-34) [teriparatide] improves both cortical and cancellous bone structure. *J Bone Miner Res,* 18**,** 1932-41.

JILKA, R. L. 1998. Cytokines, bone remodeling, and estrogen deficiency: a 1998 update. *Bone,* 23**,** 75-81.

JILKA, R. L. 2007. MOLECULAR AND CELLULAR MECHANISMS OF THE ANABOLIC EFFECT OF INTERMITTENT PTH. *Bone,* 40**,** 1434-1446.

JOHNSON, L. 1964. Morphologic analysis of pathology. *In:* FROST, H. (ed.) *Bone biodynamics.* Boston: Little, Brown, and Company.

JONES, D. H., KONG, Y.-Y. & PENNINGER, J. M. 2002. Role of RANKL and RANK in bone loss and arthritis. *Annals of the Rheumatic Diseases,* 61**,** ii32-ii39.

JORGENSON, B. L., BUIE, H. R., MCERLAIN, D. D., SANDINO, C. & BOYD, S. K. 2015. A comparison of methods for in vivo assessment of cortical porosity in the human appendicular skeleton. *Bone,* 73**,** 167-175.

JOWSEY, J. 1966. Studies of Haversian systems in man and some animals. *J Anat,* 100**,** 857-864.

JUDEX, S., GROSS, T. S. & ZERNICKE, R. F. 1997. Strain gradients correlate with sites of exercise-induced bone-forming surfaces in the adult skeleton. *J Bone Miner Res,* 12**,** 1737-45.

KELLY, T. 2014. A favorable risk-benefit analysis of high dose thyroid for treatment of bipolar disorders with regard to osteoporosis. *J Affect Disord,* 166**,** 353-8.

KENKRE, J. S. & BASSETT, J. 2018. The bone remodelling cycle. 55**,** 308-327.

KENNEDY, O. D., HERMAN, B. C., LAUDIER, D. M., MAJESKA, R. J., SUN, H. B. & SCHAFFLER, M. B. 2012. Activation of resorption in fatigue-loaded bone involves both apoptosis and active pro-osteoclastogenic signaling by distinct osteocyte populations. *Bone,* 50**,** 1115-1122.

KHAN, A. A., MORRISON, A., KENDLER, D. L., RIZZOLI, R., HANLEY, D. A., FELSENBERG, D., MCCAULEY, L. K., O'RYAN, F., REID, I. R., RUGGIERO, S. L., TAGUCHI, A., TETRADIS, S., WATTS, N. B., BRANDI, M. L., PETERS, E., GUISE, T., EASTELL, R., CHEUNG, A. M., MORIN, S. N., MASRI, B., COOPER, C.,

MORGAN, S. L., OBERMAYER-PIETSCH, B., LANGDAHL, B. L., DABAGH, R. A., DAVISON, K. S., SANDOR, G. K., JOSSE, R. G., BHANDARI, M., EL RABBANY, M., PIERROZ, D. D., SULIMANI, R., SAUNDERS, D. P., BROWN, J. P. & COMPSTON, J. 2016. Case-Based Review of Osteonecrosis of the Jaw (ONJ) and Application of the International Recommendations for Management From the International Task Force on ONJ. *J Clin Densitom*.

KHAN, A. Z., RAMES, R. D. & MILLER, A. N. 2018. Clinical Management of Osteoporotic Fractures. *Current Osteoporosis Reports,* 16**,** 299-311.

KHOSLA, S. 2001. Minireview: The OPG/RANKL/RANK System. *Endocrinology,* 142**,** 5050-5055.

KHOSLA, S., OURSLER, M. J. & MONROE, D. G. 2012. Estrogen and the skeleton. *Trends in endocrinology and metabolism: TEM,* 23**,** 576-581.

KHOW, K. S., SHIBU, P., YU, S. C., CHEHADE, M. J. & VISVANATHAN, R. 2017. Epidemiology and Postoperative Outcomes of Atypical Femoral Fractures in Older Adults: A Systematic Review. *J Nutr Health Aging,* 21**,** 83-91.

KINNEY, J. H., LANE, N. E. & HAUPT, D. L. 1995. In vivo, three-dimensional microscopy of trabecular bone. *Journal of Bone and Mineral Research,* 10**,** 264-270.

KLINCK, R. J., CAMPBELL, G. M. & BOYD, S. K. 2008. Radiation effects on bone architecture in mice and rats resulting from in vivo micro-computed tomography scanning. *Medical Engineering & Physics,* 30**,** 888-895.

KOH, J. W., KIM, J., CHO, H., HA, Y. C., KIM, T. Y., LEE, Y. K., KIM, H. Y. & JANG, S. 2020. Effects of Systemic Glucocorticoid Use on Fracture Risk: A Population-Based Study. *Endocrinol Metab (Seoul),* 35**,** 562-570.

LAFAGE-PROUST, M. H., ROCHE, B., LANGER, M., CLERET, D., VANDEN BOSSCHE, A., OLIVIER, T. & VICO, L. 2015. Assessment of bone vascularization and its role in bone remodeling. *Bonekey Rep,* 4**,** 662.

LANDRIGAN, M. D., LI, J., TURNBULL, T. L., BURR, D. B., NIEBUR, G. L. & ROEDER, R. K. 2011. Contrast-enhanced micro-computed tomography of fatigue microdamage accumulation in human cortical bone. *Bone,* 48**,** 443-50.

LANGER, M., PACUREANU, A., SUHONEN, H., GRIMAL, Q., CLOETENS, P. & PEYRIN, F. 2012. X-Ray Phase Nanotomography Resolves the 3D Human Bone Ultrastructure. *PLoS ONE,* 7**,** e35691.

LAPERRE, K., DEPYPERE, M., VAN GASTEL, N., TORREKENS, S., MOERMANS, K., BOGAERTS, R., MAES, F. & CARMELIET, G. 2011. Development of micro-CT protocols for in vivo follow-up of mouse bone architecture without major radiation side effects. *Bone,* 49**,** 613-22.

LARRUE, A., RATTNER, A., PETER, Z. A., OLIVIER, C., LAROCHE, N., VICO, L. & PEYRIN, F. 2011. Synchrotron radiation micro-CT at the micrometer scale for the analysis of the three-dimensional morphology of microcracks in human trabecular bone. *PLoS One,* 6**,** e21297.

LASSEN, N. E., ANDERSEN, T. L., PLØEN, G. G., SØE, K., HAUGE, E. M., HARVING, S., ESCHEN, G. E. T. & DELAISSE, J.-M. 2017. Coupling of Bone Resorption and Formation in Real Time: New Knowledge Gained From Human Haversian BMUs. *Journal of Bone and Mineral Research,* 32**,** 1395-1405.

LEDER, B. Z., TSAI, J. N., UIHLEIN, A. V., BURNETT-BOWIE, S.-A. M., ZHU, Y., FOLEY, K., LEE, H. & NEER, R. M. 2014. Two Years of Denosumab and Teriparatide

Administration in Postmenopausal Women With Osteoporosis (The DATA Extension Study): A Randomized Controlled Trial. *The Journal of Clinical Endocrinology & Metabolism,* 99**,** 1694-1700.
LEE, M. & PARTRIDGE, N. C. 2009. Parathyroid hormone signaling in bone and kidney. *Curr Opin Nephrol Hypertens,* 18**,** 298-302.
LEE, T. C., MOHSIN, S., TAYLOR, D., PARKESH, R., GUNNLAUGSSON, T., O'BRIEN, F. J., GIEHL, M. & GOWIN, W. 2003. Detecting microdamage in bone. *Journal of Anatomy,* 203**,** 161-172.
LELOVAS, P. P., XANTHOS, T. T., THOMA, S. E., LYRITIS, G. P. & DONTAS, I. A. 2008. The laboratory rat as an animal model for osteoporosis research. *Comp Med,* 58**,** 424-30.
LENG, H., WANG, X., ROSS, R. D., NIEBUR, G. L. & ROEDER, R. K. 2008. Micro-computed tomography of fatigue microdamage in cortical bone using a barium sulfate contrast agent. *J Mech Behav Biomed Mater,* 1**,** 68-75.
LI, L. & WANG, Z. 2018. Ovarian Aging and Osteoporosis. *In:* WANG, Z. (ed.) *Aging and Aging-Related Diseases: Mechanisms and Interventions.* Singapore: Springer Singapore.
LI, Z., KUHN, G., VON SALIS-SOGLIO, M., COOKE, S. J., SCHIRMER, M., MÜLLER, R. & RUFFONI, D. 2015. In vivo monitoring of bone architecture and remodeling after implant insertion: The different responses of cortical and trabecular bone. *Bone,* 81**,** 468-477.
LIEBERMAN, D. E., PEARSON, O. M., POLK, J. D., DEMES, B. & CROMPTON, A. W. 2003. Optimization of bone growth and remodeling in response to loading in tapered mammalian limbs. *J Exp Biol,* 206**,** 3125-38.
LINDSAY, R., COSMAN, F., ZHOU, H., BOSTROM, M. P., SHEN, V. W., CRUZ, J. D., NIEVES, J. W. & DEMPSTER, D. W. 2006. A novel tetracycline labeling schedule for longitudinal evaluation of the short-term effects of anabolic therapy with a single iliac crest bone biopsy: early actions of teriparatide. *J Bone Miner Res,* 21**,** 366-73.
LIU, X., LEI, W., WU, Z., CUI, Y., HAN, B., FU, S. & JIANG, C. 2012. Effects of glucocorticoid on BMD, micro-architecture and biomechanics of cancellous and cortical bone mass in OVX rabbits. *Med Eng Phys,* 34**,** 2-8.
LOCASCIO, V., BONUCCI, E., IMBIMBO, B., BALLANTI, P., ADAMI, S., MILANI, S., TARTAROTTI, D. & DELLAROCCA, C. 1990. Bone loss in response to long-term glucocorticoid therapy. *Bone and Mineral,* 8**,** 39-51.
LOCKLIN, R. M., KHOSLA, S., TURNER, R. T. & RIGGS, B. L. 2003. Mediators of the biphasic responses of bone to intermittent and continuously administered parathyroid hormone. *Journal of Cellular Biochemistry,* 89**,** 180-190.
LONGO, A. B., SALMON, P. L. & WARD, W. E. 2017. Comparison of ex vivo and in vivo micro-computed tomography of rat tibia at different scanning settings. *J Orthop Res,* 35**,** 1690-1698.
LOTINUN, S., EVANS, G. L., BRONK, J. T., BOLANDER, M. E., WRONSKI, T. J., RITMAN, E. L. & TURNER, R. T. 2004. Continuous parathyroid hormone induces cortical porosity in the rat: effects on bone turnover and mechanical properties. *J Bone Miner Res,* 19**,** 1165-71.
LOTINUN, S., SIBONGA, J. D. & TURNER, R. T. 2002. Differential effects of intermittent and continuous administration of parathyroid hormone on bone histomorphometry and gene expression. *Endocrine,* 17**,** 29-36.

MA, G. L., BAI, R. J., YAN, D., CHENG, X. G., QU, H., SHEN, B. Z., HAN, M. J. & WU, Z. H. 2010. [The study of an animal model in rabbits with the early primary hyperparathyroidism]. *Zhonghua Yi Xue Za Zhi,* 90**,** 3087-90.

MA, Y. L., ZENG, Q. Q., CHIANG, A. Y., BURR, D., LI, J., DOBNIG, H., FAHRLEITNER-PAMMER, A., MICHALSKÁ, D., MARIN, F., PAVO, I. & STEPAN, J. J. 2014. Effects of teriparatide on cortical histomorphometric variables in postmenopausal women with or without prior alendronate treatment. *Bone,* 59**,** 139-147.

MACDONALD, H. M., NISHIYAMA, K. K., HANLEY, D. A. & BOYD, S. K. 2011. Changes in trabecular and cortical bone microarchitecture at peripheral sites associated with 18 months of teriparatide therapy in postmenopausal women with osteoporosis. *Osteoporosis International,* 22**,** 357-362.

MADER, K. S., SCHNEIDER, P., MULLER, R. & STAMPANONI, M. 2013. A quantitative framework for the 3D characterization of the osteocyte lacunar system. *Bone,* 57**,** 142-54.

MAEDA, K., KOBAYASHI, Y., KOIDE, M., UEHARA, S., OKAMOTO, M., ISHIHARA, A., KAYAMA, T., SAITO, M. & MARUMO, K. 2019. The Regulation of Bone Metabolism and Disorders by Wnt Signaling. *International Journal of Molecular Sciences,* 20**,** 5525.

MAEDA, M., BRYANT, M. H., YAMAGATA, M., LI, G., EARLE, J. D. & CHAO, E. Y. 1988. Effects of irradiation on cortical bone and their time-related changes. A biomechanical and histomorphological study. *J Bone Joint Surg Am,* 70**,** 392-9.

MAFI GOLCHIN, M., HEIDARI, L., GHADERIAN, S. M. H. & AKHAVAN-NIAKI, H. 2016. Osteoporosis: A Silent Disease with Complex Genetic Contribution. *Journal of Genetics and Genomics,* 43**,** 49-61.

MANOLAGAS, S. C. & JILKA, R. L. 1995. Bone marrow, cytokines, and bone remodeling. Emerging insights into the pathophysiology of osteoporosis. *N Engl J Med,* 332**,** 305-11.

MAROTTI, G. 1993. A new theory of bone lamellation. *Calcified Tissue International,* 53**,** S47-S56.

MARTIN, R. B. 1991. On the significance of remodeling space and activation rate changes in bone remodeling. *Bone,* 12**,** 391-400.

MARTIN, R. B. 1994. On the histologic measurement of osteonal BMU activation frequency. *Bone,* 15**,** 547-9.

MARTIN, R. B. 2002. Is all cortical bone remodeling initiated by microdamage? *Bone,* 30**,** 8-13.

MARTIN, R. B. 2007. Targeted bone remodeling involves BMU steering as well as activation. *Bone,* 40**,** 1574-80.

MARTIN, R. B., GIBSON, V. A., STOVER, S. M., GIBELING, J. C. & GRIFFINS, L. V. 1996. Osteonal structure in the equine third metacarpus. *Bone,* 19**,** 165-171.

MARTINSON, M., SAMADI, N., BASSEY, B., GOMEZ, A. & CHAPMAN, D. 2015. Phase-preserving beam expander for biomedical X-ray imaging. *J Synchrotron Radiat,* 22**,** 801-6.

MARTINSON, M., SAMADI, N., BELEV, G., BASSEY, B., LEWIS, R., AULAKH, G. & CHAPMAN, D. 2014. Development of a bent Laue beam-expanding double-crystal monochromator for biomedical X-ray imaging. *Journal of Synchrotron Radiation,* 21**,** 479-483.

MASHIBA, T., BURR, D. B., TURNER, C. H., SATO, M., CAIN, R. L. & HOCK, J. M. 2001. Effects of human parathyroid hormone (1-34), LY333334, on bone mass, remodeling, and mechanical properties of cortical bone during the first remodeling cycle in rabbits. *Bone,* 28**,** 538-47.

MATSUMOTO, T., NISHIKAWA, K., TANAKA, M. & UESUGI, K. 2011. In Vivo CT Quantification of Trabecular Bone Dynamics in Mice after Sciatic Neurectomy Using Monochromatic Synchrotron Radiation. *Calcified Tissue International,* 88**,** 432-441.
MATSUO, H., TSURUMOTO, T., MAEDA, J., SAIKI, K., OKAMOTO, K., OGAMI-TAKAMURA, K., KONDO, H., TOMITA, M., YONEKURA, A. & OSAKI, M. 2019. Investigating interindividual variations in cortical bone quality: analysis of the morphotypes of secondary osteons and their population densities in the human femoral diaphysis. *Anatomical science international,* 94**,** 75-85.
MAUCH, T. & SCHOENWOLF, G. 2001. Developmental Biology. Sixth Edition. By Scott F. Gilbert. *American Journal of Medical Genetics,* 99**,** 170-171.
MCCALDEN, R. W., MCGEOUGH, J. A., BARKER, M. B. & COURT-BROWN, C. M. 1993. Age-related changes in the tensile properties of cortical bone. The relative importance of changes in porosity, mineralization, and microstructure. *JBJS,* 75**,** 1193-1205.
MEAKIN, L. B., PRICE, J. S. & LANYON, L. E. 2014. The Contribution of Experimental in vivo Models to Understanding the Mechanisms of Adaptation to Mechanical Loading in Bone. *Front Endocrinol (Lausanne),* 5**,** 154.
MIGLIORATI, C. A., SIEGEL, M. A. & ELTING, L. S. 2006. Bisphosphonate-associated osteonecrosis: a long-term complication of bisphosphonate treatment. *Lancet Oncol,* 7**,** 508-14.
MIKOLAJEWICZ, N., BISHOP, N., BURGHARDT, A. J., FOLKESTAD, L., HALL, A., KOZLOFF, K. M., LUKEY, P. T., MOLLOY-BLAND, M., MORIN, S. N., OFFIAH, A. C., SHAPIRO, J., VAN RIETBERGEN, B., WAGER, K., WILLIE, B. M., KOMAROVA, S. V. & GLORIEUX, F. H. 2020. HR-pQCT Measures of Bone Microarchitecture Predict Fracture: Systematic Review and Meta-Analysis. *Journal of Bone and Mineral Research,* 35**,** 446-459.
MOHSIN, S., TAYLOR, D. & LEE, T. 2002. Three-dimensional reconstruction of Haversian systems in ovine compact bone. *European journal of morphology,* 40**,** 309-315.
MOORE, K. L., AGUR, A. M. R. & II, D. 2012. *Essential clinical anatomy: Fourth edition*.
MORGAN, E. F., UNNIKRISNAN, G. U. & HUSSEIN, A. I. 2018. Bone Mechanical Properties in Healthy and Diseased States. *Annual review of biomedical engineering,* 20**,** 119-143.
MUIR, P., SAMPLE, S. J., BARRETT, J. G., MCCARTHY, J., VANDERBY, R., JR., MARKEL, M. D., PROKUSKI, L. J. & KALSCHEUR, V. L. 2007. Effect of fatigue loading and associated matrix microdamage on bone blood flow and interstitial fluid flow. *Bone,* 40**,** 948-56.
MÜLLER, R., KOLLER, B., HILDEBRAND, T., LAIB, A., GIANOLINI, S. & RÜEGSEGGER, P. 1996. Resolution dependency of microstructural properties of cancellous bone based on three-dimensional mu-tomography. *Technol Health Care,* 4**,** 113-9.
NATALIE, A. S. & MARTIN, T. J. 2014. Coupling the activities of bone formation and resorption: a multitude of signals within the basic multicellular unit. *BoneKEy Reports,* 3.
NEER, R. M., ARNAUD, C. D., ZANCHETTA, J. R., PRINCE, R., GAICH, G. A., REGINSTER, J.-Y., HODSMAN, A. B., ERIKSEN, E. F., ISH-SHALOM, S., GENANT, H. K., WANG, O., MELLSTRÖM, D., OEFJORD, E. S., MARCINOWSKA-SUCHOWIERSKA, E., SALMI, J., MULDER, H., HALSE, J., SAWICKI, A. Z. & MITLAK, B. H. 2001. Effect of Parathyroid Hormone (1-34) on Fractures and Bone

Mineral Density in Postmenopausal Women with Osteoporosis. *New England Journal of Medicine,* 344**,** 1434-1441.
NEWMAN, E., TURNER, A. S. & WARK, J. D. 1995. The potential of sheep for the study of osteopenia: current status and comparison with other animal models. *Bone,* 16**,** 277s-284s.
NG, P. Y., ONG, A. J., GALE, L. S. & DASS, C. R. 2016. Treatment of bone disorders with parathyroid hormone: success and pitfalls. *Pharmazie,* 71**,** 427-433.
NIH CONSENSUS DEVELOPMENT PANEL ON OSTEOPOROSIS PREVENTION, D. & THERAPY 2001. Osteoporosis Prevention, Diagnosis, and Therapy. *JAMA,* 285**,** 785-795.
OLIVIERO, S., GIORGI, M., LAUD, P. J. & DALL'ARA, E. 2019. Effect of repeated in vivo microCT imaging on the properties of the mouse tibia. *PloS one,* 14**,** e0225127-e0225127.
OSAGIE-CLOUARD, L., SANGHANI, A., COATHUP, M., BRIGGS, T., BOSTROM, M. & BLUNN, G. 2017. Parathyroid hormone 1-34 and skeletal anabolic action: The use of parathyroid hormone in bone formation. *Bone Joint Res,* 6**,** 14-21.
PACHECO, R. & STOCK, H. 2013. Effects of Radiation on Bone. *Current Osteoporosis Reports,* 11**,** 299-304.
PALACIO-MANCHENO, P. E., LARRIERA, A. I., DOTY, S. B., CARDOSO, L. & FRITTON, S. P. 2014. 3D assessment of cortical bone porosity and tissue mineral density using high-resolution microCT: effects of resolution and threshold method. *J Bone Miner Res,* 29**,** 142-50.
PARFITT, A. M. 1982. The coupling of bone formation to bone resorption: a critical analysis of the concept and of its relevance to the pathogenesis of osteoporosis. *Metab Bone Dis Relat Res,* 4**,** 1-6.
PARFITT, A. M. 1983. The physiologic and clinical significance of bone histomorphometric data. *Bone Histomorphometry : Techniques and Interpretation***,** 143-223.
PARFITT, A. M. 1994. Osteonal and hemi-osteonal remodeling: The spatial and temporal framework for signal traffic in adult human bone. *Journal of Cellular Biochemistry,* 55**,** 273-286.
PARFITT, A. M. 2002a. Misconceptions (2): turnover is always higher in cancellous than in cortical bone. *Bone,* 30**,** 807-809.
PARFITT, A. M. 2002b. Targeted and nontargeted bone remodeling: relationship to basic multicellular unit origination and progression. *Bone,* 30**,** 5-7.
PARFITT, A. M., MATHEWS, C. H., VILLANUEVA, A. R., KLEEREKOPER, M., FRAME, B. & RAO, D. S. 1983. Relationships between surface, volume, and thickness of iliac trabecular bone in aging and in osteoporosis. Implications for the microanatomic and cellular mechanisms of bone loss. *J Clin Invest,* 72**,** 1396-409.
PARISIEN, M., SILVERBERG, S. J., SHANE, E., DE LA CRUZ, L., LINDSAY, R., BILEZIKIAN, J. P. & DEMPSTER, D. W. 1990. The histomorphometry of bone in primary hyperparathyroidism: preservation of cancellous bone structure. *J Clin Endocrinol Metab,* 70**,** 930-8.
PAZZAGLIA, U. E., BONASPETTI, G., RODELLA, L. F., RANCHETTI, F. & AZZOLA, F. 2007. Design, morphometry and development of the secondary osteonal system in the femoral shaft of the rabbit. *J Anat,* 211**,** 303-12.

PAZZAGLIA, U. E., CONGIU, T., RASPANTI, M., RANCHETTI, F. & QUACCI, D. 2009. Anatomy of the intracortical canal system: scanning electron microscopy study in rabbit femur. *Clin Orthop Relat Res,* 467**,** 2446-56.

PAZZAGLIA, U. E., ZARATTINI, G., GIACOMINI, D., RODELLA, L., MENTI, A. M. & FELTRIN, G. 2010. Morphometric Analysis of the Canal System of Cortical Bone: An Experimental Study in the Rabbit Femur Carried Out with Standard Histology and Micro-CT. *Anatomia, Histologia, Embryologia,* 39**,** 17-26.

PEARCE, A. I., RICHARDS, R. G., MILZ, S., SCHNEIDER, E. & PEARCE, S. G. 2007. Animal models for implant biomaterial research in bone: a review. *Eur Cell Mater,* 13**,** 1-10.

PEARSON, O. M. & LIEBERMAN, D. E. 2004. The aging of Wolff's "law": Ontogeny and responses to mechanical loading in cortical bone. *American Journal of Physical Anthropology,* 125**,** 63-99.

PERILLI, E., BALA, Y., ZEBAZE, R., REYNOLDS, K. J. & SEEMAN, E. 2015. Regional Heterogeneity in the Configuration of the Intracortical Canals of the Femoral Shaft. *Calcified Tissue International,* 97**,** 327-335.

PERMUY, M. & LÓPEZ-PEÑA, M. 2019. Rabbit as model for osteoporosis research. 37**,** 573-583.

PERMUY, M., LÓPEZ-PEÑA, M., MUÑOZ, F. & GONZÁLEZ-CANTALAPIEDRA, A. 2019. Rabbit as model for osteoporosis research. *Journal of Bone and Mineral Metabolism,* 37**,** 573-583.

PETRTYL, M., HERT, J. & FIALA, P. 1996. Spatial organization of the haversian bone in man. *J Biomech,* 29**,** 161-9.

PINZONE, J. J., HALL, B. M., THUDI, N. K., VONAU, M., QIANG, Y.-W., ROSOL, T. J. & SHAUGHNESSY, J. D., JR. 2009. The role of Dickkopf-1 in bone development, homeostasis, and disease. *Blood,* 113**,** 517-525.

POOLE, K. E., TREECE, G. M., MAYHEW, P. M., VACULIK, J., DUNGL, P., HORAK, M., STEPAN, J. J. & GEE, A. H. 2012. Cortical thickness mapping to identify focal osteoporosis in patients with hip fracture. *PLoS One,* 7**,** e38466.

PRATT, I. V., BELEV, G., ZHU, N., CHAPMAN, L. D. & COOPER, D. M. L. 2015. In vivo imaging of rat cortical bone porosity by synchrotron phase contrast micro computed tomography. *Physics in Medicine and Biology,* 60**,** 211.

PRESBITERO, G., O'BRIEN, F. J., LEE, T. C. & TAYLOR, D. 2012. Distribution of microcrack lengths in bone in vivo and in vitro. *J Theor Biol,* 304**,** 164-71.

PRISBY, R. D. 2019. The Clinical Relevance of the Bone Vascular System: Age-Related Implications. *Clinical Reviews in Bone and Mineral Metabolism,* 17**,** 48-62.

QI, M., HU, J., LI, J., LI, J., DONG, W., FENG, X. & YU, J. 2012. Effect of zoledronate acid treatment on osseointegration and fixation of implants in autologous iliac bone grafts in ovariectomized rabbits. *Bone,* 50**,** 119-27.

RASHKI KEMMAK, A. & REZAPOUR, A. 2020. Economic burden of osteoporosis in the world: A systematic review. 34**,** 154.

RAUCH, F., TRAVERS, R. & GLORIEUX, F. H. 2007. Intracortical remodeling during human bone development—A histomorphometric study. *Bone,* 40**,** 274-280.

REBOLLEDO, B. J., UNNANUNTANA, A. & LANE, J. M. 2011. A comprehensive approach to fragility fractures. *Journal of orthopaedic trauma,* 25**,** 566-573.

REEVE, J., MEUNIER, P. J., PARSONS, J. A., BERNAT, M., BIJVOET, O. L., COURPRON, P., EDOUARD, C., KLENERMAN, L., NEER, R. M., RENIER, J. C., SLOVIK, D., VISMANS, F. J. & POTTS, J. T. 1980. Anabolic effect of human parathyroid hormone fragment on trabecular bone in involutional osteoporosis: a multicentre trial. *British Medical Journal,* 280**,** 1340-1344.

REINWALD, S. & BURR, D. 2008. Review of nonprimate, large animal models for osteoporosis research. *J Bone Miner Res,* 23**,** 1353-68.

RIGGS, B. L., MELTON III, L. J., ROBB, R. A., CAMP, J. J., ATKINSON, E. J., PETERSON, J. M., ROULEAU, P. A., MCCOLLOUGH, C. H., BOUXSEIN, M. L. & KHOSLA, S. 2004. Population-Based Study of Age and Sex Differences in Bone Volumetric Density, Size, Geometry, and Structure at Different Skeletal Sites. *Journal of Bone and Mineral Research,* 19**,** 1945-1954.

RINONAPOLI, G., RUGGIERO, C., MECCARIELLO, L., BISACCIA, M., CECCARINI, P. & CARAFFA, A. 2021. Osteoporosis in Men: A Review of an Underestimated Bone Condition. *International Journal of Molecular Sciences,* 22**,** 2105.

RISK, W. S. G. O. A. O. F. & OSTEOPOROSIS, I. A. T. S. F. P. 1994. *Assessment of Fracture Risk and Its Application to Screening for Postmenopausal Osteoporosis: Report of a WHO Study Group*, World Health Organization.

ROBLING, A. G. & STOUT, S. D. 1999. Morphology of the drifting osteon. *Cells Tissues Organs,* 164**,** 192-204.

ROCHEFORT, G. Y. 2014. The osteocyte as a therapeutic target in the treatment of osteoporosis. *Ther Adv Musculoskelet Dis,* 6**,** 79-91.

RUBIN, M. R. & BILEZIKIAN, J. P. 2003. The anabolic effects of parathyroid hormone therapy. *Clinics in Geriatric Medicine,* 19**,** 415-432.

RUSSELL, R. G., WATTS, N. B., EBETINO, F. H. & ROGERS, M. J. 2008. Mechanisms of action of bisphosphonates: similarities and differences and their potential influence on clinical efficacy. *Osteoporos Int,* 19**,** 733-59.

RYSER, M. D., KOMAROVA, S. V. & NIGAM, N. 2010. The Cellular Dynamics of Bone Remodeling: A Mathematical Model. *SIAM Journal on Applied Mathematics,* 70**,** 1899-1921.

RYSER, M. D., NIGAM, N. & KOMAROVA, S. V. 2009. Mathematical modeling of spatio-temporal dynamics of a single bone multicellular unit. *J Bone Miner Res,* 24**,** 860-70.

SALHOTRA, A. & SHAH, H. N. 2020. Mechanisms of bone development and repair. 21**,** 696-711.

SATO, M., WESTMORE, M., MA, Y. L., SCHMIDT, A., ZENG, Q. Q., GLASS, E. V., VAHLE, J., BROMMAGE, R., JEROME, C. P. & TURNER, C. H. 2004. Teriparatide [PTH(1-34)] strengthens the proximal femur of ovariectomized nonhuman primates despite increasing porosity. *J Bone Miner Res,* 19**,** 623-9.

SCHAFFLER, M. B., RADIN, E. L. & BURR, D. B. 1989. Mechanical and morphological effects of strain rate on fatigue of compact bone. *Bone,* 10**,** 207-14.

SCHAFFLER, M. B., RADIN, E. L. & BURR, D. B. 1990. Long-term fatigue behavior of compact bone at low strain magnitude and rate. *Bone,* 11**,** 321-6.

SCHEINER, S., PIVONKA, P. & HELLMICH, C. 2016. Poromicromechanics reveals that physiological bone strains induce osteocyte-stimulating lacunar pressure. *Biomechanics and modeling in mechanobiology,* 15**,** 9-28.

SCHNEIDER, P., STAUBER, M., VOIDE, R., STAMPANONI, M., DONAHUE, L. R. & MÜLLER, R. 2007. Ultrastructural Properties in Cortical Bone Vary Greatly in Two Inbred Strains of Mice as Assessed by Synchrotron Light Based Micro- and Nano-CT. *Journal of Bone and Mineral Research,* 22**,** 1557-1570.

SEEMAN, E. & DELMAS, P. D. 2006. Bone quality--the material and structural basis of bone strength and fragility. *N Engl J Med,* 354**,** 2250-61.

SEIBEL, M. J., COOPER, M. S. & ZHOU, H. 2013. Glucocorticoid-induced osteoporosis: mechanisms, management, and future perspectives. *Lancet Diabetes Endocrinol,* 1**,** 59-70.

SEREF-FERLENGEZ, Z., BASTA-PLJAKIC, J., KENNEDY, O. D., PHILEMON, C. J. & SCHAFFLER, M. B. 2014. Structural and Mechanical Repair of Diffuse Damage in Cortical Bone in vivo. *Journal of bone and mineral research : the official journal of the American Society for Bone and Mineral Research,* 29**,** 2537-2544.

SETIAWATI, R. & RAHARDJO, P. 2018. Bone Development and Growth.

SEVIL, F. & KARA, M. E. 2010. The effects of ovariectomy on bone mineral density, geometrical, and biomechanical characteristics in the rabbit femur. *Vet Comp Orthop Traumatol,* 23**,** 31-6.

SHAPIRO, F. 2008. Bone development and its relation to fracture repair. The role of mesenchymal osteoblasts and surface osteoblasts. *Eur Cell Mater,* 15**,** 53-76.

SHARMA, D., LARRIERA, A. I., PALACIO-MANCHENO, P. E., GATTI, V., FRITTON, J. C., BROMAGE, T. G., CARDOSO, L., DOTY, S. B. & FRITTON, S. P. 2018. The effects of estrogen deficiency on cortical bone microporosity and mineralization. *Bone,* 110**,** 1-10.

SHER, L. B., WOITGE, H. W., ADAMS, D. J., GRONOWICZ, G. A., KROZOWSKI, Z., HARRISON, J. R. & KREAM, B. E. 2004. Transgenic Expression of 11β-Hydroxysteroid Dehydrogenase Type 2 in Osteoblasts Reveals an Anabolic Role for Endogenous Glucocorticoids in Bone. *Endocrinology,* 145**,** 922-929.

SHIM, K. S. 2015. Pubertal growth and epiphyseal fusion. *Ann Pediatr Endocrinol Metab,* 20**,** 8-12.

SHIPOV, A., ZASLANSKY, P., RIESEMEIER, H., SEGEV, G., ATKINS, A. & SHAHAR, R. 2013. Unremodeled endochondral bone is a major architectural component of the cortical bone of the rat (Rattus norvegicus). *J Struct Biol,* 183**,** 132-40.

SIETSEMA, W. K. 1995. Animal models of cortical porosity. *Bone,* 17**,** 297s-305s.

SILVA, B. C. & BILEZIKIAN, J. P. 2015. Parathyroid hormone: anabolic and catabolic actions on the skeleton. *Curr Opin Pharmacol,* 22**,** 41-50.

SILVA, B. C., COSTA, A. G., CUSANO, N. E., KOUSTENI, S. & BILEZIKIAN, J. P. 2011. Catabolic and anabolic actions of parathyroid hormone on the skeleton. *J Endocrinol Invest,* 34**,** 801-10.

SILVERBERG, S. J., SHANE, E., DE LA CRUZ, L., DEMPSTER, D. W., FELDMAN, F., SELDIN, D., JACOBS, T. P., SIRIS, E. S., CAFFERTY, M., PARISIEN, M. V. & ET AL. 1989. Skeletal disease in primary hyperparathyroidism. *J Bone Miner Res,* 4**,** 283-91.

SIMONET, W. S., LACEY, D. L., DUNSTAN, C. R., KELLEY, M., CHANG, M. S., LÜTHY, R., NGUYEN, H. Q., WOODEN, S., BENNETT, L., BOONE, T., SHIMAMOTO, G., DEROSE, M., ELLIOTT, R., COLOMBERO, A., TAN, H. L., TRAIL, G., SULLIVAN, J., DAVY, E., BUCAY, N., RENSHAW-GEGG, L., HUGHES, T. M., HILL, D., PATTISON, W., CAMPBELL, P., SANDER, S., VAN, G., TARPLEY, J., DERBY, P.,

LEE, R. & BOYLE, W. J. 1997. Osteoprotegerin: A Novel Secreted Protein Involved in the Regulation of Bone Density. *Cell,* 89**,** 309-319.
SIMS, N. A. & MARTIN, T. J. 2014. Coupling the activities of bone formation and resorption: a multitude of signals within the basic multicellular unit. *Bonekey Rep,* 3**,** 481.
SIRIS, E. S., CHEN, Y.-T., ABBOTT, T. A., BARRETT-CONNOR, E., MILLER, P. D., WEHREN, L. E. & BERGER, M. L. 2004. Bone Mineral Density Thresholds for Pharmacological Intervention to Prevent Fractures. *Archives of Internal Medicine,* 164**,** 1108-1112.
SKEDROS, J. G., MENDENHALL, S. D., KISER, C. J. & WINET, H. 2009. Interpreting cortical bone adaptation and load history by quantifying osteon morphotypes in circularly polarized light images. *Bone,* 44**,** 392-403.
SKEDROS, J. G., SORENSON, S. M. & JENSON, N. H. 2007. Are distributions of secondary osteon variants useful for interpreting load history in mammalian bones? *Cells Tissues Organs,* 185**,** 285-307.
SKEDROS, J. G., SYBROWSKY, C. L., ANDERSON, W. E. & CHOW, F. 2011. Relationships between in vivo microdamage and the remarkable regional material and strain heterogeneity of cortical bone of adult deer, elk, sheep and horse calcanei. *J Anat,* 219**,** 722-33.
SKEDROS, J. G., SYBROWSKY, C. L., PARRY, T. R. & BLOEBAUM, R. D. 2003. Regional differences in cortical bone organization and microdamage prevalence in Rocky Mountain mule deer. *Anat Rec A Discov Mol Cell Evol Biol,* 274**,** 837-50.
SMIT, T. H. & BURGER, E. H. 2000. Is BMU-Coupling a Strain-Regulated Phenomenon? A Finite Element Analysis. *Journal of Bone and Mineral Research,* 15**,** 301-307.
SMIT, T. H., BURGER, E. H. & HUYGHE, J. M. 2002. A Case for Strain-Induced Fluid Flow as a Regulator of BMU-Coupling and Osteonal Alignment. *Journal of Bone and Mineral Research,* 17**,** 2021-2029.
SÖZEN, T., ÖZıŞıK, L. & BAŞARAN, N. Ç. 2017. An overview and management of osteoporosis. *European journal of rheumatology,* 4**,** 46-56.
STEINBUCH, M., YOUKET, T. E. & COHEN, S. 2004. Oral glucocorticoid use is associated with an increased risk of fracture. *Osteoporos Int,* 15**,** 323-8.
STOUT, S. D., BRUNSDEN, B. S., HILDEBOLT, C. F., COMMEAN, P. K., SMITH, K. E. & TAPPEN, N. C. 1999. Computer-Assisted 3D Reconstruction of Serial Sections of Cortical Bone to Determine the 3D Structure of Osteons. *Calcified Tissue International,* 65**,** 280-284.
SU, N., YANG, J., XIE, Y., DU, X., CHEN, H., ZHOU, H. & CHEN, L. 2019. Bone function, dysfunction and its role in diseases including critical illness. *International journal of biological sciences,* 15**,** 776-787.
SUGIMOTO, M., TAKAHASHI, S., TOGUCHIDA, J., KOTOURA, Y., SHIBAMOTO, Y. & YAMAMURO, T. 1991. Changes in bone after high-dose irradiation. Biomechanics and histomorphology. *J Bone Joint Surg Br,* 73**,** 492-7.
SWARTHOUT, J. T., D'ALONZO, R. C., SELVAMURUGAN, N. & PARTRIDGE, N. C. 2002. Parathyroid hormone-dependent signaling pathways regulating genes in bone cells. *Gene,* 282**,** 1-17.
TAKAHASHI, H. & NORIMATSU, H. 1976. The longitudinal and transverse rate of resorption of the Haversian system in canine bone. *Jaworski JF,* 143.

TAKAHASHI, S., SUGIMOTO, M., KOTOURA, Y., SASAI, K., OKA, M. & YAMAMURO, T. 1994. Long-term changes in the haversian systems following high-dose irradiation. An ultrastructural and quantitative histomorphological study. *J Bone Joint Surg Am,* 76**,** 722-38.

TAKAKURA, A., LEE, J.-W., HIRANO, K., ISOGAI, Y., ISHIZUYA, T., TAKAO-KAWABATA, R. & IIMURA, T. 2017. Administration frequency as well as dosage of PTH are associated with development of cortical porosity in ovariectomized rats. *Bone Research,* 5**,** 17002.

TAMI, A. E., NASSER, P., SCHAFFLER, M. B. & TATE, M. L. K. 2003. Noninvasive fatigue fracture model of the rat ulna. *Journal of Orthopaedic Research,* 21**,** 1018-1024.

TAPPEN, N. C. 1977. Three dimensional studies of resorption spaces and developing osteons. *American Journal of Anatomy,* 149**,** 301-317.

TARRIDE, J. E., HOPKINS, R. B., LESLIE, W. D., MORIN, S., ADACHI, J. D., PAPAIOANNOU, A., BESSETTE, L., BROWN, J. P. & GOEREE, R. 2012. The burden of illness of osteoporosis in Canada. *Osteoporosis International,* 23**,** 2591-2600.

THOMAS, C. D., FEIK, S. A. & CLEMENT, J. G. 2006. Increase in pore area, and not pore density, is the main determinant in the development of porosity in human cortical bone. *J Anat,* 209**,** 219-30.

THOMPSON, D. D., SIMMONS, H. A., PIRIE, C. M. & KE, H. Z. 1995. FDA guidelines and animal models for osteoporosis. *Bone,* 17**,** S125-S133.

THURNER, P. J., WYSS, P., VOIDE, R., STAUBER, M., STAMPANONI, M., SENNHAUSER, U. & MULLER, R. 2006. Time-lapsed investigation of three-dimensional failure and damage accumulation in trabecular bone using synchrotron light. *Bone,* 39**,** 289-99.

TOBEIHA, M., MOGHADASIAN, M. H., AMIN, N. & JAFARNEJAD, S. 2020. RANKL/RANK/OPG Pathway: A Mechanism Involved in Exercise-Induced Bone Remodeling. 2020**,** 6910312.

TOMES, J. & MORGAN, C. D. 1853. Observations on the Structure and Development of Bone. *Philosophical Transactions of the Royal Society of London,* 143**,** 109-139.

TORRANCE, A. G., MOSLEY, J. R., SUSWILLO, R. F. & LANYON, L. E. 1994. Noninvasive loading of the rat ulna in vivo induces a strain-related modeling response uncomplicated by trauma or periostal pressure. *Calcif Tissue Int,* 54**,** 241-7.

TORRES-DEL-PLIEGO, E., VILAPLANA, L., GUERRI-FERNANDEZ, R. & DIEZ-PEREZ, A. 2013. Measuring bone quality. *Curr Rheumatol Rep,* 15**,** 373.

TSAI, J. N., UIHLEIN, A. V., LEE, H., KUMBHANI, R., SIWILA-SACKMAN, E., MCKAY, E. A., BURNETT-BOWIE, S.-A. M., NEER, R. M. & LEDER, B. Z. 2013. Teriparatide and denosumab, alone or combined, in women with postmenopausal osteoporosis: the DATA study randomised trial. *The Lancet,* 382**,** 50-56.

TURNBULL, T. L., GARGAC, J. A., NIEBUR, G. L. & ROEDER, R. K. 2011. Detection of fatigue microdamage in whole rat femora using contrast-enhanced micro-computed tomography. *J Biomech,* 44**,** 2395-400.

TURNER, A. S. 2001. Animal models of osteoporosis--necessity and limitations. *Eur Cell Mater,* 1**,** 66-81.

TURNER, C., BURR, D., JEE, W. S., SMITH, S., RECKER, R. R., AXELROD, D. W., TAKAHASHI, H. E., VILLANUEVA, A. R., HIGH, W. B., MARTIN, R. B. &

PARFITT, A. M. 2004. Tribute to Harold M. Frost M.D. *J Musculoskelet Neuronal Interact,* 4**,** 347-56.
TURNER, R. T., HANNON, K. S., GREENE, V. S. & BELL, N. H. 1995. Prednisone inhibits formation of cortical bone in sham-operated and ovariectomized female rats. *Calcif Tissue Int,* 56**,** 311-5.
TURNER, R. T., MARAN, A., LOTINUN, S., HEFFERAN, T., EVANS, G. L., ZHANG, M. & SIBONGA, J. D. 2001. Animal Models For Osteoporosis. *Reviews in Endocrine and Metabolic Disorders,* 2**,** 117-127.
UZAWA, T., HORI, M., EJIRI, S. & OZAWA, H. 1995. Comparison of the effects of intermittent and continuous administration of human parathyroid hormone(1-34) on rat bone. *Bone,* 16**,** 477-84.
VAN OERS, R. F. M., RUIMERMAN, R., VAN RIETBERGEN, B., HILBERS, P. A. J. & HUISKES, R. 2008. Relating osteon diameter to strain. *Bone,* 43**,** 476-482.
VAN STAA, T. P., LAAN, R. F., BARTON, I. P., COHEN, S., REID, D. M. & COOPER, C. 2003. Bone density threshold and other predictors of vertebral fracture in patients receiving oral glucocorticoid therapy. *Arthritis Rheum,* 48**,** 3224-9.
VAN STAA, T. P., LEUFKENS, H. G. M., ABENHAIM, L., ZHANG, B. & COOPER, C. 2000. Use of Oral Corticosteroids and Risk of Fractures. *Journal of Bone and Mineral Research,* 15**,** 993-1000.
VEDI, S., ELKIN, S. L. & COMPSTON, J. E. 2005. A Histomorphometric Study of Cortical Bone of the Iliac Crest in Patients Treated with Glucocorticoids. *Calcified Tissue International,* 77**,** 79-83.
VERBORGT, O., GIBSON, G. J. & SCHAFFLER, M. B. 2000. Loss of Osteocyte Integrity in Association with Microdamage and Bone Remodeling After Fatigue In Vivo. *Journal of Bone and Mineral Research,* 15**,** 60-67.
VOIDE, R., SCHNEIDER, P., STAUBER, M., VAN LENTHE, G. H., STAMPANONI, M. & MULLER, R. 2011. The importance of murine cortical bone microstructure for microcrack initiation and propagation. *Bone,* 49**,** 1186-93.
VOIDE, R., SCHNEIDER, P., STAUBER, M., WYSS, P., STAMPANONI, M., SENNHAUSER, U., VAN LENTHE, G. H. & MULLER, R. 2009. Time-lapsed assessment of microcrack initiation and propagation in murine cortical bone at submicrometer resolution. *Bone,* 45**,** 164-73.
VOOR, M. J., YANG, S., BURDEN, R. L. & WADDELL, S. W. 2008. In vivo micro-CT scanning of a rabbit distal femur: Repeatability and reproducibility. *Journal of Biomechanics,* 41**,** 186-193.
VRAHNAS, C., BUENZLI, P. R., PEARSON, T. A., PENNYPACKER, B. L., TOBIN, M. J., BAMBERY, K. R., DUONG, L. T. & SIMS, N. A. 2018. Differing Effects of Parathyroid Hormone, Alendronate, and Odanacatib on Bone Formation and on the Mineralization Process in Intracortical and Endocortical Bone of Ovariectomized Rabbits. 103**,** 625-637.
VU, T. D., WANG, X. F., WANG, Q., CUSANO, N. E., IRANI, D., SILVA, B. C., GHASEM-ZADEH, A., UDESKY, J., ROMANO, M. E., ZEBAZE, R., JERUMS, G., BOUTROY, S., BILEZIKIAN, J. P. & SEEMAN, E. 2013. New insights into the effects of primary hyperparathyroidism on the cortical and trabecular compartments of bone. *Bone,* 55**,** 57-63.

WAARSING, J., DAY, J., VAN DER LINDEN, J., EDERVEEN, A., SPANJERS, C., DE CLERCK, N., SASOV, A., VERHAAR, J. & WEINANS, H. 2004. Detecting and tracking local changes in the tibiae of individual rats: a novel method to analyse longitudinal in vivo micro-CT data. *Bone,* 34**,** 163-169.

WANDERMAN, N. R., MALLET, C., GIAMBINI, H., BAO, N., ZHAO, C., AN, K. N., FREEDMAN, B. A. & NASSR, A. 2018. An Ovariectomy-Induced Rabbit Osteoporotic Model: A New Perspective. *Asian Spine J,* 12**,** 12-17.

WANG, X., MASSE, D. B., LENG, H., HESS, K. P., ROSS, R. D., ROEDER, R. K. & NIEBUR, G. L. 2007. Detection of trabecular bone microdamage by micro-computed tomography. *J Biomech,* 40**,** 3397-403.

WEIN, M. N. & KRONENBERG, H. M. 2018. Regulation of Bone Remodeling by Parathyroid Hormone. *Cold Spring Harb Perspect Med,* 8.

WEINSTEIN, R. S. 2011. Glucocorticoid-Induced Bone Disease. *The New England Journal of Medicine,* 365**,** 62-70.

WEINSTEIN, R. S. 2012. Glucocorticoid-induced osteoporosis and osteonecrosis. *Endocrinology and metabolism clinics of North America,* 41**,** 595-611.

WEINSTEIN, R. S., JILKA, R. L., PARFITT, A. M. & MANOLAGAS, S. C. 1998. Inhibition of osteoblastogenesis and promotion of apoptosis of osteoblasts and osteocytes by glucocorticoids. Potential mechanisms of their deleterious effects on bone. *The Journal of Clinical Investigation,* 102**,** 274-282.

WEITZMANN, M. N., ROGGIA, C., TORALDO, G., WEITZMANN, L. & PACIFICI, R. 2002. Increased production of IL-7 uncouples bone formation from bone resporption during estrogen deficiency. *Journal of Clinical Investigation,* 110**,** 1643-50.

WEN, X.-X., XU, C., WANG, F.-Q., FENG, Y.-F., ZHAO, X., YAN, Y.-B. & LEI, W. 2015. Temporal Changes of Microarchitectural and Mechanical Parameters of Cancellous Bone in the Osteoporotic Rabbit. *BioMed Research International,* 2015**,** 11.

WESTENDORF, J. J., KAHLER, R. A. & SCHROEDER, T. M. 2004. Wnt signaling in osteoblasts and bone diseases. *Gene,* 341**,** 19-39.

WILLIE, B. M., BIRKHOLD, A. I., RAZI, H., THIELE, T., AIDO, M., KRUCK, B., SCHILL, A., CHECA, S., MAIN, R. P. & DUDA, G. N. 2013. Diminished response to in vivo mechanical loading in trabecular and not cortical bone in adulthood of female C57Bl/6 mice coincides with a reduction in deformation to load. *Bone,* 55**,** 335-46.

WINZENRIETH, R., HUMBERT, L., DI GREGORIO, S., BONEL, E., GARCÍA, M. & DEL RIO, L. 2018. Effects of osteoporosis drug treatments on cortical and trabecular bone in the femur using DXA-based 3D modeling. *Osteoporosis International,* 29**,** 2323-2333.

WOJDA, S. J., WEYLAND, D. R., GRAY, S. K., MCGEE-LAWRENCE, M. E., DRUMMER, T. D. & DONAHUE, S. W. 2013. Black bears with longer disuse (hibernation) periods have lower femoral osteon population density and greater mineralization and intracortical porosity. *Anat Rec (Hoboken),* 296**,** 1148-53.

WOLFF, J. 1892. *Das Gesetz der Transformation der Knochen,* Berlin, Hirschwald Verlag.

WWW.IOFBONEHEALTH.ORG. Available: www.iofbonehealth.org.

YAMAMOTO, T., HASEGAWA, T., SASAKI, M., HONGO, H., TSUBOI, K., SHIMIZU, T., OTA, M., HARAGUCHI, M., TAKAHATA, M., ODA, K., LUIZ DE FREITAS, P. H., TAKAKURA, A., TAKAO-KAWABATA, R., ISOGAI, Y. & AMIZUKA, N. 2016. Frequency of Teriparatide Administration Affects the Histological Pattern of Bone Formation in Young Adult Male Mice. *Endocrinology,* 157**,** 2604-20.

YAMANE, H., TAKAKURA, A., SHIMADZU, Y., KODAMA, T., LEE, J. W., ISOGAI, Y., ISHIZUYA, T., TAKAO-KAWABATA, R. & IIMURA, T. 2017. Acute development of cortical porosity and endosteal naive bone formation from the daily but not weekly short-term administration of PTH in rabbit. 12**,** e0175329.

YAVROPOULOU, M. P. & PAPAPOULOS, S. E. 2010. Targeting the Wnt signaling pathway for the development of novel therapies for osteoporosis. *Expert Review of Endocrinology & Metabolism,* 5**,** 711+.

YONEDA, T., HAGINO, H., SUGIMOTO, T., OHTA, H., TAKAHASHI, S., SOEN, S., TAGUCHI, A., NAGATA, T., URADE, M., SHIBAHARA, T. & TOYOSAWA, S. 2016. Antiresorptive agent-related osteonecrosis of the jaw: Position Paper 2017 of the Japanese Allied Committee on Osteonecrosis of the Jaw. *J Bone Miner Metab*.

YOUSEFZADEH, N., KASHFI, K., JEDDI, S. & GHASEMI, A. 2020. Ovariectomized rat model of osteoporosis: a practical guide. *Excli j,* 19**,** 89-107.

ZEBAZE, R. & SEEMAN, E. 2015. Cortical Bone: A Challenging Geography. *Journal of Bone and Mineral Research,* 30**,** 24-29.

ZEBAZE, R., TAKAO-KAWABATA, R., PENG, Y., ZADEH, A. G., HIRANO, K., YAMANE, H., TAKAKURA, A., ISOGAI, Y., ISHIZUYA, T. & SEEMAN, E. 2017. Increased cortical porosity is associated with daily, not weekly, administration of equivalent doses of teriparatide. *Bone,* 99**,** 80-84.

ZEBAZE, R. M. D., GHASEM-ZADEH, A., BOHTE, A., IULIANO-BURNS, S., MIRAMS, M., PRICE, R. I., MACKIE, E. J. & SEEMAN, E. 2010. Intracortical remodelling and porosity in the distal radius and post-mortem femurs of women: a cross-sectional study. *The Lancet,* 375**,** 1729-1736.

ZHOU, H., SHEN, V., DEMPSTER, D. W. & LINDSAY, R. 2001. Continuous parathyroid hormone and estrogen administration increases vertebral cancellous bone volume and cortical width in the estrogen-deficient rat. *J Bone Miner Res,* 16**,** 1300-7.

ZHOU, S.-A. & BRAHME, A. 2008. Development of phase-contrast X-ray imaging techniques and potential medical applications. *Physica Medica,* 24**,** 129-148.

TURNBULL, T. L., GARGAC, J. A., NIEBUR, G. L. & ROEDER, R. K. 2011. Detection of fatigue microdamage in whole rat femora using contrast-enhanced micro-computed tomography. *J Biomech,* 44**,** 2395-400.